1997

Studies of the Morphology and Dynamics of Flame-Generated Agglomerates Using Dynamic Light Scattering.

Glenn Michael Waguespack
Louisiana State University and Agricultural & Mechanical College

INFORMATION TO USERS

This manuscript has been reproduced from the microfilm master. UMI films the text directly from the original or copy submitted. Thus, some thesis and dissertation copies are in typewriter face, while others may be from any type of computer printer.

The quality of this reproduction is dependent upon the quality of the copy submitted. Broken or indistinct print, colored or poor quality illustrations and photographs, print bleedthrough, substandard margins, and improper alignment can adversely affect reproduction.

In the unlikely event that the author did not send UMI a complete manuscript and there are missing pages, these will be noted. Also, if unauthorized copyright material had to be removed, a note will indicate the deletion.

Oversize materials (e.g., maps, drawings, charts) are reproduced by sectioning the original, beginning at the upper left-hand corner and continuing from left to right in equal sections with small overlaps. Each original is also photographed in one exposure and is included in reduced form at the back of the book.

Photographs included in the original manuscript have been reproduced xerographically in this copy. Higher quality 6" x 9" black and white photographic prints are available for any photographs or illustrations appearing in this copy for an additional charge. Contact UMI directly to order.

UMI

A Bell & Howell Information Company
300 North Zeeb Road, Ann Arbor MI 48106-1346 USA
313/761-4700 800/521-0600

STUDIES OF THE MORPHOLOGY AND DYNAMICS OF FLAME-GENERATED AGGLOMERATES USING DYNAMIC LIGHT SCATTERING

A Dissertation

Submitted to the Graduate Faculty of the
Louisiana State University and
Agricultural and Mechanical College
in partial fulfillment of the
requirements for the degree of
Doctor of Philosophy

in

The Department of Mechanical Engineering

by
Glenn Waguespack
B.S., Louisiana State University, 1989
May 1997

Acknowledgements

This author wishes to express his gratitude to all whose contributions have made this research possible. Particular thanks are due to this author's major professor, Dr. Tryfon T. Charalampopoulos. Without his supportful advice and tireless efforts none of this work would have been possible. Additional acknowledgements are due to my colleagues and predecessors Zhiqing Zhang, Demetris Venizelos, and David Hahn, who, along with Dr. Charalampopoulos, all played key roles in the design and construction of the experimental facility used in this study. This author also wishes to thank all other colleagues and friends, including Pradipta Panigrahi, Ruben Munoz, Venkatesh Shanmugam, Anna Omeltchenko, Barry Stagg, and many others, who have provided cheerful encouragement and stimulating conversations, frequently accompanying the consumption of massive amounts of caffeine. The technical support offered by Rodger Conway, Victor Ramirez, Alaric Haag, and Tyrone Schultz is also greatly appreciated. This author also wishes to thank Dr. Paul S. Russo for providing a version of CONTIN compiled for use on a PC along with technical suggestions that have proved extremely valuable in this research.

Acknowledgements are also due to the Air Force Office of Scientific Research and the National Science Foundation, who have both contributed monetary support for this work through research grants (numbers F49620-0477 and CTS-9528598, respectively). The Louisiana State University Board of Regents have also supplied financial contributions in the form of a three-year fellowship.

Finally, this research could never have been completed without strong support from home. This author wishes to thank his parents Mrs. Gerard N. Waguespack and Mr. Robert G. Waguespack, along with the rest of his family, for their loving encouragement and support throughout the years.

Table of Contents

page

page

Abstract

Accurate determination of the morphology and dynamics of aerosols consisting of agglomerated sub-micron sized particulates is needed for soot formation studies, process monitoring in flame-based materials synthesis applications, and pollution control studies. The objective of the current study is to investigate the application of dynamic light scattering (DLS) to flames as an extension of current measurement technologies. Unlike previous DLS flame studies, conventional polarized DLS is supplemented with depolarized DLS measurements to account for the agglomerates' anisotropy. Because unavailable relationships between the agglomerates' morphological parameters and the Brownian translational and rotational diffusion coefficients under non-continuum conditions are required for accurately determining agglomerate morphology from DLS flame measurements, the potential of combining DLS-determined diffusion coefficients with independently-determined morphology measurements to provide the necessary experimental relationships is investigated.

For this study DLS measurements and thermophoretic agglomerate sampling were performed on chainlike iron oxide agglomerates occurring within a 1/2" diameter $Fe(CO)_5$-seeded CO/O_2 diffusion flame. Systematic detection system errors in the DLS measurements, caused by dead time and afterpulsing, were virtually eliminated by cross-correlating the outputs of two separate photomultiplier tubes. The accompanying decrease in the signal-to-noise ratio was compensated by increasing the incident laser power and experiment duration time. This duration time increase was accomplished by combining the data from multiple five-minute experiments because of severe iron oxide deposition on the burner and flame stabilizer occurring with longtime, continuous flame operation. Accurate depolarized DLS data was thus generated from a flame environment for the first time.

Inverse Laplace transform analyses of the DLS data using CONTIN produced unacceptable fits of the data. Cumulants fits were more accurate but systematically produced negative second cumulant coefficients, which prevent a complete linewidth distribution analysis and indicate the presence of invalid assumptions used in the conventional theoretical DLS interpretations. Additional experiments implicated incident beam nonuniformities as a partial cause of this effect. Average diffusion coefficients extracted from the first cumulants exhibited an order-of-magnitude agreement with theoretical estimates based on ex situ morphology and flame temperature measurements.

Chapter 1

Introduction

Continual developments in the technology of materials synthesis from combustion-generated particles and increasing interest in pollution control and the study of combustion processes create a growing need for accurate and efficient characterization and measurement of the morphological and dynamic properties of flame-generated, submicron-sized agglomerates. Within the field of materials synthesis, flame generation techniques are becoming increasingly widespread because of their inherent cleanliness, high output, low capital cost, speed, and ability to produce high-purity products ([Ulrich, 1984], [Pratsinis and Mastrangleo, 1989]). For example, carbon black is one of the most commonly used flame-generated commodities. Frequently used as a pigment in inks and paints and as a strengthening agent in rubber (especially for tires) and other polymers, carbon black occurs as carbonaceous soot that is collected from oil-seeded natural gas and liquid fuel flames [Ulrich, 1984]. The various grades of carbon black, which determine the properties imparted to rubber and govern its appropriateness for other applications, are determined by the morphological properties of their constituent agglomerates [Medalia and Heckman, 1969].

Other common materials formed using flame processes are fumed silica, titanium dioxide, uranium dioxide, and numerous advanced ceramics ([Ulrich, 1984], [Wu, et al., 1993]). Fumed silica, which was originally produced as a substitute for carbon black by the Germans during World War II, is used in silicone rubber products, glass-fiber-reinforced polyester resins, and other commodities [Ulrich, 1984]. Titanium dioxide is a common pigment in paints. Additionally, pellets compressed from flame-generated uranium dioxide are utilized in nuclear power plants.

Flame technology permits the production of ceramic powders with grain sizes as small as one nanometer. Ceramics consisting of superfine grains exhibit different properties from coarser-grained ceramics because a larger proportion of the molecules occur on the grain surfaces and the number of molecules within each grain is too small to define bulk properties [Wu, et al., 1993]. These small grain sizes typically increase the strength, hardness, and toughness of the ceramics. Additionally, the large surface area per unit volume reduces the ceramic's sintering temperature. This increased area also makes flame generated ceramic particles ideal for use as catalysts and as substrates for catalysts [Wu, et al., 1993]. As with carbon black, this dependence of the applicability and properties of flame-synthesized ceramic powders upon particle size and morphology requires careful particle monitoring and control during the production process. Thus, a need exists for efficient real-time measurements of the morphology of agglomerates generated by combustion processes for applications in quality control.

In addition to product monitoring applications, however, accurate measurements of the morphology of the agglomerates present within their developmental stages in flames are needed in order to test theories regarding the mechanisms of particulate formation and agglomeration. Such theories are important for developing a greater understanding of flame processes in order to advance the development of new flame synthesis and anti-pollution technologies. Additionally, accurate measurements of the morphological and optical properties of particulate matter in flames provides information necessary for determining the flames' radiative properties.

Current theories describing the formation and subsequent agglomeration of particles within a flame propose that at the earliest growth stages small groups of molecules precipitate from the vapor phase in a process known as *nucleation*. When different particles of condensed matter collide due to Brownian motion, they typically fuse together and *coalesce* into a single particle, which is usually spherical because of the aggregate's physical tendency to minimize its surface free energy [Wu, et al., 1993]. The

tendency of the fused particles to coalesce is strongly related to the particles' viscosity and temperature [Wu, et al., 1993]. When coalescence is rapid enough that the process is generally complete before any further collisions occur, the particle growth rate is governed predominantly by the collision rate [Ulrich and Subramanian, 1977]. As the particles cool, the viscosity increases to a point at which the particles no longer coalesce upon collision but instead form fused aggregates consisting of discrete primary particles [Ulrich, 1984]. At later stages, these aggregates collide to form weakly joined agglomerates. In some cases, the particles do not readily coalesce during the early formative stages, but instead fuse together to form irregular flocs. In such cases, the particle growth rate can be dominated by the rate of coalescence [Ulrich and Subramanian, 1977]. With cooling and the occurrence of further collisions, these flocs continue to form aggregates and agglomerates in a manner similar to the later stages of the collision-governed formation process. Variations in the properties of the condensed material and the cooling rate within the flame cause variations in the formation mechanisms of particles and agglomerates. For experimentally studying these formation mechanisms, accurate measurements of the particulates' morphological parameters at various locations within the flame are crucial [Ulrich and Subramanian, 1977].

In addition to the above-mentioned applications, accurate knowledge of agglomerate morphology and dynamics is needed for pollution control studies. Some metal oxides formed by incineration processes are known toxins that can cause lung damage [Wu, et al., 1993]. Studies of the deposition rates of fibrous particulates, such as asbestos or metal oxide agglomerates, within lung airways rely upon information about the dynamic behavior of such particles [Asgharian, et al., 1988]. Knowledge about the dynamics of fibrous particles is also useful in particle filtration investigations because of the dependency of the filters' collection efficiencies on the particles' orientation distribution [Cheng, et al., 1991].

Current particulate measurement techniques are generally classified according to two general categories: ex situ techniques and in situ techniques. Ex situ techniques are based upon the removal of a sample (the agglomerates) from its natural environment (the flame) so that it can be studied under different controlled conditions. In situ measurements are measurements that are performed on the sample within its natural environment.

Ex situ measurements of the properties of particulate matter in flames generally involve the extraction of the sample from the flame using a probe and an analysis of the extracted sample's properties using techniques such as transmission electron microscopy or powder X-ray diffraction. These procedures frequently permit the use of sophisticated and accurate analysis techniques because the samples can be placed in well-controlled environments that are optimized for the determination of the desired measurable quantities. Often, however, little is known about the extent of unintentional changes to the sample's properties incurred by removing it from its natural environment and preparing it for analysis. This possible source of error is one of the primary disadvantages of ex situ methods. Additionally, ex situ measurement techniques are typically labor-intensive, multi-step processes in that they require removal of the sample from its environment, preparation of the sample for analysis, operation of the chosen method of analysis, and interpretation of the results.

In situ methods generally simplify the number of required steps by eliminating the necessity of removing and preparing the sample prior to analysis. Thus, in situ techniques are generally more suitable for automation than ex situ techniques. More importantly, by measuring the sample's properties within its natural environment, in situ measurement methods eliminate possible disturbances to the sample due to extraction and preparation procedures. Frequently based upon the use of optics, in situ methods do have one disadvantage: accurate data interpretation often relies upon accurate theoretical or empirical knowledge of the physical processes exploited by the measurement technique,

which often requires some foreknowledge about the sample being measured. For example, classical light scattering diagnostics are often strongly dependent upon the refractive index of the measured particles. Since accurate refractive index data are seldom available for particulate matter under flame conditions, this dependence produces a major source of uncertainty in the interpretation of the data.

Despite these disadvantages, the important advantages offered by in situ methods inspire ongoing research to develop and refine in situ measurement techniques for determining the properties of particulate matter within flames and other solvent media. The ultimate goal of these ongoing investigations is to be able to use exclusively in situ methods to accurately and completely characterize the optical, morphological, and dynamic properties of aerosols of any arbitrary structure.

The greatest advantage of in situ optical measurement methods is that disturbances to the sample during measurement are virtually eliminated. Optical diagnostics are generally classified according to two types of measurements: *classical light scattering* (CLS), in which the particle properties are inferred from the average intensity of the scattered light, and *dynamic light scattering* (DLS), in which the particle properties are inferred from the scattered light's temporal fluctuations.

Classical light scattering measurements are interpreted by relating the variation of the average scattered light intensity with either scattering angle, wavelength, or polarization to theoretical light scattering models given by electromagnetic theory. Although the theoretical scattered light solutions are sometimes complicated, the results of electromagnetic theory are well-established and thus present an accurate theoretical basis for the inversion of classical light scattering data. This advantage, however, is offset by several disadvantages. Interpretation of classical light scattering data requires knowledge of the complex refractive index $m = n - i\kappa$ of the scattering particles. Accurate knowledge of this property for particulate matter within a high temperature flame, where the exact chemical composition is frequently unknown, is seldom present. Additional

disadvantages of classical light scattering methods are the experimental difficulties associated with the measurements. For example, calibration with respect to gases of known scattering characteristics is required in order to obtain the true average scattered light intensity. Additionally, the alteration of experimental parameters, such as the scattering angle, in order to obtain sufficient information for data inversion can sometimes cause misalignment of the optical system. Despite these disadvantages, classical light scattering has been extensively used to determine morphological and optical properties of flame-generated particulates (see for example Penner, et al. (1976b), Santoro, et al. (1983), Drolen and Tien (1987), Charalampopoulos (1987), Charalampopoulos and Chang (1991), and Sorensen, et al. (1992)).

Dynamic light scattering (DLS) methods are based upon the measurement and analysis of the scattered light's temporal fluctuations that result from the particles' random and deterministic motion. These fluctuations are either processed as an intensity correlation function or an equivalent power spectrum. An analysis of the decay characteristics of the intensity correlation function (or the broadening of the power spectrum) permits the determination of the particles' Brownian diffusion coefficients, which characterize their random motion. Information about the particles' morphological properties are subsequently inferred from the diffusion coefficient data. The major disadvantage of dynamic light scattering is that the interpretation of the results relies not only on the electromagnetic theory needed to describe the light scattering process, but also on theoretical and/or empirical information about the relationship between the statistical nature of the particle motion, the thermophysical properties of the solvent gas, and the morphological parameters of the scattering particles. Under many circumstances, such as when non-continuum flow effects are dominant, these dynamic relationships are not as well established as the electromagnetic relationships. The major advantage of dynamic light scattering, however, is that the sensitivity of the inferred results to the particles' refractive index is much lower than similar results obtained from classical light scattering

because these results depend only upon the temporal variation of the scattered field, not its absolute intensity. Additionally, normalization of the scattered light correlation functions with respect to its baseline intensity frequently simplifies the form of the theoretical expressions needed for data inversion. Because of the above-mentioned refractive-index insensitivity and the practical need for more accurate information about the dynamic motion of submicron-sized particles, this investigation concentrates predominantly upon the use of dynamic light scattering for measurements of the particulate morphological and dynamic properties.

Dynamic light scattering (DLS), which is sometimes called photon correlation spectroscopy (PCS) or diffusion broadening spectroscopy (DBS), was an outcome of the development of the laser as a high-intensity, coherent light source. These measurement and analysis techniques were developed and refined in the 1960's and 1970's by Forrester (1961), Pecora (1964, 1968), Benedek (1969), Jakeman (1970), Cummins and Swinney (1970), and others. Since then, dynamic light scattering has been used for numerous applications within the field of biochemistry ([Pecora, 1985], [Ford, 1972]) requiring the determination of the dynamics of various macromolecules in liquid solutions.

The use of dynamic light scattering in the study of aerosols was first investigated by Hinds and Reist (1972), who, assuming size monodispersity and correcting their results for slip flow effects, demonstrated that the sizes inferred from condensing dibutylpthalate droplets and nebulized polystyrene spheres agree with CLS results and manufacturer's specifications, respectively, to within 10%. This work was followed by Penner, et al. (1976a,b), who extended the theory to account for the effects of non-uniform illumination of moving flows and proceeded to perform the first polarized DLS experiments on flame systems. In comparing the inferred diameters to those obtained from classical light scattering and extinction measurements, Penner and coworkers found

a large discrepancy that probably resulted from their neglect of slip flow effects. They also assumed that their samples consisted entirely of monodisperse spherical particles.

Additional flame studies were later performed by Driscoll, et al. (1979); Penner and Chang (1981); King, et al. (1982, 1983); Flower (1983); Scrivner, et al. (1986); Charalampopoulos (1987); Charalampopoulos and Chang (1988); Venizelos (1989); Ueyama, et al. (1993); and Cai and Sorenson (1994). All of these studies utilized polarized light scattering, where the incident light and the detected light share the same polarization, and were thus able to infer the Brownian translational diffusion coefficients of the flame-borne particulates. Some discrepancies were noted by King, et al. (1983) between the measured diffusion coefficients and those calculated through the use of the slip-corrected Stokes-Einstein equations with particles of known size, suggesting possible deficiencies in the current correction factors for slip flow and non-continuum effects. With the exception of Cai and Sorensen (1994), these investigators assumed that the measured particles were spherical and either assumed that particle sizes were monodisperse ([Penner, et al., 1976b], [Driscoll, et al., 1979], [Penner and Chang, 1981]) or utilized a second-order cumulant analysis, as developed by Koppel (1972), to determine the first two moments of the particle size density function. King, et al. (1982) discussed the use of cumulants for data inversion but only used a first-order analysis, which is equivalent to assuming that the particles are monodisperse.

Nonspherical agglomerates were considered in the investigations of Cai and Sorenson (1994) and Xie, et al. (1995). Considering the scattering particles as fractal aggregates, Cai and Sorenson experimentally determined a relationship for an effective translational diffusion radius by comparing the polarized DLS results with the aggregate parameters inferred from CLS measurements. A second-order cumulants fit was used in this investigation. Alternatively, Xie, et al. (1995) utilized polarized DLS with ex situ sampling and TEM analysis to determine the average aspect ratios of straight-chain agglomerates within an aerosol flow extracted from the exhaust gases of an iron-

pentacarbonyl-seeded CO diffusion flame . The inferred aspect ratios were obtained from the first moment of a third-order cumulants analysis by substituting the ex-situ-determined primary particle diameters into a slip-corrected relationship for the cylindrical particles' translational diffusion coefficient (taken from [Zero, 1983]). The results were consistent with the aspect ratios measured using ex situ sampling and TEM analysis.

The previous dynamic light scattering investigations predominantly treated the scattering particles as spheres and accounted for polydispersity through cumulants analyses. The only aerosol study that attempts to measure nonspherical characteristics is the investigation by Xie, et al. (1995). Their measurements, however, suffer from the primary disadvantage of reliance upon ex situ TEM results for the primary particle diameter.

Investigations are currently underway in this laboratory to develop optical diagnostic techniques to efficiently and accurately characterize and measure the optical, morphological, and dynamic properties of nonspherical agglomerated aerosols. These agglomerates are typically classified into three categories: straight chains, which consist of linear strings of primary particles; clusters, which, resembling large spheres, consist of closely packed primary particles; and randomly-branched chains, which are strings of primary particles that branch at random locations into random directions. Representing the simplest agglomerate morphology exhibiting anisotropy, straight chain agglomerates were utilized within the current study to investigate the extension of DLS flame measurement techniques beyond the assumption of particle sphericity. Towards this end, this investigation examines the possibilities presented by depolarized light scattering (DDLS), which measures the fluctuations of light scattered from the agglomerates at a polarization orthogonal to the incident light polarization. Because depolarized scattering is a result of anisotropy within the scattering particles, the corresponding intensity fluctuations are governed by changes in the particles' orientation, which are characterized by the particles' Brownian rotational diffusion coefficients. Simultaneous knowledge of

both the rotational and translational diffusion coefficients, along with accurate relationships describing their dependencies on agglomerate morphology, permits the inference of both the primary particle diameter and aspect ratio of chain-like agglomerates.

Though depolarized dynamic light scattering (DDLS) has not been used for the analysis of aerosols in flames prior to this study, the technique has been used by other investigators for determining the rotational dynamics of macromolecules in liquid solutions. Rotational diffusion constants are determined from DDLS either by measuring the depolarized intensity fluctuations at a zero scattering angle (ie. along the same axis as the incident laser beam) to obtain a correlation function that is solely dependent upon the translational diffusion coefficient or by combining the depolarized correlation functions obtained either at different scattering angles or different detector polarizations to extract the rotational diffusion coefficient.

Zero-angle measurements ([Wada, et al., 1968, 1970], [Schurr and Schmitz, 1973a,b], [Russo, et al., 1986], [Crosby, et al., 1981], [DeLong and Russo, 1990]) are easier to analyze and accommodate large scattering volumes. Additionally, effects of interparticle interference, which can sometimes complicate the analysis of finite-angle measurements, are non-existent. However, inhomogeneities and polarizer leakage can corrupt the data obtained from spatially nonuniform samples, such as the agglomerates occurring within a diffusion flame. Previous finite-scattering-angle studies determining the translational and rotational diffusion coefficients from sets of multi-angle depolarized intensity correlation functions [King and McAdam, 1973] or a combination of polarized and depolarized intensity correlation functions ([Michielsen and Pecora, 1981], [Zero and Pecora, 1982]) assumed monodisperse scattering particles, an assumption that is not generally applicable to combustion systems.

Because the inference of diffusion coefficient and morphology information from dynamic light scattering data requires accurate theoretical relationships representing the scattered light correlation functions, the next chapter of this dissertation presents a detailed

investigation and review of dynamic light scattering theory, eventually establishing relationships between the correlation functions and the Brownian diffusion coefficients that provide the basis for the design, implementation, and interpretation of the optical measurements performed in this study. This theoretical discussion also presents established models relating the semiaxis lengths of a prolate ellipsoid, which is considered as a possible approximation for a chain-like agglomerate, to its Brownian translational and rotational diffusion coefficients and the associated optical polarizability factors necessary for interpreting DLS data. Chapter 2 then concludes by reformulating the final theoretical results in terms of Laplace integrals and in terms of moment generating functions for eventual use in analyzing and interpreting experimental DLS data.

In Chapter 3 the experimental apparatus used within this investigation is described. This apparatus consists of an enclosed burner system for generating chain-like agglomerates of iron oxide by oxidizing iron pentacarbonyl $Fe(CO)_5$ in a CO/O_2 diffusion flame, a thermophoretic probe for ex situ sampling of the agglomerates, and a customized light scattering spectrometer for performing optical measurements.

Chapter 4 then presents the experiments performed using both the apparatus discussed in Chapter 3 and the theory reviewed in Chapter 2 and discusses the analysis and results of each experiment. These experiments utilize thermophoretic agglomerate sampling, flame temperature measurements, measurements of the classical depolarization ratio of light scattered from the flame, and polarized and depolarized dynamic light scattering measurements. The flame temperature measurements and thermophoretic sampling establish the properties of the flame and of the agglomerates relevant to the determination of the agglomerates' Brownian translational and rotational diffusion coefficients. The optical measurements are then used to determine these diffusion coefficients experimentally from the flame. The optically-obtained diffusion coefficients are next related to the thermophoretically obtained morphology parameters and compared with theoretical estimates computed using the measured morphology and flame

temperature results. Considerable attention is given to the methods used to obtain and analyze the DLS results, for depolarized dynamic light scattering measurements are inherently problematic because of the typically low signals obtained and the analysis techniques used for DLS measurements obtained at both polarizations vary in their suitability, based on the functional nature of the data.

The main body of this dissertation is then concluded in Chapter 5 with a summary of the experiments and results, followed by recommendations for future research.

Chapter 2

Theoretical Considerations

This chapter addresses the theory relevant to the use of dynamic light scattering for determining the dynamic properties of straight-chain-agglomerated particulates in a flame. The theory of dynamic light scattering has been investigated thoroughly by various authors since the 1960's, with each investigator typically concentrating on a different aspect or theoretical viewpoint. This chapter attempts to unify many of the aspects of dynamic light scattering theory considered by these investigators by reviewing the theory in a general form and utilizing various physical specifications and approximations to obtain a more specific formulation upon which an experimental scheme for determining the dynamics and morphology of flame-generated straight-chain agglomerates can be based. By considering this theory in the general-to-specific mode, any inadequacies encountered when using the final theoretical model to interpret DLS data can be logically corrected by relaxing or altering some of the assumptions used to obtain the specific model. Alternatively, the design of an experiment can be altered to more accurately accommodate the assumptions necessary for obtaining the final form of the DLS theoretical model.

This chapter does not attempt to present every aspect of dynamic light scattering theory, only those aspects which may be relevant to the present investigation. Hence, primary consideration is given to the theoretical relationship between the translational and rotational diffusion coefficients of the scattering particles and the digital photocount correlation function obtained from the scattered signal. Relationships involving alternative types of dynamic light scattering experiments, such as the use of a Fabry-Perot interferometer to measure the frequency distribution of the scattered light or the

establishment of an analog correlation function of the photocurrent output from a photomultiplier tube detecting the scattered signal, are not considered in detail.

2.1 Dynamic Light Scattering (DLS) Fundamentals

When light is incident upon matter, the fluctuating electromagnetic field of the light waves distorts the matter's interatomic electronic charge distribution to produce fluctuating dipoles that reradiate (or scatter) the light in all directions. The measurement of the properties of this scattered light from a suspension of particulates forms the basis for both classical and dynamic light scattering measurement techniques. In classical techniques, the temporal average of the scattered light intensity is measured to provide information about the physical properties of the particles. In dynamic techniques, the temporal fluctuations of the scattered light are measured and analyzed to provide information about the dynamics of the scattering particles.

The ensuing discussion presents the fundamental principles governing the use of dynamic light scattering techniques to infer various dynamic properties of a cloud of particles suspended in a fluid medium. This discussion first considers a general representation of the electric field scattered from a single particle in the far-field regime so that the various sources of temporal fluctuations in the scattered field resulting from particle motion may be identified. Next, correlation functions are introduced as a tool for statistically quantifying the average dynamic properties of the scattering particles in terms of decay or relaxation times. The general technique of dynamic light scattering is then presented as a method of measuring the correlation function of the scattered light and isolating the different relaxation times corresponding to various dynamic processes by varying the design and user-set parameters of the measurement system. Particularly, pre-detection and post-detection schemes are compared on the basis of their ranges of ability for accurately resolving the temporal variations of the scattered field.

2.1.1 Matrix Representation of the Scattered Field

The propagation and scattering of electromagnetic waves is governed by the Maxwell equations (see [Jackson, 1975]). The fundamental solution of the Maxwell equations for the electric field $\mathbf{E}(\mathbf{r},t)$ of a propagating electromagnetic wave at position $\mathbf{r}$ and time t takes the following form†:

$$\mathbf{E}(\mathbf{r},t) = \mathbf{E}(\mathbf{r}) \exp(-i\omega t), \tag{2.1.1}$$

where $\mathbf{E}(\mathbf{r})$ is a solution of the Helmholtz equation [Guenther, 1990]:

$$\nabla^2\mathbf{E}(\mathbf{r}) + k^2\mathbf{E}(\mathbf{r}) = 0 \tag{2.1.2}$$

with

$$k \equiv \frac{2\pi m}{\lambda}, \tag{2.1.3}$$

where k is propagation constant of the wave, $m \equiv n - i\kappa$ is the complex refractive index of the medium, and λ is the wave's *in vacuo* wavelength. In cases where the wave is propagating through a non-conducting medium, such as air, both the propagation constant k and the refractive index m are real numbers. The simplest solution of the Helmholtz equation corresponds to a plane wave:

$$\mathbf{E}(\mathbf{r}) = \mathbf{E}_0 \exp(i\mathbf{k}\cdot\mathbf{r}) \tag{2.1.4}$$

where $\mathbf{E}_0$ is a vector constant and $\mathbf{k} \equiv k\mathbf{n}$ is the wave vector, with $\mathbf{n}$ being a unit vector along the wavefront's propagation direction.

In scattering theory, the incident electric field $\mathbf{E}_i(\mathbf{r},t)$ is assumed to be a plane wave traveling in the direction of incident wave vector $\mathbf{k}_i$. The scattered wave, which is characterized by its electric field $\mathbf{E}_s(\mathbf{r},t)$, travels in the direction of scattered wave vector $\mathbf{k}_f$, which has the same magnitude as the incident wave vector but is oriented at a scattering angle of θ from the direction of $\mathbf{k}_i$, as illustrated in figure 2.1. The scattering plane is defined as the plane parallel to both $\mathbf{k}_i$ and $\mathbf{k}_f$ that passes through the irradiated volume of scattering particles (the *scattering volume*). The incident light basis vectors $\mathbf{e}_{Hi}$

† All periodic fields are represented in complex notation. The physical value of the field is the real part of the complex field.

and $\mathbf{e}_{Vi}$ are unit vectors used to define the polarization state of the incident electric field $\mathbf{E}_i(\mathbf{r},t)$. These unit vectors, which are both perpendicular to $\mathbf{k}_i$, are respectively oriented parallel and perpendicular to the scattering plane. Similarly-defined scattered light basis vectors $\mathbf{e}_{Hs}$ and $\mathbf{e}_{Vs}$, which are both perpendicular to $\mathbf{k}_f$, are used to characterize the

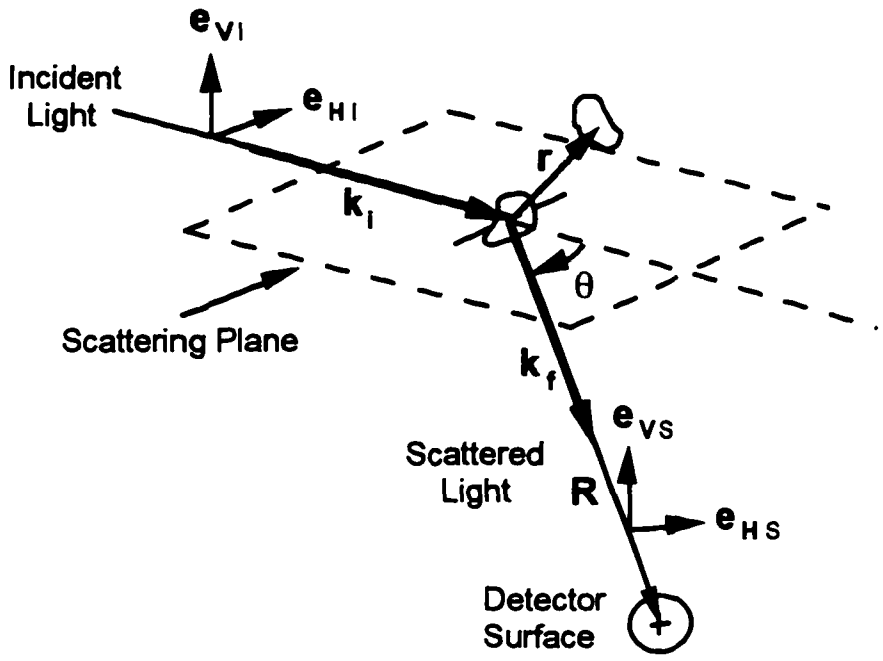

Figure 2.1.1: Illustration of coordinate system and nomenclature used for light scattering experiments.

polarization of the scattered electric field $\mathbf{E}_s(\mathbf{r},t)$. The subscripts H and V respectively refer to the horizontal and vertical directions in deference to the fact that most experimental light scattering spectrometers have horizontal scattering planes. The incident and scattered electric fields can thus be expressed in terms of their polarization components:

$$\mathbf{E}_i(\mathbf{r},t) = [E_{iH}(\mathbf{r},t)\mathbf{e}_{Hi} + E_{iV}(\mathbf{r},t)\mathbf{e}_{Vi}] \qquad (2.1.5a)$$

and

$$\mathbf{E}_s(\mathbf{r},t) = [E_{sH}(\mathbf{r},t)\mathbf{e}_{Hs} + E_{sV}(\mathbf{r},t)\mathbf{e}_{Vs}], \qquad (2.1.5b)$$

where, for simplicity, the r-dependence of the scattered-field basis vector $\mathbf{e}_{Hs}$ (refer to figure 2.1) is not explicitly denoted by the chosen notation. For convenience, the incident

electric field $\mathbf{E}_i(\mathbf{r},t)$ is expressed as the product of a complex vector amplitude factor and an $\mathbf{r}$- and t-dependent phase factor as follows:

$$\mathbf{E}_i(\mathbf{r},t) = [E_{iH}(\mathbf{r})\mathbf{e}_{Hi} + E_{iV}(\mathbf{r})\mathbf{e}_{Vi}] \exp[i(\mathbf{k}_i\cdot\mathbf{r} - \omega t)] \qquad (2.1.6)$$

where the amplitude factor $[E_{iH}(\mathbf{r})\mathbf{e}_{Hi} + E_{iV}(\mathbf{r})\mathbf{e}_{Vi}]$ is expressed as a function of $\mathbf{r}$ to account for any position dependencies of the incident light intensity.

When the incident light encounters a particle located at the origin ($\mathbf{r} = 0$) of the chosen coordinate system the resulting scattered field at a point $\mathbf{R}$ resembles a spherical wave when $R \equiv |\mathbf{R}|$ is much larger than the dimensions of the scattering particle (or larger than the size of the scattering volume when light is scattered from a cloud of particles). This far-field scattered electric field is represented in terms of the amplitude scattering matrix [Bohren and Huffman, 1983]:

$$\begin{Bmatrix} E_{sH}(\mathbf{R},t) \\ E_{sV}(\mathbf{R},t) \end{Bmatrix} = \frac{\exp(ik_f\mathbf{R})}{-ikR} \begin{bmatrix} S_2 & S_3 \\ S_4 & S_1 \end{bmatrix} \begin{Bmatrix} E_{iH}(0,t) \\ E_{iV}(0,t) \end{Bmatrix}$$

or (2.1.7)

$$\begin{Bmatrix} E_{sH}(\mathbf{R},t) \\ E_{sV}(\mathbf{R},t) \end{Bmatrix} = \frac{\exp[i(k_f\mathbf{R} - \omega t)]}{-ikR} \begin{bmatrix} S_2 & S_3 \\ S_4 & S_1 \end{bmatrix} \begin{Bmatrix} E_{iH}(0) \\ E_{iV}(0) \end{Bmatrix},$$

where the amplitude scattering matrix elements S_1, S_2, S_3, and S_4 depend upon the size, shape, orientation, and refractive index of the scattering particle as well as the wavelength of the incident light and the refractive index of the surrounding medium.

Equation 2.1.7 is valid only for a scattering particle located at the origin of the coordinate system. In order to understand the effects of particle translation on the scattered field, this expression is recast for a particle located at a general position $\mathbf{r}$. Displacement of the scatterer's location from the origin to position $\mathbf{r}$ changes the phase of the incident field by $\mathbf{k}_i\cdot\mathbf{r}$. Additionally, the displacement vector between the particle and the detector changes from $\mathbf{R}$ to $\mathbf{R} - \mathbf{r}$ and the scattered field wave vector changes from $\mathbf{k}_f \equiv k\mathbf{R}/R$ to $\mathbf{k}_f' \equiv k(\mathbf{R} - \mathbf{r})/|\mathbf{R} - \mathbf{r}|$. Thus, the $\exp(ik_f\mathbf{R})$ term in equation 2.1.7 changes to $\exp[i\mathbf{k}_f'\cdot(\mathbf{R} - \mathbf{r})]$ or, equivalently, $\exp(ik|\mathbf{R} - \mathbf{r}|)$. Incorporating these effects into equation

2.1.7 gives the following expressions for the scattered electric field from a particle located at position **r**:

$$\begin{Bmatrix} E_{sH}(\mathbf{R},t) \\ E_{sV}(\mathbf{R},t) \end{Bmatrix} = \frac{\exp[i\mathbf{k}_f'\cdot(\mathbf{R}-\mathbf{r})]\exp(-i\omega t)}{-ik|\mathbf{R}-\mathbf{r}|}\begin{bmatrix} S_2 & S_3 \\ S_4 & S_1 \end{bmatrix}\begin{Bmatrix} E_{iH}(\mathbf{r},t) \\ E_{iV}(\mathbf{r},t) \end{Bmatrix}$$

$$= \frac{\exp[i\mathbf{k}_f'\cdot(\mathbf{R}-\mathbf{r})+i\mathbf{k}_i\cdot\mathbf{r}]\exp(-i\omega t)}{-ik|\mathbf{R}-\mathbf{r}|}\begin{bmatrix} S_2 & S_3 \\ S_4 & S_1 \end{bmatrix}\begin{Bmatrix} E_{iH}(\mathbf{r}) \\ E_{iV}(\mathbf{r}) \end{Bmatrix} \quad (2.1.8)$$

$$= \frac{\exp[ik|\mathbf{R}-\mathbf{r}|+i\mathbf{k}_i\cdot\mathbf{r}]\exp(-i\omega t)}{-ik|\mathbf{R}-\mathbf{r}|}\begin{bmatrix} S_2 & S_3 \\ S_4 & S_1 \end{bmatrix}\begin{Bmatrix} E_{iH}(\mathbf{r}) \\ E_{iV}(\mathbf{r}) \end{Bmatrix}.$$

When $|\mathbf{R}| \gg |\mathbf{r}|$ equation 2.1.8 is simplified by approximating the magnitude of the displacement vector $\mathbf{R}-\mathbf{r}$ between the scatterer and the detector as the sum of the first two terms of its Taylor series expansion about $\mathbf{r} = 0$:

$$|\mathbf{R}-\mathbf{r}| \cong R - \mathbf{n}\cdot\mathbf{r},$$

where $\mathbf{n}$ ($\equiv \mathbf{R}/R$) is a unit vector in the direction of $\mathbf{R}$. Additionally, if $\mathbf{n}\cdot\mathbf{r} \ll R$ then $|\mathbf{R}-\mathbf{r}|^{-1} \cong R^{-1}$. Incorporating these approximations into equation 2.1.8 results in the following expression for the scattered electric field:

$$\begin{Bmatrix} E_{sH}(\mathbf{R},t) \\ E_{sV}(\mathbf{R},t) \end{Bmatrix} \cong \frac{\exp(ik_f R)\exp(i\mathbf{q}\cdot\mathbf{r})\exp(-i\omega t)}{-ikR}\begin{bmatrix} S_2 & S_3 \\ S_4 & S_1 \end{bmatrix}\begin{Bmatrix} E_{iH}(\mathbf{r}) \\ E_{iV}(\mathbf{r}) \end{Bmatrix}, \quad (2.1.9)$$

where $\mathbf{k}_f \equiv k\mathbf{n} = k\mathbf{R}/R$ and $\mathbf{q} \equiv \mathbf{k}_i - \mathbf{k}_f$ is the scattering vector, whose magnitude in an ambient medium of refractive index n is [Berne and Pecora, 1976]:

$$q \equiv |\mathbf{q}| = \frac{4\pi n}{\lambda}\sin\left(\frac{\theta}{2}\right). \quad (2.1.10)$$

The factor $\exp(i\mathbf{q}\cdot\mathbf{r})$ that arises from the translation of the particle position accounts for the Doppler frequency shift observed in light scattered from moving particles. When the particle moves at a constant velocity **v**, the particle position **r** at time t is equal to **v**t plus a constant. Thus, a time-dependent phase of $\mathbf{q}\cdot\mathbf{v}t$ is added to the frequency phase term $-\omega t$ to produce an effective "Doppler-shifted" frequency of $\omega - \mathbf{q}\cdot\mathbf{v}$.

On the basis of the form of equation 2.1.8 the temporal variation of the scattered electric field $\mathbf{E}_s(\mathbf{r},t)$ is generally affected by both particle translation and rotation. Particle translation affects the scattered field through two mechanisms: 1) changing the particle position alters the optical path lengths of both the incident and scattered light, causing a variation in the phase of the scattered light that manifests itself as the Doppler phase factor $\exp(i\mathbf{q}\cdot\mathbf{r})$, and 2) variations of the incident field amplitude encountered by the scattering particle as it translates through a spatially non-uniform incident beam changes the scattered field by altering the incident field vector $\{E_{iH}(\mathbf{r}),E_{iV}(\mathbf{r})\}$. Particle rotation also affects the scattered field in situations where the scattering particle exhibits an effective optical anisotropy, which causes the scattered field to be dependent upon the particle orientation. This orientation dependence manifests itself within the specific functional form of the amplitude scattering matrix elements.

2.1.2 Characterization of Random Electric Field Fluctuations Using Correlation Functions

If the motion of the scattering particles is governed by random processes, such as Brownian motion, the quantification of the particle motion is accomplished via temporal averages. For the case of dynamic light scattering experiments, these averages usually take the form of a time-based correlation function† of the scattered electric field. Electric field correlation functions are statistical quantities that are typically used to characterize the coherence properties of electromagnetic radiation. In this respect, the general definition of an Nth order electric field correlation function in both space and time is defined in terms of the electric field's complex amplitude $E_{ji}(x_i)$ as [Mandel and Wolf, 1965]

$$G^{(N)}{}_{j1,j2,\ldots,j2N}(x_1,\ldots,x_{2N}) = \langle E^*{}_{j1}(x_1)\ldots E^*{}_{jN}(x_N)E_{jN+1}(x_{N+1})\ldots E_{j2N}(x_{2N})\rangle, \quad (2.1.11)$$

† Some dynamic light scattering experiments are based upon the measurement of the frequency spectrum of the scattered field. This spectrum is related to the first order electric field correlation function through the Weiner-Khintchine theorem, which states that the frequency spectrum is simply the Fourier transform of the temporal correlation function.

where the subscripts $j_1, j_2, \ldots, j_i$ refer to the cartesian components of $E_{j_i}(x_i)$ and $x_{j_i} \equiv \{r_{j_i}, t_{j_i}\}$ are the space and time coordinates of the specified field. These correlation functions are frequently expressed in a normalized form as

$$g^{(N)}_{j_1 j_2, \ldots j_{2N}}(x_1, \ldots, x_{2N}) \equiv$$
$$G^{(N)}_{j_1 j_2, \ldots j_{2N}}(x_1, \ldots, x_{2N}) \Big/ \prod_{r=1}^{2N} \{G^{(1)}_{j_r j_r}(x_r; x_r)\}^{1/2}. \tag{2.1.12}$$

These correlation functions are frequently used to describe the fundamental coherence properties of electromagnetic radiation. The absolute value of the normalized first-order correlation function $|g^{(1)}_{j,j}(x_1, x_2)|$, which has values between 0 and 1, is indeed the classical *degree of first order coherence* ([Mandel and Wolf, 1965], [Fowles, 1975]) that is often used to characterize partially coherent light because the visibility of interference fringes in partially coherent light is proportional to this quantity.

A closer examination of the first order correlation function $g^{(1)}_{j,j}(x_1, x_2)$ reveals various trends and properties useful in understanding the results of a dynamic light scattering experiment when the results are cast in terms of a correlation function. The first order correlation function relating the electric field detected at a single location in space at two different times t and $t + \tau$ is expressed as follows (from equations 2.1.11 and 2.1.12):

$$g^{(1)}_{i,i}(t, t+\tau) \equiv \frac{\langle E_i^*(t) E_i(t+\tau) \rangle}{[\langle E_i^*(t) E_i(t) \rangle \langle E_i^*(t+\tau) E_i(t+\tau) \rangle]^{1/2}}. \tag{2.1.13}$$

If the statistical properties of the electric field are stationary (ie. all statistical averages of $E_i(t)$ are independent of t) then equation 2.1.13 reduces to

$$g^{(1)}_{i,i}(t, t+\tau) \equiv g^{(1)}_{i,i}(0, \tau) \equiv \frac{\langle E_i^*(0) E_i(\tau) \rangle}{\langle E_i^*(0) E_i(0) \rangle}, \tag{2.1.14}$$

where the denominator is proportional to the average intensity of the electromagnetic radiation. When $\tau = 0$, the numerator is equal to the denominator, causing $g^{(1)}_{i,i}(0, \tau)$ to equal unity. If the electric field is indeed a random quantity, then the quantities $E_i^*(0)$ and

$E_i(\tau)$ become statistically uncorrelated as the delay time τ increases towards infinity, meaning that the average of their product becomes equal to the product of their averages. For electric fields undergoing uniform random phase fluctuations, the statistical averages $\langle E_i^*(0)\rangle$ and $\langle E_i(\tau)\rangle$ are both equal to zero. Therefore, the random electric field's first order temporal correlation function $g^{(1)}_{i,i}(0, \tau)$, which has a value of unity at $\tau = 0$, approaches zero as the delay time τ approaches infinity. This decay is characterized by the coherence time τ_c, sometimes referred to as the decay time, which has been defined by Mandel (1959) as (see also [Mandel and Wolf, 1965])

$$\tau_c \equiv \int_{-\infty}^{\infty} |g^{(1)}_{i,i}(0, \tau)|^2 \, d\tau. \qquad (2.1.15)$$

Qualitatively, the coherence time τ_c represents a time proportional to the delay time τ required for the correlation function to decay to essentially zero.

Because the temporal variation of the scattered light depends upon various translational and rotational contributions from the scattering particles, the coherence time τ_c is a function of statistical averages characterizing each of these contributions. A causal decomposition of τ_c is most easily illustrated by considering the first-order correlation function of light scattered from a suspension consisting of numerous statistically-independent monodisperse scatterers whose translational and rotational motions are independent of each other. Since the motion of each particle is independent of the motions of the other particles and the average of a uniform-phase random electric field is zero, the total scattered light correlation function is the sum of the identical correlation functions of the light scattered from each individual scatterer, which is expressed in equation 2.1.9. Furthermore, because the translational and rotational motions are independent of each other, the correlation function of the electric fields from each scatterer, and thus the correlation function of the total field, is equal to the product of a correlation function governed by the particle's translational motion and a correlation function governed by the particle's rotational motion. Under these conditions the

"coherence times" corresponding to these translation- and rotation-governed correlation functions, known as *relaxation times*, determine the overall decay characteristics of the correlation function of the total scattered field. If, for example, the rotational relaxation time is much faster than the translational relaxation time, then the rotational factor of the correlation function will decay to its baseline (infinite-delay-time) value before the translational factor can exhibit any significant variations. Under this condition, the rotational decay time governs the initial decay characteristics of the total field correlation function while the translational decay time governs its long-delay-time decay characteristics. Fundamentally, both the translational and rotational relaxation times are functions of the translational and rotational dynamics of the scattering particles, which in turn are functions of the particle morphology and the physical properties of both the particles and the surrounding gases. Additionally, however, these relaxation times also depend upon various adjustable experimental parameters, such as the scattering angle θ and the polarizations of the incident and detected light.

The factorization of the translation- and rotation-governed scattering terms in equation 2.1.8 reveals the sources of various experimental contributions to the translational and rotational relaxation times. The translation dependency of the scattered electric field occurs through the Doppler phase factor $\exp(i\mathbf{q}\cdot\mathbf{r})$ and the spatial dependence of the incident electric field amplitude $\{E_{iH}(\mathbf{r}),E_{iV}(\mathbf{r})\}$. Therefore, the translational decay time is a function of the scattering vector $\mathbf{q}$ and the spatial distribution of the incident field amplitude (which is characterized by the beam waist ω_0 when the incident beam exhibits a Gaussian intensity profile). Alternatively, the rotation dependency of the scattered electric field occurs through the amplitude scattering matrix, whose elements are generally not only functions of the particle orientation but are also functions of the polarizations of the incident and detected light and the optical and morphological properties of the scattering particles. Therefore, the rotational relaxation time is a function of each of these parameters. Accurate knowledge of the dependencies

of the translational and rotational relaxation times on the above-mentioned experimental parameters and the scattering particles' dynamic properties facilitates the design of light scattering experiments that isolate or vary each relaxation time in order to extract the translational and rotational properties of the scattering particles.

2.1.3 DLS Measurement and Detection Techniques

In order to measure and isolate the respective correlation function relaxation times, the light scattering spectrometer is designed to control all of the experimental parameters that influence the translational and rotational relaxation times of light scattered from a suspension of particulates. Typically, laser light of known wavelength is transmitted through a linear polarizer and focused into the particulate suspension. The linear polarizer is used to select the polarization of the incident beam. Knowledge of the minimum unfocused spot size and intrinsic beam divergence (both are given by the manufacturer's specifications) of the incident laser beam and the focal length of the focusing lens permits an estimation of the spatial amplitude distribution of the incident light using Gaussian beam theory (when the laser is emitting in the TEM 00 mode). The light scattered from the particle suspension at a predetermined scattering angle of θ is then focused through another linear polarizer (the analyzer), a series of aperture diaphragms, and a laser-line filter onto a detector. The signal from the detector is then electronically processed to determine the correlation function (or, alternatively, the spectral density) of the detected signal. In some cases the scattered light is mixed with coherent unscattered light (called a local oscillator) prior to detection in order to establish a beating effect between the two light sources. This technique is called *heterodyne* detection. The alternative detection mode is the *homodyne* technique, in which only the scattered light is detected.

Though the physical principles governing the use of dynamic light scattering (DLS) techniques as a diagnostic tool are fundamental and common throughout the various DLS experimental schemes, many different types of detection and signal processing techniques are used. Some detection techniques involve the determination of

the frequency spectrum of the scattered light signal. Through the Weiner-Khintchine theorem ([Benedek, 1969], [Berne and Pecora, 1976]), this frequency spectrum is equivalent to the Fourier transform of a correlation function. The frequency spectrum can be resolved either before or after detection.

Pre-detection resolution of the scattered light frequency spectrum is accomplished through the use of an optical filtration device, such as a monochromator or a Fabry-Perot interferometer, prior to the detection of the scattered light. The optical filtration device transmits only the portion of the scattered light occurring within a narrow frequency band surrounding a variable central frequency. Upon receiving this signal, the detector produces an electric current whose average is proportional to the average intensity of scattered light detected within this frequency band. The optical frequency spectrum is thus obtained by scanning a range of frequencies to obtain the average signal intensity as a function of frequency. This optical frequency spectrum is the Fourier transform of the *first order* electric field correlation function. This technique corresponds to traditional optical spectroscopy [Benedek, 1969].

Post-detection resolution of the scattered light frequency spectrum is accomplished by filtering the photodetector output signal using electronic band pass filters. This technique provides the frequency spectrum of the random fluctuations in the photocurrent. Because the photocurrent from optical detectors, such as the photomultiplier tube, is proportional to the intensity of the detected light, which is proportional to the *square* of the magnitude of the electric field at the detector, the resulting spectrum is equivalent to the Fourier transform of the *second order* (intensity) electric field correlation function.

Other detection schemes function by directly determining the temporal correlation function of the intensity fluctuations of the scattered light. In these detection schemes, the unfiltered scattered light is incident upon a photomultiplier tube (or a similar photodetector), which converts the intensity fluctuations into electrical impulses that are subsequently recorded and processed by a correlator. The correlator computes a

correlation function from the resulting data. The data used for determining the intensity correlation function is obtainable using either analog or digital techniques. The analog technique involves electronically determining the correlation function of the anode current output of the photomultiplier tube. The resulting correlation function is thus proportional to the second order scattered electric field correlation function plus a shot noise term, which is approximately proportional to a dirac delta function ([Mandel, 1966], [Cummins and Swinney, 1970]) centered at a delay time of zero. In the digital technique, individual current pulses corresponding to each detected photon are discriminated from noise by a preamplifier discriminator. The preamplifier/discriminator then sends a TTL pulse to the digital correlator for each photocurrent pulse detected. The digital correlator counts the number of pulses $n(t_j)$ detected within a sample time interval Δt, centered around various times t_j, and establishes a correlation function of the photon count values [Brookhaven Instruments Corporation, 1993]:

$$\langle n(0)n(\tau_j)\rangle = \lim_{N \to \infty} \frac{1}{N} \sum_{i=1}^{N} n_i \, n_{i-j} \quad (j = 1, 2, ..., M) \quad (2.1.16)$$

When the sample time Δt is much shorter than the detected field's coherence time τ_c, the photon count (photocount) correlation function is proportional to the photocurrent correlation function obtained using analog techniques at non-zero delay times. The principal advantage of the digital photon count technique is that much of the inherent noise within the detection system is eliminated both through the photon discrimination process, which filters much of the noise generated within photomultiplier tube, and through the subsequent transmission of a digital signal, which does not degrade when transferred.

A comparison of the frequency-based detection schemes with the time-based detection schemes shows that the post-detection frequency resolution technique is entirely equivalent to the time-based techniques in that the temporal (or frequency) information is processed *after* the optical detection process. Such post-detection resolution techniques are commonly denoted *optical mixing techniques* ([Benedek, 1969], [Berne and Pecora,

1976]). The results of optical mixing experiments are thus based upon the detected intensity fluctuations of unfiltered light. The pre-detection frequency-based technique differs from optical mixing techniques in that the use of an optical filter prior to the detection of the *average* intensity produces a spectrum determined directly by the fluctuations of the scattered electric field instead of its intensity.

The applicability of post-detection (optical mixing) techniques is limited by the speed at which the signal processing apparatus can interpret the scattered signal. For photon counting applications, current technology provides minimum sample times on the order of 25 ns. Thus, in order to have enough data points in the transient portion of the correlation function to obtain an accurate value of the linewidth Γ ($\equiv \tau_c^{-1}$) the coherence time of the measured field should be greater than approximately 250 ns (see [Jakeman, et al. (1971)]).

Conversely, the applicability of pre-detection frequency-based detection schemes (conventional optical spectroscopy) is limited by the resolving power of the optical filtration device used to scan the scattered-light frequency spectrum. At optical frequencies the best resolving powers are obtained from Fabry-Perot interferometers, which are at best approximately $\omega/\Delta\omega_{fp} = 10^7$, where ω is the central frequency and $\Delta\omega_{fp}$ is the minimum resolvable frequency difference. For scattering processes exhibiting a Lorentzian frequency spectrum, which corresponds to an exponentially decaying correlation function in the time domain, the absolute frequency difference $|\Delta\omega_{1/2}|$ between the half-maximum intensities of the spectrum is related to the coherence time τ_c of the electric field by the relationship [Benedek, 1969]

$$|\Delta\omega_{1/2}| \equiv 2\Gamma = 2/\tau_c, \qquad (2.1.17)$$

where Γ is the *linewidth* of the frequency spectrum. In order to resolve at least 10 data points between the half-maximum points of the intensity-versus-frequency curve, the minimum resolvable frequency difference $\Delta\omega_{fp}$ should be at least ten times smaller than

the total frequency difference $\Delta\omega_{1/2}$ between the half-maximum points of the scattered light spectrum. For a Lorentzian spectrum, this condition reduces to the following:

$$\frac{\Delta\omega_{fp}}{\Delta\omega_{1/2}} = \frac{\omega\,\tau_c}{2\omega/\Delta\omega_{fp}} < 0.1. \qquad (2.1.18)$$

For a Fabry-Perot interferometer with a resolving power of $\omega/\Delta\omega = 10^7$ the above condition provides a maximum measurable coherence time of $\tau_c = 0.5$ ns at a laser wavelength λ of 488 nm. Since the width of the frequency spectrum is inversely proportional to the decay (coherence) time of its corresponding correlation function, the applicability of pre-detection filtration methods is constrained by a maximum coherence time, which contrasts with the fact that post-detection filtration methods are constrained by a minimum measurable coherence time.

For the present study, the photon-counting time-based post-detection filtration scheme is selected. This choice is partially based upon rough estimates of the rotational relaxation times of tumbling chainlike agglomerates within a flame environment, which indicate an order of magnitude occurring within the range of approximately 10^1 to 10^3 ns, which occurs outside the estimated applicable range of pre-detection frequency-based techniques. The immunity of photon counting techniques to detection- and transmission-based noise sources that are normally associated with analog techniques, as well as the overall speed and data recording convenience of modern digital correlators, also demonstrates the superiority of the photon counting time-based detection scheme for the current application. Therefore, the necessity arises to relate the dynamic properties of the scattering agglomerates to the measured time-based correlation function of the number of photon counts n(t) detected during each sample time Δt.

2.2 Theoretical Formulation of Photon Correlation Functions for Cylindrically Symmetric Scatterers

The theoretical considerations necessary to relate the photon count correlation function to the dynamic properties of the scattering particles are presented in the following

discussion as a series of successive developments that follow from the general theory of photon detection processes to the effects of the particle motions on the fluctuations in the scattered electric field. First, the theory of photon detection statistics is used to relate the temporal correlation function of the photon counts obtained during sample time Δt from a finite-area detector to the correlation function of the optical energy incident upon the detector surface. Next, this incident energy correlation function is expressed in terms of the electric field of the scattered light being detected. The combination of these relations thus provides a relationship between the photon count correlation function and the electric field correlation function. Through the use of equation 2.1.9 and various specifics and approximations about the structure, motion, and scattering characteristics of the agglomerates, the electric field correlation function is then related to the physical experimental parameters of the system and the translational and rotational properties of the scattering particles. The combination of these relations then provides the theoretical equations necessary for the design of an appropriate measurement scheme and the subsequent data analysis techniques.

2.2.1 Photodetection Statistics

When light is incident upon the photosensitive surface (photocathode) of a photomultiplier tube the probability (p dt) of the emission of a single photoelectron from the surface during an infinitesimal time interval dt is governed by the equation [Mandel, et al., 1964] (see also [Thorn EMI, 1986])

$$p\,dt = \frac{\eta\,dt}{h\nu}\int_A I(\mathbf{R},t)\,d^2R \qquad (2.2.1)$$

where η is the quantum efficiency of the photocathode, h is Planck's constant, and ν ($= \omega/(2\pi)$) and $I(\mathbf{R},t)$ are the frequency and intensity, respectively, of the electromagnetic radiation incident upon the photocathode at position $\mathbf{R}$ and time t. The integral in equation 2.2.1 is over the area A of the photocathode surface. In Gaussian units the intensity

$I(\mathbf{R},t)$ is equal to the following function of the incident electric field $\mathbf{E}(\mathbf{R}, t)$ [van de Hulst, 1981]:

$$I(\mathbf{R},t) = \frac{c}{8\pi}\mathbf{E}^*(\mathbf{R}, t)\cdot\mathbf{E}(\mathbf{R}, t), \tag{2.2.2}$$

where c is the speed of light and the asterick denotes the complex conjugate of the field quantity. On the basis of equation 2.2.1 and the physical condition that the probability of the detection of an incident photon during any infinitesimal time interval dt is independent of the detection of previous photons, the probability of the detection of n photons during a finite time interval Δt centered at time t is given by the following Poisson distribution [Mandel, 1959]:

$$p(n,\Delta t) = \int_0^\infty \frac{(\alpha U)^n}{n!}\exp(-\alpha U)\, f(U)\, dU, \tag{2.2.3}$$

where

$$\begin{aligned} U = U(t) &= \int_{t-\Delta t/2}^{t+\Delta t/2} dt' \int_A d^2R\ I(\mathbf{R},t') \\ &= \frac{c}{8\pi}\int_{t-\Delta t/2}^{t+\Delta t/2} dt' \int_A d^2R\ \mathbf{E}^*(\mathbf{R}, t')\cdot\mathbf{E}(\mathbf{R}, t'), \end{aligned} \tag{2.2.4}$$

$$\alpha = \frac{\eta}{h\nu},$$

and f(U) is the probability density function of the randomly fluctuating incident optical energy U (= U(t)). Following from the fact that for a fixed value of U(t) the conditional probabilities of detecting a photon at different times are statistically independent, equation 2.2.3 can be further generalized to express the conditional probability of detecting both n photons during a sample time Δt centered at time t and n' photons during a sample time Δt centered at a different time t' as [Jakeman, 1970]

$$p(n,n',\Delta t) = \int_0^\infty \int_0^\infty \frac{(\alpha U)^n (\alpha U')^{n'}}{n!\ n'!} \exp[-\alpha(U + U')]\ f(U,U')\ dU\ dU', \quad (2.2.5)$$

where f(U,U') is the joint probability density function of the occurrence of the incident optical energies U and U' during the times corresponding to the detection of n and n'. This joint photodetection probability provides the theoretical foundation for relating the photon count correlation function to a correlation function of the incident optical energies U(t).

2.2.2 Statistical Formulation of Photon Correlation Functions

In the following discussion, the statistical principles governing the photon detection process that were discussed in the previous section are used to establish relationships between the correlation function of photons detected during finite time intervals Δt from a single volume of scattering particles and the correlation function of the optical energies U(t) received by the detector(s) during these intervals. Expressions are developed for the autocorrelation function of photons detected by a single photomultiplier tube and the cross-correlation function of photons detected by two photomultiplier tubes viewing the same scattering volume at the same scattering angle θ via a beam splitter†.

2.2.2.1 Autocorrelation of Photon Pulses from a Single Detector

For the autocorrelation of photons detected by a single photomultiplier tube the stationary-field photon correlation function $\langle n(0)n(\tau)\rangle$ is determined using an analysis outlined by Jakeman (1970). This analysis utilizes the probability functions of equations 2.2.3 and 2.2.5 to evaluate the averages of $n(0)n(\tau)$ separately for the cases of a zero and a nonzero delay time τ.

At $\tau = 0$ the photon count correlation function is equal to the average of the square of the number of photons detected during Δt centered at $t = 0$. Thus,

† See Section 2.3 for a description of these detection schemes.

$$\langle n(0)n(\tau)\rangle = \langle n^2(0)\rangle = \sum_{n=0}^{\infty} n^2\, p(n,\Delta t). \tag{2.2.6}$$

Substituting the expression for $p(n,\Delta t)$ from equation 2.2.3 into this expression and interchanging the order of the summation and the integration produces the following relation:

$$\langle n^2(0)\rangle = \int_0^{\infty} \sum_{n=0}^{\infty} \frac{n^2\,(\alpha U)^n}{n!} \exp(-\alpha U)\, f(U)\, dU. \tag{2.2.7}$$

Using

$$\frac{n^2}{n!} = \frac{n(n-1)+n}{n!} = \frac{n(n-1)}{n!} + \frac{n}{n!} = \frac{1}{(n-2)!} + \frac{1}{(n-1)!}$$

equation 2.2.7 is re-expressed as

$$\begin{aligned}\langle n^2(0)\rangle = &\int_0^{\infty} (\alpha U)^2 \left\{ \sum_{n=2}^{\infty} \frac{(\alpha U)^{n-2}}{(n-2)!} \right\} \exp(-\alpha U)\, f(U)\, dU \\ &+ \int_0^{\infty} \alpha U \left\{ \sum_{n=1}^{\infty} \frac{(\alpha U)^{n-1}}{(n-1)!} \right\} \exp(-\alpha U)\, f(U)\, dU.\end{aligned} \tag{2.2.8}$$

The factors in the braces {} are Taylor series expansions of $\exp(\alpha U)$, which cancel with the $\exp(-\alpha U)$ factors. Therefore, equation 2.26 reduces to

$$\begin{aligned}\langle n(0)n(\tau)\rangle\big|_{\tau=0} = \langle n^2(0)\rangle &= \int_0^{\infty} (\alpha U)^2\, f(U)\, dU + \int_0^{\infty} \alpha U\, f(U)\, dU \\ &= \langle (\alpha U)^2\rangle + \langle \alpha U\rangle \\ &= \alpha^2 \langle U^2(0)\rangle + \alpha \langle U(0)\rangle.\end{aligned} \tag{2.2.9}$$

At non-zero delay times ($\tau \neq 0$) the number of counts detected during the sample times centered at $t = 0$ and $t = \tau$ are related by their joint probability $p(n,n',\Delta t)$, where $n = n(0)$ and $n' = n(\tau)$. Thus,

$$\langle n(0)n(\tau)\rangle = \langle nn'\rangle = \sum_{n=0}^{\infty}\sum_{n'=0}^{\infty} n\, n'\, p(n,n',\Delta t) \qquad (2.2.10)$$

Substituting the expression for p(n,n',Δt) from equation 2.2.5 into equation 2.2.10 and interchanging the order of the summation and the integration gives the following expression:

$$\langle nn'\rangle = \int_0^{\infty}\int_0^{\infty} dU\; dU' \sum_{n=0}^{\infty} \frac{n(\alpha U)^n}{n!}\exp(-\alpha U) \times \sum_{n'=0}^{\infty} \frac{n'(\alpha U')^{n'}}{n'!}\exp(-\alpha U')\, f(U,U'). \qquad (2.2.11)$$

Using n/n! = 1/(n - 1)!, equation 2.2.11 is recast as

$$\langle nn'\rangle = \int_0^{\infty}\int_0^{\infty} dU\; dU'\; \alpha^2\, U\, U'\, f(U,U') \left\{\sum_{n=1}^{\infty} \frac{(\alpha U)^{n-1}}{(n-1)!}\right\}\exp(-\alpha U) \times \left\{\sum_{n'=1}^{\infty} \frac{(\alpha U')^{n'-1}}{(n'-1)!}\right\}\exp(-\alpha U'). \qquad (2.2.12)$$

As before, the terms in the braces {} are series expansions of exponentials, which cancel the two exponentials occurring in equation 2.2.12. Therefore, at $\tau \neq 0$ the photon count correlation function is equal to

$$\langle nn'\rangle = \int_0^{\infty}\int_0^{\infty} \alpha^2\, U\, U'\, f(U,U')\, dU\, dU'$$

$$= \langle \alpha^2\, U\, U'\rangle = \alpha^2 \langle U\, U'\rangle,$$

or

$$\langle n(0)n(\tau)\rangle\big|_{\tau\neq 0} = \alpha^2 \langle U(0)\, U(\tau)\rangle. \qquad (2.2.13)$$

Combining the results of equations 2.2.9 and 2.2.13 yields the following expression, which relates the single-detector photon count correlation function $\langle n(0)n(\tau)\rangle$ to the incident optical energy U(t) [Jakeman, 1970]:

$$\langle n(0)n(\tau)\rangle = \alpha^2 \langle U(0)\, U(\tau)\rangle + \alpha\langle U(0)\rangle\, u(\tau), \qquad (2.2.14)$$

where

$$u(\tau) = \begin{cases} 1 & \text{when } \tau = 0 \\ 0 & \text{when } \tau \neq 0 \end{cases}.$$

The first term on the right side of equation 2.2.14 contains the usable temporal information, from which the particle dynamics can be inferred. The second term is a "shot noise" term, which is a result of the statistical nature of the photodetection process. This shot noise term is finite only at the zero delay time.

2.2.2.2 Cross-Correlation of Photon Pulses from Two Detectors Viewing the Same Scattering Volume

When a photon count correlation function is determined by cross-correlating the photon counts from two different photodetectors that view the same scattering volume through the use of a beam splitter, the zero-delay-time shot noise term no longer occurs because of the conditional statistical photon-detection independence between the two detectors. In the two-detector scheme, the single-photon-detection probabilities $p_A\, dt$ and $p_B\, dt$ of detectors A and B are both proportional to the total optical power incident upon the beam splitter. Therefore, by analogy with equation 2.2.5, the joint probability $p(n_A,n_B,\Delta t)$ of detector A detecting n_A photons and detector B detecting n_B photons during sample times Δt centered at times $t = 0$ and $t = \tau$, respectively, is given by

$$p(n_A,n_B',\Delta t) = \int_0^\infty \int_0^\infty \frac{(\alpha_A U)^{n_A}\,(\alpha_B U')^{n_B'}}{n_A!\; n_B'!} \exp[-(\alpha_A U + \alpha_B U')]\, f(U,U')\, dU\, dU', \qquad (2.2.15)$$

where $U = U(0)$ and $U' = U(\tau)$ are the total optical energies incident upon the beam splitter during time intervals Δt centered at times $t = 0$ and $t = \tau$ and α_A and α_B are

constants that are dependent upon the fraction of the total optical energy that is incident upon each detector and the detectors' respective quantum efficiencies. By following the same steps as the $\tau > 0$ single-detector development of equations 2.2.10 to 2.2.14, replacing n, n', αU, and $\alpha U'$ by n_A, n_B', $\alpha_A U$, and $\alpha_A U'$, the two-detector cross-correlation function $\langle n_A(0)n_B(\tau)\rangle$ is shown to be

$$\langle n_A(0)n_B(\tau)\rangle = \alpha_A\alpha_B\langle U(0)\, U(\tau)\rangle \qquad (2.2.16)$$

for all delay times, theoretically confirming the absence of the shot noise term that occurs in the single-detector correlation function.

Equations 2.2.14 and 2.2.16 demonstrate that the photon count correlation function $\langle n(0)n(\tau)\rangle$ is proportional to the correlation function $\langle U(0)\, U(\tau)\rangle$ of the total optical energies incident upon the detector during time intervals of duration Δt. The major difference between the photon correlation functions resulting from these detection configurations is the $\tau = 0$ shot noise term, which occurs in the single-detector autocorrelation function but is absent from the two-detector cross-correlation function.

2.2.3 Effects of Finite Detector Area and Sample Time

The relationships derived in the previous section demonstrate that the correlation function of the number photons detected from a single scattering volume using both single-detector and double-detector techniques is linearly related to the correlation function $\langle U(0)\, U(\tau)\rangle$ of the optical energy incident upon the detector. Use of the definition of U(t), as given by equation 2.2.4, permits the expression of $\langle U(0)\, U(\tau)\rangle$ as a function of the detected light intensity $I(\mathbf{R},t)$ by the integral

$$\langle U(0)\, U(\tau)\rangle = \int_{-\Delta t/2}^{\Delta t/2} dt \int_{\tau-\Delta t/2}^{\tau+\Delta t/2} dt' \int_A d^2R \int_A d^2R' \,\langle I(\mathbf{R},t)\, I(\mathbf{R}',t')\rangle, \qquad (2.2.17)$$

where the order of integration and averaging has been interchanged.

The integrand $\langle I(\mathbf{R},t)\, I(\mathbf{R}',t')\rangle$ of equation 2.2.17 is the correlation function of the detected intensity over both time and space. Because the motion of the scattering particles

influences temporal variation of both the amplitude and the phase of the scattered light, any random particle motion produces a randomly fluctuating component of the scattered field that manifests itself as a partial temporal incoherence. Additionally, partial spatial incoherence occurs between different locations on the detector surface as a result of the relative optical pathlength differences of the temporally incoherent fields scattered from different parts of the scattering volume. Therefore, as $|t - t'|$ and/or $|\mathbf{R} - \mathbf{R}'|$ increases, the randomly fluctuating intensities $I(\mathbf{R},t)$ and $I(\mathbf{R}',t')$ become increasingly uncorrelated.

An ideal light scattering spectrometer would measure the single point time-correlation function $\langle I(\mathbf{R},0)\ I(\mathbf{R},\tau)\rangle$ of the instantaneous intensity of the light incident upon the detector, which depends only upon the temporal coherence of the scattered light and, if a local oscillator is used, any average scattered light frequency shift. Because of the physical limitations of the detection process, however, this correlation function cannot be measured exactly. The discussions leading to equations 2.2.14 and 2.2.16 have demonstrated that, because of photodetection inefficiencies, one can only measure, at best, a correlation function that is linearly related to the true intensity correlation function. Additionally, the necessity of using a finite detector area A and a finite sample time Δt in order to obtain a usable signal can cause deviations between delay-time variations of the measured correlation function $\langle n(0)n(\tau)\rangle$ and the single-point intensity correlation function $\langle I(\mathbf{R},0)\ I(\mathbf{R}',\tau)\rangle$. These deviations are studied by considering the effects of the integrations of equation 2.2.17 over the detector area and the sample time. To facilitate the discussion of these effects equation 2.2.17 is recast in terms of the optical power incident upon the detector P(t) as follows:

$$\langle U(0)\,U(\tau)\rangle = \int_{-\Delta t/2}^{\Delta t/2} dt \int_{\tau-\Delta t/2}^{\tau+\Delta t/2} dt'\ \langle P(t)\ P(t')\rangle, \qquad (2.2.18)$$

where

$$P(t) = \int_A I(\mathbf{R},t)\, d^2R.$$

The spatial integration is thus considered by relating $\langle P(t)\, P(t')\rangle$ to $\langle I(\mathbf{R},t)\, I(\mathbf{R}',t')\rangle$ and the temporal integration is considered by relating $\langle U(0)\, U(\tau)\rangle$ to $\langle P(t)\, P(t')\rangle$.

2.2.3.1 Detector Area Integration: Spatial Coherence Effects

The predominant effect of the spatial integrations of equation 2.2.17 on the measured correlation function is a decrease in the magnitude of the correlation function's time-dependent portion in relation to its constant, or baseline, component. This effect is caused by the spatial incoherence of the detected intensity between different locations on the detector surface. Through the use of various assumptions and approximations regarding the nature of the scattered light, quantitative relationships have been obtained that account for these spatial integrations without considering the specific properties of the scattering particles.

2.2.3.1.1 Discrete Coherence Area Approximation

One technique of approximating the spatial integration of the intensity over the detector area, as considered by Forrester (1961) and Benedict (1969), is to subdivide the detector surface of total area A into N_c coherence areas A_{ci} (i = 1, 2,..., N_c). Each coherence area represents the maximum area of a spatial region of the detector surface within which the detected light is spatially correlated. The total optical power incident upon the detector at time t is thus equal to

$$P(t) = \sum_{i=1}^{N_c} P_{ci}(t), \qquad (2.2.19)$$

where

$$P_{ci}(t) = \int_{A_{ci}} I(\mathbf{R},t)\, d^2R \qquad (2.2.20)$$

is the power incident into coherence area A_{ci} at time t. This subdivision permits the representation of the power correlation function $\langle P(t)\, P(t')\rangle$ as

$$\langle P(t)\, P(t')\rangle = \left\langle \sum_{i=1}^{N_c} P_{ci}(t) \sum_{j=1}^{N_c} P_{cj}(t') \right\rangle = \sum_{i=1}^{N_c} \sum_{j=1}^{N_c} \langle P_{ci}(t)\, P_{cj}(t')\rangle. \tag{2.2.21}$$

Separating the above expression into two summations, corresponding to $i = j$ and $i \neq j$, and applying the approximation, based on the definition of a coherence area, that the optical powers received within different coherence areas ($i \neq j$) are uncorrelated yields

$$\langle P(t)\, P(t')\rangle = \sum_{i=1}^{N_c} \langle P_{ci}(t)\, P_{ci}(t')\rangle + \sum_{i \neq j = 1}^{N_c} \langle P_{ci}(t)\rangle\langle P_{cj}(t')\rangle. \tag{2.2.22}$$

To further simplify this expression, the correlation function $\langle P_{ci}(t)\, P_{ci}(t')\rangle$ is assumed to be equal for all coherence areas, hence

$$\langle P_{ci}(t)\, P_{ci}(t')\rangle = \langle P_{ci}(t)\rangle\langle P_{cj}(t')\rangle \equiv \langle P_c(t)\, P_c(t')\rangle.$$

Also, in addition to the common assumption of stationary random processes, the mean optical powers received into all coherence areas are assumed equal. Therefore,

$$\langle P_{ci}(t)\rangle = \langle P_{ci}(t')\rangle = \langle P_{ci}(t')\rangle \equiv \langle P_{ci}(t)\rangle.$$

Incorporating these assumptions into equation 2.2.22 and evaluating the sums gives

$$\langle P(t)\, P(t')\rangle = N_c \langle P_c(t)\, P_c(t')\rangle + N_c(N_c - 1)\langle P_c(t)\rangle^2,$$

which, using the fact that $\langle P(t)\rangle = N_c \langle P_c(t)\rangle$, reduces to [Benedek, 1969]

$$\langle P(t)\, P(t')\rangle = \langle P(t)\rangle^2 \left\{ 1 + \frac{1}{N_c}\left[\frac{\langle P_c(t)\, P_c(t')\rangle}{\langle P_c(t)\rangle^2} - 1 \right] \right\}. \tag{2.2.23}$$

Because the time dependent term of this correlation function is scaled by $1/N_c$, the magnitude of this term in comparison with the constant baseline term $\langle P(t)\rangle^2$ decreases as the number of detected coherence areas N_c increases. The number of coherence areas N_c is determined by dividing the total detector area A by a typical coherence area A_c, which is given by the expression ([Forrester, et al., 1955], [Cummins and Swinney, 1970])

$$A_c \approx \frac{\lambda^2}{\Omega}, \tag{2.2.24}$$

where Ω is the solid angle of the scattered light seen by the detector. This solid angle is equal to the cross-sectional area of the scattering volume, as seen by the detector, divided by the square of the distance between the scattering volume and the detector. For all cases where A_c is larger than A, however, $\langle P(t)\ P(t')\rangle$ is equal to a single-point correlation function and N_c is thus equal to unity.

If the detected intensity is essentially uniform within each single coherence area, which is a valid assumption since the coherence area sizes are of the same order as the sizes of diffraction images from the scattering volume [Forrester, et al., 1955], then

$$\begin{aligned}\frac{\langle P_c(t)\ P_c(t')\rangle}{\langle P_c(t)\rangle^2} &= \frac{\langle |\mathbf{E}(\mathbf{R},t)|^2\ |\mathbf{E}(\mathbf{R},t')|^2\rangle}{\langle |\mathbf{E}(\mathbf{R},t)|^2\rangle^2} \\ &= g^{(2)}(\mathbf{R},t;\mathbf{R},t'),\end{aligned} \tag{2.2.25}$$

where $g^{(2)}(\mathbf{R},t;\mathbf{R},t')$ is the normalized second order electric field correlation function. The assumption that $\langle P_{ci}(t)\ P_{ci}(t')\rangle$ is equal for all coherence areas, in combination with the assumption that the detected intensity is uniform within each coherence area, is equivalent to assuming that $g^{(2)}(\mathbf{R},t;\mathbf{R},t')$ is independent of $\mathbf{R}$. Substitution of this result into equation 2.2.23 yields

$$\langle P(t)\ P(t')\rangle = \langle P(t)\rangle^2\left\{1 + \frac{1}{N_c}\left[g^{(2)}(t' - t \mid 0) - 1\right]\right\}, \tag{2.2.26}$$

where $g^{(2)}(t' - t \mid 0) \equiv g^{(2)}(\mathbf{R},t;\mathbf{R},t')$. This new nomenclature is given for the single-point normalized second order electric field correlation function as a reminder that, due to its **R**-

independence and the assumption of stationary random processes, $g^{(2)}(\mathbf{R},t;\mathbf{R},t')$ depends only upon the delay time $t' - t$. Equation 2.2.26 thus relates the correlation function of the optical power incident upon the photodetector to its normalized second order electric field correlation function under the previously-mentioned assumptions.

2.2.3.1.2 Gaussian Approximation With Cross-Spectral Purity

A second relationship between $\langle P(t)\, P(t')\rangle$ and $g^{(2)}(t' - t \mid 0)$ that forgoes the discretization of the detector surface into coherence areas that are either completely correlated or completely uncorrelated was obtained by Jakeman, Oliver, and Pike (1970) for detected electric fields conforming to Gaussian statistics. The use of Gaussian statistics is justified when the number of independent scatterers within the scattering volume undergoing similar statistical motions is very large. The scattered electric field at each point on the detector surface consists of a superposition of the fundamental electric fields scattered from each particle within the scattering volume. Because each of these particles undergo random Brownian motion, each of these fundamental scattered fields is a random variable. Due to the central limit theorem, as the number of statistically independent fundamental scattered fields in the superposition increases, the total field increasingly resembles a Gaussian random variable. Glauber (1963) uses quantum optical arguments to rigorously demonstrate this fact.

If the electric field is governed by Gaussian statistics, then the second order electric field correlation function $G^{(2)}(\mathbf{R},t;\mathbf{R}',t') = \langle |E_i(\mathbf{R},t)|^2\, |E_i(\mathbf{R}',t')|^2\rangle$ is directly related to the electric field's first order correlation function $G^{(1)}(\mathbf{R},t;\mathbf{R}',t') = \langle E_i^*(\mathbf{R},t)\, E_i(\mathbf{R}',t')\rangle$ by the relationship [Glauber, 1963]:

$$G^{(2)}(\mathbf{R},t;\mathbf{R}',t') = G^{(1)}(\mathbf{R},t;\mathbf{R},t)\, G^{(1)}(\mathbf{R}',t';\mathbf{R}',t') + G^{(1)}(\mathbf{R},t;\mathbf{R}',t')\, G^{(1)}(\mathbf{R}',t';\mathbf{R},t),$$

which normalizes to

$$g^{(2)}(\mathbf{R},t;\mathbf{R}',t') = 1 + |g^{(1)}(\mathbf{R},t;\mathbf{R}',t')|^2. \qquad (2.2.27)$$

In real systems the deviation of $g^{(2)}(\mathbf{R},t;\mathbf{R}',t')$ from the Gaussian relationship of equation 2.2.27 is proportional to the inverse of the average number of independent

scatterers in the scattering volume [Berne and Pecora, 1976]. Thus, for a scattering volume containing 1000 independent scatterers, the maximum deviation of $g^{(2)}(\mathbf{R},t;\mathbf{R}',t')$ from the Gaussian approximation of equation 2.2.27 is 0.1%.

In terms of the normalized second order electric field correlation function $g^{(2)}(\mathbf{R},t;\mathbf{R}',t')$, the correlation function of the optical power P(t) incident upon the detector is

$$\langle P(t)\, P(t')\rangle = I_o^2 \int_A d^2R \int_A d^2R'\; g^{(2)}(\mathbf{R},t;\mathbf{R}',t'), \tag{2.2.28}$$

where the mean scattered intensity $I_o \equiv \langle I(\mathbf{R},t)\rangle$ is assumed to be independent of both position $\mathbf{R}$ and time t. Application of Gaussian statistics to $\langle P(t)\, P(t')\rangle$ through the use of equation 2.2.27 reduces equation 2.2.28 to

$$\begin{aligned}\langle P(t)\, P(t')\rangle &= I_o^2 \int_A d^2R \int_A d^2R' \left[1 + |g^{(1)}(\mathbf{R},t;\mathbf{R}',t')|^2\right] \\ &= P_o^2 \left[1 + \frac{1}{A^2}\int_A d^2R \int_A d^2R' \,|g^{(1)}(\mathbf{R},t;\mathbf{R}',t')|^2\right],\end{aligned} \tag{2.2.29}$$

where $P_o \equiv I_o A$ is the mean power incident upon the detector.

In some cases the spatial and temporal dependencies of $g^{(1)}(\mathbf{R},t;\mathbf{R}',t')$ can be factored. Specifically, if $g^{(1)}(\mathbf{R},t;\mathbf{R},t')$ is independent of $\mathbf{R}$ on the photodetector surface and a spatial region exists at which a hypothetical superposition of light from two arbitrary points on the detector surface exhibits the same normalized first order correlation function as $g^{(1)}(\mathbf{R},t;\mathbf{R},t')$ then the light incident upon the detector is *cross-spectrally pure* and its first order correlation function therefore exhibits the following property [Mandel and Wolf, 1965]:

$$g^{(1)}(\mathbf{R},t;\mathbf{R}',t') = g^{(1)}(\mathbf{R},t;\mathbf{R}',t)\; g^{(1)}(\mathbf{R},t;\mathbf{R},t') \tag{2.2.30}$$

Incorporating this relationship into equation 2.2.29 gives (see [Jakeman, el al., 1970])

$$\langle P(t)\,P(t')\rangle = P_o^2\left[1 + \frac{1}{A^2}\int_A d^2R \int_A d^2R' \,|g^{(1)}(\mathbf{R},t;\mathbf{R}',t)|^2\,|g^{(1)}(\mathbf{R},t;\mathbf{R},t')|^2\right]$$

or

$$\langle P(t)\,P(t')\rangle = P_o^2\,[1 + f(A)\,|g^{(1)}(\mathbf{R},t;\mathbf{R},t')|^2], \tag{2.2.31}$$

where

$$f(A) = \frac{1}{A^2}\int_A d^2R \int_A d^2R' \,|g^{(1)}(\mathbf{R},t;\mathbf{R}',t)|^2. \tag{2.2.32}$$

Equation 2.2.31 utilizes the assumptions that $g^{(1)}(\mathbf{R},t;\mathbf{R}',t)$ is independent of t and $g^{(1)}(\mathbf{R},t;\mathbf{R},t')$ is independent of $\mathbf{R}$. The spatial coherence factor f(A) is presented by Jakeman, et al. (1970) for a scattering volume whose cross section as seen by the detector is circular with area A_{sv} located at a distance Z from the detector, whose area is circular with area A. The resulting expression for f(A) is expressed as the following infinite series [Jakeman, et al., 1970]:

$$f(A) = \sum_{s=0}^{\infty}\left[\frac{(2s+2)!}{\{(s+1)!\}^2\,(s+2)!}\right]^2\left(-\frac{N}{4}\right)^s, \tag{2.2.33}$$

where

$$N = \frac{\Omega\,A}{\lambda^2} = \frac{A_{sv}\,A}{\lambda^2\,Z^2}. \tag{2.2.34}$$

Comparing equation 2.2.34 to equation 2.2.24 demonstrates that N is approximately equal to the number of coherence areas N_c when more than one coherence area is detected. The summation for f(A) given by equation 2.2.33 decreases to zero monotonically with increasing N and approaches unity as N approaches zero. This trend is consistent with the result of the discrete coherence area analysis that is given by equation 2.2.26, which, by analogy with equation 2.2.31, states that f(A) is equal to N_c^{-1}.

2.2.3.2 Temporal Integration: Finite Sample Time Effects

Equations 2.2.26 and 2.2.31 account for the spatial integration of equation 2.2.17 by expressing the temporal correlation function of the detected power $\langle P(t)\, P(t')\rangle$ in terms of the normalized single-point intensity correlation function $g^{(2)}(\mathbf{R},t;\mathbf{R},t') \equiv \langle I(\mathbf{R},t)\, I(\mathbf{R},t')\rangle / \langle I(\mathbf{R},t)\rangle^2 \equiv g^{(2)}(t' - t \mid 0)$. The detected energy correlation function $\langle U(0)\, U(\tau)\rangle$ is evaluated by integrating this result over the sample time Δt in accordance with equation 2.2.18. A differential equation relating the normalized energy correlation function

$$g_P^{(2)}(\tau \mid \Delta t) \equiv \frac{\langle U(0)\, U(\tau)\rangle}{\langle U(0)\rangle^2} \tag{2.2.35}$$

to the normalized correlation function of the instantaneous power

$$g_P^{(2)}(\tau \mid 0) \equiv \frac{\langle P(0)\, P(\tau)\rangle}{\langle P(0)\rangle^2} \tag{2.2.36}$$

is given by Jakeman (1970) for delay times τ greater than or equal to the sample time Δt as

$$\frac{d^2}{d(\Delta t)^2}\{g_P^{(2)}(\tau \mid \Delta t)\} = g_P^{(2)}(\tau + \Delta t \mid 0) + g_P^{(2)}(\tau - \Delta t \mid 0), \tag{2.2.37}$$

subject to the condition that $g_P^{(2)}(\tau \mid \Delta t) \rightarrow g_P^{(2)}(\tau \mid 0)$ as $\Delta t \rightarrow 0$. The solution to this equation that satisfies the initial condition is the integral

$$g_P^{(2)}(\tau \mid \Delta t) = \frac{1}{(\Delta t)^2}\int_0^{\Delta t} d\,T \int_0^{T} dT' \; \{g_P^{(2)}(\tau + T' \mid 0) + g_P^{(2)}(\tau - T' \mid 0)\}, \tag{2.2.38}$$

which expands as the following series:

$$g_P^{(2)}(\tau \mid \Delta t) = g_P^{(2)}(\tau \mid 0) + \sum_{m=1}^{\infty} \frac{2}{(2m+2)!}\left[\frac{d^{2m}}{dt^{2m}} g_P^{(2)}(t \mid 0)\right]_{t=\tau} (\Delta t)^{2m}. \tag{2.2.39}$$

The summation of equation 2.2.39 represents the finite-sample-time correction to the normalized power correlation function $g_P^{(2)}(\tau \mid 0)$ used to determine the normalized energy correlation function $g_P^{(2)}(\tau \mid \Delta t)$.

Applying equation 2.2.38 to the discrete-coherence-area formulation of the power correlation function, as given by equation 2.2.26, yields

$$g_P^{(2)}(\tau \mid \Delta t) = 1 + \frac{1}{N_c}\left[g^{(2)}(\tau \mid \Delta t) - 1\right], \tag{2.2.40}$$

where

$$g^{(2)}(\tau \mid \Delta t) = \frac{1}{(\Delta t)^2}\int_0^{\Delta t} d\,T \int_0^{T} dT' \; \{g^{(2)}(\tau + T' \mid 0) + g_P^{(2)}(\tau - T' \mid 0)\}$$

$$= g^{(2)}(\tau \mid 0) + \sum_{m=1}^{\infty} \frac{2}{(2m+2)!}\left[\frac{d^{2m}}{dt^{2m}} g_P^{(2)}(t \mid 0)\right]_{t=\tau} (\Delta t)^{2m}. \tag{2.2.41}$$

Likewise, the finite-sample-time correction to the power correlation formula given by equation 2.2.31, which was obtained using the Gaussian approximation, takes the form

$$g_P^{(2)}(\tau \mid \Delta t) = 1 + f(A)\,[(g^{(2)}(\tau \mid \Delta t) - 1], \tag{2.2.42}$$

where the property $g^{(2)}(\mathbf{R},0;\mathbf{R},\tau) = g^{(2)}(\tau \mid 0) = 1 + |g^{(1)}(\mathbf{R},0;\mathbf{R},\tau)|^2$ has been used.

One of the most prevalent forms of the second-order normalized electric field correlation function $g^{(2)}(\tau \mid 0)$, which often occurs as a result of pure Brownian motion of monodisperse scatterers, is the exponential function

$$g^{(2)}(\tau \mid 0) = 1 + \exp(-2\Gamma\tau), \tag{2.2.43}$$

where Γ is the linewidth of the corresponding frequency spectrum, which, for a Gaussian random field, is equal to the inverse of the coherence time τ_c. Substitution of equation 2.2.43 into equation 2.2.41 yields the following expression for $g^{(2)}(\tau \mid \Delta t)$ [Jakeman, 1970]:

$$g^{(2)}(\tau \mid \Delta t) = 1 + \left[\frac{\sinh(\Gamma\Delta t)}{\Gamma\Delta t}\right]^2 \exp(-2\Gamma\tau). \tag{2.2.44}$$

The term in the brackets is approximately equal to unity when $\Gamma\Delta t$ is less than 0.1, indicating that for exponentially decaying power correlation functions the effect of a finite sample time on the normalized energy correlation function is negligible when the sample time is much smaller than the detected field's coherence time.

For other forms of the normalized electric field correlation function $g^{(2)}(\tau \mid 0)$ the error introduced to the normalized energy correlation function $g^{(2)}(\tau \mid \Delta t)$ by neglecting the effects of the finite sample time Δt can be determined through evaluating either the integral or the numerically significant terms of the series in equation 2.2.41.

2.2.3.3 Combination of Spatial and Temporal Integrations

Combining the results of the spatial and temporal integrations that account for spatial coherence and finite sample time with equations 2.2.14 and 2.2.16, which relate the photon count correlation function to the detected energy correlation function, results in the following relationships between the photon count correlation function and the normalized second order electric field correlation function:

1) Single-detector autocorrelation:

$$\langle n(0)n(\tau)\rangle = \langle n(0)\rangle^2 \left\{1 + f(A)\ [g^{(2)}(\tau \mid \Delta t) - 1]\right\} + \langle n(0)\rangle\ u(\tau) \qquad (2.2.45)$$

2) Two-detector cross-correlation:

$$\langle n_A(0)n_B(\tau)\rangle = \langle n_A(0)\rangle\ \langle n_B(0)\rangle \left\{1 + f(A)\ [g^{(2)}(\tau \mid \Delta t) - 1]\right\}, \qquad (2.2.46)$$

where $g^{(2)}(\tau \mid \Delta t)$ is given by equation 2.2.41. In these expressions $\langle n_I(0)\rangle = \alpha_I \langle U(0)\rangle$ is the average number of photons detected by detector I during sample time Δt. These expressions utilize the spatial coherence factor of Jakeman, et al. (1970), which relies on the assumption that the detected field is a Gaussian random variable. Replacing f(A) by N_c^{-1} transforms these results into those obtained utilizing the discrete-coherence-area approximation (equation 2.2.26), which does not rely on Gaussian statistics.

2.2.4 Formulation of the Detected Intensity Correlation Functions

In this section, specific theoretical forms for the detected intensity correlation functions of polarized (VV) and depolarized (VH) light scattered from a suspension of polydisperse, cylindrically symmetric particles are developed. The detected intensity correlation function is initially related to the first and second order scattered electric field correlation functions for heterodyne and homodyne detection modes. These scattered

field correlation functions are then evaluated through various assumptions using the appropriate elements of the scattered field's matrix representation, as given by equation 2.1.9. Use of an electric dipole approximation to represent the light scattered from the cylindrically symmetric scatterers, along with Brownian diffusion models to describe the scatterers' random translation and reorientation, yields specific formulations of the correlation functions in terms of the scatterers' average velocities, translational and rotational Brownian diffusion coefficients, effective optical polarizability components, and polydispersity distribution function.

2.2.4.1 Optical Mixing: Heterodyne and Homodyne Correlation Functions

The photon count correlation function is related to the normalized second order electric field correlation function of the light incident upon the detector through equations 2.2.45 and 2.2.46, with use of equations 2.2.33, 2.2.34, and 2.2.41. In order to theoretically relate the photon correlation function to the specific dynamics of the scattering particles, the detected light must first be related to the light scattered from the illuminated suspension of particulates. This relationship depends strongly upon whether or not the scattered light is mixed with an unscattered reference beam (called a *local oscillator*) prior to detection.

When a local oscillator is used, corresponding to heterodyne detection, a beat frequency equal to the difference between the local oscillator frequency and the scattered light frequency is established in the detected light. This beat frequency can be related to the Doppler shift to determine the average velocity of the scattering particles. The absence of a local oscillator corresponds to the homodyne detection mode. This mode is called a self-beating process because the beat frequencies are established between different frequency components of the scattered light itself.

In the most general case of heterodyne detection, the total electric field $\mathbf{E}(\mathbf{R},t)$ reaching the detector at position $\mathbf{R}$ and time t is the sum of the scattered light field $\mathbf{E}_s(\mathbf{R},t)$

and the local oscillator field $\mathbf{E}_{LO}(\mathbf{R},t)$. The total detected intensity $I(\mathbf{R},t)$ at this point is thus given by the expression

$$I(\mathbf{R},t) = \frac{c}{8\pi}|\mathbf{E}(\mathbf{R},t)|^2 = \frac{c}{8\pi}|\mathbf{E}_s(\mathbf{R},t) + \mathbf{E}_{LO}(\mathbf{R},t)|^2$$
$$= \frac{c}{8\pi}[\mathbf{E}_s^*(\mathbf{R},t) + \mathbf{E}_{LO}^*(\mathbf{R},t)]\cdot[\mathbf{E}_s(\mathbf{R},t) + \mathbf{E}_{LO}(\mathbf{R},t)]. \quad (2.2.47)$$

Utilization of equation 2.2.47 to express the intensity correlation function $\langle I(\mathbf{R},t)\, I(\mathbf{R}',t')\rangle$ in terms of the scattered field and the local oscillator field provides an expression consisting of 16 terms. If the probability distribution of the scattered field's phase is uniform, which is particularly true for Gaussian light, then 10 of these 16 terms average to zero, giving the following expression for $\langle I(\mathbf{R},t)\, I(\mathbf{R}',t')\rangle$:

$$\langle I(\mathbf{R},t)\, I(\mathbf{R}',t')\rangle = \left(\frac{c}{8\pi}\right)^2 \Big[\langle|\mathbf{E}_{LO}(\mathbf{R},t)|^2\,|\mathbf{E}_{LO}(\mathbf{R}',t')|^2\rangle + \langle|\mathbf{E}_{LO}(\mathbf{R}',t')|^2\,|\mathbf{E}_s(\mathbf{R},t)|^2\rangle$$
$$+ \langle|\mathbf{E}_{LO}(\mathbf{R},t)|^2\,|\mathbf{E}_s(\mathbf{R}',t')|^2\rangle + \langle|\mathbf{E}_s(\mathbf{R},t)|^2\,|\mathbf{E}_s(\mathbf{R}',t')|^2\rangle \quad (2.2.48)$$
$$+ 2\,\mathrm{Re}\{\langle[\mathbf{E}_{LO}^*(\mathbf{R}',t')\cdot\mathbf{E}_s(\mathbf{R}',t')][\mathbf{E}_{LO}(\mathbf{R},t)\cdot\mathbf{E}_s^*(\mathbf{R},t)]\rangle\}\Big].$$

In heterodyne light scattering applications the local oscillator is a source of constant-intensity, coherent light of angular frequency ω_{LO} that is statistically independent of the scattered light. Under this condition, if the average scattered light intensity $i_s = (c/8\pi)\langle|\mathbf{E}_s(\mathbf{R},t)|^2\rangle$ is time-invariant then the first three terms on the right side of equation 2.2.48 are also independent of time. The fourth term is the homodyne or self-beat correlation function that would be detected if no local oscillator were present. The final term of equation 2.2.48 contains the mutual beating information between the scattered light and the local oscillator. Because this beating term is a function of the inner product of the scattered field with the local oscillator field, beating occurs only between the components of the scattered light and local oscillator that share the same polarization. Henceforth, the electric fields of the scattered light and the local oscillator will be treated as scalars, under the condition that both fields share the same polarization.

Because the local oscillator does not normally correspond to a Gaussian random process, the probability density of the detected light, which is a superposition of the local oscillator and scattered electric fields, is generally not Gaussian. Therefore, the discrete-coherence-area approximation of equation 2.2.23 is used to account for the effects of a finite detector area since this approximation does not rely on Gaussian statistics. In order to properly evaluate equation 2.2.23 the correlation function of the power received within a coherence area $\langle P_c(t)\, P_c(t')\rangle$ is first evaluated by integrating $\langle I(\mathbf{R},t)\, I(\mathbf{R}',t')\rangle$ over the coherence area A_c:

$$\begin{aligned}\langle P_c(t)\, P_c(t')\rangle &= \int_{A_c} d^2R \int_{A_c} d^2R' \,\langle I(\mathbf{R},t)\, I(\mathbf{R}',t')\rangle \\ &= I_{LO}^2 A_c^2 + 2 I_{LO} i_s A_c^2 + i_s^2 A_c^2 g^{(2)}(\mathbf{R},t;\mathbf{R},t') \\ &\quad + 2 I_{LO} i_s A_c^2 \varepsilon^2 \mathrm{Re}\{g^{(1)}(\mathbf{R},t;\mathbf{R},t') \exp[-i\omega_{LO}(t' - t)]\},\end{aligned} \tag{2.2.49}$$

where

$$I_{LO} = \langle I_{LO}(\mathbf{R},t)\rangle = \frac{c}{8\pi A_c} \int_{A_c} |E_{LO}(\mathbf{R},t)|^2 \, d^2R, \tag{2.2.50}$$

$$i_s = \frac{c}{8\pi A_c} \int_{A_c} \langle |E_s(\mathbf{R},t)|^2 \rangle \, d^2R, \tag{2.2.51}$$

and

$$\varepsilon^2 = \frac{1}{A_c^2 I_{LO} i_s} \left\langle \left| \int_{A_c} E_{LO}^*(\mathbf{R},t)\, E_s(\mathbf{R},t)\, d^2R \right|^2 \right\rangle. \tag{2.2.52}$$

The quantities I_{LO} and i_s respectively refer to the average intensities of the local oscillator and the scattered light. Additionally, the quantity ε^2 is the *heterodyne mixing efficiency*, which characterizes the degree of matching between the phase fronts of the scattered light and the local oscillator within the coherence area [Benedek, 1969]. Equation 2.2.49 is obtained by assuming that the scattered light is cross-spectrally pure, the average intensities of both the scattered light and the local oscillator depend neither on $\mathbf{R}$ nor t, the

local oscillator is monochromatic light of angular frequency ω_{LO}, and the second order normalized scattered-field correlation function $g^{(2)}(\mathbf{R},t;\mathbf{R},t')$ is independent of $\mathbf{R}$.

If $\langle P_c(t)\, P_c(t')\rangle$ is assumed equal for all coherence areas, then normalization of equation 2.2.49 and substitution of the result into equation 2.2.23 yields the following finite-detector-area normalized power correlation function:

$$g_P^{(2)}(\tau \mid 0) = \frac{\langle P(0)\, P(\tau)\rangle}{\langle P(0)\rangle^2} \tag{2.2.53}$$

$$= 1 + \frac{i_s^2\,[g^{(2)}(\mathbf{R},0;\mathbf{R},\tau) - 1]}{N_c\,(I_{LO} + i_s)^2} + \frac{2\, I_{LO}\, i_s\, \varepsilon^2\, \mathrm{Re}[g^{(1)}(\mathbf{R},0;\mathbf{R},\tau)\, \exp(-i\omega_{LO}\tau)]}{N_c\,(I_{LO} + i_s)^2}.$$

In order to consider the effects of a finite sample time Δt on the normalized energy correlation function, this expression can be substituted into equation 2.2.38 to yield the appropriate form of $g_P^{(2)}(\tau \mid \Delta t)$.

In order to simplify data inversion, practical heterodyne dynamic light scattering experiments are typically designed such that the local oscillator intensity I_{LO} is much greater than the average scattered light intensity i_s. Under this condition equation 2.2.53 reduces to

$$g_P^{(2)}(\tau \mid 0) \cong 1 + \frac{2\,\varepsilon^2}{N_c}\frac{i_s}{I_{LO}}\,\mathrm{Re}[g^{(1)}(\mathbf{R},0;\mathbf{R},\tau)\, \exp(-i\omega_{LO}\tau)]. \tag{2.2.54}$$

Thus, the heterodyne correlation function is proportional to the real part of the first order electric field correlation function after its frequency has been shifted down by the local oscillator frequency ω_{LO}.

The major difficulties associated with heterodyne techniques are that critical alignment and phase-front matching are necessary to produce a mixing efficiency ε^2 large enough to obtain a usable signal and that vibrations within the optics can generate large periodic signals that can completely mask the desired signal, even when the vibration's amplitude is as small as the incident light wavelength [Ford, 1985].

In homodyne light scattering experiments, no local oscillator is used. The homodyne power correlation function is thus obtained from equation 2.2.53 by letting the local oscillator intensity I_{LO} equal zero to obtain

$$g_P^{(2)}(\tau \mid 0) = 1 + \frac{1}{N_c}[g^{(2)}(\mathbf{R},0;\mathbf{R},\tau) - 1], \qquad (2.2.55)$$

which is equivalent to equation 2.2.26. Because the scattered light beats with itself $g_P^{(2)}(\tau \mid 0)$ is not a function of ε^2. Therefore, phase matching problems typically encountered in heterodyne experiments do not occur in the homodyne detection mode. Unlike the heterodyne case, if the probability distribution of the scattered electric field is approximately Gaussian the spatial coherence correction of Jakeman, et al. (1970) (equations 2.2.31 - 2.2.34) is applicable to homodyne detection and thus provides a more accurate alternative to equation 2.2.54.

2.2.4.2 Scattered Field Correlation Functions for Cylindrically Symmetric Scatterers

The relationships given by equation 2.2.54 for heterodyne detection and equations 2.2.31 and 2.2.55 for homodyne detection express the normalized power correlation function in terms of the scattered light's normalized correlation functions. In order to relate the detected intensity correlation functions to the optical and dynamic properties of the particles, the specific theoretical forms of the scattered light correlation functions are developed through the use of equation 2.1.9, which relates the electric field $E_{sj}(\mathbf{R},t)$ scattered from a single particle to the optical properties of the scattering particle and the incident light.

2.2.4.2.1 General Expressions for the First and Second Order Electric Field Correlation Functions for a Collection of Scatterers

The total scattered electric field $E_s(\mathbf{R},t)$ received at position $\mathbf{R}$ and time t by the detector is the sum of the electric fields $E_{sj}(\mathbf{R},t)$ scattered from each particle within the detector's field of view. Thus,

$$E_s(\mathbf{R},t) = \sum_{j=1}^{N_T} E_{sj}(\mathbf{R},t), \qquad (2.2.56)$$

where N_T is the total number of scattering particles contained within a volume V_T that encompasses the entire scattering volume. The second order scattered electric field correlation function $G^{(2)}(\mathbf{R},0;\mathbf{R},\tau) = \langle |E_{sf}(\mathbf{R},0)|^2 |E_{sf}(\mathbf{R},\tau)|^2 \rangle$ is thus given by

$$G^{(2)}(\mathbf{R},0;\mathbf{R},\tau) = \sum_{j=1}^{N_T} \sum_{k=1}^{N_T} \sum_{l=1}^{N_T} \sum_{m=1}^{N_T} \langle E_{sfj}^*(\mathbf{R},0)\, E_{sfk}(\mathbf{R},0)\, E_{sfl}^*(\mathbf{R},\tau)\, E_{sfm}(\mathbf{R},\tau) \rangle. \tag{2.2.57}$$

In order to simplify the evaluation of this correlation function, the number of statistically independent scatterers within the scattering volume is assumed large enough to validate the Gaussian approximation. Under this approximation the second order correlation function $G^{(2)}(\mathbf{R},0;\mathbf{R},\tau)$, through the application of equation 2.2.27, becomes the following function of the first-order correlation function $G^{(1)}(\mathbf{R},0;\mathbf{R},\tau)$:

$$G^{(2)}(\mathbf{R},0;\mathbf{R},\tau) = |G^{(1)}(\mathbf{R},0;\mathbf{R},0)|^2 + |G^{(1)}(\mathbf{R},0;\mathbf{R},\tau)|^2. \tag{2.2.58}$$

Evaluation of $G^{(2)}(\mathbf{R},0;\mathbf{R},\tau)$ therefore reduces to the less-complicated problem of evaluating $G^{(1)}(\mathbf{R},0;\mathbf{R},\tau)$.

This first-order electric field correlation function can be theoretically represented through the use of equations 2.1.9 and 2.2.56 as follows:

$$G^{(1)}(\mathbf{R},0;\mathbf{R},\tau) = \langle E_{sf}^*(\mathbf{R},0)\, E_{sf}(\mathbf{R},\tau) \rangle = \frac{\exp(-i\omega\tau)}{k^2 R^2} \sum_{j=1}^{N_T} \sum_{k=1}^{N_T} \langle E_i^*(\mathbf{r}_j)\, E_i(\mathbf{r}_k')\, S_{pj}^*(\Omega_j,\mathbf{a}_j)\, S_{pk}(\Omega_k',\mathbf{a}_k)\, \exp[i\mathbf{q}\cdot(\mathbf{r}_k' - \mathbf{r}_j)] \rangle, \tag{2.2.59}$$

where $\mathbf{r}_j$ is the position of the center of particle j, Ω_j is a set of parameters describing the orientation of particle j, and $\mathbf{a}_j$ is a set of particle morphological and optical parameters. Unprimed parameters are evaluated at time $t = 0$ and primed parameters are evaluated at $t = \tau$. The index p denotes an appropriate element of the amplitude scattering matrix, according to the polarizations of the incident and detected electric fields. The average of each term of equation 2.2.59 given by integrals of the following form:

$$\langle E_i^*(\mathbf{r}_j)\, E_i(\mathbf{r}_k')\, S_{pj}^*(\Omega_j,\mathbf{a}_j)\, S_{pk}(\Omega_k',\mathbf{a}_k)\, \exp[i\mathbf{q}\cdot(\mathbf{r}_k' - \mathbf{r}_j)]\rangle$$

$$= \int d\mathbf{r}_j \int d\mathbf{r}_k' \int d\Omega_j \int d\Omega_k' \int d\mathbf{a}_j \int d\mathbf{a}_k\, E_i^*(\mathbf{r}_j)\, E_i(\mathbf{r}_k')\, S_{pj}^*(\Omega_j,\mathbf{a}_j) \quad (2.2.60)$$

$$\times\, S_{pk}(\Omega_k',\mathbf{a}_k)\, \exp[i\mathbf{q}\cdot(\mathbf{r}_k' - \mathbf{r}_j)]\, f(\mathbf{r}_j,\mathbf{r}_k',\Omega_j,\Omega_k',\mathbf{a}_j,\mathbf{a}_k),$$

where $f(\mathbf{r}_j,\mathbf{r}_k',\Omega_j,\Omega_k',\mathbf{a}_j,\mathbf{a}_k)$ is the joint probability density function of $\mathbf{r}_j$, $\mathbf{r}_k'$, Ω_j, Ω_k', $\mathbf{a}_j$, and $\mathbf{a}_k$. A general derivation of $G^{(1)}(\mathbf{R},0;\mathbf{R},\tau)$ requires integrating specific forms of $E_i(\mathbf{r}_j)$, $S_{pj}(\Omega_j,\mathbf{a})$, and $f(\mathbf{r}_j,\mathbf{r}_k',\Omega_j,\Omega_k',\mathbf{a}_j,\mathbf{a}_k)$ over the range of all possible values of $\mathbf{r}_j$, $\mathbf{r}_k'$, Ω_j, Ω_k', $\mathbf{a}_j$, and $\mathbf{a}_k$ and summing these results according to equation 2.2.59.

Further simplification of the derivation of a usable relationship between $G^{(2)}(\mathbf{R},0;\mathbf{R},\tau)$ and the relevant optical, structural, and thermophysical properties is possible through various commonly used assumptions. First, the position, orientation, and motion of each particle are assumed to be statistically independent of each other as well as independent of the presence of other particles. This is equivalent to assuming that none of these quantities has any effect upon the behavior of the other quantities. Splitting the summation of equation 2.2.59 into its $j = k$ and $j \neq k$ terms and applying this assumption results in the following expression:

$$G^{(1)}(\mathbf{R},0;\mathbf{R},\tau) = \frac{\exp(-i\omega\tau)}{k^2\, R^2}$$

$$\times \left\{ \sum_{j=1}^{N_T} \langle E_i^*(\mathbf{r}_j)\, E_i(\mathbf{r}_j')\, S_{pj}^*(\Omega_j,\mathbf{a}_j)\, S_{pj}(\Omega_j',\mathbf{a}_j)\, \exp[i\mathbf{q}\cdot(\mathbf{r}_j' - \mathbf{r}_j)]\rangle \right. \quad (2.2.61)$$

$$+ \sum_{k \neq j = 1}^{N_T} \sum_{j=1}^{N_T} \langle E_i^*(\mathbf{r}_j)\, S_{pj}^*(\Omega_j,\mathbf{a}_j)\, \exp(-i\mathbf{q}\cdot\mathbf{r}_j)\rangle$$

$$\left. \times\, \langle E_i(\mathbf{r}_k')\, S_{pk}(\Omega_k',\mathbf{a}_k)\, \exp(i\mathbf{q}\cdot\mathbf{r}_k')\rangle \right\} .$$

Next, the translational and rotational dynamics of each particle are assumed to be statistically independent of each other. This permits factorization of the averages in the first summation of equation 2.2.61 to obtain the following:

$$G^{(1)}(\mathbf{R},0;\mathbf{R},\tau) = \frac{\exp(-i\omega\tau)}{k^2 R^2}$$

$$\times\Bigg\{ \sum_{j=1}^{N_T} \langle E_i^*(\mathbf{r}_j)\, E_i(\mathbf{r}_j')\, \exp[i\mathbf{q}\cdot(\mathbf{r}_j' - \mathbf{r}_j)]\rangle \langle S_{pj}^*(\Omega_j,\mathbf{a}_j)\, S_{pj}(\Omega_j',\mathbf{a}_j)\rangle$$

$$+ \sum_{k\neq j=1}^{N_T} \sum_{j=1}^{N_T} \langle S_{pj}^*(\Omega_j,\mathbf{a}_j)\rangle \langle S_{pk}(\Omega_k',\mathbf{a}_k)\rangle \qquad (2.2.62)$$

$$\times \langle E_i^*(\mathbf{r}_j)\exp(-i\mathbf{q}\cdot\mathbf{r}_j)\rangle \langle E_i(\mathbf{r}_k')\exp(i\mathbf{q}\cdot\mathbf{r}_k')\rangle \Bigg\}.$$

Each of the averages in equation 2.2.62 can henceforth be separately evaluated, given specific forms of the amplitude scattering matrix elements $S_{pj}(\Omega_j,\mathbf{a}_j)$ and the probability density functions governing the translation and reorientation of the scattering particles.

In order to avoid unnecessary complications during the evaluation of the averages of equation 2.2.62 the following additional specifications and assumptions relevant to this experimental study are made:

1. The position and orientation probabilities of all scattering particles at any single time t are assumed to be uniform.
2. The internal electric field within each scattering particle is assumed uniform throughout the particle and in phase with the local incident field. Thus, each particle acts as an oscillating dipole with dipole moment $p_i = \alpha_{ij} E_{ij}$, where E_{ij} is the electric field incident upon the particle and α_{ij} is the *polarizability tensor*. This uniform internal field approximation, known as the Rayleigh or electrostatics approximation, is valid when $|m|\, l \ll \lambda/2\pi$, where m is the ratio of the particle's refractive index to the

refractive index of the surrounding medium, l is the length of the particle, and λ is the *in vacuo* incident light wavelength [van de Hulst, 1981].

2. The scattering particles are assumed to be cylindrically symmetric, both optically and geometrically. Therefore, α_{ij} is a diagonal tensor in a body-fixed coordinate system oriented along the particle's principle axes, with $\alpha_{11} \equiv \alpha_{\parallel}$ and $\alpha_{22} = \alpha_{33} \equiv \alpha_{\perp}$. Furthermore, the optical symmetry axis is assumed to be coincident with the geometric symmetry axis for each particle. The orientational coordinates are thus specified by the angles θ and φ of a spherical coordinate system, as illustrated in figure 2.2.1. These orientational angles form the set Ω_j for each scattering particle.

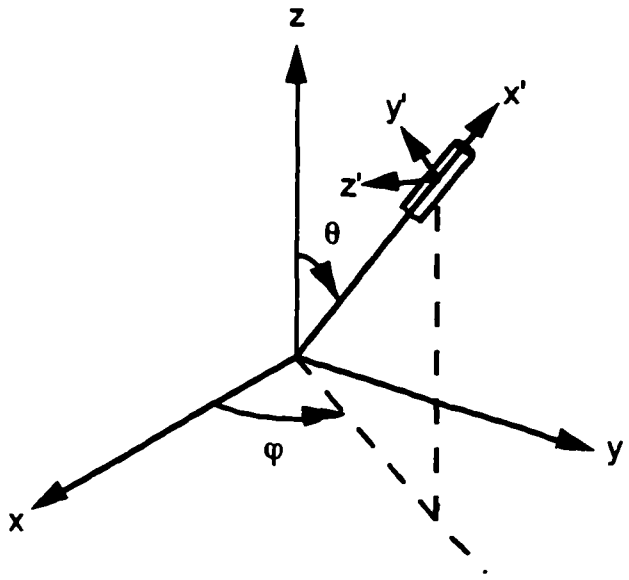

Figure 2.2.1: Spherical coordinate system illustrating body-fixed and laboratory-fixed coordinates.

4. Since the incident light is supplied by a laser operating in the TEM 00 mode, the intensity distribution along the radius of the beam is Gaussian [Guenther, 1990]. Therefore, the scattering volume is approximated as a cylindrical volume with length L and radius ω_0. The incident field amplitude within the scattering volume is approximated as

$$E_i(\mathbf{r}) = E_o \exp(-|\mathbf{r}_\perp|^2/\omega_o^2), \qquad (2.2.63)$$

where $\mathbf{r}_\perp$ is the component of the particle position $\mathbf{r}$ perpendicular to the direction of the incident light.

2.2.4.2.2 Particle Dynamics: Translational and Rotational Brownian Motion

Proper evaluation of the averages occurring in equation 2.2.62 requires knowledge of the dynamic processes governing the particle motion. In the current study, each scattering particle is assumed to undergo a combination of deterministic translation and random translation and rotation. The average velocity V of the scatterers is assumed uniform throughout the scattering volume. This velocity, which characterizes the deterministic motion of the particles, is often the result of Stoke's drag induced upon the particles by a non-zero solvent (surrounding gas medium) velocity or a variety of phoretic forces, such as thermophoresis, photophoresis, diffusiophoresis, or electrophoresis. The random motion of the scattering particles is governed by Brownian processes, in which momentum is randomly imparted to the particle through collisions with the thermally-agitated molecules of the surrounding fluid medium. These molecule-particle collisions result in particle motion that resembles a random walk process.

The total displacement Δr_B produced by Brownian processes during a time τ is the sum of the random displacements produced by each molecule-particle collision during this time. As a result of the central limit theorem of probability theory [Ross, 1988] the sum of these random displacements increasingly resembles a Gaussian random process as the number of molecule-particle collisions occurring during time τ increases. Thus, the probability density $f(\Delta r_B|\tau)$ governing the Brownian displacement Δr_B of a spherical particle during time τ is approximately equal to the following Gaussian distribution [Berne and Pecora, 1976]:

$$f(\Delta r_B|\tau) = \left(\frac{2\pi}{3}\langle|\Delta r_B|^2\rangle\right)^{3/2} \exp\left(-\frac{3\,|\Delta r_B|^2}{2\,\langle|\Delta r_B|^2\rangle}\right), \qquad (2.2.64)$$

where

$$\langle |\Delta \mathbf{r}_B|^2 \rangle = 6\, D\, \tau \tag{2.2.65}$$

with

$$D = \frac{k_B\, T}{f}. \tag{2.2.66}$$

In equation 2.2.66, k_B is Boltzmann's constant and f is the spherical particle's friction coefficient, which relates the drag force **F** exerted on the particle to it's velocity **v** via the equation $\mathbf{F} = f\mathbf{v}$.

Successive differentiation of equation 2.2.64 with respect to τ and the components of $\Delta \mathbf{r}_B$ reveals that $f(\Delta \mathbf{r}_B|\tau)$ is a solution of the following diffusion equation

$$D\, \nabla^2 f(\Delta \mathbf{r}_B|\tau) = \frac{\partial}{\partial \tau} f(\Delta \mathbf{r}_B|\tau), \tag{2.2.67}$$

subject to the initial condition: $f(\Delta \mathbf{r}_B|0) = \delta(\Delta \mathbf{r}_B)$. The constant D is known as the *Brownian translational diffusion coefficient.*

The more general case of Brownian translation of a non-spherical particle is governed by a similar diffusion equation [Berne and Pecora, 1976]:

$$\nabla \cdot \mathbf{D} \cdot \nabla f(\Omega'|\Omega,\tau) = \frac{\partial}{\partial \tau} f(\Omega'|\Omega,\tau), \tag{2.2.68}$$

where $\mathbf{D} \equiv D_{ij}$ is a second-rank tensor of directional diffusion coefficients. The elements of D_{ij} are related to the particle's friction coefficient in a manner analogous to equation 2.2.66:

$$D_{ij} = \frac{k_B\, T}{f_{ij}}. \tag{2.2.69}$$

In this case the friction coefficient f_{ij} is a tensor, which is defined by the following relationship between the particle's velocity v_j with respect to the surrounding fluid medium and the resulting drag force F_i:

$$F_i = \sum_{j=1}^{3} f_{ij}\, v_j. \tag{2.2.70}$$

In a manner similar to the translational displacement of the particle, as described by equations 2.2.64 to 2.2.70, Brownian forces also affect the orientation Ω of each particle suspended within a finite-temperature fluid environment. In the most general case, the conditional probability density function $f(\Omega'|\Omega,\tau)$, governing the rotation of a particle from an initial orientation Ω to a later orientation Ω' after a time interval of duration τ, is given by the relation [Favro, 1965]:

$$- \mathbf{M}\cdot\mathbf{D}_R\cdot\mathbf{M}\, f(\Omega'|\Omega,\tau) = \frac{\partial}{\partial\tau} f(\Omega'|\Omega,\tau), \tag{2.2.71}$$

where $\mathbf{M}$ is the general rigid-body quantum mechanical angular momentum operator and $\mathbf{D}_R \equiv D_{Rij}$ is a rotational diffusion tensor, whose elements are given by the following relationship [Favro, 1960]:

$$D_{Rij} = \frac{1}{2} k_B T (\beta_{ij}^{-1} + \beta_{ji}^{-1}). \tag{2.2.72}$$

In this equation β_{ij} refers to the elements of the rotational friction tensor, which is defined by the following relationship between the angular velocity ω_j of the particle with respect to its fluid surroundings and the frictional torque τ_i exerted on the particle as a result of this motion:

$$\tau_i = \sum_{j=1}^{3} \beta_{ij}\, \omega_j. \tag{2.2.73}$$

When subjected to the initial condition $f(\Omega'|\Omega,0) = \delta(\Omega' - \Omega)$, the rotational diffusion of equation 2.2.71 provides the conditional probability density $f(\Omega'|\Omega,\tau)$ of finding a particle at orientation Ω' at a time τ after it was initially at orientation Ω. The explicit form of this conditional probability density function is determined by solving equation 2.2.71 for $f(\Omega'|\Omega,\tau)$ and applying the initial condition. The joint probability density $f(\Omega',\Omega|\tau)$ of finding the particle at orientation Ω at the initial time $\tau = 0$ and at orientation Ω' at a later time $\tau > 0$ is then determined by multiplying $f(\Omega'|\Omega,\tau)$ by the initial ($\tau = 0$) orientation probability density $f(\Omega)$. The solution of the rotational diffusion equation for cylindrically symmetric scatterers presented in the following discussion and

its application to evaluating the rotation dependent averages occurring in equation 2.2.62 follows the methodology presented by Berne and Pecora (1976).

The solution of the rotational diffusion equation (equation 2.2.71) simplifies considerably if each scattering particle exhibits a cylindrical geometric symmetry with an axis of symmetry coincident with its axis of optical symmetry. In this case, spinning about this axis of symmetry does not affect the scattered-light correlation function and the particle's orientation is sufficiently specified by the two spherical coordinates θ and φ that are defined by figure 2.2. The general rotational diffusion equation thus simplifies to [Favro, 1965]

$$- D_R \mathbf{L}^2 f(\Omega'|\Omega,\tau) = \frac{\partial}{\partial\tau} f(\Omega'|\Omega,\tau), \qquad (2.2.74)$$

where

$$- \mathbf{L}^2 \equiv \frac{1}{\sin\theta}\frac{\partial}{\partial\theta}\left(\sin\theta\,\frac{\partial}{\partial\theta}\right) + \frac{1}{\sin^2\theta}\frac{\partial^2}{\partial\varphi^2}.$$

The formal solution of this diffusion equation takes the following form [Berne and Pecora, 1976]:

$$f(\Omega'|\Omega,\tau) = \exp(-\tau D_R \mathbf{L}^2)\, f(\Omega'|\Omega,0), \qquad (2.2.75)$$

where $f(\Omega'|\Omega,0)$ is the initial ($\tau = 0$) value of $f(\Omega'|\Omega,\tau)$. The eigenfunctions of the $\mathbf{L}^2$ operator, which are the spherical harmonics $Y_{l,m}(\Omega)$, obey the eigenvalue equation

$$\mathbf{L}^2 Y_{l,m}(\Omega) = l(l+1)\, Y_{l,m}(\Omega), \qquad (2.2.76)$$

where l is an integer. Therefore, the general solution of equation 2.2.74 is a linear combination of the fundamental solutions $\exp[-l(l+1)D_R\tau]\, Y_{l,m}(\Omega)$.

The spherical harmonics are defined as follows [Arfken, 1985]:

$$Y_{l,m}(\Omega) \equiv Y_{l,m}(\theta,\varphi) \qquad (2.2.77)$$

$$= (-1)^m \sqrt{\frac{2l+1}{4\pi}\frac{(l-m)!}{(l+m)!}}\, P_{l,m}(\cos\theta)\exp(im\varphi),$$

where $P_{l,m}(x)$ are the associated Legendre polynomials:

$$P_{l,m}(x) = \frac{1}{2^l\, l!}(1 - x^2)^{m/2}\frac{d^{l+m}}{dx^{l+m}}(x^2 - 1)^l. \tag{2.2.78}$$

The spherical harmonics $Y_{l,m}(\theta,\varphi)$ form a complete set of basis functions in Hilbert space and obey the following orthogonality condition:

$$\int d\Omega\, Y_{l,m}^*(\Omega)\, Y_{l',m'}(\Omega) = \int_{\varphi=0}^{2\pi}\int_{\theta=0}^{\pi} Y_{l,m}(\theta,\varphi)\, Y_{l',m'}(\theta,\varphi)\sin\theta\, d\theta\, d\varphi = \delta_{l,l'}\,\delta_{m,m'}. \tag{2.2.79}$$

Specific expressions for some of the lower order spherical harmonics in terms of θ and φ that are necessary for the evaluation of $\langle S_p^*(\Omega,\mathbf{a})\, S_p(\Omega',\mathbf{a})\rangle$ follow [Arfken, 1985]:

$$Y_{0,0}(\theta,\varphi) = \frac{1}{\sqrt{4\pi}} \tag{2.2.80a}$$

$$Y_{2,0}(\theta,\varphi) = \sqrt{\frac{5}{16\pi}}\,(3\cos^2\theta - 1) \tag{2.2.80b}$$

$$Y_{2,1}(\theta,\varphi) = -\sqrt{\frac{15}{8\pi}}\sin\theta\cos\theta\exp(i\varphi) \tag{2.2.80c}$$

$$Y_{2,-1}(\theta,\varphi) = \sqrt{\frac{15}{8\pi}}\sin\theta\cos\theta\exp(-i\varphi). \tag{2.2.80d}$$

Applying the initial condition $f(\Omega'|\Omega,0) = \delta(\Omega' - \Omega)$ to the series of fundamental solutions and making use of the orthogonality property (equation 2.2.79) in order to determine $f(\Omega'|\Omega,\tau)$ results in

$$f(\Omega'|\Omega,\tau) = \sum_{l=0}^{\infty}\sum_{m=-l}^{l} Y_{l,m}^*(\Omega)\, Y_{l,m}(\Omega')\exp[-l(l+1)D_R\tau] = \sum_{l=0}^{\infty}\sum_{m=-l}^{l} Y_{l,m}(\Omega)\, Y_{l,m}^*(\Omega')\exp[-l(l+1)D_R\tau], \tag{2.2.81}$$

where the second expression results from the fact that $f(\Omega'|\Omega,\tau)$ is a real function.

The joint probability density of Ω and Ω' is the product of the conditional probability density of Ω' at time τ, given an initial orientation of Ω, and the probability density of the occurrence of orientation Ω at the initial time:

$$f(\Omega',\Omega|\tau) = f(\Omega'|\Omega,\tau)\, f(\Omega). \tag{2.2.82}$$

The initial orientation probability $f(\Omega)$ is assumed to be the same as the equilibrium or infinite-delay-time orientation probability. Thus,

$$f(\Omega) = \lim_{\tau \to \infty} f(\Omega'|\Omega,\tau) = Y_{0,0}(\Omega)\, Y_{0,0}^*(\Omega') = \frac{1}{4\pi}, \tag{2.2.83}$$

which is uniform over all possible orientations. The joint probability density of the occurrence of orientation Ω' at time $t = \tau$ and Ω at time $t = 0$ is thus

$$f(\Omega',\Omega|\tau) = \frac{1}{4\pi} \sum_{l=0}^{\infty} \sum_{m=-l}^{l} Y_{l,m}(\Omega)\, Y_{l,m}^*(\Omega') \exp[-l(l+1)D_R\tau]. \tag{2.2.84}$$

In subsequent discussions, this probability density function is used to evaluate the rotation-dependent averages occurring in equation 2.2.62.

The Brownian translation probability density function $f(\Delta r_B|\tau)$, which is needed to evaluate the translation-dependent averages of equation 2.2.62, is approximated by the use of the orientation-averaged translational diffusion coefficient [Perrin, 1936]

$$D = \frac{k_B T}{3}(f_{11}^{-1} + f_{22}^{-1} + f_{33}^{-1}) \tag{2.2.85}$$

with the spherical-particle Gaussian density function given by equation 2.2.64. This approximation of $f(\Delta r_B|\tau)$ relies on the assumption that the reorientation time scale is much lower than the translational time scale.

The Brownian probability density functions $f(\Delta r_B|\tau)$ and $f(\Omega',\Omega|\tau)$ given by equations 2.2.64 and 2.2.84 thoroughly characterize the relevant random translational and rotational motions of the cylindrically symmetric particles under consideration and thus provide sufficient information about their dynamics to evaluate the averages occurring in equation 2.2.62 in terms of the particles' translational and rotational diffusion

coefficients. The correlation functions determined from these averages can then be related to the geometric properties of the particles and the physical properties of the surrounding fluid medium by using appropriate expressions for the drag coefficients occurring in equations 2.2.69 and 2.2.72 to express the diffusion coefficients in terms of these physical properties.

2.2.4.2.3 Evaluation of Self-Correlation Functions

The first summation ($i = j$) of equation 2.2.62 is evaluated by utilizing the translational and rotational probability density functions obtained in the previous section to separately determine the translation- and rotation-dependent averages, corresponding to the factors $\langle E_i^*(\mathbf{r}_j)\, E_i(\mathbf{r}_j')\, \exp[i\mathbf{q}\cdot(\mathbf{r}_j' - \mathbf{r}_j)]\rangle$ and $\langle S_{pj}^*(\Omega_j, \mathbf{a}_j)\, S_{pj}(\Omega_j', \mathbf{a}_j)\rangle$, for a typical scattering particle. The subscript j is therefore dropped. The products of these averages, which are called the *self-correlation functions* [Berne and Pecora, 1976], are then summed according to equation 2.2.62 while accounting for polydispersity in the particles' morphological and/or optical properties by averaging the typical-particle results over the distribution of morphological and optical parameters $f(\mathbf{a})$.

Translation-Dependent Averages

To facilitate the evaluation of the translation-dependent average $\langle E_i^*(\mathbf{r})\, E_i(\mathbf{r}')\, \exp[i\mathbf{q}\cdot(\mathbf{r}' - \mathbf{r})]\rangle$ for a typical particle, the particle position $\mathbf{r}' \equiv \mathbf{r}(\tau)$ at time τ is expressed as follows:

$$\mathbf{r}' = \Delta\mathbf{r}_B + \mathbf{V}\tau + \mathbf{r}, \tag{2.2.86}$$

where $\Delta\mathbf{r}_B$ is the position change attributed to Brownian diffusion, $\mathbf{V}\tau$ is the position change associated with the particle's average velocity $\mathbf{V}$ (assumed constant during time τ), and $\mathbf{r} \equiv \mathbf{r}(0)$ is the particle's initial position. Considerable simplification of the analysis and results occurs if the Brownian component of the particle's motion does not produce a significant contribution to the correlation function through the spatial variation of the incident field $E_i(\mathbf{r})$ [Chowdhury, et al., 1984]. This condition is satisfied when $q\omega_0 \gg 1$ because under this condition Brownian translation over a distance $\approx q^{-1}$, which is

sufficient to significantly change the phase factor $\exp(i\mathbf{q}\cdot\mathbf{r})$, has little effect on the incident electric field $E_i(\mathbf{r})$ as given by equation 2.2.63. This approximation permits the deletion of the Δr_B contribution to $\mathbf{r}'$ when it occurs as the argument of $E_i(\mathbf{r})$, making the amplitude factors and the phase factors statistically independent of each other. Thus, the translation-dependent average can be factored as follows:

$$\langle E_i^*(\mathbf{r})\, E_i(\mathbf{r}')\, \exp[i\mathbf{q}\cdot(\mathbf{r}' - \mathbf{r})]\rangle = \langle E_i^*(\mathbf{r})\, E_i(\mathbf{r}')\rangle \langle \exp[i\mathbf{q}\cdot(\mathbf{r}' - \mathbf{r})]\rangle. \quad (2.2.87)$$

The incident electric field correlation function $\langle E_i^*(\mathbf{r})\, E_i(\mathbf{r}')\rangle$ is found by integrating the product $E_i^*(\mathbf{r})\, E_i(\mathbf{V}\tau + \mathbf{r})$ times the initial-position probability density function $f(\mathbf{r})$ over the volume V_T. Using equation 2.2.63 for $E_i(\mathbf{r})$:

$$\langle E_i^*(\mathbf{r})\, E_i(\mathbf{r}')\rangle = |E_o|^2 \int\int\int d^3r\, f(\mathbf{r}) \exp\left(-\frac{|\mathbf{r}_\perp|^2}{\omega_o^2}\right) \exp\left(-\frac{|\mathbf{r}_\perp + \mathbf{V}_\perp\tau|^2}{\omega_o^2}\right), \quad (2.2.88)$$

where $\mathbf{V}_\perp$ is the component of the particle's average velocity $\mathbf{V}$ perpendicular to the propagation direction of the incident light. Since the position probability density at any single time is assumed uniform,

$$f(\mathbf{r}) = \frac{\rho_N(\mathbf{r})}{N_T} = \frac{1}{V_T}, \quad (2.2.89)$$

where $\rho_N(\mathbf{r})$ is the agglomerate number density and N_T is the total number of agglomerates in V_T. Utilizing this uniform probability density to evaluate the integral in equation 2.2.88 provides the following result:

$$\langle E_i^*(\mathbf{r})\, E_i(\mathbf{r}')\rangle = \frac{|E_o|^2}{2} \frac{V_s}{V_T} \exp\left(-\frac{V_\perp^2\, \tau^2}{2\, \omega_o^2}\right), \quad (2.2.90)$$

where $V_s = \pi\omega_o^2 L$ is the volume of the scattering volume. This result is similar in form to the amplitude correlations obtained by Penner, et al. (1976) and Chowdhury, et al. (1984) for a spherically-symmetric incident field.

Similarly, the correlation function of the Doppler phase factor $\langle \exp[i\mathbf{q}\cdot(\mathbf{r}' - \mathbf{r})]\rangle$ is found through the expression:

$$\langle \exp[i\mathbf{q}\cdot(\mathbf{r}' - \mathbf{r})] \rangle = \langle \exp[i\mathbf{q}\cdot(\Delta\mathbf{r}_B + \mathbf{V}\tau)] \rangle$$
$$= \int \exp[i\mathbf{q}\cdot(\Delta\mathbf{r}_B + \mathbf{V}\tau)]\, f(\Delta\mathbf{r}_B|\tau)\, d(\Delta\mathbf{r}_B). \tag{2.2.91}$$

Substitution of equation 2.2.64 for $f(\Delta\mathbf{r}_B|\tau)$ into equation 2.2.91 leads to the following result upon evaluating the integral:

$$\langle \exp[i\mathbf{q}\cdot(\Delta\mathbf{r}_B + \mathbf{V}\tau)] \rangle = \frac{\exp(i\mathbf{q}\cdot\mathbf{V}\tau)}{(4\pi D\tau)^{3/2}} \int \exp(i\mathbf{q}\cdot\Delta\mathbf{r}_B) \exp\left(-\frac{|\Delta\mathbf{r}_B|^2}{4D\tau}\right) d(\Delta\mathbf{r}_B)$$
$$= \exp(i\mathbf{q}\cdot\mathbf{V}\tau) \exp(-q^2 D\tau). \tag{2.2.92}$$

Combination of the incident field correlation function of equation 2.2.90 with the phase factor correlation function of equation 2.2.92 results in the following expression for the translation-dependent factors of the first summation ($j = k$) of equation 2.2.62:

$$\langle E_i^*(\mathbf{r})\, E_i(\mathbf{r}') \exp[i\mathbf{q}\cdot(\mathbf{r}' - \mathbf{r})] \rangle$$
$$= \frac{|E_0|^2}{2} \frac{V_s}{V_T} \exp(i\mathbf{q}\cdot\mathbf{V}\tau) \exp(-q^2 D\tau) \exp\left(-\frac{V_\perp^2 \tau^2}{2\omega_0^2}\right). \tag{2.2.93}$$

Rotation-Dependent Averages

In addition to the previously evaluated translation-dependent factor, the first summation ($j = k$) of equation 2.2.62 also contains the factor $\langle S_{pj}^*(\Omega_j, \mathbf{a}_j)\, S_{pj}(\Omega_j', \mathbf{a}_j) \rangle$, which generally depends upon the rotational motion of the scattering particles. Evaluation of this factor requires specifying the dependence of the amplitude scattering elements $S_{pj}(\Omega_j, \mathbf{a}_j)$ on orientation and integrating the time-delayed product of amplitude scattering elements times the orientational probability density function $f(\Omega', \Omega|\tau)$ over all possible orientations. The subsequent development follows the derivation in Berne and Pecora (1976).

The orientation-dependence of the amplitude scattering matrix elements is found by utilizing the previously-discussed assumption that each scattering particle behaves as an oscillating dipole with dipole moment $\mathbf{p} = \alpha \cdot \mathbf{E}_i$. A comparison of equation 2.1.9 with the classical far-field solution of the electric field from a radiating dipole [Jackson, 1975],

[Berne and Pecora, 1976] yields the following expressions for the amplitude scattering matrix elements corresponding to VV ($p = 1$) and VH ($p = 3$) detection:

$$S_1(\Omega,\mathbf{a}) = - i k^3 \, \mathbf{e}_{Vs} \cdot \alpha \cdot \mathbf{e}_{Vi} \tag{2.2.94a}$$

and

$$S_3(\Omega,\mathbf{a}) = - i k^3 \, \mathbf{e}_{Hs} \cdot \alpha \cdot \mathbf{e}_{Vi}. \tag{2.2.94b}$$

For particles exhibiting a cylindrical optical symmetry, the polarizability tensor has the following representation in body-fixed coordinates whose axes correspond to the scattering particle's principal axes:

$$\alpha = \begin{bmatrix} \alpha_{\parallel} & 0 & 0 \\ 0 & \alpha_{\perp} & 0 \\ 0 & 0 & \alpha_{\perp} \end{bmatrix}. \tag{2.2.95}$$

In order to evaluate the vector products of equations 2.2.94, the polarization basis vectors $\mathbf{e}_{Vi}$, $\mathbf{e}_{Vs}$, and $\mathbf{e}_{Hs}$ are first represented in terms of the body-fixed coordinate system. Using the coordinate systems defined by figure 2.2

$$\mathbf{e}_{Vi} = \mathbf{e}_{Vs} = \{\cos\theta, \sin\theta, 0\} \tag{2.2.96a}$$

and

$$\mathbf{e}_{Hs} = \{\sin\theta\cos\varphi, - \cos\theta\cos\varphi, \sin\varphi\}. \tag{2.2.96b}$$

Substitution of equations 2.2.95 and 2.2.96 into equations 2.2.94 results in the following:

$$S_1(\Omega,\mathbf{a}) = - i k^3 \left[\alpha + \frac{1}{3}\beta \, (3\cos^2\theta - 1)\right] \tag{2.2.97a}$$

and

$$S_3(\Omega,\mathbf{a}) = - i k^3 \beta \cos\theta \sin\theta \cos\varphi, \tag{2.2.97b}$$

where α and β are defined as follows:

$$\alpha \equiv \frac{1}{3}(\alpha_{\parallel} + 2\alpha_{\perp}) \tag{2.2.98a}$$

and

$$\beta \equiv \alpha_{\parallel} - \alpha_{\perp}. \tag{2.2.98b}$$

The quantity α is the *isotropic part* of the polarizability tensor and β is denoted the scattering particle's *optical anisotropy* [Berne and Pecora, 1976]. Equations 2.2.97 thus specify the orientation-dependence of the amplitude matrix elements through their dependence upon the angles θ and φ.

Since $f(\Omega',\Omega|\tau)$ is expressed by equation 2.2.84 as a series of spherical harmonics, evaluation of the amplitude scattering element correlation functions is simplified by expressing the scattering matrix elements in terms of spherical harmonics and utilizing the orthogonality property of equation 2.2.79 to perform the averaging integrations. The elements of the amplitude scattering matrix for VV and VH detection are thus expressed in terms of spherical harmonics by combining equations 2.2.97 with equations 2.2.80:

$$S_1(\Omega,\mathbf{a}) = -\,i\,k^3\left[\alpha + \sqrt{\frac{16\pi}{45}}\,\beta\,Y_{2,0}(\theta,\varphi)\right] \qquad (2.2.99a)$$

$$S_3(\Omega,\mathbf{a}) = -\,i\,k^3\,\beta\sqrt{\frac{2\pi}{15}}\,[Y_{2,-1}(\theta,\varphi) - Y_{2,1}(\theta,\varphi)]. \qquad (2.2.99b)$$

Utilizing the fact that $\langle Y_{2,0}(\Omega')\rangle = \langle Y_{2,0}(\Omega)\rangle = 0$ [Berne and Pecora, 1976], the scattering element correlation functions are then expressed as functions of spherical harmonic correlation functions $\langle Y_{j,k}^*(\Omega)\,Y_{j',k'}(\Omega')\rangle$ as follows:

$$\langle S_1^*(\Omega,\mathbf{a})\,S_1(\Omega',\mathbf{a})\rangle = k^6\left[\,|\alpha|^2 + \frac{16\pi}{45}|\beta|^2\,\langle Y_{2,0}^*(\Omega)\,Y_{2,0}(\Omega')\rangle\right] \qquad (2.2.100a)$$

and

$$\langle S_3^*(\Omega,\mathbf{a})\,S_3(\Omega',\mathbf{a})\rangle$$

$$= \frac{2\pi}{15}k^6\,|\beta|^2\,[\langle Y_{2,-1}^*(\Omega)\,Y_{2,-1}(\Omega')\rangle - \langle Y_{2,-1}^*(\Omega)\,Y_{2,1}(\Omega')\rangle \qquad (2.2.100b)$$

$$- \langle Y_{2,1}^*(\Omega)\,Y_{2,-1}(\Omega')\rangle + \langle Y_{2,1}^*(\Omega)\,Y_{2,1}(\Omega')\rangle].$$

The spherical harmonic correlation functions are evaluated by integrating over all possible orientations the products $Y_{j,k}^*(\Omega)\, Y_{j',k'}(\Omega')$ times the joint probability density function $f(\Omega',\Omega|\tau)$, which is given by equation 2.2.84:

$$\langle Y_{j,k}^*(\Omega)\, Y_{j',k'}(\Omega')\rangle = \int\int d\Omega\ d\Omega'\ f(\Omega',\Omega|\tau)\, Y_{j,k}^*(\Omega)\, Y_{j',k'}(\Omega') \qquad (2.2.101)$$

$$= \frac{1}{4\pi} \sum_{l=0}^{\infty} \sum_{m=-l}^{l} \left[\int d\Omega'\, Y_{l,m}^*(\Omega')\, Y_{j',k'}(\Omega') \right] \qquad (2.2.102)$$

$$\times \left[\int d\Omega\, Y_{j,k}^*(\Omega)\, Y_{l,m}(\Omega) \right] \exp[-l(l+1)D_R\tau].$$

Application of the orthogonality condition (equation 2.2.79) to equation 2.2.102 yields the result [Berne and Pecora, 1976]:

$$\langle Y_{j,k}^*(\Omega)\, Y_{j',k'}(\Omega')\rangle = \frac{1}{4\pi} \exp[-l(l+1)D_R\tau]\, \delta_{j,j'}\, \delta_{k,k'}, \qquad (2.2.103)$$

which produces the following expressions for the amplitude scattering element correlation functions when substituted into equations 2.2.100:

$$\langle S_1^*(\Omega,\mathbf{a})\, S_1(\Omega',\mathbf{a})\rangle = k^6 \left[|\alpha|^2 + \frac{4}{45}|\beta|^2 \exp(-6D_R\tau) \right] \qquad (2.2.104a)$$

and

$$\langle S_3^*(\Omega,\mathbf{a})\, S_3(\Omega',\mathbf{a})\rangle = \frac{k^6}{15}|\beta|^2 \exp(-6D_R\tau). \qquad (2.2.104b)$$

These correlation functions of the amplitude scattering matrix elements are exponential functions that depend upon the rotational diffusion coefficient D_R and the squares of the magnitudes of the optical anisotropy β and the isotropic polarizability component α.

Summation of Self-Correlation Functions

The first ($j = k$) summation of equation 2.2.62 is thus evaluated by summing the products of the translation- and rotation-governed averages expressed by equations 2.2.93 and 2.2.104. Polydispersity in the morphology and/or optical properties of the particles is considered by assigning to each particle within V_T a probability density $f(\mathbf{a})$

that describes the likelihood of the particle exhibiting a given set of morphological parameters and/or optical properties. The summation then reduces to the following:

$$\sum_{j=1}^{N_T} \langle E_i^*(\mathbf{r}_j)\, E_i(\mathbf{r}_j')\, \exp[i\mathbf{q}\cdot(\mathbf{r}_j' - \mathbf{r}_j)]\rangle \langle S_{pj}^*(\Omega_j,\mathbf{a}_j)\, S_{pj}(\Omega_j',\mathbf{a}_j)\rangle$$

$$= \frac{\langle N\rangle |E_o|^2}{2} \int d\mathbf{a}\, f(\mathbf{a}) \langle S_p^*(\Omega,\mathbf{a})\, S_p(\Omega',\mathbf{a})\rangle \exp(i\mathbf{q}\cdot\mathbf{V}\tau) \exp(-q^2 D\tau) \exp\left(-\frac{V_\perp^2 \tau^2}{2\omega_o^2}\right), \quad (2.2.105)$$

where $\langle S_p^*(\Omega,\mathbf{a})\, S_p(\Omega',\mathbf{a})\rangle$ is given by equation 2.2.104a for VV detection and equation 2.2.104b for VH detection and $\langle N\rangle = N_T V_s/V_T$ is the average number of particles in the scattering volume. This expression represents the time-dependent portion of the first-order correlation function from which the particle dynamic properties can be inferred.

2.2.4.2.4 Evaluation of Cross-Scatterer Correlation Functions

Evaluation of the second summation ($j \neq k$) of equation 2.2.62 is accomplished using an approach similar to that used to evaluate the first summation ($j = k$). Since all random processes considered in this analysis are assumed to be statistically stationary, each term of this summation is expected to be independent of the delay time τ. The $j \neq k$ terms are evaluated by averaging the orientation-dependent and position-dependent factors separately and then summing their products, which are here denoted the *cross-scatterer correlation functions*, according to equation 2.2.62.

Orientation-Dependent Averages

The average value of an amplitude scattering matrix element $\langle S_p(\Omega,\mathbf{a})\rangle$ at any time is evaluated by integrating over all possible equilibrium orientations Ω and morphological and/or optical properties $\mathbf{a}$ the product of $S_p(\Omega,\mathbf{a})$ and the joint probability density function of Ω and $\mathbf{a}$. Assuming that the equilibrium orientation is statistically independent of the scattering particle's morphological and optical properties, this averaging integral is expressed as

$$\langle S_p(\Omega,\mathbf{a})\rangle = \int d\mathbf{a} \int d\Omega\, S_p(\Omega,\mathbf{a})\, f(\Omega,\mathbf{a})$$
$$= \int d\mathbf{a} \int d\Omega\, S_p(\Omega,\mathbf{a})\, f(\Omega)\, f(\mathbf{a}) \qquad (2.2.106)$$

Evaluation of the orientation integral for the VV ($p = 1$) and VH ($p = 3$) detection modes using the expressions for the amplitude scattering matrix elements given by equations 2.2.97 and the uniform equilibrium orientation probability density $f(\Omega) = 1/4\pi$, as given by equation 2.2.83, results in

$$\langle S_1(\Omega,\mathbf{a})\rangle = -\,i\,k^3 \int \alpha\, f(\mathbf{a})\, d\mathbf{a} \qquad (2.2.107a)$$

and

$$\langle S_3(\Omega,\mathbf{a})\rangle = 0. \qquad (2.2.107b)$$

These expressions, along with their complex conjugates, represent the factors within the second summation ($j \neq k$) of equation 2.2.62 that require averaging with respect to the particle orientation Ω.

Position-Dependent Averages

The position-dependent factor $\langle E_i(\mathbf{r})\, \exp(i\mathbf{q}\cdot\mathbf{r})\rangle$ is averaged with respect to the particle position $\mathbf{r}$ through the use of equation 2.2.63 for $E_i(\mathbf{r})$ and equation 2.2.89 for $f(\mathbf{r})$ as follows:

$$\langle E_i(\mathbf{r})\, \exp(i\mathbf{q}\cdot\mathbf{r})\rangle = \frac{E_0}{V_T} \int_{V_T} \exp(i\mathbf{q}\cdot\mathbf{r})\, \exp\left(-\frac{|\mathbf{r}_\perp|^2}{\omega_0{}^2}\right) d^3r \qquad (2.2.108)$$

$$= \frac{2\,E_0}{q_z\,L}\frac{V_s}{V_T} \sin\left(\frac{q_z\,L}{2}\right) \exp\left(-\frac{q^2\,\omega_0{}^2}{4}\right), \qquad (2.2.109)$$

where $q_z \equiv \mathbf{q}\cdot\mathbf{k}_i/k = k(1 - \cos\theta)$ is the component of the scattering vector in the incident beam's propagation direction.

Summation of Cross-Scatterer Correlation Functions

The second summation ($j \neq k$) of equation 2.2.62 is hence the double sum of the products of the squares of the magnitudes of the orientation- and position-averaged quantities of equations 2.2.107 and 2.2.109:

$$\sum_{k \neq j = 1}^{N_T} \sum_{j = 1}^{N_T} \langle S_{pj}^*(\Omega_j,\mathbf{a}_j)\rangle \langle S_{pk}(\Omega_k',\mathbf{a}_k)\rangle \langle E_i^*(\mathbf{r}_j)\exp(-i\mathbf{q}\cdot\mathbf{r}_j)\rangle \langle E_i(\mathbf{r}_k')\exp(i\mathbf{q}\cdot\mathbf{r}_k')\rangle$$

$$= N_T(N_T - 1)\,|\langle S_p(\Omega,\mathbf{a})\rangle|^2\,|\langle E_i(\mathbf{r})\exp(i\mathbf{q}\cdot\mathbf{r})\rangle|^2$$

$$\approx \frac{4\langle N\rangle^2 |E_o|^2}{(q_z L)^2}\,|\langle S_p(\Omega,\mathbf{a})\rangle|^2 \sin^2\left(\frac{q_z L}{2}\right)\exp\left(-\frac{q^2\omega_o^2}{2}\right), \qquad (2.2.110)$$

where $\langle S_p(\Omega,\mathbf{a})\rangle$ is given by equation 2.2.107a for VV detection ($p = 1$) and by equation 2.2.107b for VH detection ($p = 3$) and the total number of particles within V_T is assumed to be much larger than 1.

Most of the previous literature presenting dynamic light scattering theory assumes that the incident beam exhibits a uniform intensity (and electric field) profile when performing the averaging integrals necessary for the evaluation of the second summation ($j \neq k$) of equation 2.2.62, resulting in all $j \neq k$ terms being proportional to $\delta(\mathbf{q})$. According to this uniform-incident-field result, the $j \neq k$ terms are thus equal to zero when $\mathbf{q}$ is non-zero and equal to infinity when $\mathbf{q}$ equals zero. The $\mathbf{q} = 0$ result is consistent with the common assumption that the phase of the scattered field is uniformly distributed, which is true for electric fields adhering to Gaussian statistics. This uniform-phase assumption was utilized in the derivation of relationships (equations 2.2.48 - 2.2.54) between the heterodyne correlation function and the first-order scattered field correlation function.

According to the present results derived for a Gaussian incident beam profile, the $j \neq k$ terms are equal to zero at all scattering angles in the VH detection mode since the orientation average of the amplitude scattering matrix element $S_3(\Omega,\mathbf{a})$ is equal to zero. In the VV detection mode, however, the orientation-averaged scattering matrix element

$\langle S_1(\Omega,\mathbf{a})\rangle$ is finite. Using values typical of dynamic light scattering experiments ($\omega_0 \approx L \approx 0.055$ mm, $\lambda = 488$ nm, and $\langle N\rangle \approx 10^4$) to numerically evaluate the ratio of equation 2.2.62's $j \neq k$ summation, as given by equation 2.2.110, to the $\tau = 0$ value of its $j = k$ summation, as given by equation 2.2.105, demonstrates that this ratio is less than 10^{-32} when the scattering angle θ is greater than 1°. This ratio, however, tends to infinity as θ tends to zero. Thus, the $j \neq k$ term of equation 2.2.110 behaves much like $\delta(\mathbf{r})$ in that it is infinite at $\mathbf{q} = 0$ and negligible in comparison to the $j = k$ terms at most finite values of $\mathbf{q}$ (corresponding to $\theta \geq 1°$). Because all experiments under consideration are to be performed either at finite scattering angles (specifically, $\theta \geq 1°$) or in the VH detection mode, the $j \neq k$ term, as given by equation 2.2.110, is neglected in all subsequent analyses.

2.2.4.2.5 Theoretical Results for the Homodyne Correlation Functions of Light Scattered from Cylindrically Symmetric Particles

The following expressions for the VV and VH first-order electric field correlation functions are obtained by substituting equations 2.2.104 and 2.133 into equation 2.2.62 and neglecting the $j \neq k$ terms:

$$G^{(1)}(\mathbf{R},0;\mathbf{R},\tau)_{VV} = \langle E_{sV}^*(\mathbf{R},0)\, E_{sV}(\mathbf{R},\tau)\rangle$$

$$= \frac{k^4 \langle N\rangle |E_0|^2}{2R^2} \exp[-i(\omega - \mathbf{q}\cdot\mathbf{V})\tau] \qquad (2.2.111a)$$

$$\times \int \left[|\alpha|^2 + \frac{4}{45}|\beta|^2 \exp(-6D_R\tau)\right] \exp\left(-q^2 D\tau - \frac{V_\perp^2 \tau^2}{2\omega_0^2}\right) f(\mathbf{a})\, d\mathbf{a}$$

and

$$G^{(1)}(\mathbf{R},0;\mathbf{R},\tau)_{VH} = \langle E_{sH}^*(\mathbf{R},0)\, E_{sH}(\mathbf{R},\tau)\rangle \qquad (2.2.111b)$$

$$= \frac{k^4 \langle N\rangle |E_0|^2}{30R^2} \exp[-i(\omega - \mathbf{q}\cdot\mathbf{V})\tau] \int |\beta|^2 \exp\left[-(q^2 D + 6D_R)\tau - \frac{V_\perp^2 \tau^2}{2\omega_0^2}\right] f(\mathbf{a})\, d\mathbf{a}.$$

Evaluation of these expressions at $\tau = 0$ gives the following equations for the VV and VH forms of $G^{(1)}(\mathbf{R},0;\mathbf{R},0) = \langle |E(0)|^2 \rangle$, which is proportional to the scattered light's average detected intensity (see equation 2.2.2):

$$G^{(1)}(\mathbf{R},0;\mathbf{R},0)_{VV} = \frac{k^4 \langle N \rangle |E_o|^2}{2R^2} \int \left[|\alpha|^2 + \frac{4}{45} |\beta|^2 \right] f(\mathbf{a})\, d\mathbf{a} \qquad (2.2.112a)$$

and

$$G^{(1)}(\mathbf{R},0;\mathbf{R},0)_{VH} = \frac{k^4 \langle N \rangle |E_o|^2}{30R^2} \int |\beta|^2 f(\mathbf{a})\, d\mathbf{a}. \qquad (2.2.112b)$$

The first-order electric field correlation functions of equations 2.2.111 are normalized through division by equations 2.2.112. The normalized detected power correlation functions $g_P^{(2)}(\tau \mid 0)$ are thus found by substituting these normalized first-order electric field correlation functions into equation 2.2.54 for heterodyne detection and equation 2.2.31 for homodyne detection. Specifically, the normalized homodyne power correlation functions $g_P^{(2)}(\tau \mid 0)$ exhibit the following forms for VV and VH detection:

$$g_P^{(2)}(\tau \mid 0)_{VV} = 1 + f(A) \left[\frac{\int \left[|\alpha|^2 + \frac{4}{45} |\beta|^2 \exp(-6D_R\tau) \right] \exp\left(-q^2 D\tau - \frac{V_\perp^2 \tau^2}{2\omega_o^2} \right) f(\mathbf{a})\, d\mathbf{a}}{\int \left[|\alpha|^2 + \frac{4}{45} |\beta|^2 \right] f(\mathbf{a})\, d\mathbf{a}} \right]^2 \qquad (2.2.113a)$$

and

$$g_P^{(2)}(\tau \mid 0)_{VH} = 1 + f(A) \left[\frac{\int |\beta|^2 \exp\left[-(q^2 D + 6D_R)\tau - \frac{V_\perp^2 \tau^2}{2\omega_o^2} \right] f(\mathbf{a})\, d\mathbf{a}}{\int |\beta|^2 f(\mathbf{a})\, d\mathbf{a}} \right]^2 . \qquad (2.2.113b)$$

If the effects of finite sample time Δt are neglected, these normalized power correlation functions are proportional (through equations 2.2.14 and 2.2.16) to the

photon correlation functions $\langle n(0)\, n(\tau)\rangle$ for delay times $\tau > 0$ when a single detector is used and for delay times $\tau \geq 0$ when the output of two detectors are cross-correlated. Normalization of the photon correlation functions $\langle n(0)n(\tau)\rangle$ with respect to $\langle n(0)\rangle^2$ eliminates the proportionality constants relating $\langle n(0)n(\tau)\rangle$ to $g_P^{(2)}(\tau \mid 0)$. Thus, the normalized photon count correlation functions $\langle n(0)n(\tau)\rangle/\langle n(0)\rangle^2$ are equal to the normalized power correlation functions $g_P^{(2)}(\tau \mid 0)$ that are given by equations 2.2.113. Under conditions in which the assumptions utilized in the derivation of equations 2.2.113 are valid, these equations provide the general theoretical forms necessary for analyzing and interpreting the measured correlation function data.

2.3 Morphological Dependencies of Effective Optical Polarizability Components and Brownian Diffusion Coefficients

Use of the theoretical relationships given by equations 2.2.113 to infer the morphological parameters and Brownian diffusion coefficients of a suspension of agglomerated particles from dynamic light scattering data requires accurate knowledge of the dependencies of the optical parameters α and β and the Brownian diffusion coefficients D and D_R upon the morphological parameters of the scattering particles. This requirement presents one of the most significant disadvantages to the use of dynamic light scattering as a measurement technique, as these relationships are not accurately known under many conditions (to be discussed later) and depend upon accurate knowledge of the optical properties of the scatterers and the thermophysical properties of the solvent medium. The following discussion presents approximate relationships for α, β, D, and D_R obtained by approximating the straight chain agglomerates as volume-equivalent prolate ellipsoids of semiaxes $a > b = c$ (see figure 2.3). Within this approximation, the long semiaxis a is equal to half of the chain agglomerate's total length l and the short semiaxes b are equal to half of the mean diameter d of the agglomerate's constituent primary particles.

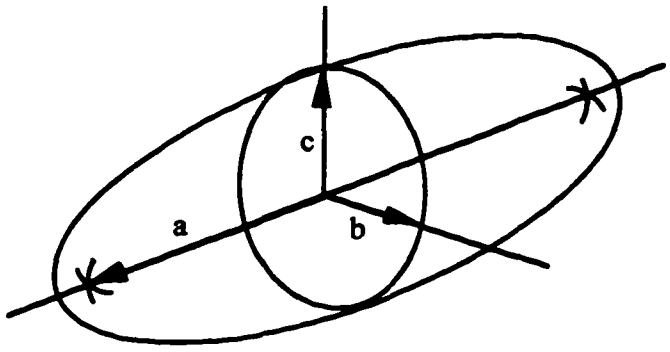

Figure 2.3.1: Illustration of the major and minor semiaxes a and b of a prolate ellipsoid.

2.3.1 Isotropic and Anisotropic Polarizability Components of a Prolate Ellipsoid

By describing the light scattered from each agglomerate in terms of dipole radiation (permitting the use of the polarizability tensor α) implicit use is made of the assumption that the scattered light is adequately represented by the first non-zero term of a general multipole expansion. As previously mentioned, this assumption is technically valid only when $|m|\, l \ll \lambda/2\pi$. When the chainlike agglomerate is approximated as a prolate ellipsoid, this first non-zero term corresponds to the Rayleigh solution for light scattered from a small ellipsoid. Within this approximation, the particle is small enough compared to the light wavelength that the electric field at any time in and around the ellipsoidal particle is approximately uniform. Thus, the problem reduces to determining the electrostatic perturbation to the incident field caused by the field's interaction with the ellipsoid, determining the particle's effective polarizability based upon this result, and determining the time-dependent scattered field that would result if this dipole were oscillating at the frequency of the incident light by using equations 2.1.9 and 2.2.94.

The Rayleigh solution for the polarizability components α_{ij} with respect to the principle axes of a prolate ellipsoid composed of an optically isotropic material is ([Kerker, 1969], [van de Hulst, 1981], [Bohren and Huffman, 1983])

$$\frac{V}{4\pi\alpha_{jj}} = L_j + \frac{1}{m^2 - 1} \tag{2.3.1a}$$

and

$$\alpha_{ij} = 0, \qquad (i \neq j) \tag{2.3.1b}$$

where

$$L_1 = \frac{1 - e^2}{e^2}\left[-1 + \frac{1}{2e}\ln\left(\frac{1 + e}{1 - e}\right)\right], \tag{2.3.2}$$

$$e^2 = 1 - \left[\frac{b}{a}\right]^2 = 1 - \left[\frac{d}{l}\right]^2, \tag{2.3.3}$$

and

$$L_2 = L_3 = \frac{1 - L_1}{2}. \tag{2.3.4}$$

In the above expressions m is the ratio of the refractive index of the scattering particle to the refractive index of the ambient medium and

$$V = \frac{4}{3}\pi abc = \frac{\pi}{6}\left[\frac{l}{d}\right] d^2. \tag{2.3.5}$$

is the volume of the ellipsoidal particle. The isotropic and anisotropic parts (α and β) of the polarizability tensor are thus determined by substituting the polarizability components $\alpha_{\parallel} = \alpha_1$ and $\alpha_{\perp} = \alpha_2 = \alpha_3$ given by equations 2.3.1 to 2.3.5 into equations 2.2.98.

As the size of the scattering particle increases relative to the incident light wavelength, the effects of interference between the light scattered from different parts of the same particle become significant. This interference occurs as a result of the variation of the Doppler phase factor $\exp(i\mathbf{q}\cdot\mathbf{r})$ at different locations $\mathbf{r}$ within the same particle. This interference effect is frequently described in terms of a form factor, which is proportional to the integral of the phase factor $\exp(i\mathbf{q}\cdot\mathbf{r})$ throughout the volume of the particle [Berne and Pecora, 1976]. At $\mathbf{q} = 0$ (which corresponds to $\theta = 0$) interparticle interference does not occur because the phase factor is equal to unity for all $\mathbf{r}$. The interference effect occurs at non-zero scattering angles and increases with increasing

scattering angle because |q| is proportional to sin(θ/2). When significant, interparticle interference can affect the temporal variation of the scattered light such that the relationships obtained through the dipole approximation are no longer valid. Therefore, when using equations 2.2.111 or 2.2.113 to interpret dynamic light scattering data, the experiment should be configured such that ql « 1 [Berne and Pecora, 1976] to make the interparticle interference effect negligible.

2.3.2 Translational and Rotational Brownian Diffusion Coefficients

The functional dependencies of the Brownian diffusion coefficients D and D_R on the morphological parameters (d and l/d) of the scattering particles are determined by substituting appropriate expressions for the translational and rotational friction coefficients f_{ij} and β_{ij} into equations 2.2.69 and 2.2.72. The functional forms of these friction coefficients, however, are accurately known only under certain special circumstances that are discussed within this section.

The problem of theoretically determining the frictional drag exerted by a gaseous medium upon a moving particle is dramatically influenced by the ratio of the gas mean free path λ_g to a characteristic particle dimension l. This dimensionless ratio is called the *Knudsen number* (Kn). On the basis of the magnitude of the Knudsen number, fluid flow around a particle is categorized into four different regimes: continuum flow, slip flow, transition flow, and free-molecular flow.

When Kn is much less than 0.01 the gas surrounding the particle approximately obeys the laws of continuum mechanics. Under this condition, the Navier-Stokes equations apply under *stick* or non-slip boundary conditions, in which the gas velocity at the gas-particle interface is equal to the velocity of the adjacent point on the particle surface. This limiting range of Knudsen numbers corresponds to the *continuum* regime.

As the Knudsen number increases, stick boundary conditions become increasingly inaccurate. For Knudsen numbers greater than approximately 0.01 that are still much less

than unity, the gas is still treated as a continuum. Under this condition, however, alternate slip-flow boundary conditions must be applied that permit unequal velocities of the gas and the particle surface at each point on the gas-particle interface. This range of Knudsen numbers corresponds to the *slip flow* regime.

In situations where the Knudsen number is of the order of unity, the approximation of the gas as a continuum loses its accuracy. Solutions to flow problems in this *transition* regime are particularly difficult to obtain because the particle is too small relative to the gas mean free path to consider the gas as a continuum, yet large enough to significantly affect the velocity distribution of the surrounding gas molecules.

When the Knudsen number is much larger than unity, however, the particle size is so small relative to the mean free path that its presence does not significantly affect the velocity distribution of the surrounding gas molecules, thus simplifying the solution of flow problems. This large Knudsen number limit is called the *free molecule* regime.

The solutions for the translational and rotational friction coefficients of spherical particles in the continuum regime with stick boundary conditions (Kn « 0.01) are [Cantor and Schimmel, 1980]

$$f = 6\pi\mu a \tag{2.3.6}$$

and

$$\beta = 8\pi\mu a^3, \tag{2.3.7}$$

where a is the radius of the particle and μ is the dynamic viscosity of the surrounding gas medium. The first of these equations is the Stokes law governing the low-Reynolds-number drag on a sphere.

The translational and rotational friction coefficients of a prolate ellipsoid of semiaxes $a > b = c$ in the continuum regime are given by Perrin (1934) as

$$\begin{aligned} f &= \frac{1}{3}\left[\frac{1}{f_{11}} + \frac{1}{f_{22}} + \frac{1}{f_{33}}\right] = \frac{6\pi\mu a}{G(\rho)} = \frac{6\pi\mu R_{eq}}{\rho^{2/3}G(\rho)}, \\ \dot{f} &= \frac{1}{3}\left[\frac{\dot{1}}{f_{11}} + \frac{\dot{1}}{f_{22}} + \frac{\dot{1}}{f_{33}}\right] = \frac{\dot{1}}{G(\rho)} = \frac{\dot{1}}{\rho^{2/3}G(\rho)}, \end{aligned} \tag{2.3.8}$$

$$\beta_{11} = \frac{16\pi}{3}\mu a^3 \frac{\rho^2(1-\rho^2)}{1-\rho G(\rho)} = \frac{16\pi\mu}{3}\frac{R_{eq}^3}{\rho^2}\frac{\rho^2(1-\rho^2)}{1-\rho G(\rho)}, \tag{2.3.9}$$

and

$$\beta_{22} = \beta_{33} = \frac{16\pi}{3}\mu a^3 \frac{1-\rho^4}{(2-\rho^2)G(\rho)-1} = \frac{16\pi\mu}{3}\frac{R_{eq}^3}{\rho^2}\frac{1-\rho^4}{(2-\rho^2)G(\rho)-1}, \tag{2.3.10}$$

where

$$\rho \equiv b/a = d/l$$

and

$$G(\rho) \equiv \frac{1}{\sqrt{1-\rho^2}} \ln\left[\frac{1+\sqrt{1-\rho^2}}{\rho}\right]. \tag{2.3.11}$$

In these equations f is the orientation-averaged translational friction coefficient, β_{11} is the friction coefficient of rotation about the ellipsoid's long axis, β_{22} and β_{33} are the rotational friction coefficients about the ellipsoid's two short axes, ρ is the inverse of the ellipsoid's aspect ratio, and $R_{eq} = (ab^2)^{1/3}$ is the ellipsoid's volume-equivalent sphere radius.

In cases where the gas mean free path is large enough relative to the particle size that stick boundary conditions no longer apply, corresponding to the slip-flow regime, the translational friction coefficient for a sphere is modified using the empirically-determined *Cunningham correction factor* C_s, which is given by the relationship [Dahneke, 1973c]

$$C_s = 1 + \frac{\lambda_g}{a}\left[1.234 + 0.414\exp\left(-0.876\frac{a}{\lambda_g}\right)\right]. \tag{2.3.12}$$

The slip-corrected translational friction coefficient thus becomes

$$f = \frac{6\pi\mu a}{C_s}. \tag{2.3.13}$$

Though the use of C_s is only valid for correcting the friction coefficient of a spherical particle for slip-flow effects, it is sometimes used, often without justification, to correct the orientation-averaged translational friction coefficients of non-spherical particles for

slip flow effects by replacing the sphere radius a in equation 2.3.12 with the particle's volume-equivalent sphere radius R_{eq} [Dahneke, 1973c].

Solutions for the translational friction coefficients of various spherical and non-spherical particles in the free molecular regime (Kn » 1) are presented by Dahneke (1973a,b,c). His comparison of the theoretical free-molecule results with the results of using an equivalent-sphere radius in equation 2.3.12 for C_s demonstrates that in this regime the equivalent sphere analysis exhibits an error of less than 33% for aspect ratios less than 100 and less than 8% for aspect ratios less than 10. In an effort to predict the translational friction factors in the slip-flow and transition regimes, Dahneke empirically links the free-molecular solutions to the continuum solutions through the use of equation 2.3.12 by computing morphology-based correction factors to the characteristic dimension a that appears in this equation. Corrections of the rotational friction coefficients for slip-flow and non-continuum effects are not addressed by Dahneke and are apparently unavailable in the literature.

In applying these friction factor results to the problem of relating the translational and rotational diffusion coefficients obtained from dynamic light scattering experiments to the morphological properties of a chain-like agglomerate or its volume-equivalent ellipsoid, one should note that the translational diffusion coefficient D occurring in equations 2.2.113 is averaged with respect to orientation and that the rotational diffusion coefficient D_R is the component of the rotational diffusion tensor describing particle rotation about its short axis ($D_{R\perp} = D_{R22} = D_{R33}$). Hence, for stick boundary conditions:

$$D = \frac{k_B T}{6\pi\mu a} G(\rho) = \frac{k_B T}{6\pi\mu R_{eq}} \rho^{2/3} G(\rho) \qquad (2.3.14)$$

and

$$D_R = D_{R22} = D_{R33} = \frac{k_B T}{\beta_{22}} = \frac{k_B T}{\beta_{33}}$$

$$= \frac{3k_BT}{16\pi\mu a^3} \frac{(2 - \rho^2)G(\rho) - 1}{1 - \rho^4} \qquad (2.3.15)$$

$$= \frac{3k_BT}{16\pi\mu R_{eq}^3} \frac{\rho^2[(2 - \rho^2)G(\rho) - 1]}{1 - \rho^4}.$$

Because the combination of high flame temperatures and small particle sizes occurring within a flame environment typically dictates a flow environment within either the transition or free-molecular regime, these equations for D and D_R do not accurately represent the true translational and rotational diffusion coefficients because they are not corrected for slip-flow and non-continuum effects. As mentioned above, an approximate correction for the orientation-averaged translational diffusion coefficient D is obtained by substituting the volume-equivalent sphere radius into equation 2.3.12 for C_s and multiplying the continuum value for D, as given by equation 2.3.14, by this result. No correction, however, exists for the rotational diffusion coefficient D_R at this time. One of the goals of this study, therefore, is to investigate the potential combination of dynamic light scattering with independent morphology measurements, such as the TEM analysis of thermophoretically-sampled agglomerates, to provide an experimental relationship between the Brownian diffusion coefficients and the agglomerate morphology within the non-continuum conditions of a high-temperature flame.

2.4 Fundamental Considerations in the Interpretation of Experimental Photon Correlation Functions

According to equations 2.2.113, the polarized and depolarized correlation functions of photons scattered from a suspension of cylindrically-symmetric scatterers represent integral equations depending upon the translational and rotational Brownian diffusion coefficients D and D_R, the isotropic and anisotropic components α and β of the scattering particles' polarizability tensors, the average particle velocity component $V_\perp$ orthogonal to the incident light direction, the density function of the scatterers' morphological parameters f(**a**), and the spectrometer-dependent parameters f(A) and ω_0.

Extraction of quantitative diffusion coefficient information from experimentally obtained correlation functions requires solutions to these integral equations appropriate to the form of the information required. These solutions are facilitated by the fact that the integral terms of equation 2.2.113 reduce to Laplace integrals when the quadratic bulk velocity term resulting from non-uniform illumination of the scattering volume is either neglected or factored out of the integration. Negligence of this term is justified when $(V_\perp \tau_f)^2/(2\omega_o^2) \ll q^2 D \tau_f$, where τ_f is the final measured delay time. In an earlier DLS study using a premixed propane/oxygen flame, Venizelos (1989) reported the satisfaction of this criterion. At present, the assumption is made that it is also satisfied by the seeded CO/O_2 flame considered in this study, thus permitting the representation of equations 2.2.113 as a combination of Laplace integrals. In order to take advantage of the properties of Laplace integrals for interpreting experimental DLS data, the data must first be recombined to isolate each integral term occurring within equations 2.2.113.

Dynamic light scattering measurements at scattering angle θ_k using a digital correlator are processed within the correlator to determine estimates $G_{if,k}(\tau)$ and $B_{if,k}$ of the photon correlation function $\langle n(0)n(\tau)\rangle$ and its baseline $\langle n(0)\rangle^2$ at discrete delay times τ using equations 3.3.5 and 3.3.6 of Chapter 3. The subscripts i and f used above respectively refer to the polarizations of the incident and detected fields, where $\{i, f\} \in \{V, H\}$. Also, the subscript k is included for future reference to distinguish between measurements at different scattering angles θ_k. Division of $G_{if,k}(\tau)$ by its baseline $B_{if,k}$ produces an estimate of the normalized power correlation function $g_P^{(2)}(\tau \mid 0)_{if}$. Using the theoretical expressions given by equations 2.2.113, the functions

$$C_{if,k}(\tau) \equiv \left[\frac{G_{if,k}(\tau)}{B_{if,k}} - 1\right]^{1/2} \equiv [g_P^{(2)}(\tau \mid 0)_{if} - 1]^{1/2} \qquad (2.4.1)$$

are equivalent to

$$C_{VV,k}(\tau) = A_{VV} \int \left[|\alpha|^2 + \frac{4}{45}|\beta|^2 \exp(-6D_R\tau)\right] \exp(-q_k^2 D\tau)\, f(\mathbf{a})\, d\mathbf{a} \quad (2.4.2a)$$

and

$$C_{VH,k}(\tau) = A_{VH} \int |\beta|^2 \exp[-(q_k^2 D + 6D_R)\tau] f(\mathbf{a})\, d\mathbf{a}, \qquad (2.4.2b)$$

where

$$A_{VV} = \frac{\sqrt{f(A)}}{\int \left[|\alpha|^2 + \frac{4}{45}|\beta|^2\right] f(\mathbf{a})\, d\mathbf{a}} \qquad (2.4.3a)$$

and

$$A_{VH} = \frac{\sqrt{f(A)}}{\int |\beta|^2 f(\mathbf{a})\, d\mathbf{a}}. \qquad (2.4.3b)$$

As implied above, these expressions neglect the bulk velocity term resulting from non-uniform illumination of the scattering volume that occurs in equations 2.2.113. In situations where the non-uniform illumination term is not negligible, it must either be retained in the inversion equations or divided out of $C_{if,k}(\tau)$.

Equations 2.4.2 demonstrate that the $C_{if,k}(\tau)$ are linear functions of integrals of weighted exponentials. These integrals are evaluated over all possible values of the morphological parameters, which are always positive quantities. The forms of these integrals are equivalent to the definition of a Laplace transform [Arfken, 1985]

$$F(s) = L\{f(x)\} = \int_0^\infty f(x) \exp(-sx)\, dx. \qquad (2.4.4)$$

Thus, equations 2.4.2 can be solved by isolating each integral term and determining the inverse Laplace transforms of the results.

The depolarized function $C_{VH,k}(\tau)$ already consists of a single integral and thus requires no further modification. The polarized function $C_{VV,k}(\tau)$, however, is equivalent to a weighted sum of two Laplace transforms. Isolation of these Laplace

integrals can be accomplished through the use of the classical depolarization ratio R_{VH}, which is determined by ratioing the average VH scattered light intensity to the corresponding average VV intensity. These average intensities, which are both measurable using classical light scattering techniques, are proportional to the $\tau = 0$ values of the first-order electric field correlation functions $G^{(1)}(\mathbf{R},0;\mathbf{R},0)_{if}$ given by equations 2.2.112. Ratioing the depolarized intensity to the polarized intensity using equations 2.2.112 results in the following expression for R_{VH}:

$$R_{VH} \equiv \frac{I_{VH}}{I_{VV}} = \frac{\int |\beta|^2 f(\mathbf{a})\, d\mathbf{a}}{15 \int \left[|\alpha|^2 + \frac{4}{45}|\beta|^2\right] f(\mathbf{a})\, d\mathbf{a}} = \frac{A_{VV}}{15 A_{VH}}. \tag{2.4.5}$$

Using this result, the integral terms are isolated through the following operations:

$$\zeta_{V,k}(\tau) \equiv C_{VV,k}(\tau) - \frac{4}{3} R_{VH}\, C_{VH,k}(\tau) \tag{2.4.6a}$$

$$= A_{VV} \int |\alpha|^2 \exp(-q_k^2 D\tau)\, f(\mathbf{a})\, d\mathbf{a} \tag{2.4.6b}$$

and

$$\zeta_{H,k}(\tau) \equiv C_{VH,k}(\tau) \tag{2.4.6c}$$

$$= A_{VH} \int |\beta|^2 \exp[-(q_k^2 D + 6D_R)\tau]\, f(\mathbf{a})\, d\mathbf{a}. \tag{2.4.6d}$$

Thus, according to these results proper isolation of the separate integrals within equations 2.2.13 requires measurements of both the polarized and depolarized scattered-light correlation functions and the classical depolarization ratio R_{VH} under identical experimental conditions. Establishing the equivalence between the integrals of equations 2.4.6 and the standard Laplace integral of equation 2.4.4 requires reducing the dimensions of the integration variables $\mathbf{a}$ prior a transformation of the single resulting integration variable.

Both of the integrals given in equations 2.4.6 are generally multiple integrations over the set of morphological parameters **a** characterizing the scattering particles. For DLS measurements on spherical particles, **a** contains a single element: the diameter of the particle. In considering the agglomerates occurring within the seeded flame being studied as geometrically anisotropic particles, a minimum of two morphological parameters require consideration: an aspect ratio A and a characteristic length D. In order to reduce the dimensions of the set of integration variables, one of these two variables (or a combination of them) must be assumed monodisperse. Since the current study mostly concerns the effects of anisotropy, D is assumed monodisperse so that the aspect ratio may be considered as polydisperse. The characteristic length D is defined for this study as the minor semi-axis length a of a prolate ellipsoid fitted to the agglomerate shape. By assuming monodispersity in $D \equiv$ a, equations 2.4.6 can be expressed as integrals over A alone, replacing the joint probability density $f(\mathbf{a}) = f(A, D)$ with the marginal density function $f(A)$. Both integrals thus reduce to the following general form

$$\zeta_{f,k}(\tau) = A_{if} \int_0^\infty |\phi_f|^2 \exp(-\Gamma_{f,k}\tau)\, f(A)\, dA, \tag{2.4.7}$$

where

$$\phi_f \equiv \begin{cases} \alpha & f = \mathrm{V} \\ \beta & f = \mathrm{H} \end{cases} \tag{2.4.8}$$

and

$$\Gamma_{f,k} = \begin{cases} q_k^2 D & f = \mathrm{V} \\ q_k^2 D + 6D_R & f = \mathrm{H} \end{cases}. \tag{2.4.9}$$

This integral can be cast as a Laplace integral by changing the integration variable from A to $\Gamma_{f,k}$, which is possible if $\Gamma_{f,k}$ either increases or decreases monotonically with increasing aspect ratio A over the range within which the integrand is finite. The continuum expressions for the translational and rotational diffusion coefficients D and D_R given by equations 2.3.14 and 2.3.15 in both decrease monotonically with increasing

aspect ratio. A similar trend is exhibited by the Cunningham correction factor (equation 2.3.12) when a volume-equivalent sphere radius R_{eq} is assumed. Thus, the slip-corrected translational diffusion coefficient, which is the product of the continuum solution for D and the Cunningham correction factor, also decreases monotonically with increasing aspect ratio. As the aspect ratio A approaches infinity, both D and D_R approach zero. Thus, through equations 2.4.9, $\Gamma_{f,k}$ also decreases monotonically with increasing A, approaching zero as A approaches infinity. Therefore, $d\Gamma_{f,k}/dA$ is always a negative quantity and the transformation of the integration variable of equation 2.4.7 from A to $\Gamma_{f,k}$ produces

$$\zeta_{f,k}(\tau) = - A_{if} \int_0^{\infty} |\phi_f|^2 \exp(-\Gamma_{f,k}\tau)\, f(A) \left[\frac{d\Gamma_{f,k}}{dA}\right]^{-1} d\Gamma_{f,k}. \qquad (2.4.10)$$

The inverse Laplace transform of $\zeta_{f,k}(\tau)$ can thus be interpreted in terms of physical quantities by comparison of equation 2.4.10 with the Laplace integral of equation 2.4.4, producing

$$F_{f,k}(\Gamma_{f,k}) \equiv L^{-1}\{\zeta_{f,k}(\tau)\} = - A_{if}|\phi_f|^2 f(A') \left[\frac{d\Gamma_{f,k}}{dA'}\right]^{-1}. \qquad (2.4.11)$$

The inverse Laplace transforms $F_{f,k}(\Gamma_{f,k})$ represent the densities of the decay-rate parameters $\Gamma_{f,k}$. The availability of theoretical relationships between the $|\phi_f|^2$, $\Gamma_{f,k}$, and the morphological parameters $A \equiv b/a$ and $D \equiv a$ would permit an optical determination of the aspect ratio probability density function f(A) by measuring the polarized and depolarized correlation functions and the classical depolarization ratio R_{VH}, computing the quantities $\zeta_{f,k}(\tau)$ from the resulting data using equations 2.4.6, numerically computing the inverse Laplace transform of the $\zeta_{f,k}(\tau)$ using an algorithm such as Provencher's CONTIN ([Provencher, 1982a,b], [Provencher, 1984]), and solving equations 2.4.11 for f(A) and D.

In addition to its interpretation as a Laplace integral, equation 2.4.10 may also be represented as a moment generating function by noting that

$$\zeta_{f,k}(\tau)/\zeta_{f,k}(0) = \langle \exp(-\Gamma_{f,k}\tau) \rangle_{\phi} \tag{2.4.12}$$

where $\langle\ \rangle_{\phi}$ denotes averaging with respect to the density function $F_{f,k}(\Gamma_{f,k})/\zeta_{f,k}(0)$, or more specifically:

$$\langle\ \rangle_{\phi} = \frac{1}{\zeta_{f,k}(0)} \int_0^{\infty} d\Gamma_{f,k}\, F_{f,k}(\Gamma_{f,k}). \tag{2.4.13}$$

The nth order $|\phi_f|^2$-weighted moment of $\Gamma_{f,k}$ is thus equal to the value at $\tau = 0$ of the nth derivative of $\zeta_{f,k}(\tau)/\zeta_{f,k}(0)$ with respect to $(-\tau)$ [Ross, 1988].

This property forms the basis of the method of cumulants, which was first proposed by Koppel (1972). The theory of cumulants derives from the MacLaurin series expansion of $\ln[\zeta_{f,k}(\tau)]$:

$$\ln[\zeta_{f,k}(\tau)] = \sum_{i=0}^{\infty} \frac{K_i}{i!} (-\tau)^i, \tag{2.4.14}$$

where K_i is the ith cumulant of $\ln[\zeta_{f,k}(\tau)]$. Evaluation of the first three cumulant coefficients using equations 2.4.10, 2.4.11, and 2.4.13 yields:

$$K_0 = \ln[\zeta_{f,k}(0)] \tag{2.4.15a}$$

$$K_1 = \langle \Gamma_{f,k} \rangle_{\phi} \tag{2.4.15b}$$

and

$$K_2 = \langle (\Gamma_{f,k} - \langle \Gamma_{f,k} \rangle_{\phi})^2 \rangle_{\phi} = \mathrm{Var}_{\phi}(\Gamma_{f,k}). \tag{2.4.15c}$$

These cumulant coefficients are evaluated through the use of a polynomial least squares curve fit to the experimentally determined values of $\ln[\zeta_{f,k}(\tau)]$, thus providing the first two $|\phi_f|^2$-weighted moments of $\Gamma_{f,k}$.

The theory and developments presented in this chapter provide some of the theoretical and analytical tools necessary for interpreting polarized and depolarized dynamic light scattering data obtained from anisotropic agglomerates occurring within a flame. The next chapter describes the experimental apparatus used to generate a flame appropriate for this study and to perform optical measurements and thermophoretic sampling of the agglomerates generated by this flame.

Chapter 3

Experimental Apparatus

The apparatus necessary for performing the experimental portion of this study must be able to generate chainlike agglomerates in a flame environment, perform in situ light scattering measurements of these agglomerates, and perform ex situ sampling of the agglomerates for comparison with the in situ results. The apparatus thus consists of 1) a burner system for generating the agglomerates in a controlled flame environment, 2) various sample probes for extracting the agglomerates from the flame at different locations to facilitate subsequent transmission electron microscopy (TEM) analysis, and 3) a light scattering spectrometer designed to control, detect, and analyze laser light scattered through the flame.

3.1 Burner System

The burner system is used for generating chainlike agglomerates in a controlled manner within a stable flame environment. Based upon results by Kasper, et al. (1980) the burner system is designed to generate agglomerates of iron oxide particulates by seeding a CO/O_2 flame with iron pentacarbonyl ($Fe(CO)_5$) vapor. The iron pentacarbonyl decomposes at approximately 300°C to form iron oxide and CO_2 in the presence of oxygen [Kasper, et al., 1980]. Under appropriate flame conditions, the iron oxide forms as straight chainlike agglomerates consisting of polyhedral primary particles, whose mean diameters are typically on the order of 50 nm [Zhang, 1995]. Thus, use of a $Fe(CO)_5$-seeded CO/O_2 flame under these conditions satisfies the primary function of the burner system.

In order to use this flame for the experimental portion of the research project, the burner system should ideally exhibit the following properties:

1. **Reproducibility and Controllability -**

The burner system should be able to accurately control the properties of the flame and agglomerates. These properties should be reproducible to insure that multiple experiments under the same control conditions provide consistent results. To accomplish this design goal, the gas supply system and burner must be able to supply controlled flow rates of each combustion gas to the flame in a steady-state process. Thus, care must be taken to prevent any deposition of iron pentacarbonyl or iron oxide within the system. The maintenance of a steady-state flame and agglomerate generation process prevents the critical flame and agglomerate parameters from changing either between separate experiments or within the duration time of a single experiment. Additionally, the ability to control the flowrates to the flame provides the freedom to adjust the flame to conditions appropriate for the measurement techniques employed.

3. **Stability -**

In order to provide an appropriate environment for both light scattering and extractive sampling applications, the flame should be stable. Methods used to stabilize the flame include isolating the flame as much as possible from random air currents, utilizing a ceramic honeycomb stabilizer over the flame to straighten the gas flow streamlines and provide an anchor for the top of the flame, and generating the flame with reactant flow combinations that are experimentally determined to encourage flame stability.

3. **Radial Uniformity -**

In order to provide a flame that supports measurements at both finite and zero degree scattering angles, all relevant properties of the flame and agglomerates should ideally be independent of the radial position within the flame. These properties include flame temperature; species concentrations; agglomerate composition, size, and

aspect ratio distributions; and the average translational and rotational velocities of the agglomerates.

Light scattering measurements performed at the zero degree scattering angle, in which the scattering volume traverses the entire width of the flame, are most readily analyzed when the properties within the scattering volume are uniform. Alternatively, because the scattering volume in light scattering measurements performed at non-zero scattering angles is highly localized, radial uniformity within the flame may not be necessary for the validity of the assumption of spatial uniformity in the finite-angle case. The assumption of spatial uniformity is still valid if the size of the scattering volume is small in comparison to the characteristic scale of the nonuniformities. Under these circumstances the expressions relating the non-zero dynamic light scattering results to the agglomerate morphology and dynamics are simplified by eliminating the need to account for spatial nonuniformities.

In accordance with the design objectives described above, the burner system consists of a reactant supply system, which supplies the combustion gases to the burner and regulates the flowrates of all gases used in the combustion process; a burner, which mixes the combustion gases and produces the flame; and a burner mounting apparatus and housing chamber, which respectively controls the location of the burner with respect to the experimental measurement apparatus and isolates the flame from the laboratory while exhausting the combustion products out of the building.

3.1.1 Reactant Supply System

The reactant supply system is designed to supply all the combustion gases to the burner in controlled proportions. As illustrated in figure 3.1.1, the reactant supply system consists of a network of compressed gas cylinders, flowmeters, valves, and tubing. This system, which is usable for both premixed-flame and diffusion-flame burners, supplies a regulated amount of iron-pentacarbonyl-seeded carbon monoxide, oxygen, and nitrogen to the burner. The capabilities of this system include the ability to

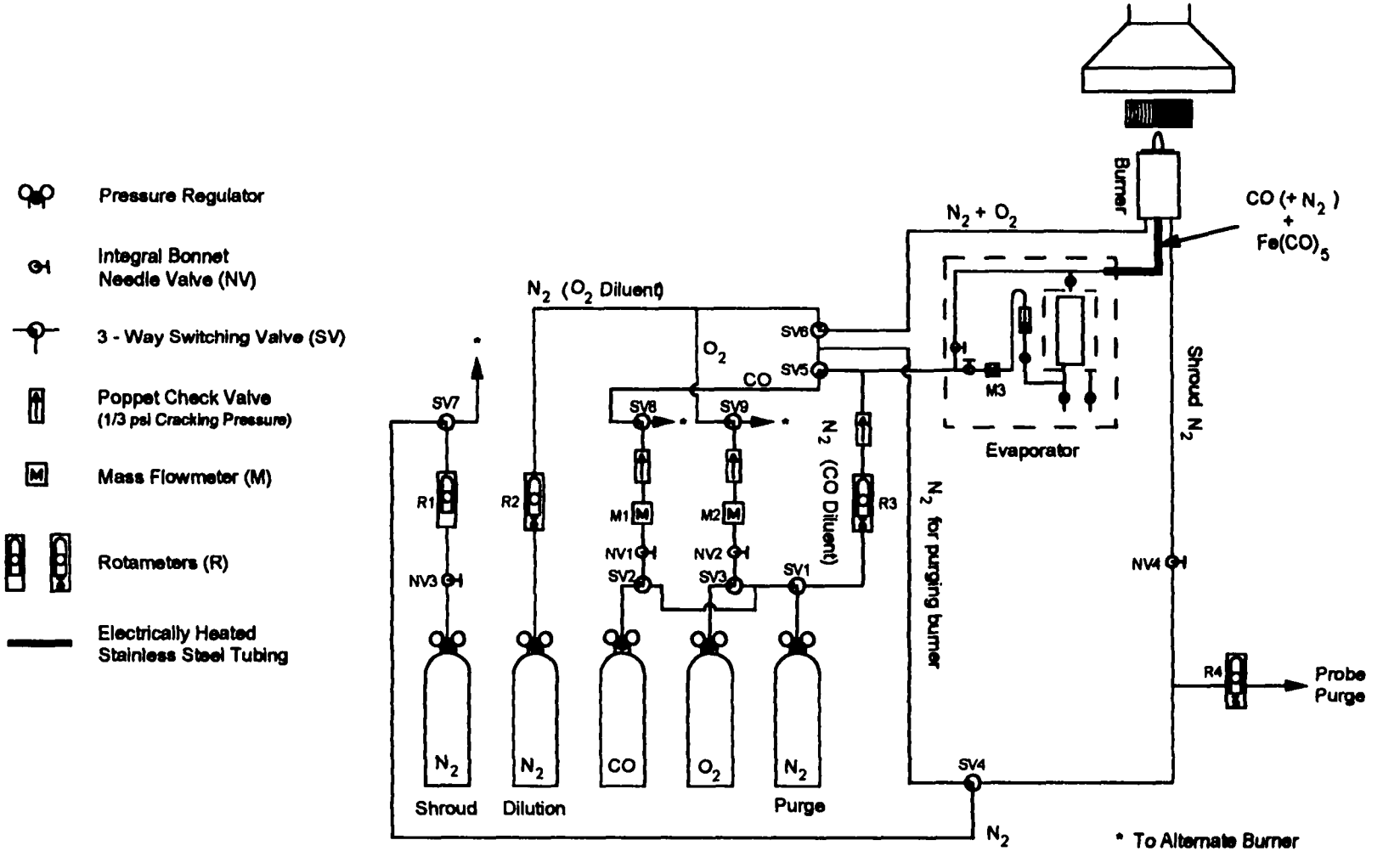

Figure 3.1.1: Schematic diagram of the reactant supply system.

independently dilute both the fuel (CO) and oxidizer (O_2) with nitrogen and the ability to control the concentration of iron pentacarbonyl with respect to its carbon monoxide carrier gas. An independent source of nitrogen is also supplied to the burner for use as a shroud if required. This system incorporates heated stainless steel tubing downstream of the evaporator (which seeds the CO with $Fe(CO)_5$) in order to minimize contamination by condensation of the $Fe(CO)_5$ within the supply tubing. The design also incorporates nitrogen purging systems for both the mass flow meters and the burner in order to prevent fouling of these components.

The flow rates of the critical reactants, CO and O_2, are monitored by thermal-type digital mass flow meters M1 and M2 (Hastings HFM - 200H), as depicted in figure 3.1.1, with an accuracy of ± 1% of their full scale of 5 slpm air. A similar digital mass flowmeter M3 (Hastings HFM - 200L, with a full scale of 300 sccm air) is used to monitor the flow rate of the carrier CO, which is split from the main CO line and bubbled through a $Fe(CO)_5$ bath in the evaporator system to seed the fuel supply. Each mass flowmeter is protected by a downstream poppet check valve (Nupro SS - 4C - 1/3, cracking pressure = 1/3 psi) to prevent flow reversal of the combustion gases back into the mass flow meters. This is especially critical in the CO line, where a backflow of $Fe(CO)_5$ into the digital mass flow meters could cause serious instrumentation damage and calibration errors. All nitrogen flowrates are monitored with standard rotameters R1, R2, R3, and R4 (Brooks 1110 - 06F1D1A and Matheson FM - 1050 - VIA).

The CO flow rate is regulated by needle valve NV1 and monitored by mass flow meter M1. The CO flow can be diluted with nitrogen split off from the N_2 Purge canister by switching valve SV1 to the CO dilution setting and regulating the nitrogen flowrate with the valve on rotameter R3. The CO then enters the evaporator (see figure 3.1.2), which seeds the mixture with $Fe(CO)_5$ by splitting off a portion of the CO stream (the carrier stream), bubbling it through a temperature-regulated bath of liquid $Fe(CO)_5$, and recombining it with the rest of the CO stream (the bypass stream). Iron pentacarbonyl

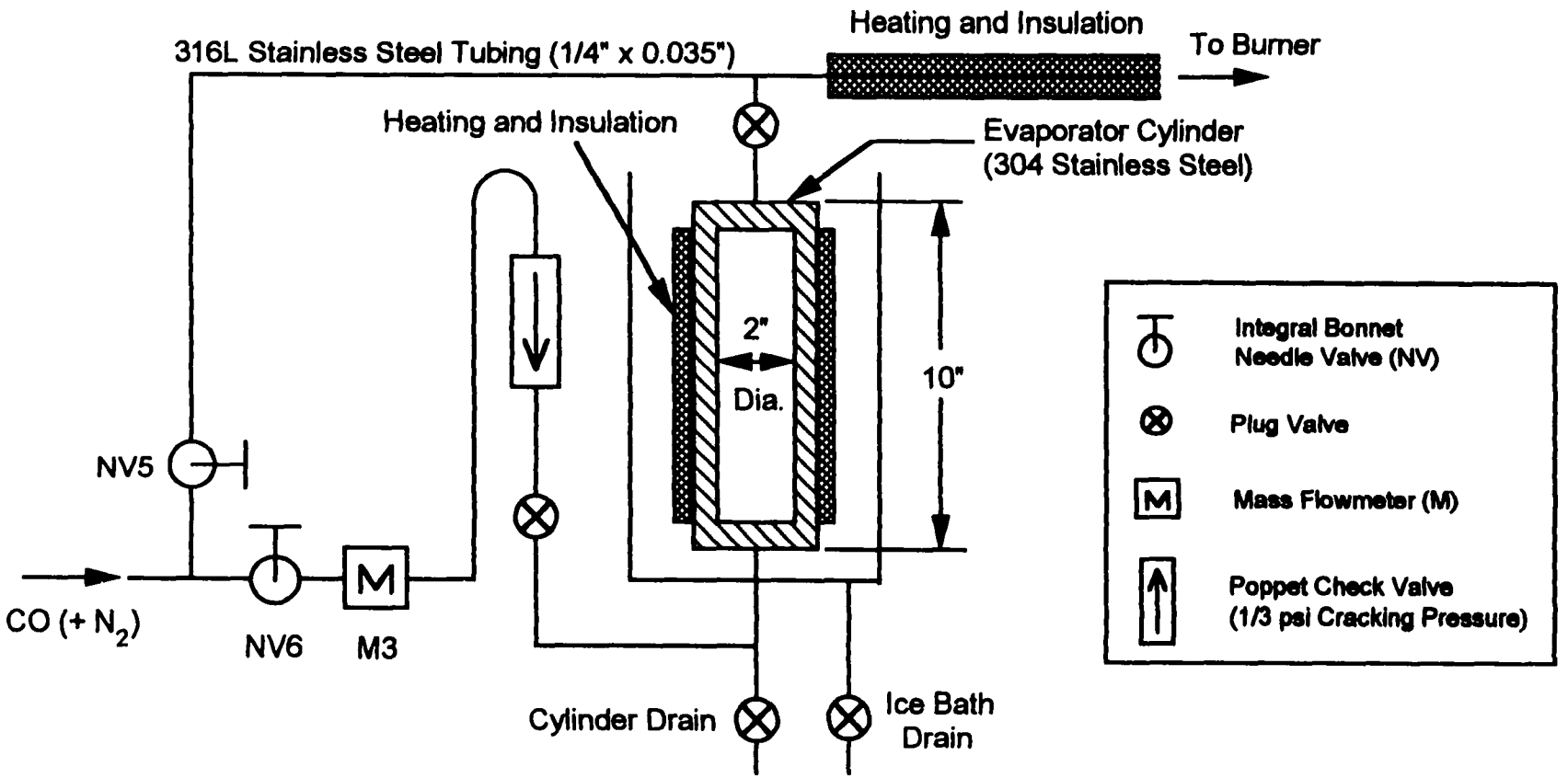

Figure 3.1.2: Diagram of the evaporator system.

vapor is absorbed by the carrier stream because of the high room temperature vapor pressure of $Fe(CO)_5$ (≈ 50 mm Hg at 35°C).

The concentration of $Fe(CO)_5$ in the CO stream is regulated by controlling the carrier stream flowrate and the evaporator cylinder temperature. The carrier stream flowrate is controlled by needle valves NV5 and NV6 and monitored by mass flow meter M3. The cylinder temperature is controlled either by immersing the evaporator cylinder in a bath of ice water to maintain a temperature of 0°C or by heating the evaporator cylinder with a feedback-controlled electrical heating tape (Omegalux FGH101 - 020 heating tape with an Omega CN9000 temperature controller) to maintain a temperature greater than room temperature. The actual mass flowrate of iron pentacarbonyl supplied by the evaporator for a given carrier gas flowrate and cylinder temperature is determined by weighing the amount of $Fe(CO)_5$ that condenses during a measured time interval into a coiled glass tube immersed in a bath of ethylene glycol and dry ice as the evaporator outlet gas passes through the tube. Detailed procedures and results of this calibration procedure are presented by Zhang (1995).

In order to minimize the condensation of $Fe(CO)_5$ in the supply tubing between the evaporator and the burner, this section of tubing is heated to an average temperature of 102°C through the use of an insulated nichrome heating element (Ace Glass 12065). The grounded 316L stainless steel fuel supply line is wrapped with 3M/Scotch high-temperature electrical tape to prevent accidental shorting between the heating element and the tubing. The heating element is wrapped around the electrical tape and surrounded by a layer of Lewco FT60-2 glass fiber insulating tape for thermal insulation. The power to the heating element is controlled by an on/off feedback temperature controller (Omega 6100) and a variable transformer (Powerstat 3PN1168). Five thermocouples are welded to the supply tube at various locations along its length. One of these thermocouples is used as a feedback sensor for the temperature controller while the others are used to monitor the wall temperature at the various locations along the tube.

The O_2 flow rate is regulated by needle valve NV2 and monitored by mass flow meter M3. The O_2 flow is diluted by nitrogen from the N_2 Dilution canister. The flow rate of this dilution nitrogen is regulated and monitored by rotameter R3. The diluted O_2 is then sent to the burner to be mixed with the seeded CO for subsequent combustion.

An independent supply of nitrogen for shrouding the flame is supplied to the burner from the N_2 Shroud canister when the switching valve SV4 is set to the Shroud and Probe Purge setting and the needle valve NV4 is at least partially open. This shroud nitrogen is useful for isolating the flame from the oxygen in the ambient air and providing a stabilizing annular flow around the flame. Alternatively, this nitrogen supply can be used as a combustion inhibitor in diffusion flames by directing the nitrogen between the fuel and oxidizer flows to delay fuel/oxidizer mixing and combustion. The purpose and effect of this procedure is to lift the flame from the burner surface to reduce the possibility of burner overheating and clogging.

A nitrogen line for purging an extractive isokinetic sampling probe, which was utilized in the study by Zhang (1995), splits off from the shroud nitrogen line upstream of needle valve NV4. The flow of nitrogen through the probe purge line is controlled by rotameter R4 and needle valve NV4. (The purpose of needle valve NV4 is to increase the pressure drop in the shroud N_2 line to permit nitrogen flow through the much narrower sampling probe.) This nitrogen is directed through the sampling probe to prevent the deposition of particulates within the probe when the probe is not sampling the particulates.

Purging is also important for proper maintenance of the digital mass flowmeters. In order to reduce the possibility of altering the calibration of the flow transducers due to fouling, the reactant supply system incorporates a meter purge system that facilitates the purging of all digital mass flowmeters with nitrogen after the completion of all experiments. The meter purge system operates by switching the gas supply canisters for the fuel and oxygen supply lines from CO and O_2 to N_2 via two 3-way switching valves

SV2 and SV3 located upstream of the mass flowmeters M1, M2, and M3. Thus, setting valves SV2 and SV3 to the inert gas setting and SV1 to the meter purge setting purges the digital mass flowmeters in the system by sending nitrogen through the lines instead of fuel and oxygen.

Since the purge nitrogen from the meter purge system eventually passes through the burner, it acts to remove some of the deposits within the burner. However, since mass flowmeters M1 and M2 only permit a maximum flow rate of 5 slpm each, the maximum possible flow of N_2 through the burner from this source is unlikely to be enough to physically dislodge solid deposits from the burner's inner walls and propel them out of the burner. Therefore, a system for specifically purging the burner is also incorporated into the reactant supply system. The burner purge system directs nitrogen from the N_2 Shroud canister into the fuel and oxidizer lines downstream of the digital mass flowmeters to provide a high-speed flow of nitrogen through the burner. High speeds are possible in this case because the maximum flow rate accommodated by rotameter R1 (Brooks 1110 - 06F1D1A) far exceeds the 5 slpm maximum flow rates of the digital mass flowmeters (Hastings HFM - 200H) and the other rotameters (Matheson FM - 1050 - VIA). This flow of nitrogen, first through the heated fuel lines, then through the burner, provides an inert medium to expel solids deposited within the burner and to vaporize any $Fe(CO)_5$ deposited within the burner and supply lines without risking the formation of oxides.

The purging systems thus act to maintain the cleanliness of the reactant supply system and burner for continuous accuracy in supplying the necessary combustion gases to the flame. The reactant supply system is largely responsible for establishing the necessary qualities of repeatability and control for flame experiments because the reactant flow rates are the most easily controllable independent variables used to establish the flame conditions. Once these flow rates are determined, the flame structure is determined by the configuration of the burner.

3.1.2 Concentric Tube Diffusion Burner

The main purpose of the burner is to mix the reactant gases and establish a flow field suitable for the formation of a stable flame. In this capacity, the burner design is the most crucial aspect for the proper formation of a usable flame because it governs the structure of the flame itself. A flame suitable for use with light scattering measurements should be stable and should maintain an environment conducive to the formation of straight chain agglomerates. Additionally, the physical and chemical properties of the flame and the agglomerates, as well as the morphology distribution of the agglomerates, should ideally be radially uniform within the flame, which would potentially simplify the interpretation zero-angle depolarized DLS measurements. In this study, three different burners were initially tested to determine whether or not they can maintain a flame suitable for the desired in situ and ex situ measurements: a flat-flame diffusion burner, a premixed flat-flame burner, and a concentric-tube diffusion burner. The results of these tests are presented in Appendix A. Of the three burner types tested, only the concentric-tube diffusion burner was suitable for the desired measurements because all other burners exhibited severe clogging problems. Because concentric-tube diffusion flames exhibit radial nonuniformities by nature, the optical measurements performed in this study were limited to finite scattering angles to permit the approximation of spatially uniform properties within the scattering volume.

The concentric tube diffusion burner is designed to produce a nearly conical diffusion flame by separately directing the fuel and oxidizer through concentric stainless steel tubes into the flame. As illustrated in figure 3.1.3, this burner consists of three stainless steel (type 316) tubes that screw into each other along a common axis to form two concentric annular outlets and one central cylindrical outlet, through which the combustion gases can be directed. The annular spaces between the tubes are each 1/16" thick and the central tube has an inner diameter of 1/2". Each inner tube has a wall thickness of 1/16".

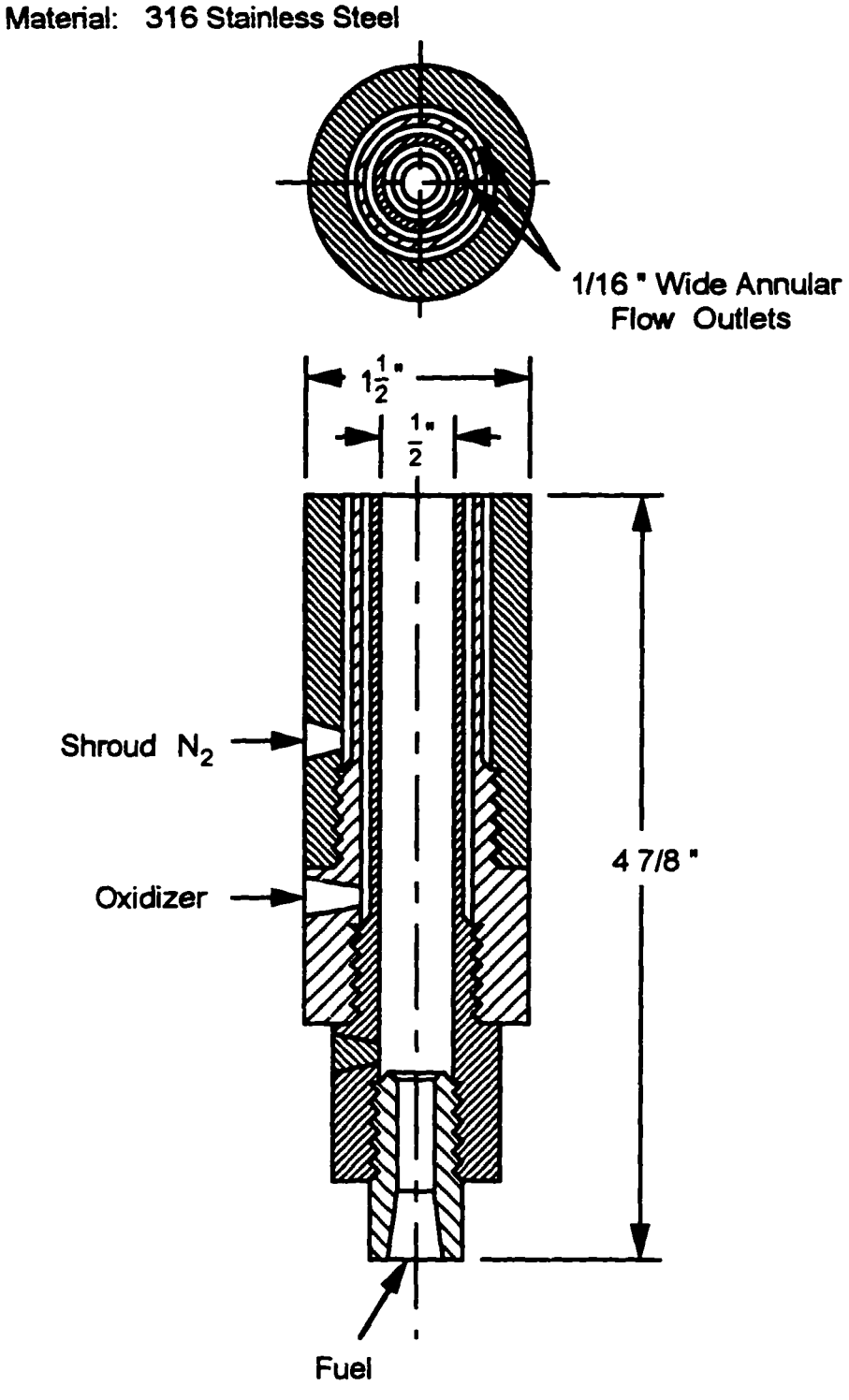

Figure 3.1.3: Concentric tube diffusion burner

Emerging from the central tube, the fuel mixes through diffusion with the oxidizer, which is either obtained from ambient room air or directed through an annular region surrounding the fuel tube. This oxidation of the outer edges of the fuel jet causes a conical flame whose diameter decreases with increasing height above the burner surface. Because the burner has three independent outlets, the operational configuration, based on which gas flows through each outlet, can easily be varied to obtain different flame configurations. The configuration used for this study has the $Fe(CO)_5$-seeded CO emerging from the central tube, surrounded by an annulus of oxygen from the surrounding outlet. The outer ring of the burner supports a stream of shroud nitrogen to isolate the flame from ambient air. This burner is a modified version of the concentric tube diffusion burner used in the preliminary studies by Zhang (1995), as described in Appendix A. The modification consisted of removing a previously existing 1/4" central fuel tube to increase the flame's diameter in an attempt to obtain greater stability than that of the flame investigated by Zhang. Like the results of the similar studies by Kasper, et al. (1980) and Zhang (1995), this burner successfully produces chainlike agglomerates of iron oxide particles when operated using iron-pentacarbonyl-seeded carbon monoxide as the fuel. Transmission electron micrographs of agglomerates extracted from this flame are presented in section 4.1.2 of the next chapter, along with a statistical analysis of the morphological parameters obtained.

3.1.3 Burner Positioning and Housing System

In order to promote precision during flame experiments, the flame must be isolated from air currents and positioned accurately relative to the optics. Additionally, for safety, the products of combustion and unburnt reactants must be effectively exhausted from the laboratory. The burner positioning and housing system is designed to accomplish these requirements. This system consists of a solid metal optical table, upon which both the burner and the optics are mounted; a burner translation mechanism, which determines the vertical position of the burner with respect to the optics; a fume hood,

which exhausts the combustion products and unburnt reactants from the laboratory; and a wooden isolation chamber, which surrounds the entire optical table to prevent stray room-air currents from disturbing the flame and to minimize the occurrence of room-air contamination from unexhausted combustion products and unburnt reactants. This system, with the exception of the wooden isolation chamber, is illustrated in figure 3.1.4.

The optical table consists of a 5' diameter 3/4" thick aluminum plate bolted to a frame consisting of 2 1/2" wide steel L-beams, which form the legs of the table. The bottom of each leg rests on an adjustment screw, so that the table can be properly balanced and stabilized. Resting over a rectangular hole in the center of the aluminum plate is a system of cylindrical bearings that permits the rotation of three 31" long aluminum arms about a central cylinder. This entire bearing assembly can be balanced independently of the table via the four support screws upon which it rests. The three arms are used as movable platforms for mounting optics and probing instruments. The burner is mounted on a separate cylinder that slides through the central cylinder, thus allowing the burner height to be varied with respect to the height of the arms. A burner translation mechanism, which adjusts the vertical position of the burner with respect to the arms, is bolted to the underside of the bearing assembly's base plate.

The burner translation mechanism adjusts the height of the burner by utilizing a 1/50 horsepower electric motor to drive a system of gears and screws. The motor drives a pair of spur gears, which decreases the effective rotational speed of the motor's output. The driven spur gear turns a lead screw that shares its axis of rotation. The rotation of this lead screw causes the vertical motion of a threaded collar, which is attached to the bottom of the burner cylinder by a rigid support screw. The vertical motion of this collar thus causes vertical burner translation.

The displacement of the burner is measured by counting the pulses detected by a photodetector as infrared light emitted from a photoemitter passes through equidistant

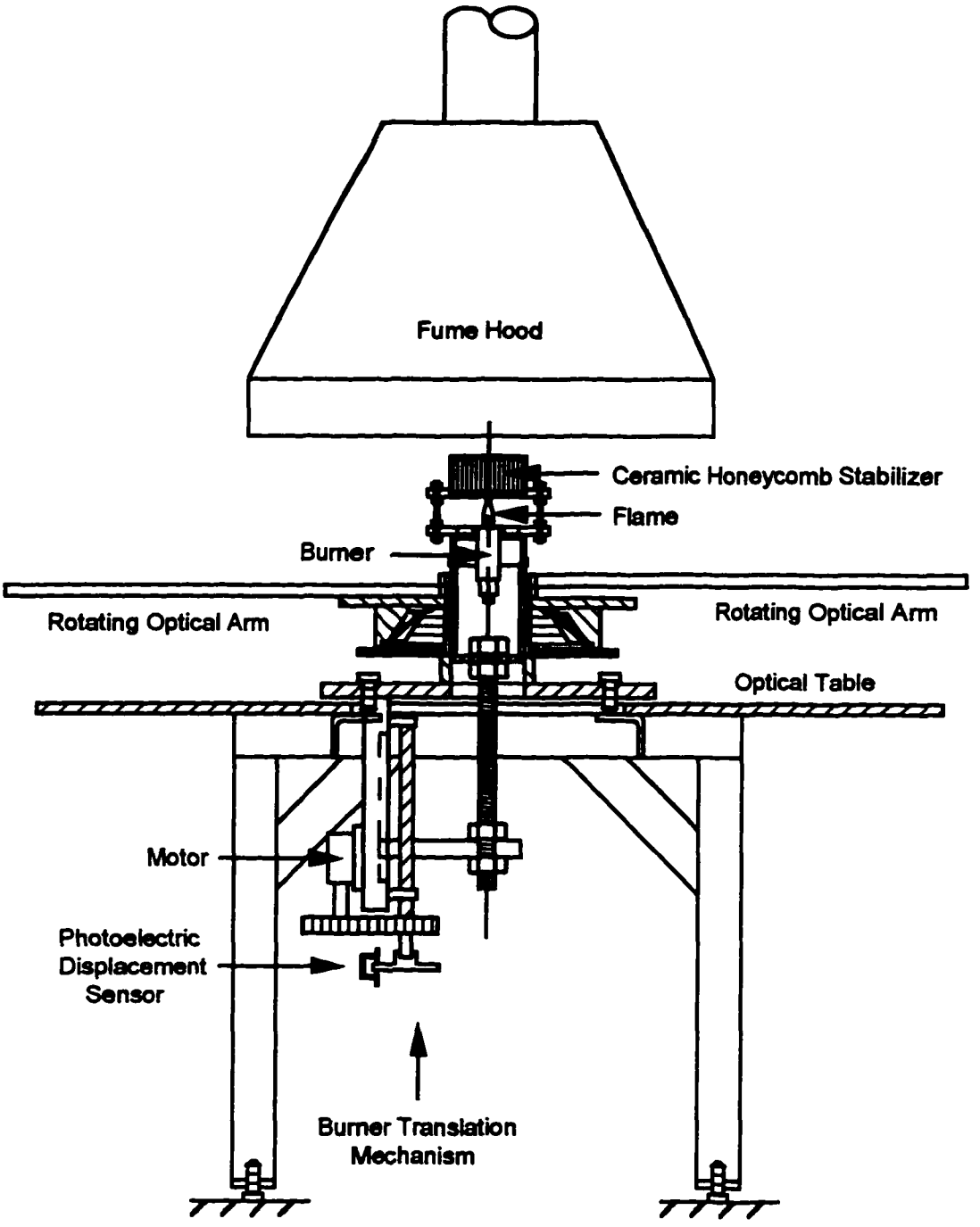

Figure 3.1.4: Optical table and burner positioning system.

holes located around the circumference of a disk that is attached to the bottom of the lead screw shaft. As the lead screw turns, the disk rotates, causing the holes to pass between the photoemitter and the photodetector, which are located on opposite sides of the disk. The detected pulses are then counted by a digital counter. Calibration of this measurement system using an optical spotting scope to measure the actual burner height has determined that the photodetector system registers 9.95 ± 0.07 pulses per millimeter of burner translation.

Accurate mounting and positioning of the burner relative to the optics, as described above, is a major factor necessary for the insurance of precision during experiments. Another requirement for the proper performance of precise experiments is the maintenance of the flame's stability. In addition to the utilization of a ceramic honeycomb flame stabilizer, an appropriate choice of reactant flow rates, and, when appropriate, an inert shroud flow to stabilize the flame, a large wooden chamber has been constructed around the optical table to isolate the flame from stray ambient air currents. This 75" high chamber is large enough (96" x 87") to enclose the entire optical table while allowing enough room for a person to enter the chamber to adjust the experimental apparatus. Constructed of 1/4" thick flat-black-painted plywood screwed to a metal frame, the chamber incorporates two doors for ease of access, Plexiglass windows to allow visual inspection of the experiment from outside the chamber, and ventilation screens at the top of the walls to permit a limited-area diffuse inflow of air from the chamber's surroundings.

Besides acting as a stabilizing influence on the flame, the isolation chamber also decreases the risk of contamination of the ambient air in the laboratory from combustion products and unburnt reactants. By minimizing disturbances to the flame from stray air currents, the presence of the chamber encourages the hot combustion gases to flow in an undisturbed upward direction into a fume hood located over the burner. Also, the presence of limited-area ventilation screens in the chamber walls limits the flow area of the

ambient air as it is sucked into the chamber by the fume hood. For constant suction from the fume hood, smaller flow areas produce larger average velocities of the ambient laboratory air into the chamber. These larger velocities act to overtake the potential diffusion of toxic gases out of the chamber.

The fume hood is constructed of stainless steel sheet metal and has a 26 1/4" x 28" suction area. The minimum operational volume flow rate of air through the hood, calculated from velocity measurements made by a Davis anemometer, is 1570 lpm. This suction flowrate surpasses any reasonable total flowrate of combustion gases from the burner. Because of its wide suction area, the hood must be positioned as close to the optical table as feasibly possible, without interfering with the optical path and burner accessibility, to maximize the average suction velocity between the hood inlet and the table surface. This helps counteract any diffusion of toxic gases away from the flame area. The wide inlet area, along with the hood's 21" height, provides ample room to position suction probes over the flame in order to sample the particulates from the flame.

3.2 Thermophoretic Sampling System

Ex situ sampling methods are techniques in which the experimental samples are physically removed from their natural environment to be examined under a different controlled environment. Performance of ex situ studies of the morphology of flame-generated agglomerates thus involves physically removing agglomerates from the flame for analysis utilizing transmission electron microscope (TEM) analysis.

The great advantage of the use of ex situ sampling in conjunction with TEM analysis is that photographs of the actual agglomerates are obtained. Thus, the morphology of the sample is clearly visible. Data used to directly obtain the statistical distributions of the agglomerates' morphological parameters is simply measured from the appropriate TEM photographs. Because of the simplicity and directness of the analysis of morphological data obtained from the TEM observations, this extractive sampling

technique is valuable for providing agglomerate morphology information to compare with the results of the optical measurements.

The main disadvantage of this technique is that the act of removing the agglomerates from their flame environment and preparing them as TEM samples may cause unacceptable changes to the very morphological parameters being measured. For example, in order to remove the sample from the flame, a probe must be inserted into the flame. Insertion of the probe into the flame causes the flow field and the temperature distribution of the flame to change from their undisturbed values, thereby altering the physical conditions that govern the growth and agglomeration of the solid particulates. Additionally, certain probe types may not be effective in preventing additional reaction and agglomeration of the solid products after they are removed from the flame. Thus, the design of the probe used to extract the sample from the flame is most crucial for obtaining accurate results from ex situ methods. In this study, a thermophoretic probe is used to extract agglomerate samples from the iron-pentacarbonyl-seeded CO/O_2 flame.

A thermophoretic probe is an extractive probe whose operational principle is based on the tendency of particles to move along temperature gradients within its surrounding fluid environment. Thermophoretic sampling occurs when a room-temperature plate is inserted into the flame for a brief time interval. Heat transfer between the cool plate and the hot flame gases establishes a temperature gradient in the gases adjacent to the plate's surface. Since molecules from the hot regions of the flame gases impart greater momentum to a suspended particle than molecules from cooler regions of the flame gases, the particles are propelled towards the cooler gas regions to eventually deposit on the probe, which then quenches further heterogeneous reactions with the particles. The phenomenon by which particles are subjected to a net force due to a temperature-induced momentum imbalance of molecular collisions from the surrounding gas medium is known as *thermophoresis*.

Studies performed by Rosner, et al. (1991) have shown that the orientation-averaged thermophoretic drift velocity (the velocity that results when the thermophoretic force on a particle balances the corresponding drag force) of agglomerates is roughly equal to the thermophoretic drift velocity of a primary particle and is thus relatively insensitive to the agglomerate's shape and number of primary particles. Additionally, theoretical results for spherical particles due to Waldmann (1959) and Brock (1962) indicate that the thermophoretic drift velocity is insensitive to the particle diameter, especially when this diameter is much smaller than the mean free path of the surrounding gas molecules. As a result, thermophoretic sampling should exhibit no significant bias towards any particular agglomerate morphology. Because thermophoretically sampled agglomerates are quenched while still in the flame, preventing further reactions, and are sampled without significant bias to any particular morphology type or trend, insuring that sampling of all agglomerates is equally likely, the technique of thermophoretic sampling is well suited for determining the morphological parameters of agglomerates as they occur in the flame [Dobbins and Megaridis, 1987].

Thermophoretic sampling from the iron-pentacarbonyl-seeded CO/air diffusion flame is accomplished by using a double acting pneumatic cylinder (Bimba MRS - 04 - DXP) to insert a 20 x 4 x 0.2 mm strip into the flame for a time period ranging from 75 ms to 200 ms. The entire thermophoretic sampling apparatus is depicted in figure 3.2.1. While the probe is in the flame, the agglomerates are thermophoretically deposited onto a 3 mm diameter carbon-coated copper electron microscope grid (Electron Microscopy Sciences FCF - 200 - Cu, 200 mesh), which is taped to the stainless steel strip probe. The strip enters the flame in the radial direction, oriented parallel to the streamlines of the flow in order to minimize disturbances to the flame. Additionally, a vertical slotted plate (a flow deflector) is placed between the initial probe position and the flame in order to minimize flame disturbances caused by air currents induced by the probe's sudden

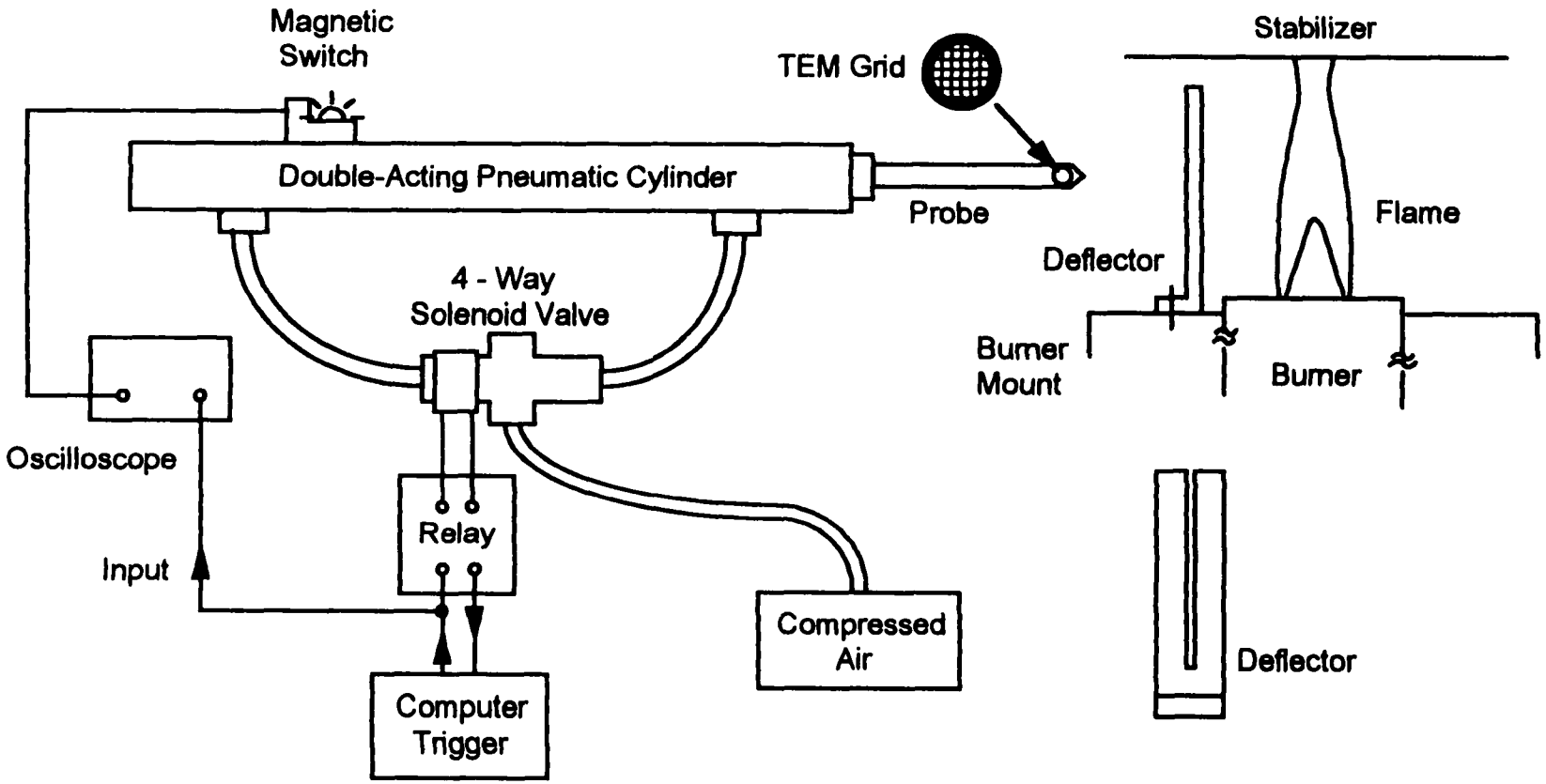

Figure 3.2.1: Thermophoretic sampling system.

motion. By blocking some of the radiative heat transfer between the flame and the probe, this flow deflector also helps prevent premature heating of the probe.

The duration time of the thermophoretic sampling experiment is controlled by a Macintosh SE computer equipped with an Omega WB - AAI - SE data acquisition and control system. The digital output of the computer acts as a solid state switching device that, when connected in series with an 9V battery, supplies a timed pulse to the low voltage input of a solid state relay (Potter and Brumfield SSRT - 120D25). During the application of this DC pulse, the relay energizes a 4-way solenoid valve (ASCO 8342C1) by supplying it with a 115V 60Hz AC signal. Energizing the solenoid valve opens the rear side of the pneumatic cylinder to a 40 psi air supply while exhausting the front side to the atmosphere in order to force the probe into the flame. Termination of the timed pulse from the computer deenergizes the solenoid valve, causing the probe to retract by introducing high pressure air into the front of the pneumatic cylinder while exhausting its rear chamber.

In order to calibrate the performance of the probe actuator with respect to the pulse output from the computer, a hall effect switch (Bimba HSCX - 04) is used in conjunction with an oscilloscope to determine the location of the piston in the pneumatic cylinder at particular times. When mounted to the outside of the cylinder, the hall effect switch detects the presence of the piston when the piston is directly adjacent to the switch. This detection is based on the fact that the magnetic field from a permanent magnet mounted to the piston produces a voltage output from the hall effect switch by disrupting the electrical current distribution flowing through the switch. Placement of the switch at the end of the piston stroke permits the measurement of the actual sample time (the time interval during which the probe is fully extended) for a given pulse duration from the computer. Also, placement of the switch at the center of the cylinder permits the determination of the translational speed of the probe during extension and retraction. This is accomplished by measuring the time interval between the pulses generated as the piston passes the hall

effect switch during extension and retraction, subtracting the corresponding sample time, and dividing half of this result into the stroke length (3") of the pneumatic cylinder. Calibration tests performed at an air supply pressure of 40 psi give the translational speed of the probe to be 0.86 m/s [Zhang, 1995]. This speed can be used to verify that the transit time of the probe entering and leaving the flame is much shorter than the sample time, a condition necessary to insure that the majority of collected particles are obtained while the probe is at full extension.

Based on the considerations described above, the thermophoretic probe is appropriate for the sampling of agglomerates from flames for morphological analysis. Measurement of the morphological parameters of agglomerates thus obtained provides data needed for comparison with the results of optical experiments. The apparatus required for the optical experiments is described in the next section.

3.3 Optical Measurement System

The purpose of the optical measurement system is to non-intrusively determine the dynamics of the agglomerates within the flame by measuring the intensity fluctuations of light scattered from the flame. Knowledge of the agglomerate dynamics permits a comparison with the morphology information from the ex situ measurements to determine experimental values of the functional relationship between the morphological properties and dynamic coefficients of chainlike agglomerates in a non-continuum environment. With this information, the agglomerate morphological parameters can then be extracted from the optical measurements alone in subsequent tests.

Effective measurements of the intensity fluctuations of light scattered from the agglomerates in the flame require an assembly of optics and signal processing apparatus that is collectively known as a light scattering spectrometer. The major components of the light scattering spectrometer are the source optics, which supplies a suitable beam of incident light into the particle suspension (the flame); the detection optics, which gathers the desired component of the scattered light and converts its intensity into an electronic

signal; and the signal processing apparatus, which analyzes the dynamic signal from the detection optics and stores the results. Many of the considerations necessary for the proper design and operation of a light scattering spectrometer are reviewed in the papers by Ford (1985) and Charalampopoulos (1987). The following discussion presents the design of the light scattering spectrometer used in this study. The effects of the various design and operation variables on the accuracy of the measurement are also considered.

The overall design of the light scattering spectrometer is shown schematically in figure 3.3.1. As shown in the figure, the source optics focus polarized laser light into the flame, and the detection optics, which can be rotated to vary the scattering angle θ, collect a polarized component of the scattered light and utilizes a photomultiplier tube to convert the detected photons into current pulses, which are then processed, counted, and analyzed by a pulse amplifier discriminator and a digital correlator.

3.3.1 Source Optics

The purpose of the source optics is to focus a polarized beam of light into the particle laden flame as an incident light source for the scattering experiment. Properties of the incident light that affect the success of the light scattering experiment are the power of the light, the coherence of the beam, and the radius of the incident beam at the region of the flame seen by the detector.

Increasing the total power of the incident light generally increases the precision of the light scattering measurement because the higher power decreases the relative statistical fluctuation of the number of photons detected during a sample time Δt and because the additional power helps overcome the relative effects of dark counts (random power-independent signals) in the photomultiplier tube. The decrease in the relative statistical fluctuation of the detected photons results from the fact that the photon detection process is a Poisson random process for constant intensity detected light (see Mandel and Wolf (1965) and Ford (1985)). When Δt is much less than the time scale of the detected intensity fluctuations, the intensity during Δt is nearly constant (when the incident source

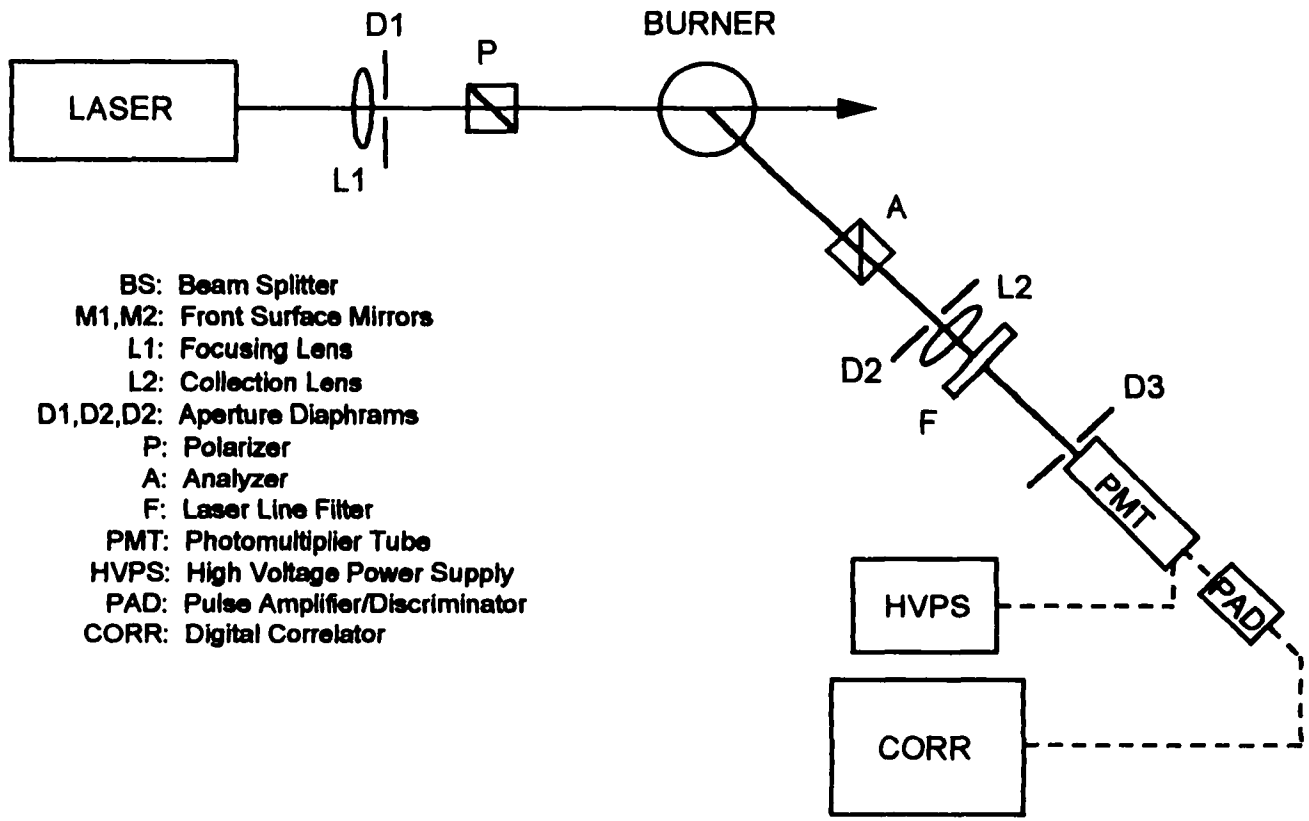

Figure 3.3.1: Schematic diagram of the optical measurement system.

is a laser), producing a Poisson detection process whose variance is equal to the mean number of photons detected during Δt. Therefore, the percent uncertainty of the photon count is inversely proportional to the square root of the number of photons detected during Δt.

Coherence criteria for dynamic light scattering experiments, as presented by Jakeman, Pusey, and Vaughan (1976), are that the illuminated area of each scattering particle must be much less than the coherence area of the incident beam and that the coherence length of the incident beam must be longer than the maximum optical path difference between the scatterers. Though these criteria can be met using conventional light sources, such as a filtered mercury arc lamp ([Cummins and Swinney, 1970], [Jakeman, et al., 1976]), the loss of intensity resulting from the filtration of this light to conform to these coherence criteria increases the statistical uncertainty of the measurements for a given experiment duration. For this reason, the best light source for the scattering experiment is a laser, which emits high intensity light whose coherence properties far exceed the coherence criteria for a successful scattering experiment.

The incident beam's radius (spot size) at the region seen by the detector affects the size of the scattering volume. Reducing the size of the scattering volume increases the spatial coherence of the scattered light at the surface of the detector. A high degree of spatial coherence of the scattered light at the detector is advantageous because it strengthens the relative magnitude of the time-dependent component of the photon count correlation function. It is this time dependent component that contains the information on the dynamics of the agglomerates. Therefore, the spot size at the scattering volume should be minimized by focusing the incident beam through a lens. In this application, the high degree of spatial coherence of laser light offers an additional advantage by producing smaller focused spot sizes than those obtainable from conventional light sources.

The light source for the light scattering spectrometer used in this study is a Spectra Physics 2085A-20 argon ion laser, which is capable of producing a 1.85 mm diameter laser beam at a maximum power of 7 W when emitting light at a wavelength of 488 nm. The full-angle intrinsic beam divergence is 0.44 mrad. This vertically polarized beam is focused by a BK7 glass plano-convex focusing lens L1 (Melles Griot 01 LPX 313, f_1 = 400 mm) to a point within the flame.

The spot size ω_0 at the beam waist (point of minimum spot size) is calculated utilizing standard Gaussian beam theory [Guenther, 1990] and several approximations regarding the nature of the laser light and the focusing lens L1. When the laser is emitting in the TEM 00 mode, the laser light exhibits a Gaussian intensity (and electric field amplitude) profile. Additionally, use of the paraxial approximation, in which the light wave's propagation direction at any point deviates very little from the axis of the beam, is justified because the beam divergence is very small (0.44 mrad maximum).

Applying Gaussian beam theory to thin lenses, the radius of curvature of the wavefront of the laser light changes when passing through lens L1 according to the following equation:

$$\frac{1}{R_1} = \frac{1}{R_L} - \frac{1}{f_1}, \qquad (3.3.1)$$

where f_1 is the focal length of lens L1 and R_L and R_1 are the respective radii of curvature of the incident and transmitted optical wavefronts. When $f_1/R_L \ll 1$, which is true in this case ($f_1/R_L \approx 0.036$ at λ = 488 nm), the radius of the transmitted optical wavefront R_1 is approximately equal to - f_1. The spot size ω_1 of the transmitted beam at the location of the lens exit is equivalent to either the incident beam's spot size or the radius ($d_1/2$) of the opening in an iris diaphragm D1 (Melles Griot 04 IDM 005 or equivalent) located adjacent to lens L1, whichever is smaller.

The spot size ω_0 at the beam waist of the focused beam is then determined from the spot size ω_1 and the wavefront radius of curvature R_1 at the outlet of lens L1 by the relationship (see Guenther (1990)):

$$\omega_0 = \left[\frac{\omega_1^2}{1 + \left(\frac{\pi\omega_1^2}{\lambda R_1}\right)^2}\right]^{1/2} \cong \left[\frac{\omega_1^2}{1 + \left(\frac{\pi\omega_1^2}{\lambda f_1}\right)^2}\right]^{1/2} \qquad (3.3.2)$$

or

$$\omega_0 \cong \frac{\lambda f_1}{\pi\omega_1} \qquad \left(\text{when } \frac{\pi\omega_1^2}{\lambda f_1} \gg 1\right). \qquad (3.3.3)$$

For this particular experimental system, the validity of the approximation used in equation 3.3.3 is indicated by the fact that $(\pi\omega_1^2)/(\lambda f_1)$ is approximately equal to 27 when the diameter d_1 of aperture D1 is large enough to pass the entire beam. When recast in terms of the laser beam's intrinsic (half-angle) beam divergence $d_\beta \cong \lambda/(\pi\omega_{OL})$, equation 3.3.3 takes the form

$$\omega_0 \cong d_\beta\left(\frac{\omega_{OL}}{\omega_1}\right)f_1, \qquad (3.3.4)$$

where ω_{OL} is the minimum spot size of the unfocused laser beam. For the present system, with λ = 488 nm and $d_1 \cong$ 3.6 mm, the minimum focused spot size, which occurs at a distance of approximately f_1 (= 400 mm) from lens L1, is approximately 0.055 mm.

Upon exiting the focusing lens L1 and aperture D1, the laser light passes through a high quality prism polarizer P (Karl Lambrecht MGLSW8), which is oriented with its transmission axis perpendicular to the scattering plane. The purpose of this polarizer is to increase the extinction ratio of the incident beam to at least 10^{-6}. The polarizer is mounted in a precision polarization rotator (Karl Lambrecht DCGF) that exhibits an angular resolution of 50 arc seconds for high positioning accuracy.

The combination of the argon ion laser, beam splitter BS, positioning mirrors, focusing lens L1, diaphragm D1, and polarizer P thus projects a focused, polarized laser beam into the flame. Power measurements of the incident beam at various locations using a power and energy meter (Scientech 365) indicate that, with the present configuration,

the laser power at the scattering volume is approximately 30% of the power at the laser outlet when the diameter of aperture D1 is set to 2.78 mm. Thus, in its present configuration, the source optics can ideally provide a 0.11 mm diameter vertically polarized beam of laser light to the scattering volume at a maximum power of 2.4 W with a polarization extinction ratio of 10^{-6} at a wavelength of 488 nm. When operating with an appropriate flame, the particles within the flame scatter this laser light into the detection optics, which measures the resulting intensity fluctuations.

3.3.2 Detection Optics

The detection system is an assembly of optical devices designed to gather the desired component of the scattered light and convert its transient intensity fluctuations into electrical signals for subsequent processing and recording. The configuration of the detection optics determines the polarization component of the scattered light to be studied and affects the size of the scattering volume and the number of detected coherence areas. By mounting the detection optics on an arm that rotates about the flame's central axis, the scattering angle θ can also be varied. Additionally, the detection optics are responsible for distinguishing the scattered laser light from extraneous light from sources such as flame emissions and room lights so that a pure signal is measured. The detection system used in this study consists of a polarizer A (called an *analyzer* in this application), a collection lens L2, a laser line filter F, variable apertures D2 and D3, and a photomultiplier tube PMT.

The first optical component encountered by the scattered light is the analyzer A. The purpose of the analyzer is to select the linear polarization component of the scattered light to be studied. The analyzer is a prism polarizer with specifications identical to the polarizer P of the source optics system. Like the polarizer P, the analyzer A is mounted in a Karl Lambrecht DCGF precision polarization rotator to accommodate accurate angular positioning.

After polarization is determined by A, the scattered light passes through iris diaphragm D2 into the collection lens L2 (Oriel 41365, f_2 = 125 mm). The aperture diaphragm D2 functions to block extraneous light and define the effective detection area. When keeping all other experimental parameters constant, increasing the diameter d_2 of aperture D2 simultaneously increases the total detected scattered power and the number of detected spatial coherence areas.

The function of the collection lens L2 is to focus the scattered light onto aperture D3, which is mounted directly in front of the photomultiplier tube's (PMT) photocathode. The distance between the scattering volume and the collection lens L2, which is equal to the distance between the collection lens and the aperture D3, is twice the focal length of the lens L2 ($2f_2$ = 250 mm) so that the scattering volume is imaged onto aperture D3 with a magnification of unity. Though light scattering spectrometers can function without a collection lens, utilization of a collection lens reduces the amount of extraneous light reaching the PMT by limiting the detector's angle of view and also permits the placement of the PMT further away from the hot flame with no significant reduction of the detected power of the scattered light. Also, by using the collection lens to image the scattering volume onto aperture D3, distinct boundaries of the scattering volume are defined by the diameter d_3 of aperture D3, the spot size ω_0 of the focused laser beam, and the scattering angle θ, as depicted in figure 3.3.2.

In order to eliminate the detection of undesired light due to room lights and radiative emission from the flame, a laser line filter F (Ealing 35 - 8366) is mounted directly behind the collection lens L3. This filter only transmits light within the wavelength band of 488 ± 1 nm, with a peak transmission of 45%. This effectively filters most of the light that does not originate from the argon ion laser. The collection lens L2, the laser line filter F, and the aperture diaphragms D2 and D3 are all mounted in a metal housing that is fastened to the photomultiplier tube PMT. This housing, which is painted flat black, is designed to admit light to the PMT only through the collection optics

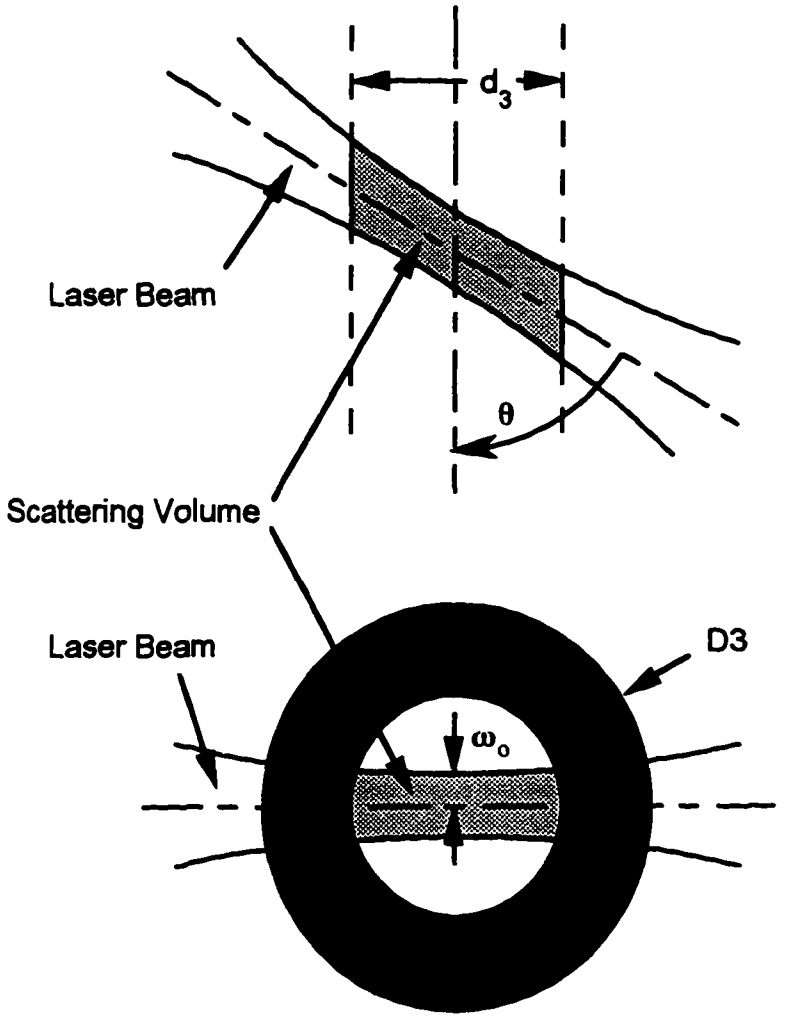

Figure 3.3.2: Determination of the scattering volume geometry for non-zero scattering angles. [$\theta > d_3$/(Flame Diameter)]

in order to prevent signal contamination and possible photomultiplier tube damage from unfiltered extraneous light. After being polarized, focused, and filtered, the scattered light reaches the photomultiplier tube PMT, which converts the light power into electrical signals.

The photomultiplier tube PMT (Thorn EMI 9863B/350) measures the total power of the light incident on its photocathode surface by generating a current proportional to the flux of incident photons. Due to the photoelectric effect, a photon incident upon the photocathode surface causes the emission of an electron with probability η, which is

called the *quantum efficiency*. An electrostatic field generated by applying a DC voltage to electrodes within the PMT accelerates the electron and redirects its trajectory, causing it to impact upon the first dynode. Upon impact, a quantity of secondary electrons, whose number is proportional to the energy of the incident electron, is emitted from the dynode. These secondary electrons are then accelerated to another dynode by another electrostatic field to produce even more electrons. This process continues through several stages until it terminates at the PMT's anode, which supplies the output signal to the signal processing system. Thus, the anode acts as a current source whose current is proportional to the photon flux incident upon the photocathode. The ratio of the anode current to the current generated at the photocathode is called the *gain* G of the PMT.

The photomultiplier tube used with the present system (Thorn EMI 9863B/350) is a 14 stage tube with BeCu dynodes and an effective cathode diameter of 9 mm. Two PMT's are used in this study: tube #1 with serial #10686 and tube #2 with serial #10679. When detecting laser light of 488 nm wavelength, the quantum efficiency η of these tubes is approximately equal to 17%. The DC voltages used to accelerate the electron flow between the dynodes is externally supplied by a Thorn EMI 3000R and a Canberra 30002D high voltage power supply (HVPS). Within each tube, this voltage is divided between the various stages by an internal resistor-based voltage divider network. The maximum allowable voltage supply for each tube has been determined by the supplier to be 2181 V for tube #1 and 2075 V for tube #3. The nominal gain of these tubes at an applied voltage of 1950 V is 27×10^6. Maximum allowable anode and cathode currents are 200 μA and 30 nA, respectively.

Detection of a single photon by any of these two photomultiplier tubes results in a current pulse with a 3.5 ns rise time and a 4 ns pulse width. The transit time of the signal through the photomultiplier network is 45 ns. The rapid response characteristics of these tubes makes them suitable for photon counting applications, where, instead of merely

measuring the average anode current, individual photoelectron pulses from the PMT are counted.

Various types of error that accompany the use of photomultiplier tubes in photon counting applications include dark counts and afterpulsing. Dark counts are current pulses generated by the photomultiplier tube that are independent of the light being detected. Afterpulsing is the occurrence of secondary or satellite pulses, following an initial photopulse, that are not directly caused by incident photons .

Dark counts result both from thermally induced electron emissions from the photocathode and from the photoelectric emission of electrons that occurs when the photocathode detects Cherenkov radiation light pulses, which are caused by Cosmic rays and the decay of radioactive materials present within the window material. These electron emissions are amplified by the dynode network to resemble normal photoelectron pulses. The dark counts are, however, random and uncorrelated; therefore, they should not significantly affect the temporal variation of the photocount correlation function, which is the statistically determined form of the experimental data used to infer the dynamic properties of the scatterers.

Afterpulsing, however, is a type of detection error that does affect the photocount correlation function. Afterpulses are caused by ionization of the gases within the PMT as collisions occur between the gas molecules and the energetic electrons from the original photoelectron pulse. The afterpulse results from the impact of a gas ion with the photocathode or a dynode. Because pulses created from ions generated between the photocathode and the first dynode are amplified by the full dynode network, these afterpulses are the most significant and troublesome. In typical photomultiplier tubes afterpulses occur from 300 ns to 3 μs after the original pulse. Estimates regarding the effects of afterpulsing on the photocount correlation function, along with suggestions for correcting these effects, are given by Ford (1985).

One variation of the detection apparatus configuration that reduces the effects of afterpulsing involves utilizing a beam splitter to direct the scattered light signal into two photomultiplier tubes ([Burstyn, et al., 1980], [Phillies, 1983]). A cross-correlation function of the outputs from these two PMT's, arranged as shown in figure 3.3.3, is equivalent to the autocorrelation function from a single PMT, except that the detected signal strength at each PMT is lower and the effects of afterpulsing are significantly reduced. This reduction in the afterpulsing effects results from the fact that the afterpulses induced in one PMT exhibit virtually no correlation with the afterpulses induced in the other PMT. The only correlation that occurs between the two sources of afterpulsing results from the fact that the probability of detecting a photon (and thus the probability of the occurrence of an afterpulse) is proportional to the intensity of the incident light, which is the same for both PMT's under ideal circumstances. A housing designed for mounting two PMT's to the apparatus for cross-correlation experiments accommodates a non-polarizing dielectric cube beam splitter (Newport 05BC16NP.2) and a collection lens with a focal length of 150 mm (Oriel 41370).

Once an output of current pulses is produced by the PMT('s), the signal must be analyzed to discriminate the individual photon pulses, processed to generate the desired correlation function, and then stored. These tasks are performed by the signal processing system.

3.3.3 Signal Processing System

In order to interpret the random intensity fluctuations scattered from the cloud of flame-generated particulates, the raw data output from the photomultiplier tube(s) must be interpreted and appropriate averages of these fluctuations must be computed and stored for subsequent data analysis. The purpose of the signal processing system, which consists of a pulse amplifier/discriminator and a digital correlator that is built into a computer, is to recognize and count the occurrence of individual detected photopulses, compute an estimate of the time-based correlation function of the number of photons

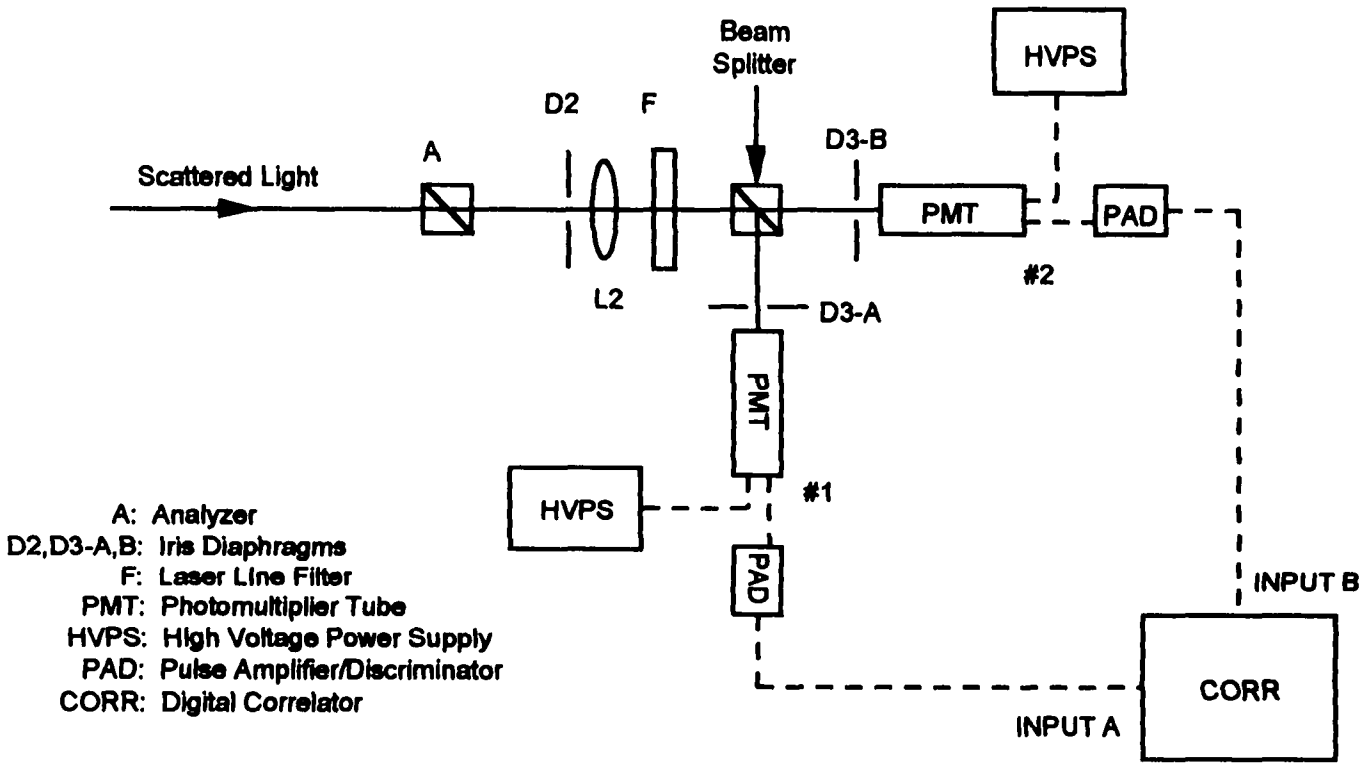

Figure 3.3.3: Schematic diagram of two-detector cross-correlation detection system.

detected during each sample time Δt, and store the values of this estimated correlation function for various delay times.

Once the photons scattered from the particle suspension are detected by the photomultiplier tube, the current pulses generated by the tube are sent to a preamplifier/discriminator PAD (Brookhaven BIC 10056). The PAD discriminates individual photopulses from the PMT by accepting any current pulse whose amplitude is larger than a certain threshold, which is set according to the gain of the PMT. Upon the detection of a photopulse, the PAD supplies a 12 ns wide TTL pulse to the digital correlator for further processing and analysis. When terminated with 50 Ω this TTL pulse has an amplitude of approximately 3.1 V.

The TTL pulses from the PAD are sent to the digital correlator, which consists of a 486DX personal computer (PC) containing a Brookhaven BI - 9000AT correlator card. The correlator reads the pulses and uses them to compute the following estimator $G(\tau_j)$ of the photon count correlation function $\langle n(0)n'(\tau_j)\rangle$:

$$G(\tau_j) = \frac{1}{N} \sum_{i=1}^{N} n_i \, n'_{i-j} \quad (j = 1, 2, 3, \ldots, M) \qquad (3.3.5)$$

where n_i is the number of photons detected from input A during sample time Δt centered at time t_i; n'_{i-j} is the number of photons detected from input B during sample time Δt centered at time $t_i - \tau_j$, where τ_j is the jth delay time; N is the number of products in the summation, which is proportional to the duration time of the experiment; and M is the number of correlator channels used in the experiment. Equation 3.3.5 defines an estimator for the cross-correlation function between two inputs: A and B. The autocorrelation function estimator is identical to the above except that both inputs are from source A, causing n'_{i-j} to be replaced by n_{i-j}. The estimator described above approaches the true photocount correlation function as N approaches infinity.

The correlator determines the time-independent baseline of the correlation function using two techniques: by averaging the correlation function values determined within a

delay time range within which the correlation function no longer exhibits a functional variation with delay time (the *measured* baseline) and by evaluating a baseline estimator using the total counts from all inputs (the *calculated* baseline). The principle governing the measured baseline determination is that at sufficiently large delay times the correlation function decays to its baseline value. Thus, the delay times for the baseline channels should be longer than the decay time of the correlation function. The principle governing the calculated baseline determination is that the baseline of a photocount correlation function is equal to the product of the average number of counts within sample time Δt from both inputs. Therefore, in the cross-correlation mode, the calculated baseline B can be estimated by the following formula:

$$B = \frac{1}{N^2}\left(\sum_{i=1}^{N} n_i \right)\left(\sum_{k=1}^{N} n'_k \right), \qquad (3.3.6)$$

where $n'_i = n_i$ when in the autocorrelation mode. In practice, the measured and calculated baselines should be within 0.1% of each other. However, when large contaminants, such as dust particles, add a slowly decaying component to the correlation function, the measured baseline could be larger than the calculated baseline. In this case, even though under normal circumstances the calculated baseline is theoretically more accurate than the measured baseline, use of the measured baseline in subsequent calculations helps correct for the effects of the large contaminants.

The Brookhaven BI - 9000AT digital correlator can provide up to 466 channels for determining the correlation function of measured photon pulses. The minimum possible sample time Δt is 25 ns, while the maximum possible sample time is 40 ms. The maximum count rate accommodated by this correlator is 40 Mcps. The delay time configuration used by this correlator can be set to either linear spacing, ratio spacing, or an arbitrarilly customized spacing determined by a delay file. In the linear mode, the delay time is an integer multiple of the sample time. In the ratio mode, the delay times are selected such that the ratio of the delay times between adjacent channels is nearly constant.

Use of the ratio mode spaces the delay time increments closer together at small delay times, where the temporal variation of the correlation function is most significant. Alternatively, the use of a delay file to customize the specific channel spacings and sample times frequently permits the measurement of the correlation function at more distinct delay times than would normally be possible with linear or ratio spacing.

By digitizing the measured optical signal prior to calculating the correlation function, the signal processing system eliminates much of the electronic noise that can contaminate analog signals. Nevertheless, the digital correlation function is not immune to errors caused by the detection and signal processing systems. The phenomena of dark counts and afterpulsing have already been discussed in relation to the photomultiplier tube. An additional possible source of error that is introduced by both the PMT and the PAD is the occurrence of a dead time following the detection of a photopulse. This dead time is a period of desensitization of the detection system, in which a reduction occurs in the probability of the detecting the presence of a second photon rapidly following an initial photon. To reduce the dead time effects on the detection of photons, the photon count rate should be selected such that the average time interval occurring between the detection of two concurrent photon pulses is greater than the system's dead time. Since the dead times of most PMT/PAD systems usually range from 10 to 50 ns, keeping the total count rate below 20 Mcps should minimize the effects of dead time on the autocorrelation function. A detailed analysis of the effects of dead time on the autocorrelation function, along with a technique for correcting the function for these effects, is given by Schatzel, et al. (1989). For a cross-correlation function formed from the output of two PMT's detecting the same scattered light (via a beam splitter) the effect of the system dead time on the correlation function is greatly reduced for the same reasons that afterpulsing effects are reduced [Schatzel, et al., 1989].

3.3.4 Optical System Adjustment

The optical system described in the previous three sections is designed to determine the time-based correlation function of the number of photons scattered into a detector from a suspension of agglomerated particles within a flame environment. In order to be able to extract meaningful dynamic properties of the particles being studied, the variable experimental parameters of the system should be adjusted to provide a small relative statistical uncertainty for the estimate of the correlation function determined by the correlator and a large magnitude for the time-dependent portion of the correlation function, which contains the useful information regarding the agglomerate dynamics. Variable system parameters requiring adjustment include the laser power, the diameters of apertures D1, D2, and D3, the scattering angle θ, and the voltage applied to the photomultiplier tubes. Additional adjustable parameters related to the operation of the correlator include the selected sample time(s) Δt, the channel spacing, the experiment duration time, and the number of correlator channels used.

Proper adjustment of these parameters requires knowledge of how they affect the relative statistical uncertainty of the measured correlation function. In addition to the systematic errors caused by afterpulsing and dead time within the detection system, random errors are also present that are governed by the statistics both of the scattered electric field and the photodetection process. These random errors result from the use of finite sample times Δt and a finite experiment duration time in the estimation of the correlation function. Theoretical considerations of the nature of these random errors and their effects on the correlation function were presented by Jakeman, Pike, and Swain (1971) and later by Saleh and Cardoso (1973).

The relative importance of the physical mechanisms governing the statistical uncertainty of the measured correlation function is determined by the average number of photons $\langle n(0) \rangle$ detected during the sample time Δt and by the magnitude of the sample time in relation to the detected electric field's coherence time τ_c ($= \Gamma^{-1}$). When $\langle n(0) \rangle \ll 1$

and $\Delta t/\tau_c \ll 1$, the uncertainty associated with the Poisson nature of the photodetection process dominates the statistical noise of the correlation function. As $\langle n(0) \rangle$ increases beyond unity the relative uncertainty associated with the photodetection process decreases to become minor in comparison to the uncertainty resulting from statistical fluctuations in the intensity of the scattered light.

Increasing $\Delta t/\tau_c$ decreases the statistical uncertainty of the correlation function because the statistical fluctuations of both the scattered field intensity and the photodetection process are increasingly averaged out by the longer sample times. Increasing $\Delta t/\tau_c$, however, also decreases the number of usable data points available for subsequent data analysis, which tends to increase the uncertainty of the inferred linewidth Γ through discretization errors. According to the theoretical investigations of Jakeman, et al. (1971), when enough correlator channels are present to insure that the entire transient range of the correlation function is measured, the decreasing photodetection errors and increasing discretization errors that occur with increasing $\Delta t/\tau_c$ balance each other when $\Delta t/\tau_c \ll 1$. At higher values of $\Delta t/\tau_c$, however, the increase in discretization errors becomes dominant and causes an increase in the uncertainty of the inferred linewidth with increasing $\Delta t/\tau_c$. Jakeman, et al. (1971) also demonstrates that the minimum error in the inferred linewidth is obtained when the entire range of measured delay times is approximately equal to 2 or 3 times the coherence time τ_c. For a linear correlator, this corresponds to $M\Delta t/\tau_c = M\Gamma\Delta t \approx 2$ or 3.

Because the most appropriate sample time Δt is usually much briefer than the coherence time τ_c and the scattered intensity in most experiments is often low enough to produce values of $\langle n(0) \rangle$ much less than unity, the statistical noise in typical DLS experiments is usually dominated by Poisson photodetection fluctuations. Under these conditions, the normalized variance of the calculated normalized correlation function $\hat{g}^{(2)}(\tau) \equiv G(\tau)/B$, as determined by Jakeman, et al. (1971) for finite-aperture detection, is

$$\frac{\mathrm{Var}\,\hat{g}^{(2)}(\tau)}{\left(g^{(2)}(\tau) - 1\right)^2} = \frac{g^{(2)}(\tau)}{\left(\langle n(0)\rangle f(A)\right)^2 N}, \tag{3.3.7}$$

where f(A) is the spatial coherence factor defined in Jakeman, Oliver, and Pike (1970); $g^{(2)}(\tau)$ is the true normalized intensity correlation function at delay time τ; and N is the number of samples measured by the correlator. The spatial coherence factor f(A) is approximately equal to 1 if the detector area A is less than a coherence area A_c and is approximately equal to A_c/A if A is greater than A_c. Though the best results are ideally obtained when the detector area is equal to one coherence area, physical limitations of the present apparatus typically limit accurate settings of the number of detected coherence areas ($N_c = A/A_c$) to values greater than 1 when obtaining measurements at finite scattering angles. Utilizing the approximation that f(A) equals A_c/A, the quantity $\langle n(0)\rangle f(A)$ is expressed as†

$$\langle n(0)\rangle f(A) = \frac{8\,\pi^4\,\rho\,\eta\,P_0\,\Delta t\,\langle|\mathbf{n}_i\cdot\alpha\cdot\mathbf{n}_f|^2\rangle}{h\,c\,\lambda\,\omega_0\sin\theta}, \tag{3.3.8}$$

where ρ is the number density of scattering particles, η is the quantum efficiency of the PMT, P_0 is the incident laser power at the scattering volume, h is Planck's constant, c is the speed of light, λ is the wavelength of the laser light, ω_0 is the spot size of the focused beam, θ is the scattering angle, $\mathbf{n}_i$ and $\mathbf{n}_f$ are unit vectors that respectively define the polarization of the incident and detected light, and α is the effective polarizability tensor of a scattering particle. Equation 3.3.8 utilizes the assumptions that the scattering angle θ is larger than the ratio of the diameter d_3 of aperture D3 to the diameter of the flame, that the scatterers are small enough relative to the wavelength λ to be considered as radiating dipoles, and that the scatterers are optically monodisperse. Comparison of equation 3.3.8 with equation 3.3.7 reveals that the relative statistical uncertainty of the measured correlation function decreases with increasing laser power, increasing particle number

† A derivation of equation 3.3.8 appears in Appendix B.

density ρ, decreasing spot size ω_0, decreasing scattering angle θ, decreasing wavelength λ, and increasing number of samples N.

Varying these parameters as indicated above increases the statistical accuracy of the measured correlation function according to equations 3.3.7 and 3.3.8. However, various physical limitations are encountered. In addition to decreasing the relative statistical uncertainty in the correlation function, increasing the laser power also increases the amount of energy absorbed by the particulates and gases in the scattering volume. This can cause a systematic error in the results by raising the temperature of the scattering volume. This effect is minimized by selecting an incident laser wavelength that does not coincide with any of the absorption bands of the combustion gases. Increasing the particle number density ρ also decreases the relative statistical noise by increasing the intensity of the scattered light. As ρ increases, however, interparticle interactions and multiple scattering effects become more significant. At sufficient levels, these effects can create difficulties in interpreting the measured data. Likewise, decreasing the spot size ω_0 and the scattering angle θ eventually causes detrimental effects by increasing the uncertainty of the scattering vector $\mathbf{q}$ [Ford, 1985]. Decreasing the wavelength λ does not directly interfere with the measurement as long as the wavelength does not coincide with any of the absorption bands of the combustion gases; however, the use of the dipole model for the scattering process becomes less valid as the wavelength becomes small with respect to length of the particle ([van de Hulst, 1981], [Bohren and Huffman, 1983], [Jackson,1975]). Finally, the number of samples N taken by the correlator, which is proportional to the total duration time of the experiment, is limited only by the logistical considerations of sustaining a steady flame for extended time periods.

In addition to the use of the theory of statistical noise as a guide in selecting the appropriate parameters for a dynamic light scattering experiment, the effect of spatial coherence of the detected light on the correlation function should be considered. For sample times Δt small compared to the coherence time τ_c of the detected light, the

autocorrelation function $\langle n(0)n(\tau)\rangle$ is related to the normalized correlation function $g^{(2)}(\tau)$ of the scattered light intensity at a point on the detector surface through equation 2.2.45 of Chapter 2, which is reproduced here:

$$\langle n(0)n(\tau)\rangle = \langle n(0)\rangle^2 \{1 + f(A) [g^{(2)}(\tau) - 1]\} + \langle n(0)\rangle u(\tau), \qquad (3.3.9)$$

where f(A) is the same spatial coherence factor mentioned in reference to equation 3.3.7 and $u(\tau)$ is a function whose value is unity at $\tau = 0$ and zero otherwise. The factor contained within the brackets, $g^{(2)}(\tau) - 1$, represents the time-dependent component of the correlation function. This time dependent component contains the information needed to extract the dynamic properties of the agglomerates under consideration. Since the other terms in equation 3.3.9 contain no useful information concerning the particle dynamics, the experiment should be adjusted to maximize the magnitude of the time dependent factor with respect to the constant terms. Therefore, experimental parameters should be adjusted to produce a large spatial coherence factor f(A).

As discussed in section 2.2.3.1 of Chapter 2, the spatial coherence factor f(A) is a factor resulting from incomplete spatial coherence between the detected intensity fluctuations at different locations on the detector surface. This factor is a function of the number of coherence areas N_c being detected. A coherence area A_c is the typical area on the detector surface within which the intensity fluctuations are correlated. The size of a coherence area depends upon the configuration of the experimental apparatus and is given by the following equation ([Forrester, et al., 1955], [Cummins and Swiney, 1970]):

$$A_c = \frac{\lambda^2}{\Omega}, \qquad (3.3.10)$$

where Ω is the solid angle seen by the detector. The number of detected coherence areas N_c is thus the ratio of the total detector area A and to coherence area A_c:

$$N_c = \frac{A}{A_c} = \frac{\pi\, d_2^2\, A_{sv}}{16\, \lambda^2\, f_2^2}, \qquad (3.3.11)$$

where A_{sv} is the area of the scattering volume as seen by the detector. For scattering angles larger than d_3/L, where L is the total optical path length through the flame, A_{sv} is approximately equal to $2\omega_0 d_3$. In this case equation 3.3.11 becomes

$$N_c = \frac{\pi \omega_0 d_2^2 d_3}{8 \lambda^2 f_2^2}. \qquad (3.3.12)$$

The functional form of f(A) was derived by Jakeman, Oliver, and Pike (1970) for scattered light conforming to Gaussian statistics from a scattering volume whose cross section, as seen by the detector, is circular. Their result is given by equation 2.2.34 of Chapter 2. This function reduces to $f(A) \cong 1$ for $N_c \ll 1$ and $f(A) \cong 1/N_c$ for $N_c \gg 1$. In practical applications the experimental parameters of the apparatus should be adjusted to provide $N_c \cong 1$. Increasing any of the apertures to detect more than one coherence area increases the average number of photons within a sample time. This, however, does not decrease the relative statistical uncertainty of the correlation function according to equation 3.3.7 because the corresponding decrease in the coherence factor f(A) offsets the increase in $\langle n(0) \rangle$. Decreasing the aperture sizes to detect less than one coherence area increases the relative statistical uncertainty of the correlation function, as given by equation 3.3.7, because for $\langle n(0) \rangle$ decreases from the smaller aperture sizes while f(A) remains relatively constant.

For the light scattering spectrometer designed for the present experiment, the apertures D2 and D3 can be closed to a minimum measurable diameter of approximately 0.6 mm. If the focal length f_2 of the collection lens L2 is 125 mm and the focused beam spot size ω_0 is 0.055 mm, then the number of detected coherence areas corresponding to $d_2 = d_3 = 0.6$ mm is approximately $N_c = 1.25$ for scattering angles θ larger than d_3/L. Similarly, when using a collection lens of focal length 150 mm (used for cross-correlation) the number of detected coherence areas corresponding to these aperture diameters is $N_c = 0.87$.

The final experimental parameter requiring adjustment is the DC voltage supplied to the photomultiplier tube(s). This voltage is divided between the dynodes within the PMT in order to accelerate the primary and secondary electron emissions at each stage of the photoelectron multiplication process. Because the number of secondary electrons emitted from each dynode is proportional to the kinetic energy of the incident electrons, increasing the DC voltage supplied to the tube increases the total gain of the tube by accelerating the intermediate electrons to higher energy levels. Therefore, for a given light flux incident upon the photocathode surface, the anode current output increases with increasing supply voltage. Increasing this voltage, however, does not increase the number of photon pulses detected by the PMT, for this quantity is determined solely by the power and wavelength of the detected light and by the quantum efficiency of the photocathode. The effect of the supply voltage in photon counting applications is to regulate the mean amplitude of the current pulses generated within the PMT by the detection of photons. Supply voltage also affects the PMT's dynamic response characteristics: increasing the supply voltage decreases the dynamic response times. The pulse amplifier/discriminator's discriminator level, which is the minimum pulse amplitude accepted by the PAD as the result of legitimate photopulse, is set according to the gain characteristics of the particular PMT being used. The discriminator levels of the Brookhaven BIC 10056 pulse amplifier/discriminators were matched by Brookhaven to the Thorn/EMI 9863B/350 photomultiplier tubes used in this experiment.

Though they are functions of the PMT supply voltage, the amplitudes of the current pulses generated by the PMT are randomly distributed. When operating the detection system using a low PMT supply voltage, most of the current pulses have amplitudes lower than the PAD's discriminator level; therefore, the photocount rate accepted by the PAD is artificially low. As the PMT supply voltage is increased, the mean amplitude of the photocurrent pulses increases, causing a larger acceptance rate. As a result, increasing the PMT voltage increases the pulse rate supplied to the correlator.

Once the PMT supply voltage is high enough to insure that most of the photopulses are accepted by the PAD, additional voltage increases do not substantially increase the pulse rate supplied to the correlator. These trends are apparent in the experimental count rate vs. PMT supply voltage for PMT #2 shown in figure 3.3.4. The ideal supply voltage setting for photon counting applications is the value at which the pulse rate supplied to the correlator becomes virtually independent of the PMT supply voltage. This voltage magnitude is subject to the maximum supply voltage constraint given by the PMT specifications. Setting the voltage at this level insures that most of the photons detected by the PMT are accepted by the PAD. Additionally, the pulse rate's virtual independence from the PMT supply voltage at this setting minimizes the effects of any voltage supply fluctuations on the experimental data. Based on the count rate vs. voltage curve depicted in figure 3.3.4, the most appropriate supply voltage for PMT #2 is approximately 1860 V. The supply voltage for PMT #1 is determined using the same technique.

The assembly of experimental apparatus described within this chapter facilitates both the generation of an aerosol of chain-like particles within a flame. The next chapter presents a set of measurements utilizing the apparatus described in this chapter to investigate the applicability of dynamic light scattering to determining the morphological parameters of flame generated agglomerates.

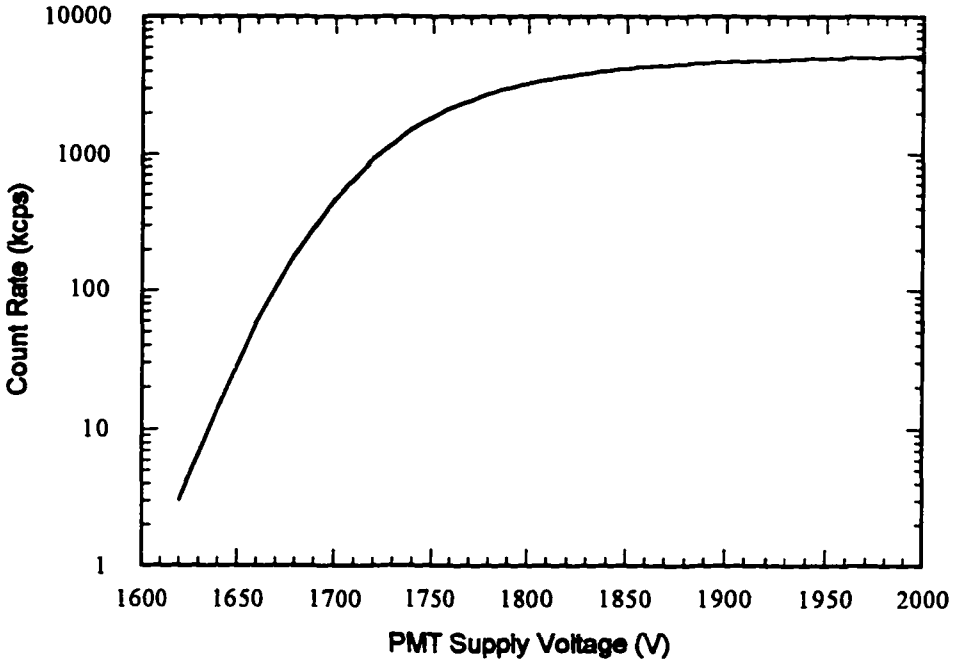

Figure 3.3.4: Experimental variation of measured count rate with PMT supply voltage for detection of a constant intensity light source.

Chapter 4

Experimental Measurements and Analysis

In order to determine the morphological parameters of flame-borne agglomerates using dynamic light scattering, the optical measurements must provide accurate information about the distribution of the agglomerates' Brownian translational and rotational diffusion coefficients. Additionally, reliable relationships between the Brownian diffusion coefficients and the agglomerates' relevant morphological parameters must be available. Once obtained, combination of the morphology-to-diffusion-coefficient relationships with the optically-obtained diffusion coefficient data can provide the density functions of the agglomerates' morphological parameters.

Even though the morphological dependencies of the Brownian diffusion coefficients of spherical and elongated (ellipsoidal) particles are well known for the continuum flow regime (as discussed in section 2.3.2), the occurrence of these particles in high temperature flames presents a special problem because the assumption of continuum flow is no longer valid. The lack of quantitative knowledge about the effect of non-continuum flow on particularly the rotational diffusion coefficient of cylindrical (or ellipsoidal) particles currently prevents the accurate inference of morphology information from DLS measurements alone.

Prior to this study, the only DLS measurements on flame systems that have been reported were performed in the polarized (VV) mode. Because chainlike agglomerates require at least two parameters, the aspect ratio A and a characteristic length D, for morphological characterization instead of the single diameter characterizing spherical particles, polarized DLS measurements alone do not provide enough information to completely characterize these agglomerates. Rotational diffusion coefficient

information obtained from depolarized (VH) DLS experiments can provide the additional information needed to close this problem.

In order to obtain more information about the Brownian diffusion coefficients, their relationship to agglomerate morphology, and their use in experimentally determining the morphology of flame-borne agglomerates from dynamic light scattering experiments, the experiments presented in this dissertation were designed to satisfy the following objectives: 1) to accurately resolve the Brownian translational and rotational diffusion coefficient (D and D_R) distributions from optical measurements, 2) to provide independently-measured morphology density functions f(a) for comparison with the diffusion coefficients, and 3) to characterize the thermodynamic state of the flame gases so that any inferred relationships between D, D_R, and a can be compared to known theoretical and empirical predictions and can alternatively be used to deduce empirical relationships between the morphology and diffusion coefficients..

The experiments conducted consist of 1) polarized and depolarized dynamic light scattering measurements from a $Fe(CO)_5$-seeded CO/O_2 diffusion flame; 2) classical depolarization ratio R_{VH} measurements; 3) thermophoretic particle extraction with subsequent transmission electron microscope (TEM) analysis; and 4) flame temperature measurements using a type S (Pt/Pt-10% Rh) thermocouple. The dynamic light scattering measurements are used to determine the relevant diffusion coefficient information of the agglomerated particulates. The classical depolarization ratio measurements provide additional information that can be used to isolate the Laplace integrals of equations 2.2.113 according to equations 2.4.6 during data analysis. The results of the optical measurements are then related to agglomerate morphology information obtained from the TEM analysis of thermophoretically-sampled particles. With the use of the measured flame temperatures and tabulated viscosity data, theoretical estimates of the diffusion coefficients are computed using the equations from section 2.3.2 of Chapter 2 for comparison with the experimental results.

The remainder of this chapter discusses in detail the procedures, analyses, and results of each of these experiments, beginning with a discussion of the experimental observations of the iron-pentacarbonyl-seeded CO/O_2 flame generated by the concentric-tube diffusion burner. The procedures and results of the temperature and ex situ agglomerate morphology measurements are then presented. Finally, the procedures and results of the optical tests are then presented and discussed in relation to the observed flame characteristics.

4.1 Experimental Flame Conditions

As mentioned in Chapter 3, the primary function of the flame in this study is to generate chainlike agglomerates in an environment suitable for testing the light scattering measurement methods under consideration. Investigations of the characteristics of a preliminary $Fe(CO)_5$-seeded CO flame considered for this study were reported by Zhang (1995). The subject of her observations was a flame generated by directing a 0.45 lpm total CO flow through the 1/4" inner diameter central tube of a concentric-tube diffusion burner and permitting it to react with the oxygen in room air. As in the current study, seeding was accomplished by bubbling a diverted portion of the CO stream through a temperature-regulated $Fe(CO)_5$ bath and recombining it with the main CO flow prior to combustion. TEM micrographs of thermophoretically-obtained samples from the central axis of this flame at heights ranging from 15 mm to 35 mm above the burner surface revealed straight chainlike agglomerates of polyhedral primary particles exhibiting polydispersity in both primary particle size and agglomerate length. The results of chemical equilibrium calculations and X-ray diffraction analyses performed in the same study both imply that the particles consist of mainly α-Fe_2O_3.

These measurements also demonstrated that the mean aspect ratio of the agglomerates increases with increasing height above the burner surface, which is consistent with theoretical expectations. Once the iron oxide particles form and cool to a temperature lower than the Neel point temperature of Fe_2O_3 (953 K [Weast, 1972]),

the magnetic domains of the antiferromagnetic iron oxide align themselves so that the magnetic moments are antiparallel. Theoretically, this should cause a zero net magnetic moment for each primary particle; however, material defects within the crystalline structure often produce a weak parasitic ferromagnetism [Neel, 1953]. Additionally, a strong possibility exists that the primary particles are so small that they consist of only a single magnetic domain [Morrish and Yu, 1955]. Either of these effects would result in a finite magnetic moment associated with each primary particle. These magnetic forces can thus cause mutual attraction between the primary particles along the direction of the magnetic moment vectors, accounting for the occurrence of chainlike agglomerates.

On the basis of the above-mentioned results, the flame studied by Zhang was deemed nearly suitable for the testing of the optical methods under consideration. This flame, however, is very sensitive to spurious air currents and tends to lean away from the vertical position at random times during the course of an experiment. In an attempt to alleviate this problem, the diameter of the flame was increased by removing the 1/4" inner fuel tube from the burner used for Zhang's investigations and replacing it with an adapter to make the 1/2" tube surrounding this fuel tube the central tube of the burner. This increase in the size of the fuel jet changed the conditions of the flame from those studied by Zhang, thus making it necessary to repeat many of the stability and extractive sampling tests previously performed on the 1/4" flame.

In an attempt to duplicate the conditions observed by Zhang as much as possible, initial tests using the modified burner were performed on a CO/room-air diffusion flame. When operated in the room-air diffusion mode the most stable configuration of this new flame was observed when the total CO flow rate was approximately 0.50 lpm. Lowering the flow rate makes the flame more sensitive to disturbances in the ambient air and raising the flow rate causes flickering instabilities in the flame. Stability tends to decrease as the honeycomb stabilizer located above the flame is raised. In order to facilitate the maximization of the depolarized scattered light

signal from the flame for the optical measurements, the stabilizer was raised to the highest point at which the flame stability was deemed acceptable so that measurements could be performed at the highest feasible height (where the longest chains are most likely to occur). This position occurs when the bottom surface of the stabilizer honeycomb is approximately 43 mm above the burner surface, permitting thermophoretic, optical, and temperature measurements at a maximum height of 35 mm.

Seeding the above-mentioned flame with iron pentacarbonyl using a carrier CO flowrate of 25 mlpm at an evaporator cylinder temperature of 23°C, thermophoretic sampling and preliminary optical measurements were performed at a height of 35 mm. TEM micrographs of the sampled agglomerates demonstrated the occurrence of chainlike agglomerates similar to those observed by Zhang (1995) and Kasper, et al. (1980); however, the results of different tests were inconclusive because of disturbances to the flame during sampling and the occasional overlapping of agglomerates on the TEM grid. Preliminary depolarized optical measurements revealed unfavorable results in that the scattered light signal was completely masked by the detection of flame emissions and was too low to establish a meaningful correlation function.

Further experimentation revealed, however, that the depolarized scattered light signal at a 35 mm measurement height increases significantly when O_2 is added to the flame through the annulus surrounding the burner's central fuel tube. Classical depolarization measurements at a 5° scattering angle demonstrated that the depolarization ratio increases from 1.6×10^{-4} ($\pm 0.4 \times 10^{-4}$) to 4.6×10^{-3} ($\pm 0.2 \times 10^{-3}$) with the addition of 0.25 lpm of O_2 to a CO/room-air diffusion flame with a CO flowrate of 0.50 lpm. Further increases were observed when the fuel flow rate was decreased lower than 0.50 lpm. Other observable effects of the addition of oxygen include an increase in the visible radiative emissions from the flame and a shortening of the total height of the flame, accompanied by an increase in flame stability. These effects are attributed to the more intense combustion caused by the addition of pure

oxygen to the flame. The enhanced combustion causes higher temperatures at the flame front, resulting in higher reaction rates and a faster flame speed. The occurrence of these effects account for the observed shortening of the flame height. The increased visible flame emissions result from the increase in temperature of the condensed solids at the flame front in accordance with Planck's law of thermal radiation [Incropera and DeWitt, 1985].

One possible mechanism for explaining the detection of an increased depolarized scattered light signal under these conditions is that the enhanced reaction causes most of the iron pentacarbonyl to decompose and oxidize at a lower height than it would in the room-air diffusion flame. The more rapid combustion and enhanced radiative heat transfer away from the flame produces more rapid cooling of the particles as they are propelled upward by the flame gases, a speculation confirmed by noting that the flame temperature measured at a 35 mm height decreases when oxygen is added to a CO/air diffusion flame. This early cooling permits the formation of the magnetic moments by the primary particles at an earlier stage and gives the particles more time to agglomerate into chains before reaching the 35 mm height.

As a result of the tests described above, the flame generated using the flowrates and conditions shown in table 4.1.1 was chosen as the primary subject for subsequent optical, morphological, and temperature measurements. In order to aid repeatability, the evaporator cylinder temperature was elevated to 308 K so that it temperature could be accurately regulated using an electric heating tape coupled to a temperature controller. The observable features of the resulting flame structure are depicted in figure 4.1.1.

The combustion zone of the unseeded flame forms a luminous rounded cone whose top is approximately 5 mm above the burner surface. A conical region of luminous gases extends beyond this point up to about 15 mm. A slight border (not visible in the photograph) surrounds the edge of the main cone, which appears to be the result of residual iron pentacarbonyl deposits from within the fuel supply tube.

Table 4.1.1: Experimental parameters defining the investigated seeded flame

CO Flowrate:	0.35 lpm
Carrier CO Flowrate:	8 mlpm
O_2 Flowrate:	0.25 lpm
Evaporator Cylinder Temperature:	308 K
Stabilizer height:	43 mm

When seeded with iron pentacarbonyl, the intensity of the visible emissions from the flame increases dramatically. The shape of the flame front apparently remains nearly identical to the unseeded flame; however, a thin, tapered stream of bright gases forms downstream of the combustion front and extends nearly to the lower surface of the honeycomb stabilizer. The intense emissions from this gas stream is most likely thermal radiation from the Fe_2O_3 particles within the flow. The external border seen in the unseeded flame becomes more prominent when the flame is seeded. Additionally, the scattering of laser light at a height of 35 mm (visible in figure 4.4.1 (b)) reveals the presence of scattering particles in both the central vertical gas stream and the external border. At the scattering position shown, the flame gas/particle mixture is still visibly luminous, even though the photograph appears dark in the specified region. At this position, a classical depolarization ratio of 0.9×10^{-2} ($\pm 0.1 \times 10^{-2}$) was measured at a 5° scattering angle, implying that the agglomerates present exhibit an optical anisotropy stronger than those in the other cases considered.

Additional observations of this flame revealed that the cells of the honeycomb stabilizer become significantly clogged after approximately 5 minutes of flame operation. This honeycomb clogging is accompanied by noticeable deposits on the top of the burner's central fuel tube. This effect imposes a 5 minute limitation on any experiment, after which the flame must be extinguished and the burner and honeycomb

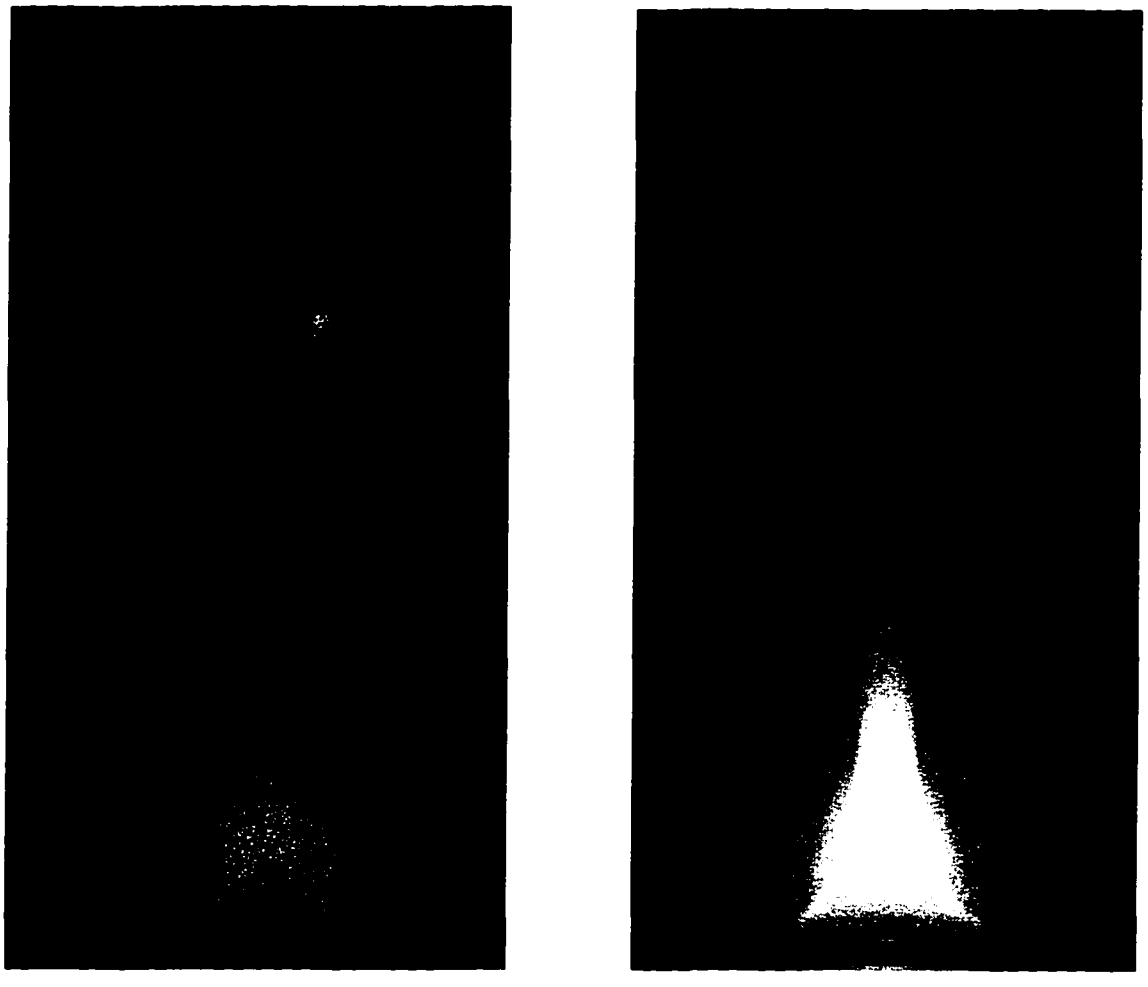

(a) (b)

Figure 4.1.1: CO/O_2 diffusion flames generated using the conditions given by table 4.1.1: a) unseeded; b) seeded with $Fe(CO)_5$.

cleaned. After running the flame several times, a noticeable black deposit forms within the central fuel tube beginning approximately 1 cm below the tube's opening and extending nearly 2 cm into the burner tube. This deposit, which can apparently only be removed with vigorous filing, appears to be the same material that clogged the flat-flame diffusion burner described in Appendix A.

In order to provide more information about the flame under consideration for interpretation of the optical measurements that follow, temperature and agglomerate morphology measurements were made at four different heights (25 mm, 30 mm, 32.5 mm, and 35 mm) along the flame's central axis. The methods and results of these measurements are discussed in the following section.

4.1.1 Measurement of Flame Temperature

In order to determine theoretical estimates of the Brownian translational and rotational diffusion coefficients using equations 2.3.11 to 2.3.15 for comparison with the optical results, the temperature and viscosity of the flame gases within the optical scattering volume at each measurement location is required. The approach used in this study was to measure the flame temperature at the appropriate locations and determine the viscosity from published tables corresponding to this temperature. Because the gas temperatures within concentric-tube diffusion flames exhibit large gradients (up to 228 K/mm in the tested CO/air diffusion flame used by Zhang (1995)), care must be taken to measure the *local* temperature within the scattering volume. The most direct method of performing this measurement is through the use of a high temperature thermocouple, correcting the measured temperature for the effects of radiation heat transfer between the thermocouple and its surroundings. Thus, temperature measurements were performed using a type S (Pt/Pt-10% Rh) thermocouple, which can accommodate temperatures up to 1723 K [Omega Engineering, Inc., 1989].

4.1.1.1 Correction of Flame Temperature Measurements for Radiative Losses

Proper interpretation of the results of thermocouple measurements from flames requires consideration of the effect of radiation heat transfer between the thermocouple and its surroundings. During a temperature measurement, the thermocouple is inserted within the high temperature flame gases. Ideally, forced convection heat transfer between the thermocouple and the flame gases should elevate the thermocouple's temperature to that of the flame gases once steady state conditions occur. Interpretation of the voltage produced by the thermocouple using type S calibration data would thus reveal the thermocouple's temperature and, henceforth, the flame gas temperature. In reality, however, heat transfer also occurs between the thermocouple and the external room walls. This radiative heat transfer maintains the equilibrium thermocouple temperature at a magnitude less than the true flame gas temperature and would thus produce an underestimation of the true flame temperature if the radiative effects were neglected.

This effect can be quantified by applying the energy conservation principle to the 0.2 mm diameter welded bead at the tip of the thermocouple, where the dissimilar metals of the thermocouple are joined. Neglecting conduction through the thermocouple wires, the energy convected to the thermocouple from the flame gases, $hA(T_f - T)$, is equal to the net radiative energy exchange between the thermocouple bead and its room temperature surroundings, $\sigma\varepsilon A(T^4 - T_{surr}^4)$. Solving for the flame temperature T_f thus gives

$$T_f = T + \frac{\sigma\varepsilon}{h}(T^4 - T_{surr}^4), \qquad (4.1.1)$$

where T is the absolute temperature of the thermocouple, σ is the Stefan-Boltzmann constant ($= 5.67051 \times 10^{-8}$ W/(m^2·K^4)), ε is the emissivity of the thermocouple bead's surface, h is the convection heat transfer coefficient between the thermocouple and the

flame gases, and T_{surr} is the absolute temperature of the radiative surroundings, which is taken to be room temperature (≈ 298 K).

Evaluation of the radiation correction given by equation 4.1.1 generally requires an iterative solution because the convection heat transfer coefficient h is a function of T_f, which is approximately given by the correlation [Incropera and DeWitt, 1985]

$$h = \frac{k_g}{d}\left[2.0 + 0.60\, Pr_g^{1/3}\left(\frac{V\, d_t}{\nu_g}\right)\right], \qquad (4.1.2)$$

where k_g, Pr_g, and ν_g, are the thermal conductivity, Prandtl number, and kinematic viscosity of the flame gases at the film temperature $(T_f + T)/2$, V is the flame velocity in the neighborhood of the thermocouple, and d_t is the diameter of the thermocouple bead. Equation 4.1.2 is valid for forced convection heat transfer from a sphere within the Reynolds number range $1 < Vd_t/\nu_g < 70{,}000$.

In addition to the heat transfer coefficient h, knowledge of the thermocouple's surface emissivity ε is required in order to evaluate the radiation-corrected flame temperature given by equation 4.1.1. In most cases, the best emissivity to use for this calculation would be one approximating the emissivity of the platinum-rhodium alloy making up the thermocouple. When used in the current flame, however, the thermocouple is rapidly coated with a layer of iron oxide that apparently increases the thermocouple's emissivity higher than that of the uncoated surface. Experimental evidence of this was observed during the first use of the thermocouple in the flame. Upon initial insertion into the flame, the thermocouple produced a voltage that steadily increased until a peak steady state value was reached. After a brief period of exposure to the flame the voltage output dropped and regained steady-state conditions at a distinctly lower value. Visual inspection of the thermocouple after retraction from the flame revealed a reddish orange deposit on the thermocouple bead, which indicates the presence of iron oxide. Noting that the emissivity used for radiation corrections for thermocouples in previous studies is $\varepsilon = 0.2$ [Seshadri and Rosner, 1984] and that the

reported emissivity of oxidized iron (at 1200°C) is $\varepsilon = 0.89$ [Weast, 1972], the most likely explanation of the observed voltage changes is that deposition increased the surface emissivity of the thermocouple from the lower emissivity of the bare thermocouple to the higher emissivity of the coating material, iron oxide. Thus, upon insertion, the thermocouple temperature increased until steady state at the uncoated emissivity was obtained. As a layer of iron oxide deposited upon the thermocouple bead, the emissivity increased, causing the rate of radiative heat transfer away from the thermocouple to increase. This increased rate of radiative heat transfer lowered the steady-state temperature of the thermocouple.

The results of the flame temperature measurements from the flame described by table 4.1.1 are presented in table 4.1.2. These measurements were obtained from the post-flame region extending from 25 mm to 35 mm above the burner surface. Within this region, the approximately 2.5 mm diameter stream of combustion gases is easily disturbed by anomalous air currents in a manner similar to the flame presented by Zhang (1995). Thus, the thermocouple temperature often varied within a 50 K to 100 K range as the flow direction of the stream of flame gases fluctuated due to air disturbances. The temperatures reported in table 4.1.2, which represent the highest temperature obtained at each location, exhibit no systematic variation with height and appear to be relatively constant with respect to height within an estimated experimental error of ± 50 K. A comparison of the mean uncorrected temperature of 1032 K to the mean radiation-corrected temperature of 1134 K demonstrates that the flame temperature would be underestimated by approximately 100 K if radiation effects were not considered. For the purposes of all subsequent analyses requiring flame temperature information, the temperature between 25 mm and 35 mm above the burner surface is taken to be 1134 K, which is the height-averaged radiation-corrected temperature for this region of the studied flame.

Table 4.1.2: Results of Flame Temperature Measurements

Height (mm)	Uncorrected	Radiation Corrected
25 mm	1023 K	1122 K
30 mm	1051 K	1159 K
32.5 mm	1014 K	1110 K
35 mm	1040 K	1144 K
Mean	1032 K	1134 K
Standard Deviation	17 K	22 K

4.1.2 Measurement and Analysis of Agglomerate Morphology Using Thermophoretic Sampling

With the measurement of the flame temperatures within the investigated region of the seeded CO/O_2 flame, along with the availability of published thermophysical property data, the thermophysical properties of the flame gases affecting the flame-borne agglomerates' Brownian diffusion coefficients are essentially determined. In addition to the thermophysical properties of the flame gases, however, the Brownian translational and rotational diffusion coefficients are also functions of the morphological parameters of the agglomerates being studied, a fact that makes the extraction of morphological properties from measured diffusion coefficient data feasible. In order to obtain information about the morphological properties of the agglomerates for comparison with optically obtained Brownian diffusion coefficients, the agglomerates were thermophoretically sampled at the four measurement heights of 25 mm, 30 mm, 32.5 mm, and 35 mm and photographed using a transmission electron microscope. Some observations and results of these measurements are presented in the

next section, followed by a statistical analysis of the morphological properties of the sampled agglomerates.

4.1.2.1 Thermophoretic Sampling Experiments

As described in Section 3.2 of Chapter 3, thermophoretic sampling is based upon the principle in which temperature gradients within a gas drives suspended particles towards the cooler zones because of a momentum imbalance between the gas molecules impacting the particle from the hot side and the gas molecules impacting the particle from the cool side. Thus, the insertion of a room-temperature plate into a hot flame causes some of the solid particles within the flame to thermophoretically deposit onto a TEM grid attached to the plate. For the current investigations, this technique was used to sample the agglomerates in the iron-pentacarbonyl-seeded CO/O_2 flame because it represents one of the most accurate ex situ sampling techniques available for morphological studies ([Dobbins and Megaridis, 1987], [Zhang, 1995]).

In applying the thermophoretic sampling technique to the flame under consideration, one difficulty encountered was that the 2.5 mm diameter stream of flame gases containing the agglomerates is easily disturbed by anomalous air currents. During sampling, the rapid motion of the probe actuator mechanism causes air disturbances that tends to push the flame away from the probe. One remedy for this effect described by Zhang (1995) is to place a slotted metal plate between the probe actuator and the flame to act as a shield against the air disturbances produced by the actuator motion.

Experimentation with the configuration of the sampling mechanism conducted during the current study has qualitatively indicated that the position of this slotted shield relative to the probe and the flame influences its effectiveness in preventing flame disturbances. Generally, the closer the shield is to the flame, the more effective it is at shielding the flame from disturbances. This is probably because air currents are produced not only by the motion of the probe's actuator but also by the motion of the probe strip itself as a result of the viscous shear forces exerted on the air as the probe

strip moves towards the flame. By positioning the shield as close to the flame as possible without distorting the flame's flow field, the shield blocks all of the viscous-shear-induced motion occurring behind the shield, allowing only the disturbances caused by the portion of the probe that extends through the shield (plus some leakage) to affect the flame. When obtaining the thermophoretic samples reported in this dissertation, the shield was positioned approximately 15 mm from the outer edge of the burner's fuel tube.

A second factor affecting the accuracy of thermophoretic samples is the number density of particles collected on the TEM grid, which is partially determined by the *sample time* that the probe is exposed to the particle-laden flame gases and the number density of agglomerates within the flame at the sampled location. In the system used for this study, the sample time is controlled by an adjustable parameter in the Omega WB - AAI - SE data acquisition and control software called the *low duration*, which is the amount of time that the probe actuator's solenoid control valve is energized once activated. When the solenoid is energized, the probe begins its 3" travel towards the flame. Based on the 0.86 m/s travel speed determined by Zhang (1995) for a supply air pressure of 40 psi, the probe requires approximately 89 ms to reach the end of its travel. The probe remains extended until the solenoid control valve is deenergized at the termination of the low duration. The sample time is thus approximately equal to the low duration time minus the 89 ms travel time.

Excessively high sample times can cause the collection of so many agglomerates that they overlap on the TEM grid and thus obscure the morphological characteristics of the individual agglomerates. Also, additional agglomeration can conceivably occur on the TEM grid itself during sampling if the proximity of neighboring agglomerates is close enough to allow the trajectories of depositing agglomerates to be influenced by the magnetic fields of captured agglomerates. The increased number density of agglomerates on the TEM grid resulting from long sample times increases the

likelihood of this effect. Some evidence of this effect was observed in samples obtained from a room-air diffusion flame generated using a 0.50 lpm CO flow in conjunction with a 25 mlpm carrier CO flow at a 23°C evaporator temperature. Even though classical depolarization optical measurements from the flame yielded depolarization ratios of only 1.6×10^{-4} ($\pm 0.4 \times 10^{-4}$), agglomerates thermophoretically sampled using a sample time of 111 ms revealed long chainlike (sometimes branched) agglomerates that were considerably longer than those obtained using shorter sample times. Because of the inconsistency between the thermophoretic results obtained using different sample times from this flame and the unsuitability of the scattered optical signal for depolarized DLS tests, no quantitative analysis was performed on the above-mentioned samples.

Another effect observed from preliminary thermophoretic samples is an occasional tendency of straight chainlike agglomerates to deposit onto the TEM grid aligned in a single direction, which is contrary to expectations that their orientations would be randomly distributed due to the randomizing nature of Brownian forces within the flame. The exact cause of this alignment is unknown. Due to a possibility that this alignment is caused by the generation of a magnetic field by rapidly inserting the conductive stainless steel probes into the ionized flame gases, the stainless steel probes were replaced with nonconductive glass plates prior to obtaining the thermophoretic samples presented later in this dissertation. The agglomerate alignment occasionally noted when using stainless steel probes did not occur when using glass probes. Since the use of glass probes was only recently implemented and the aligning effect did not always occur when stainless steel probes were used, no definite conclusions can be made about the cause of the aligning effect at this time.

Upon consideration of the effects discussed in the previous paragraphs, thermophoretic samples of the agglomerates from the flame generated by the conditions presented in table 4.1.1 were obtained using reinforced glass probes with sample times ranging from 30 ms to 111 ms (low durations from 125 ms to 200 ms). Under these

flame conditions, the optimum sample time was observed to be approximately 71 ms (low duration = 160 ms) based upon visual inspections of the degree of overlapping and the approximate number density of agglomerates present on each TEM grid. As mentioned previously, the slotted plate used for shielding the flame from probe and actuator-induced air currents was placed approximately 15 mm from the outer edge of the burner's central fuel tube. Examples of the resulting TEM images are depicted in figure 4.1.2, which reveals the presence of polydisperse chainlike agglomerates similar to those observed by Kasper, et al. (1980) and Zhang (1995). The agglomerates in this figure were obtained from the flame's central axis at a height of 35 mm. The close-up of a single agglomerate shown in figure 4.1.2 (b) clearly depicts the polyhedral shape of the primary particles.

4.1.2.2 Morphological Analysis of Thermophoretically Sampled Agglomerates

In order to utilize the results obtained from thermophoretic sampling for numerical comparisons or combinations with data obtained from other experiments, the morphological properties of the sampled agglomerates are first quantified. This process involves choosing a set of properties or dimensions $\mathbf{a}$ that sufficiently characterizes the morphology of each agglomerate, measuring these properties for each sampled agglomerate, and determining the statistics of these measured properties.

In the simplest scenario of a suspension of spherical particles, only one morphological parameter, the particle diameter, would be needed to completely characterize its morphology. The most applicable statistical representation of the morphology of a set of polydisperse spheres would thus be the probability density function of the spheres' diameters or radii. For agglomerated structures, however, the choice of morphological parameters is less obvious because the morphology depends not only on the diameters of the primary particles, but the number and positions of the primary particles relative to each other within each agglomerate.

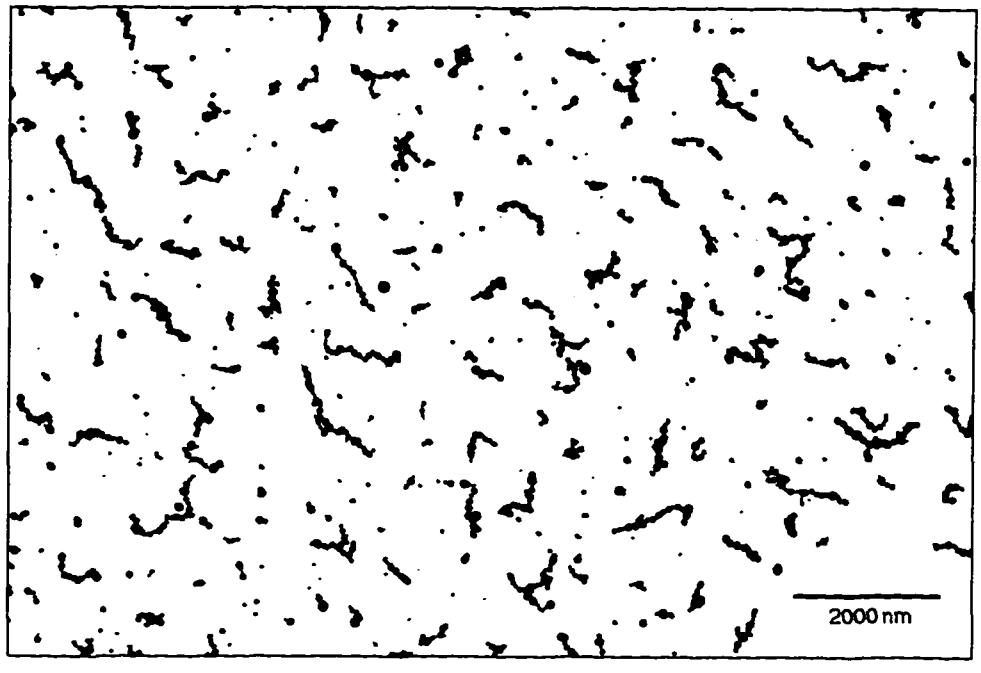

(a)

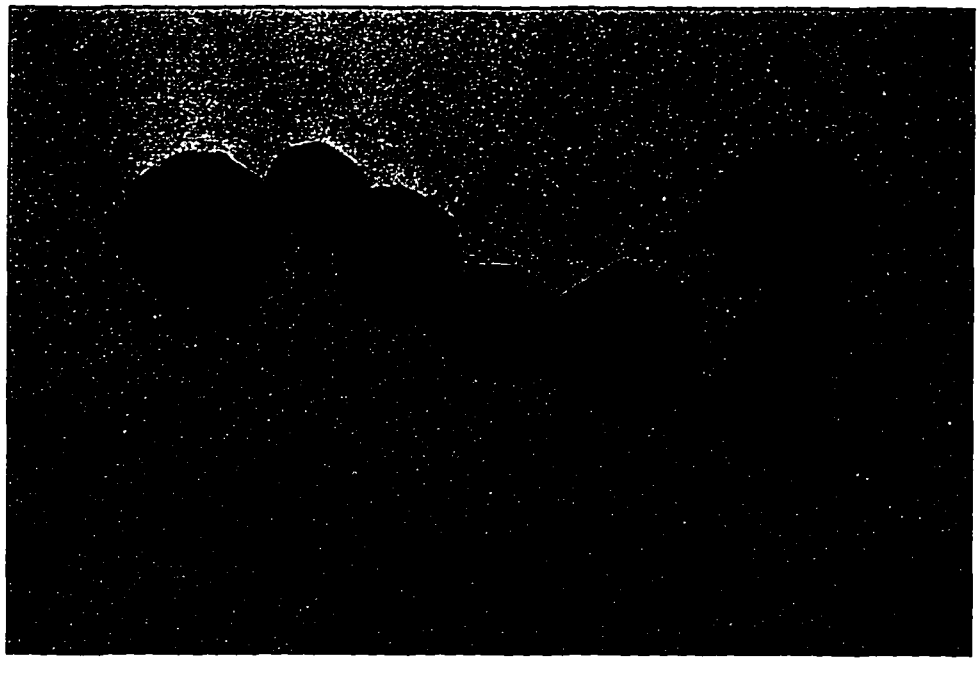

(b)

Figure 4.1.2: TEM images of agglomerates thermophoretically sampled from the $Fe(CO)_5$-seeded CO/O_2 diffusion flame of table 4.1.1.

For agglomerates consisting of perfectly straight chains of monodisperse spherical particles, an obvious choice of morphological parameters would be the number of particles per agglomerate and the diameter of the constituent primary particles or an equivalent variation of this pairing. The agglomerates obtained from the iron-pentacarbonyl-seeded CO/O_2 flame pictured in figure 4.1.2 are approximately straight chains; however, some curvature and branching is clearly exhibited by many of the agglomerates. Thus, the above morphological parameters given for straight chains of monodisperse primary particles fail to precisely represent the actual agglomerates obtained from the flame. By limiting the selection of investigated morphological parameters to anything less than the precise dimensions and relative positions of each primary particle within each agglomerate, some morphological information is lost. Therefore, the selection of morphological parameters to be considered must be consistent with the effects being studied. In almost all of the previous DLS flame studies reviewed in Chapter 1, the particulate morphologies were characterized by a single dimension: the diameter of a volume-equivalent sphere. Since a major objective of this study is to extend the use of dynamic light scattering in flames to particles exhibiting a geometric and effective optical anisotropy so that aspect ratio and rotational diffusion information can be obtained, the volume-equivalent sphere representation alone provides insufficient information about the agglomerate morphology. For this study the modeled particles must at least have one characteristic size and an aspect ratio.

The simplest mathematical representation of a three dimensional shape exhibiting both a characteristic size and aspect ratio is the prolate ellipsoid (pictured in figure 2.3.1), which is characterized by two independent morphological parameters: the major axis length 2a and the minor axis length 2b. The mathematical models relating effective optical polarizabilities and Brownian diffusion coefficients to particulate morphology presented in Section 2.3 indeed assume that the particles are prolate

ellipsoids. Thus, the minor axis length and aspect ratio of an ellipsoid fitted to the agglomerate shape are the morphological parameters chosen for this study.

In order to measure the morphological properties of the thermophoretically sampled agglomerates and determine the dimensions of the ellipsoid that best represents each agglomerate, TEM micrographs of the sampled agglomerates were electronically scanned using a Microtek ScanMaker E6 standard flatbed scanner and analyzed on a Gateway 2000 P5-76 pentium computer using the public domain NIH Image program (developed at the U.S. National Institutes of Health and available on the internet at http://rsb.info.nih.gov/nih-image/). The execution of this Macintosh-only program on the PC platform was made possible by use the Macintosh emulator program Executor 2 by ARDI (http://www.ardi.com).

The NIH Image program determines a best-fitting ellipse for each agglomerate pictured in a two-dimensional scanned image and outputs the lengths of the major and minor axes within a tab-delimeted text file, which can imported into any standard spread sheet program such as Kaleidagraph, Excel, or Lotus 1-2-3. This "best-fitting" ellipse is determined within the NIH Image program using the procedures that follow [Rodieck]. After the image of the agglomerates is scanned and properly processed, the NIH Image program analyzes the brightness values of each pixel to determine the closed contour outlining each agglomerate. Next, the second moments about the centroid of an assumed uniform distribution within each outlining contour is determined and an ellipse is found whose second moments match those of the agglomerate shape (see Cramer (1946) for details about this procedure). The resulting major and minor axis lengths are then rescaled using a common scaling factor to force the area within the fitted ellipse to match the area within the contour outlining the agglomerate. The resulting scaled axis lengths are output by NIH Image as those of the best-fitting ellipse.

In analyzing a typical TEM micrograph of agglomerates, the micrograph is first scanned directly from its negative as a 256 greyscale image at 600 dpi, which is the

maximum optical resolution of the Microtek scanner. The scanning software is then used to trim the edges off the image so that only agglomerates are visible within the scanned image, which is then saved as an uncompressed tagged image format (TIFF) file. This TIFF file is then imported into the NIH Image program for analysis.

Knowledge of the magnification of the original TEM negative and the scanning resolution of 600 dots per inch permits a determination of the distance in nanometers of the unmagnified image that is represented by a single pixel. This information is entered into NIH Image as a scaling factor to be used in its measurements. In generating TEM micrographs for this study, the agglomerate sizes were magnified either 6600 times, which corresponds to a 6.41 nm/pixel scaling factor, or 8300 times, which corresponds to a 5.10 nm/pixel scaling factor.

Once the TIFF image is loaded into NIH Image and the scaling factor set, the image is density-sliced. Density-slicing essentially permits the user to tell NIH Image which brightness values represent the particles being analyzed and which brightness values belong to the image's background. Once the density-slicing is satisfactorily completed, the program can proceed to analyze each of the particles within the image to determine the dimensions of the best fitting ellipse for each agglomerate. The output of the particle analysis routine is a table listing the lengths of the major and minor axes of the best-fit ellipses of all agglomerates in the scanned image, which can be saved as text and imported into other software so that a statistical analysis can be performed.

For any set of continuous random variables, such as the major and minor axis lengths of the ellipsoidal representation of the agglomerates, the joint probability density function [Ross, 1988] provides the most complete representation of the variables' statistical properties. To estimate the probability density functions (PDF's) of the agglomerates' morphological parameters using the measurements obtained from the TEM micrographs, the total range of each morphological parameter is subdivided into discrete regions. A histogram is next generated by counting the number of particles

whose dimensions occur within each region. This histogram is then normalized into an approximation of a probability density function by dividing the particle count for each region by the region's area and the total number of agglomerates considered. In the current study, two-variable PDF's were generated using a QBASIC program called DENSITY.BAS, which was developed for this research, and single-variable PDF's were calculated using the commercial Macintosh program Kaliedagraph by Abelbeck.

The estimated joint probability density function f(2a, 2b) of the major and minor axes of agglomerates thermophoretically sampled from the flame defined by table 4.1.1 at a height of 35 mm is shown in figure 4.1.3. According to this figure, most of the particulate matter apparently occurs as singlets, having both major and minor axes nearly equal and within the size range of 100 nm or less. The elongation of the probability density function in the direction of the axis representing the major axis length statistically demonstrates the geometric anisotropy of the sampled agglomerates. The joint probability density functions generated for agglomerates sampled at heights of 25 mm, 30 mm, and 32.5 mm exhibited identical trends. The three-dimensional representations of these PDF's are virtually indistinguishable from the 35 mm case presented in figure 4.1.3.

Figures 4.1.4 to 4.1.6 compare the major axis length, minor axis length, and aspect ratio PDF's for each sampled height. The major axis density function reaches a maximum at approximately 50 nm and is skewed towards the larger lengths. The minor axis length density function also reaches its peak at approximately 50 nm, but its skewness is much less drastic than the major axis PDF. Noting that the minor axis length of an ellipsoidal fit of a straight chain agglomerate is an approximate representation of the agglomerate's primary particle diameter, the minor axis distribution is directly comparable to the results of Zhang (1995), who also obtained a maximum percentage of primary particles with diameters of approximately 50 nm from a seeded 1/4" CO/air diffusion flame.

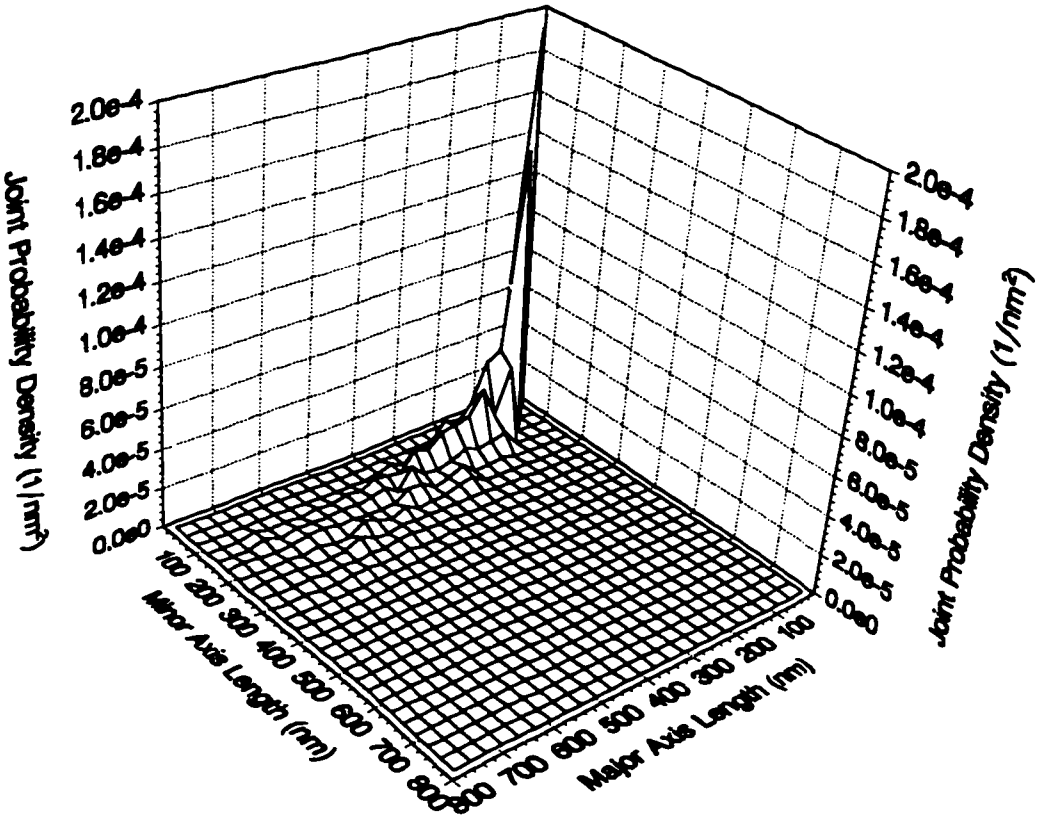

Figure 4.1.3: Joint probability density function of the major and minor axis lengths of ellipses fitted to agglomerates thermophoretically sampled 35 mm above the burner surface.

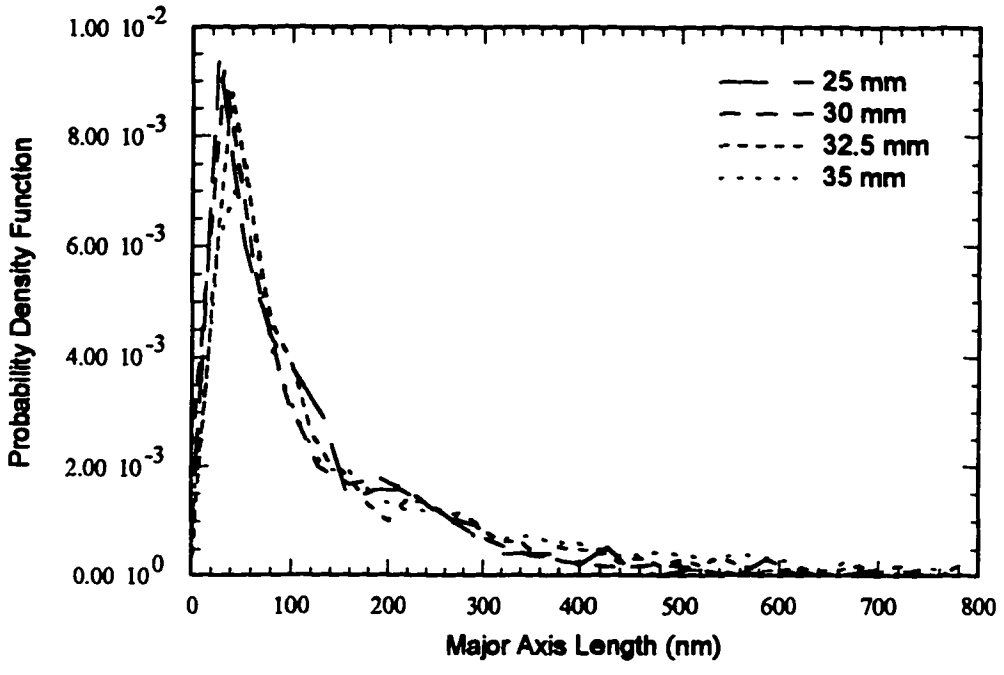

Figure 4.1.4: Probability density functions of the major axis lengths of ellipses fitted to thermophoretically-sampled agglomerates at various heights.

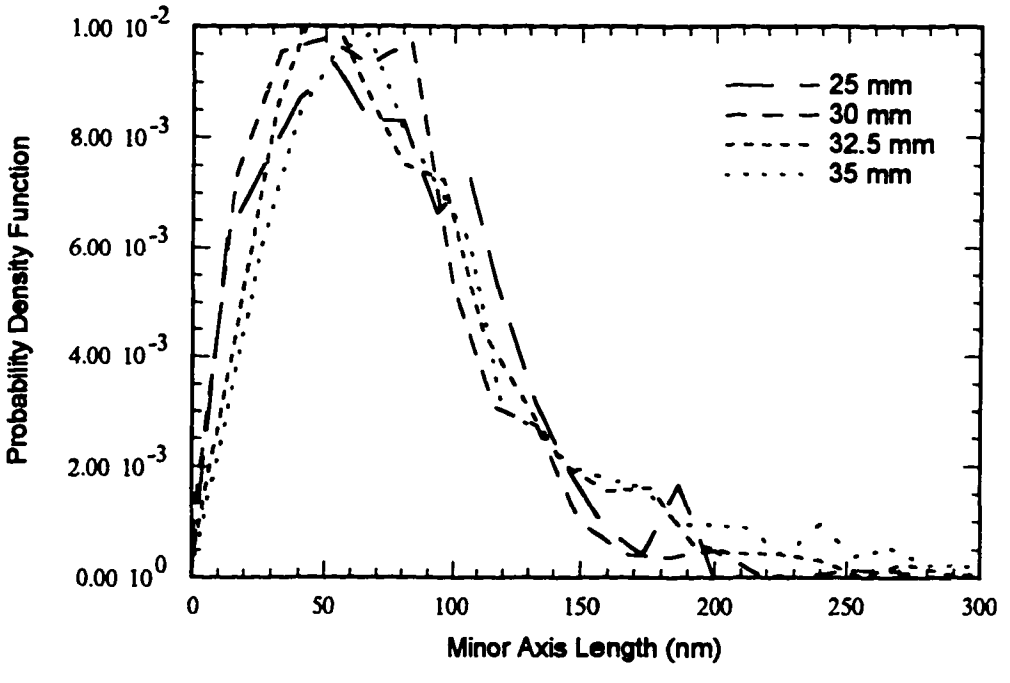

Figure 4.1.5: Probability density functions of the minor axis lengths of ellipses fitted to thermophoretically-sampled agglomerates at various heights.

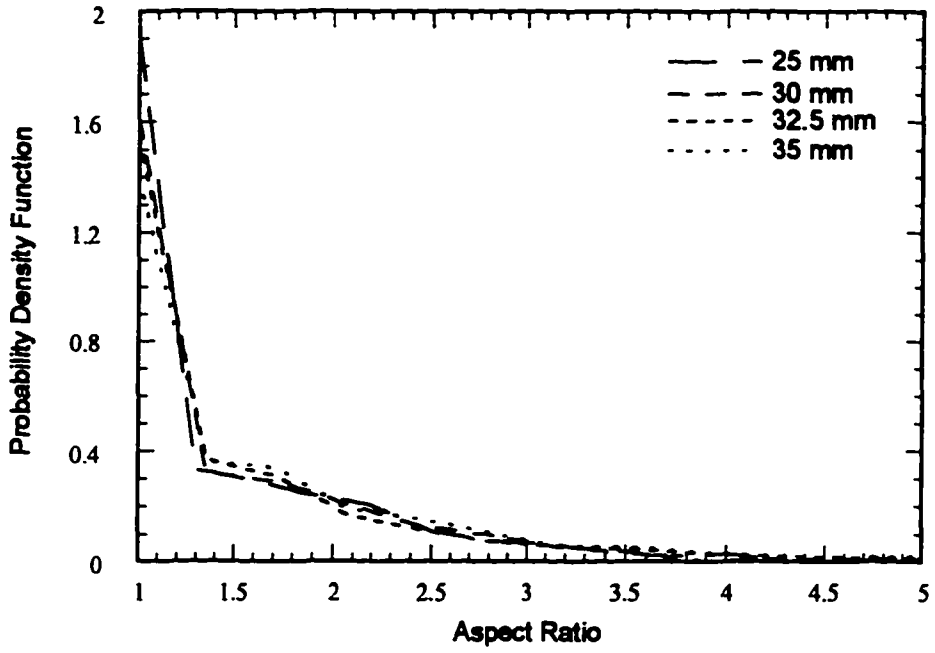

Figure 4.1.6: Probability density functions of the aspect ratios of ellipses fitted to thermophoretically-sampled agglomerates at various heights.

In combining the major axis and minor axis measurements for each particle, the aspect ratio density functions plotted in figure 4.1.6 confirm that most of the particulates occur as singlets under the sampling conditions. Furthermore, the aspect ratio PDF decreases monotonically with increasing aspect ratio at all heights tested. One notable trend exhibited by figure 4.1.6 is that the PDF value at an aspect ratio of unity decreases with increasing measurement height, indicating that smaller fractions of singlets were obtained at greater heights above the burner surface.

In order to more clearly determine how the morphological parameters of the sampled agglomerates vary with height, the mean major and minor axis lengths and aspect ratios are plotted versus height in figures 4.1.7, 4.1.8, and 4.1.9. These means were computed by summing the appropriate axis lengths (or aspect ratios) of all agglomerates and dividing the result by the total number of measured agglomerates. The error bars depict the standard error of each value, which represents the uncertainty

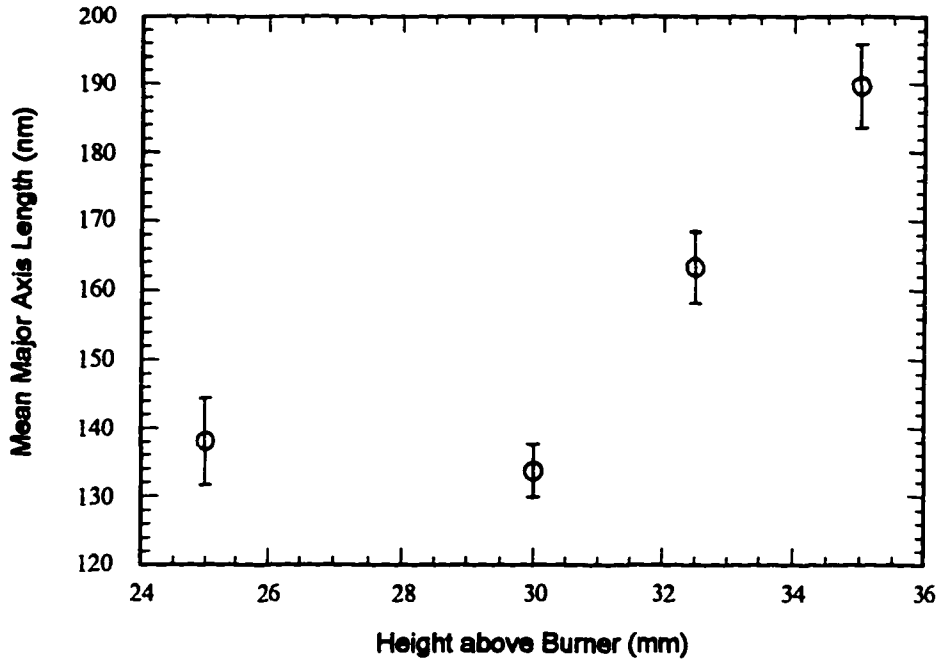

Figure 4.1.7: Mean minor axis length of ellipses fitted to thermophoretically-sampled agglomerates as a function of measurement height.

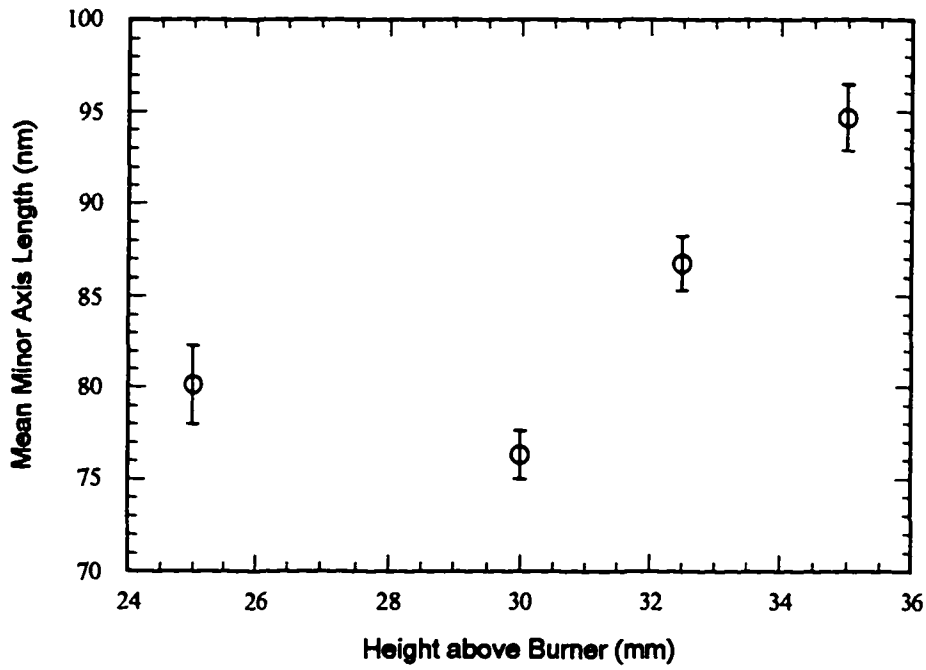

Figure 4.1.8: Mean minor axis length of ellipses fitted to thermophoretically-sampled agglomerates as a function of measurement height.

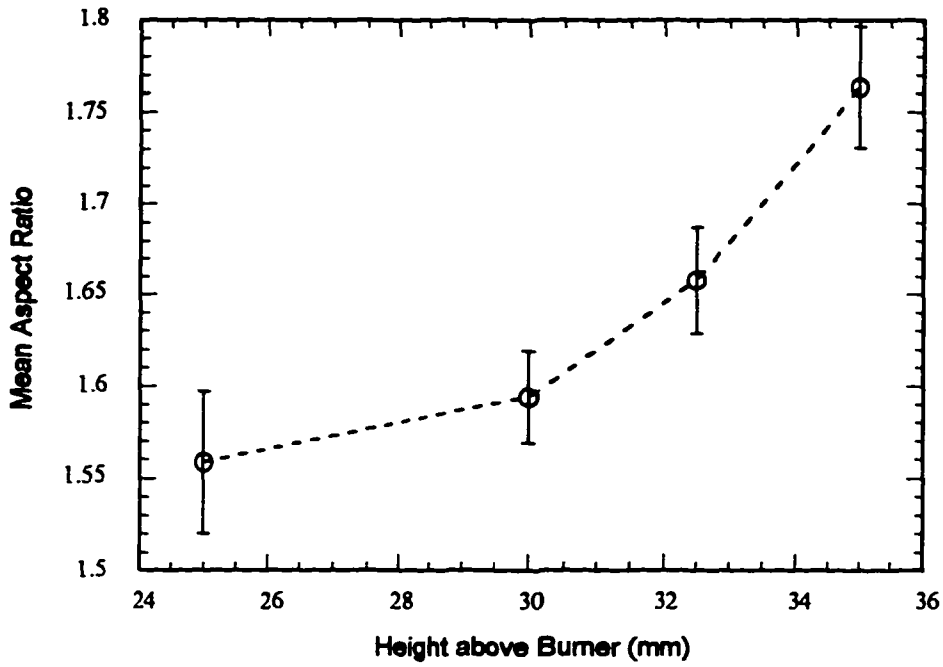

Figure 4.1.9: Mean aspect ratio of ellipses fitted to thermophoretically-sampled agglomerates as a function of measurement height.

of the mean value shown. The variations of both the mean major axis length and mean minor axis length with height exhibit nearly identical trends in that they both decrease slightly between heights of 25 mm and 30 mm and increase as height increases from 30 mm to 35 mm. This decrease in value between 25 mm and 30 mm is not shared by the mean aspect ratio, which increases continuously from 1.56 at 25 mm to 1.76 at 35 mm.

The fact that the mean major and minor axes both exhibit similar trends as functions of height may be partially attributable to the fact that the minor axes of the best-fit ellipses tend to be larger when the major axes are large because the agglomerate chains are rarely perfectly straight. Thus, any approximation of the minor axis length as being equivalent to the agglomerate's primary particle diameter is generally invalid when applied to long chains.

With the experimental determination of both the morphological distributions of the thermophoretically sampled agglomerates and the corresponding flame temperatures at heights ranging from 25 mm to 35 mm, the properties of the particle-laden flame gases are sufficiently determined for use in theoretical estimations of Brownian diffusion coefficients to compare with the results of optical experiments. The next section presents the methodology and results of these optical experiments and concludes with a comparison between the optical results and theoretically-estimated Brownian diffusion coefficients computed using the morphology and temperature measurements presented in the previous discussion.

4.2 Optical Measurements and Results

The optical measurements chosen for this study were designed to permit the use of the theoretical developments reviewed in Chapter 2 to determine the Brownian translational and rotational diffusion coefficients of the agglomerates residing within an iron-pentacarbonyl-seeded CO/O_2 diffusion flame using optical methods exclusively. In order to provide enough information to permit the extraction of these diffusion coefficients, polarized (VV) and depolarized (VH) dynamic light scattering and classical depolarization ratio R_{VH} measurements were performed. The following discussion presents the methodology, analysis, and results of these optical experiments, eventually relating the results to theoretical estimates of the Brownian diffusion coefficients using the equations presented in section 2.3.2 of Chapter 2 in conjunction with the temperature and agglomerate morphology measurements presented earlier within this chapter.

Of the optical experiments selected for this study, the depolarized dynamic light scattering (DDLS) measurement is the most difficult because the rapid decay times characteristic of depolarized correlation functions (10 ns to 1000 ns) causes the most useful information to lie within the delay time range typically corrupted by detection system errors and because the low depolarized scattered light signal typically obtained

produces signal-to-noise ratios two or more orders of magnitude lower than those obtained from polarized DLS experiments performed under identical circumstances. Overcoming these difficulties initially required careful testing and modifications to both the optical system and the overall technique used to obtain the correlation functions. The next two sections of this chapter discuss the initial testing of the optical system and the methodology chosen for obtaining accurate correlation functions.

4.2.1 Optical System Tests

The initial tests of the optical system involved performing measurements on a portion of the incident laser light scattered off a stationary surface into the detector under various conditions. These static light experiments were used to select an appropriate supply voltage for the photomultiplier tubes, check the linearity of the detection system, and detect afterpulsing and dead time errors in the measured correlation function.

The most appropriate supply voltage for the PMT's was determined by measuring the detected photon count rate as a function of supply voltage at a constant laser intensity and determining from this data the voltage at which the measured count rate becomes nearly independent of supply voltage. The optimum voltage determined for both photomultiplier tubes used in this study is approximately 1865 V. The details of this procedure are discussed fully in section 3.3.4 of Chapter 3.

A linearity check was next performed to insure that the photon counts registered by the detection system conformed to the theoretical expectation that at a constant optical wavelength the number of photons detected is a linear function of the optical power of the incident light. The count rate versus incident laser power plot shown in figure 4.2.1 confirms this expectation, implying that the detection system functions properly in this respect.

In order to check optical system errors in generating a simple correlation function, the Brookhaven BI-9000AT digital correlator was used to establish the time-

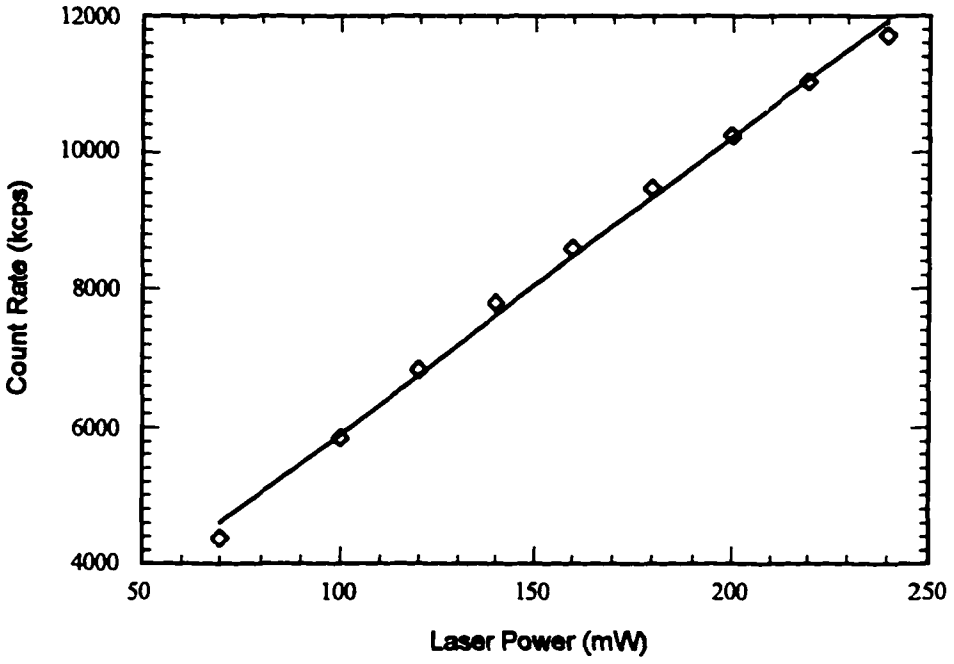

Figure 4.2.1: Results of detection system linearity test using PMT #2.

based correlation function of the detected static laser light. The theoretical correlation function of a constant intensity source, such as the static laser light, should exhibit no variation with delay time (i.e. it should be a flat line). Figure 4.2.2 depicts the normalized autocorrelation function of static light photon counts detected by a single detector using the optical configuration depicted in figure 3.3.1. This correlation function exhibits systematic noise at delay times ranging from 0.025 μs to approximately 2 μs. Initial polarized single-detector DLS measurements from an iron-pentacarbonyl-seeded CO/air diffusion flame demonstrate similar noise in the initial channels of the resulting correlation function, as shown in figure 4.2.3. A comparison of figure 4.2.2 with figure 4.2.3 reveals that these noise trends are nearly identical, indicating a systematic error resulting either from afterpulsing and dead time effects in the detection system or from high-frequency correlated intensity fluctuations in the laser.

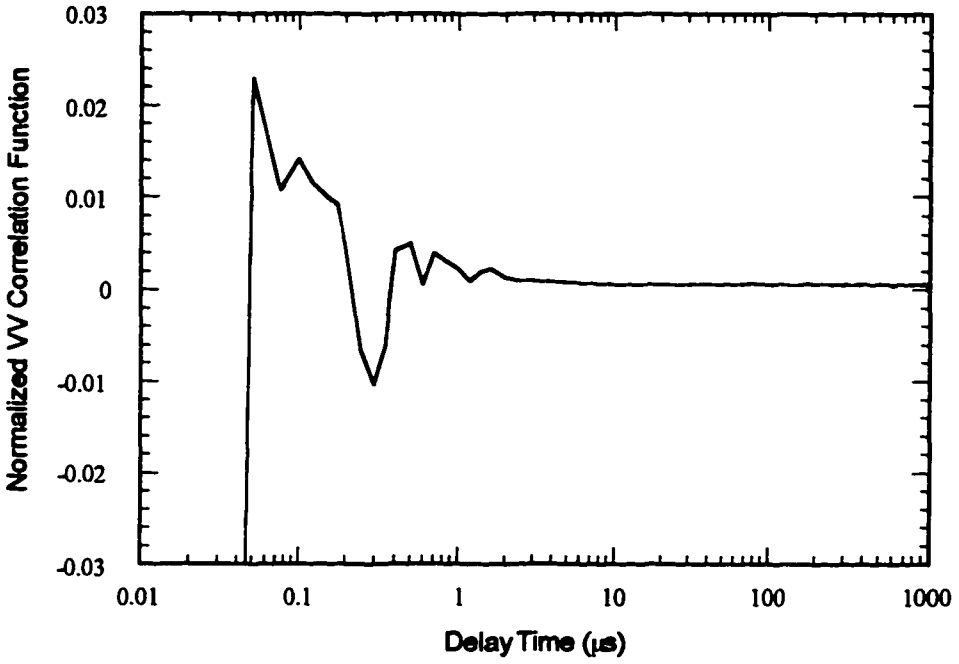

Figure 4.2.2: Normalized single-detector autocorrelation function of photons from a constant-intensity light source.

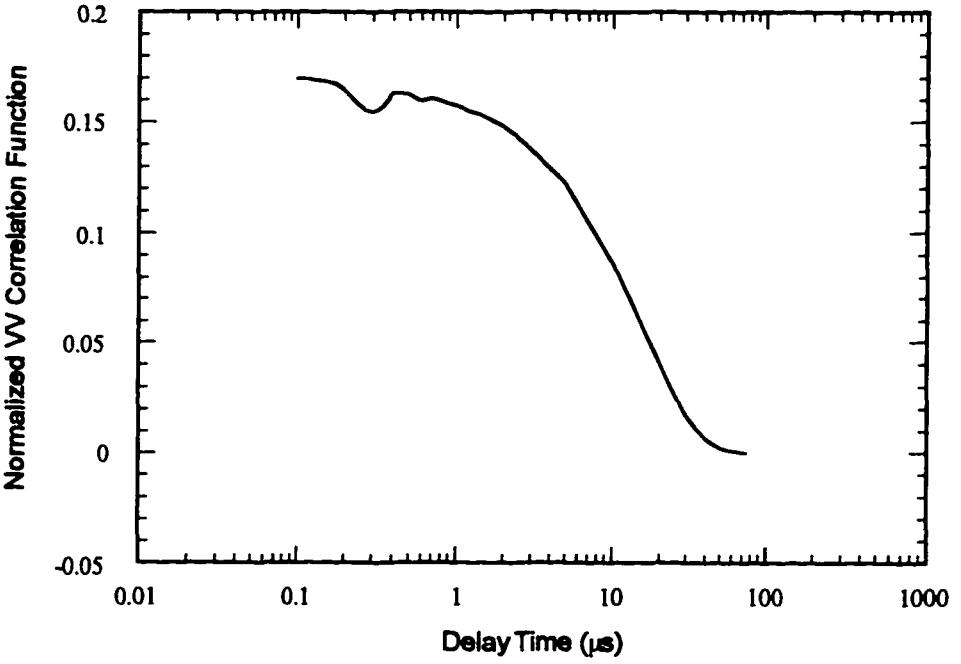

Figure 4.2.3: Normalized single-detector autocorrelation of polarized (VV) light scattered from an iron-pentacarbonyl-seeded CO/room-air diffusion flame. (CO flow rate = 0.50 lpm; carrier CO flow rate = 20 mlpm; measurement height = 30 mm)

In order to determine the source of this systematic noise, the system was modified to incorporate the two-detector arrangement described in section 3.3.2 of Chapter 3, which is illustrated in figure 3.3.3. The resulting static light cross-correlation function is shown in figure 4.2.4. This cross-correlation function was measured under the same conditions as the autocorrelation function of figure 4.2.2 and is plotted using the same vertical scale for ease of comparison. Figure 4.2.4 demonstrates a dramatic reduction in the systematic noise present in the 0.025 μs to 2 μs in the static light correlation function. The noise is also noticeably absent from the polarized (VV) cross-correlation function depicted in figure 4.2.5, which was generated using light scattered from a seeded flame. This result implies that the noise in the single-detector autocorrelation function was created by detection system effects, such as afterpulsing and dead time, not the laser. Because the 0.025 μs to 2 μs delay time range is crucial for accurate determination of the depolarized DLS correlation function from the flame-borne agglomerates due to its expected rapid decay time, the reduction of systematic noise within this range outweighs the disadvantages incurred by the reduction of signal resulting from the splitting of the scattered beam into two beams prior to detection. Compensation for the decreased signal-to-noise ratio resulting from the decrease in the intensity received by each detector can be accomplished according to equation 3.3.7 by either increasing the average number of counts $\langle n(0) \rangle$ within a sample by increasing the laser intensity or increasing the total number of samples N by increasing the duration of the experiment. In summary, cross-correlating the signal received by two separate detectors eliminates the systematic noise generated by detection system errors that occur when the output of a single detector is autocorrelated, but at the price of a lower signal-to-random-noise ratio. In addition to increasing the incident laser power, the measurement methodology described in the following section was implemented to compensate for this decrease of usable signal.

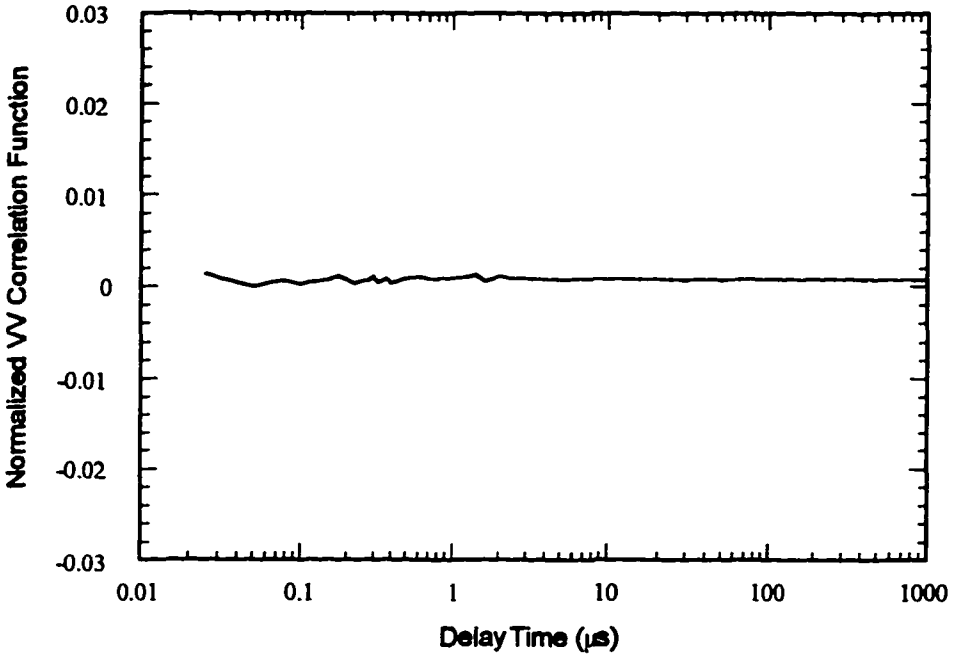

Figure 4.2.4: Normalized two-detector cross-correlation function of photons from a constant-intensity light source.

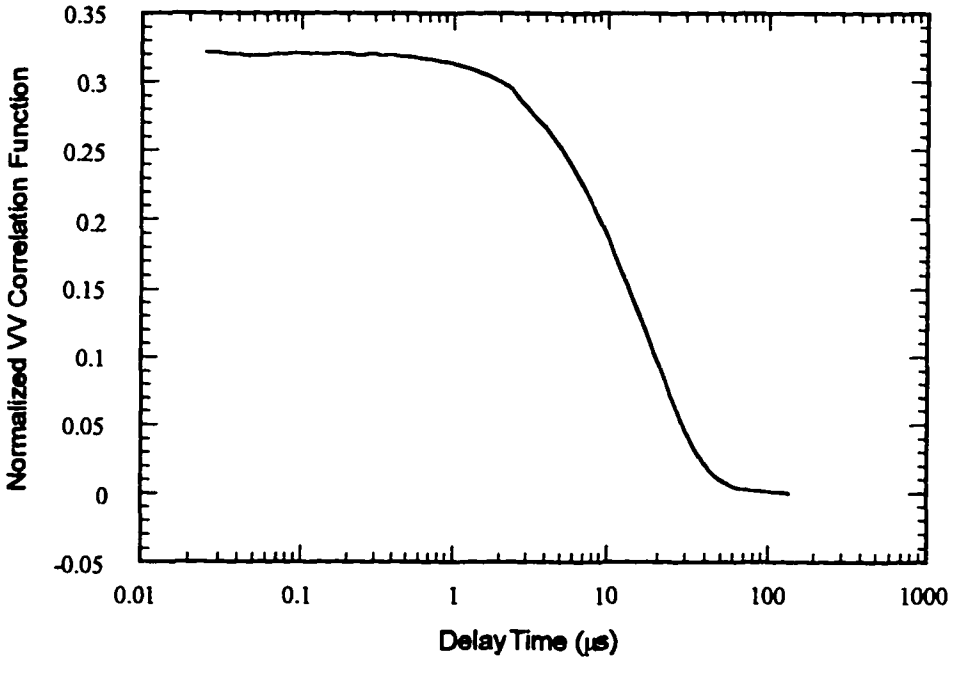

Figure 4.2.5: Normalized two-detector cross-correlation function of polarized (VV) light scattered from an iron-pentacarbonyl-seeded CO/O_2 diffusion flame. (CO flow rate = 0.50 lpm; carrier CO flow rate = 20 mlpm; O_2 flow rate = 0.25 lpm; measurement height = 35 mm.

4.2.2 Methodology of a Dynamic Light Scattering Experiment

The accurate measurement of depolarized optical correlation functions from flames poses several problems in that the intensity of the depolarized scattered light is typically less than 0.01 times the intensity of the corresponding polarized light, meaning that the signal-to-noise ratio given by the square root of equation 3.3.7 is reduced from its polarized counterpart by at least two orders of magnitude. One method of increasing this signal-to-noise ratio is to increase the incident laser power. The Spectra-Physics 2085A-20 argon-ion laser used for this study is technically capable of producing 7 W of power at the 488 nm line. Technical problems exhibited by this laser, probably cavity misalignment, have reduced this maximum sustainable power to approximately 5 W when the laser aperture is set to its maximum opening of 0 (or 10). Operating this laser using its maximum aperture, however, distorts the intensity profile of the emitted beam from the required Gaussian profile, which corresponds to TEM 00 emission, to a doughnut-shaped profile, which corresponds to a combination of one or more higher modes of laser emission. In order to reduce the possibility of corrupting the experimental data using the higher mode emissions, the laser aperture was set to 6 for the experiments performed in this study. At this aperture, the maximum sustainable power is approximately 3.00 W. To prolong the life of the laser tube, however, the laser power was limited to a maximum of 2.75 W for the DDLS measurements performed.

Another method of increasing the signal-to-noise ratio is to extend the total duration of the optical measurement, thus providing a larger number of samples N for evaluation of the correlation function. During a typical experiment, however, operation of the seeded flame for more than approximately 5 minutes causes severe clogging of the honeycomb stabilizer and noticeable deposits on the edge of the burner's fuel tube, thus changing the flame conditions. Preliminary experimental results have shown that under most of the flame conditions tested the depolarized correlation function obtained

using a laser power of 2.75 W for a duration of 5 minutes is too noisy to be able to accurately infer any reliable decay information.

In order to permit effectively longer duration times, the experiment is run as a series of short measurements, the results of which are combined after all data is collected. This procedure is based on the DLS measurement procedure used by Russo (1996) to acquire several hours of zero-scattering-angle depolarized dynamic light scattering measurements of anisotropic macromolecules in solutions. Russo subdivides his experiments into 10 s to 15 s intervals so that when combining the resulting data, the data sets corrupted by the presence of dust can be excluded. Combining multiple data sets also permits the experimental estimation of the standard error of the resulting correlation function, which is useful for data inversion techniques such as CONTIN and cumulants. Incorporating this technique into the current flame experiments, the methodology of a typical dynamic light scattering measurement from the iron-pentacarbonyl-seeded CO/O_2 diffusion flame is described in the following paragraphs.

4.2.2.1 Preliminary Setup

In preparing for a DLS flame measurement with the current system, a 1500 V voltage is continuously applied to the covered photomultiplier tubes for approximately twelve hours prior to the beginning of the experiment. This minimizes the number of dark counts registered by the system during the experiment. Additionally, the digital mass flow meters are warmed up for several hours and the argon ion laser is blocked with a beam stop and allowed to run for 30 minutes at approximately 700 mW. The heated fuel tube and the evaporator cylinder are preheated to approximately 102°C and 35°C, respectively.

Because iron pentacarbonyl naturally oxidizes in an oxygen atmosphere, 200 ml of this additive is filtered using grade 362 S|P filter paper prior to each experiment to remove the solids. This helps ensure the purity of the additive and reduces abrasion of

the O-rings within the evaporator cylinder's drain valve. After filtration, the iron pentacarbonyl is poured into the evaporator cylinder, which is immediately closed and sealed.

Preparation of the Brookhaven BI-9000AT digital correlator for data acquisition involves writing control files and delay files to permit the automation of the data acquisition process and determine the spacing of the delay channels. Control files are short customizable programs that automate the functions of the correlator. For the experiments performed in this study, control files were written that, when activated, caused the correlator to acquire data in 30 second intervals for a total duration of 5 minutes, saving the correlation function and count rate data from each 30 second interval in separate, sequentially-numbered data files. Delay files are optional files that permit customized spacing of the delay times (or correlator channels) used in the measurement of a correlation function. Delay files offer an advantage over the more conventional linear and ratio channel spacing in that the customized spacing permits the inclusion more of data channels in the measurement of a correlation function than the more standard spacing schemes, which results in the correlation function being measured at more discrete delay times τ_j. Once the correlator is satisfactorily configured, laser power is set to the desired quantity, the flame is ignited, the photomultiplier tubes are uncovered, and the execution of the experiment commences.

4.2.2.2 Execution of the DLS Flame Experiment

The flame used in this study is ignited by first setting the CO flow rate and igniting the CO/air mixture formed when the CO begins to exit the burner's fuel tube. Next, the oxygen flow rate is set, followed by the carrier CO flow. The flow rates given by table 4.1.1 were used to generate the desired flame.

Once the flame reaches steady conditions, the laser beam is unblocked and the first correlator control file is executed. Once the correlator records ten thirty-second data sets (five minutes) the correlator stops recording data. After this occurs, the flame

is extinguished, the stabilizer honeycomb is removed from its position over the burner and cleaned with compressed air, and the top of the burner's fuel tube is cleaned with a wet cotton swab, being careful to keep the deposits from falling into the burner. After completion of the cleanup, the flame is reignited and the process is repeated until a satisfactory amount of data is collected.

4.2.2.3 Shut Down

After termination of the experiment, the flame is extinguished by closing the CO tank valve, allowing the pressure in the regulator to decrease to nearly 0 psig. As the flame is about to expire, purge nitrogen is diverted into the CO line to push the remaining CO out of the fuel line, allowing it to burn. Once the flame completely extinguishes, the flow meters are purged with nitrogen and the iron pentacarbonyl is drained from the evaporator cylinder, which is then cleaned with acetone.

4.2.2.4 Correlation Data Preprocessing

After completion of the experiment, the data sets generated by the correlator are collected and combined to form a single correlation function data file and a data file containing weights to be used in subsequent decay-rate inversion procedures. A QBASIC program COMBINE3.BAS has been written to accomplish this task. The correlation data is combined by summing the contents of the correlator channels (including the baseline channels) from all selected data sets for each delay time τ_j. The values representing total number of samples for each data set are also summed. The resulting combined correlation function $G_T(\tau_j)$ takes the form

$$G_T(\tau_j) = \sum_{s=1}^{N_F} \left[\frac{N_s}{N_T}\right] G_s(\tau_j), \quad (j = 1, 2, 3, \ldots, M) \qquad (4.2.1)$$

where

$$N_T = \sum_{s=1}^{N_F} N_s$$

is the combined total number of samples, N_F is the total number of individual data files in the combination, and $G_s(\tau_j)$ is the estimated correlation function of equation 3.3.5 at delay time τ_j from data file *s*. Equation 4.2.1 is simply an extension of equation 3.3.5, which is used by the correlator to estimate the correlation function from the photon counts. Since the measured baseline is the average of a user-specified number of correlation function values measured at delay times much larger than the correlation function's coherence time, the measured baseline B_{mT} of the combined data is determined using equation 4.2.1 by replacing $G_s(\tau_j)$ with the measured baselines from each data set. The calculated baseline B_{cT} is also determined using the following extension of equation 3.3.6:

$$B_{cT} = \frac{1}{N_F^2}\left(\sum_{i=1}^{N_F} N_{Ai}\right)\left(\sum_{k=1}^{N_F} N_{Bk}\right), \qquad (4.2.2)$$

where N_{Ai} and N_{Bk} are the total counts received by input A given by file *i* and the total counts received by input B given by file *k*, respectively. Once these quantities are computed, COMBINE3.BAS outputs this information using the same file structure as the Brookhaven BI-9000AT correlator's output data files.

Taking advantage of the availability of numerous correlation function data sets obtained from the same source, weights are computed from the experimental data for use with decay rate analysis techniques, such as CONTIN and cumulants. In order to calculate these weights, COMBINE3.BAS first computes the normalized correlation functions $C_s(\tau)$ from each data file using the relationship

$$C_s(\tau_j) = \left[\frac{G_s(\tau_j)}{B_s} - 1\right]^{1/2}, \qquad (j = 1, 2, 3, \ldots, M) \qquad (4.2.3)$$

where B_s is either the measured or calculated baseline from data set *s*. Once obtained, the variance of the combined normalized correlation function is estimated as the square of the standard error of the normalized correlation function data:

$$\mathrm{Var}[C(\tau_j)] = \frac{1}{N_F(N_F - 1)}\left[\sum_{s=1}^{N_F} C_s(\tau_j)^2 - \left(\sum_{s=1}^{N_F} C_s(\tau_j)\right)^2\right]. \qquad (4.2.4)$$

The weight at each delay time τ_j is set equal to the reciprocal of $\mathrm{Var}[C(\tau_j)]$.

Figures 4.2.6 through 4.2.9 illustrate the noise reduction obtained by combining multiple sets of correlation function data. Each of these figures presents depolarized (VH) correlation functions obtained from the flame given by table 4.1.1 at a scattering angle of 5°. Figure 4.2.6 is the result of a 30 second measurement obtained at a height of 35 mm above the burner surface using a laser power of 2.50 W. The much smoother correlation function presented in figure 4.2.7 is the combination of 59 data files, each of 30 second duration, obtained under identical conditions as figure 4.2.6. Figure 4.2.8 presents the much noisier correlation function measured at a height of 25 mm using a laser power of 2.75 W at a scattering angle of 5° over a duration of 30 s. The combined depolarized correlation function of figure 4.2.9 is the resulting combination of 120 data sets obtained under identical conditions as figure 4.2.8. As would be expected, measurements acquired at lower heights tend to be noisier as a result of the shorter chain-like agglomerates present.

4.2.3 Experimentally Obtained DLS and Depolarization Ratio Results

Upon verification that both polarized and depolarized correlation functions were obtainable from the iron-pentacarbonyl-seeded CO/O_2 flame under consideration, polarized and depolarized dynamic light scattering measurements were performed at the same heights along the flame's central axis used for the flame temperature measurements and the thermophoretic sampling experiments described in section 4.1. As discussed in section 2.4 of Chapter 2, the extraction of translational and rotational Brownian diffusion coefficient information from dynamic light scattering data requires the coupling of at least two independent correlation functions. When combining VV and VH correlation functions obtained at a single scattering angle θ, the classical depolarization ratio R_{VH} is needed to separate the integral terms of equations 2.2.113.

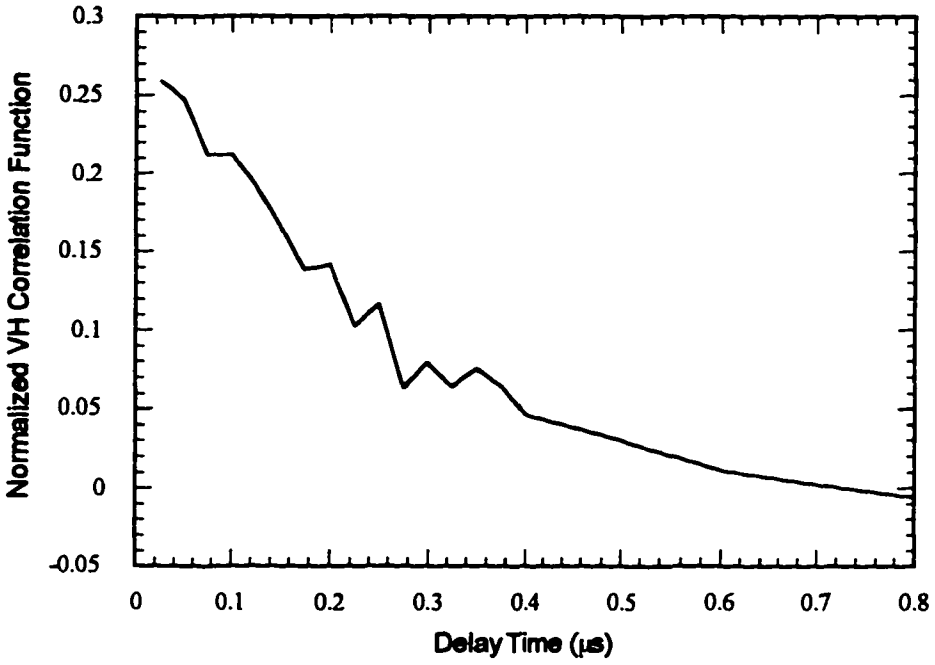

Figure 4.2.6: VH correlation function obtained from seeded CO/O_2 flame at a height of 35 mm. (laser power = 2.5 W; duration = 30 s; scattering angle = 5°)

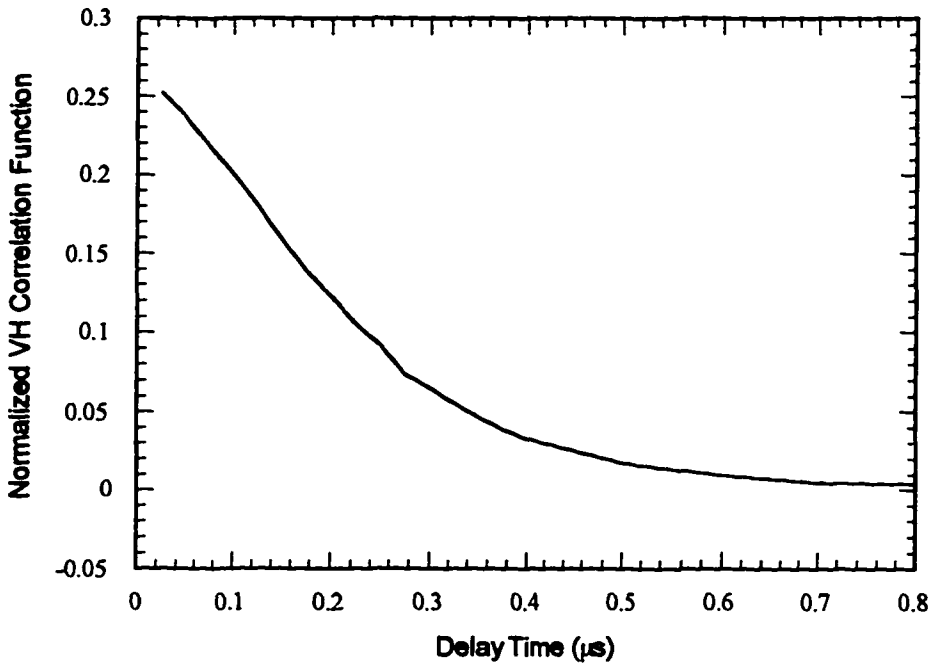

Figure 4.2.7: Combined VH correlation function obtained from seeded CO/O_2 flame at a height of 35 mm. (laser power = 2.5 W; total duration = 29.5 min; scattering angle = 5°)

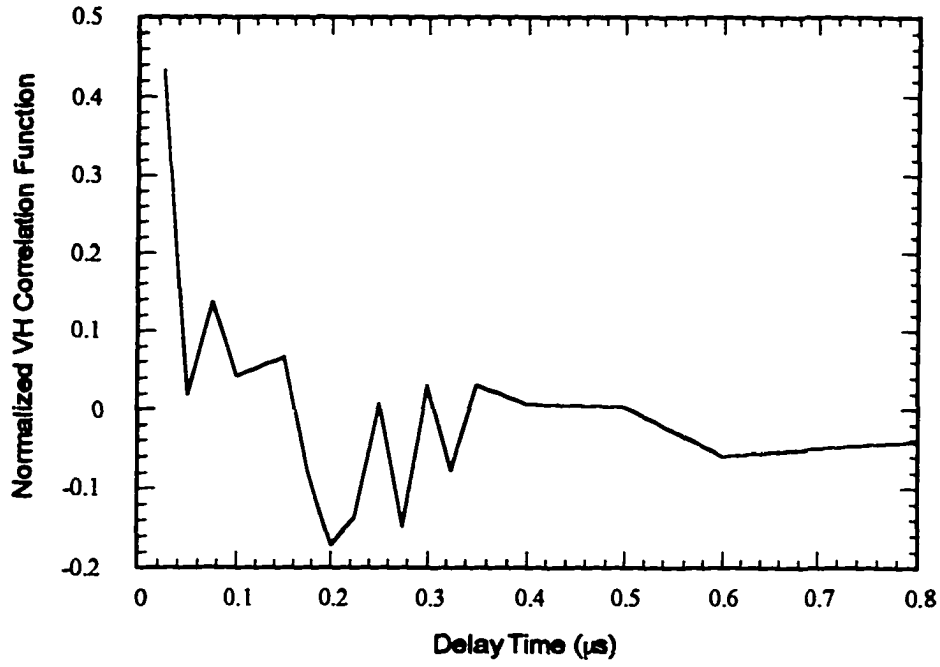

Figure 4.2.8: VH correlation function obtained from seeded CO/O_2 flame at a height of 25 mm. (laser power = 2.75 W; duration = 30 s; scattering angle = 5°)

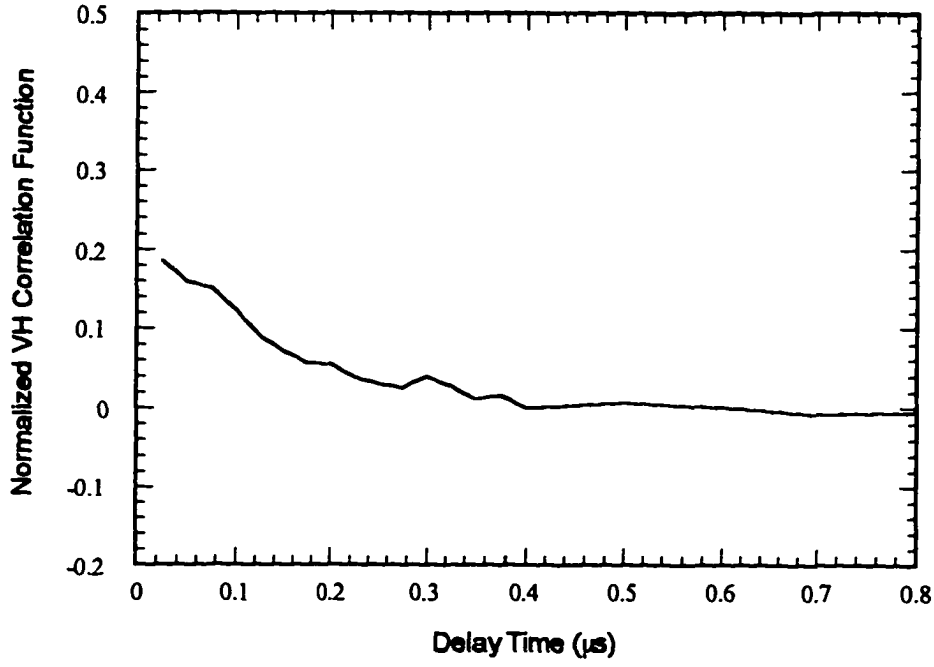

Figure 4.2.9: Combined VH correlation function obtained from seeded CO/O_2 flame at a height of 25 mm. (laser power = 2.75 W; total duration = 1 h; scattering angle = 5°)

Since the VH correlation function contains only one Laplace integral term, depolarized correlation functions obtained at two separate scattering angles θ_1 and θ_2 can alternatively be used to extract translational and rotational diffusion coefficients without the need to measure R_{VH}.

The following discussion presents the results of dynamic light scattering experiments performed using two different scattering angles, along with classical depolarization measurements obtained at the same locations within the flame. Initial observations concerning these results are considered prior to the presentation of a series of quantitative decay-rate analyses provided in the following section.

4.2.3.1 Dynamic Light Scattering Measurements

The polarized and depolarized dynamic light scattering measurements used in this study were performed along the central axis of the $Fe(CO)_5$-seeded CO/O_2 flame specified by table 4.1.1 at the heights of 20 mm, 30 mm, 32.5 mm, and 35 mm above the burner surface. The first set of measurements were performed using a scattering angle θ_1 of 5°. At this scattering angle, VV and VH correlation functions were obtained at all heights considered. With the exception of measurements performed at 25 mm, the laser power was set to 0.400 W for the polarized measurements and 2.50 W for the depolarized measurements. At 25 mm, the laser powers were increased to 0.500 W and 2.75 W in anticipation of a lower scattered signal. These measurements were obtained using the multi-experiment technique described in section 4.2.2. For all measurements except for the VH experiment performed at 25 mm, sixty 30-second data sets were collected. Due to a considerably-diminished signal, the number of data sets was doubled for the depolarized 25 mm experiment.

The next set of measurements were performed using a scattering angle θ_2 of 30°. At this scattering angle $\tilde{V}\tilde{V}$ correlation functions were obtained using a laser power of 0.700 W at all of the heights considered and a single VH correlation was measured at the 35 mm height. A laser power of 2.50 W was used for this depolarized measurement.

Because of the increased laser power over the $\theta_1 = 5°$ case, only thirty 30-second data sets were needed for the VV experiments. Like the 5° experiments, however, 60 data sets were obtained for the 30 mm depolarized experiments.

Each of the correlation functions were obtained used three separate sample times simultaneously. At delay times ranging from 0.025 μs to 0.400 μs, the sample time was 0.025 μs. At delay times ranging from 0.500 μs to 2.4 μs, the sample time was 0.100 μs. Both of these ranges correspond to the high speed section of the Brookhaven BI-9000AT correlator. Longer delay times, which generally ranged from 3 μs to 161 μs, used a 1 μs sample time, which was generated by the middle speed section of the correlator. Upon assessing the results prior to combination using the program COMBINE3.BAS a severe discontinuity was sometimes observed at a delay time of 3 μs, which is the boundary between the domains governed by the correlator's low and middle speed sections. This discontinuity occurred most frequently during the VV measurements obtained at $\theta = 5°$. During the experiment, this phenomenon was most often observed when the flame exhibited higher-than-normal instabilities. Though the exact cause of this discontinuity is unknown, it is suspected of resulting from the combined effects of differing sample rates between the correlator sections and fluctuations in the baseline intensity of the light scattered from the flame. The data sets exhibiting this discontinuity were discarded prior to combination using COMBINE3.BAS. Additionally, since the VV correlation functions obtained at $\theta = 5°$ exhibited little variation between 0.025 μs and 5 μs, the data points within this range were discarded as a precaution against the effects of the observed discontinuity.

Another effect most frequently observed during moments of high flame instability is a large difference between the measured and calculated baseline determined by the correlator. During normal flame experiments, the measured and calculated baselines would sometimes differ by up to 15%. During moments of high instability, however, this difference would sometimes climb to 200%. Additional

insight concerning the relationship between the flame instabilities and baseline difference was obtained by setting the final measured delay time equal to 10 s for a VV measurement obtained at a height of 35 mm and a scattering angle of 5°. The resulting second-order normalized correlation function is shown in figure 4.2.10. The normalized correlation function initially decays from approximately 0.56 at 0.25 μs to 0.2 at approximately 80 μs. The correlation function remains nearly constant between 100 μs and 50 ms, then it decays to its true baseline between 0.1 s and 1 s. The decay of the correlation function between 0.025 μs and 80 μs is consistent with behavior expected of particle motion within the scattering volume. The final decay between 0.1 s and 1 s, however, is too slow to be attributed to particle motion.

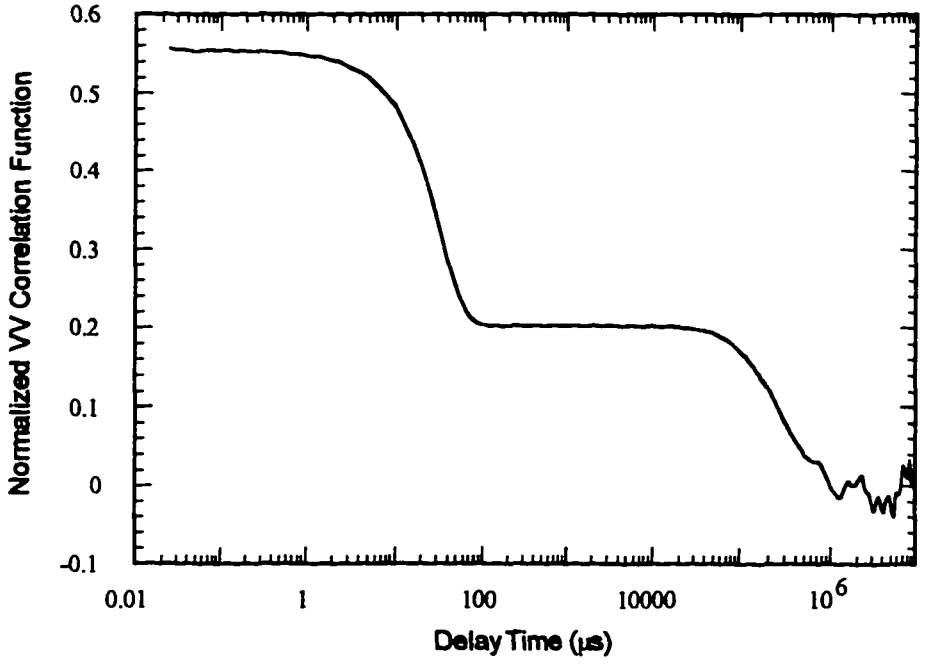

Figure 4.2.10: Extended-delay-time VV correlation function showing the effects of flame instabilities on DLS flame measurements.

Visual observation of the scattering volume during the experiment reveals the cause of this decay to be flame instabilities, which temporarily move the central stream of luminous, particle-laden flame gases shown in figure 4.1b completely out of the

scattering volume. Because the scattered light intensity is greatly diminished when this occurs, the effect on the correlation function at delay times typically characteristic of particle motion should be minimal. Because these instabilities cause the average scattered light intensity to randomly fluctuate at time scales on the order of one second, the optical correlation function exhibits a definite decay within this delay time range.

When obtaining correlation functions from the flame to determine the dynamics of the flame-borne particles, the *measured* baseline is determined by averaging sampled values of the correlation function at delay times long compared to the observed coherence time of the correlation function. For VV measurements performed in this study, the delay times at which the measured baseline is obtained is typically no longer than 161 μs. This occurs on the plateau in the correlation function of figure 4.2.10 observed between 100 μs and 50 ms. Measured baselines for the depolarized correlation functions are similarly determined by averaging the function values obtained between 3 μs and 5 μs.

In contrast, the *calculated* baseline is computed from the total signal counts using equation 3.3.3. This calculated baseline is essentially a measure of the *true* baseline of the correlation function, which is reached by the correlation function of figure 4.2.10 at a delay time of approximately 1 s. These observations account for the large discrepancies between the measured and calculated baselines. Furthermore, they also imply that by choosing the measured baseline for subsequent calculations, the major effects of flame instabilities are avoided. As a result, all DLS analyses performed for this study utilize the measured baseline.

Examples of correlation functions measured using the current cross-correlation measurement system and the measurement procedures of section 4.2.2 are plotted in figure 4.2.11, which compares the VV and VH normalized first order correlation functions obtained 35 mm above the burner surface along the central axis of the flame defined by table 4.1.1. Plotted are the normalized functions $C_{VV,1}(\tau)$ and $C_{VH,1}(\tau)$,

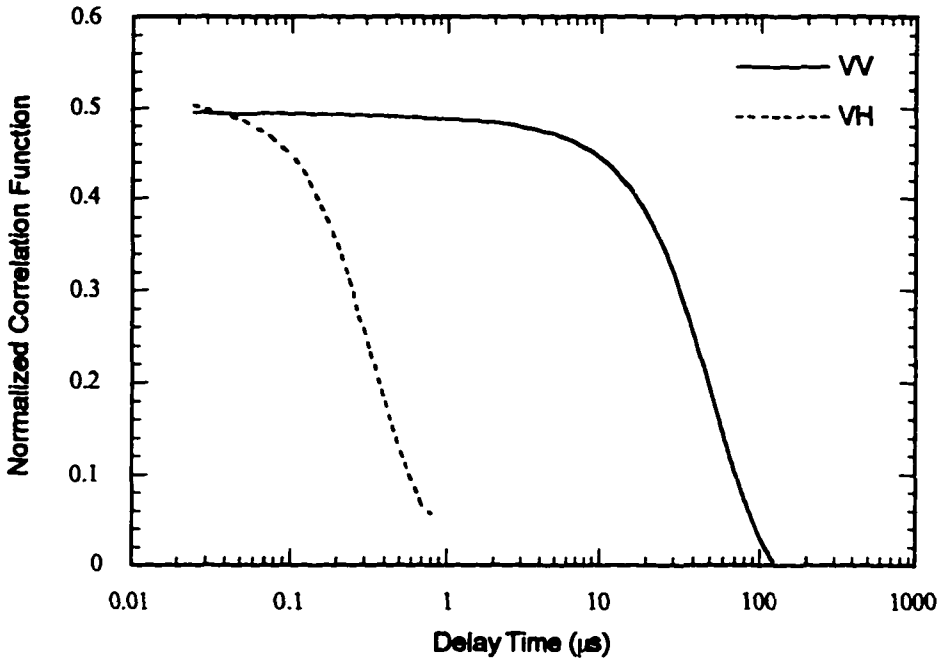

Figure 4.2.11: A comparison of experimental polarized (VV) and depolarized (VH) correlation functions obtained at a height of 35 mm and a scattering angle of 5°.

which are defined by equation 2.4.1 of Chapter 2. Comparing the decay times characterizing these two correlation functions qualitatively reveals the differences between the time scales governing intensity fluctuations due to translational (VV) and rotational (VH) particle motion. Because only delay times greater than 5 μs were considered in the analyses of VV correlation functions obtained at $\theta = 5°$, a delay time at which the normalized VH correlation function is essentially equal to zero, the coupling of the integral terms in equation 2.2.113 is virtually nonexistent. In this situation equations 2.4.6 reduce to

$$\zeta_{V,1}(\tau) = C_{VV,1}(\tau) \qquad (4.2.5a)$$

and

$$\zeta_{H,1}(\tau) = C_{VH,1}(\tau). \qquad (4.2.5b)$$

Thus, the classical depolarization ratio R_{VH} is not needed in order to isolate the Laplace integral terms occurring in equations 2.2.13.

4.2.3.2 Classical Depolarization Ratio Measurements

Though unnecessary for the inversion of the DLS data, the classical depolarization ratio R_{VH} was indeed measured at $\theta = 5^{\circ}$ and all heights considered within this study. This measurement was performed by redirecting one of the photomultiplier (PMT) outputs through a current preamplifier (EG&G 5202) into a lock-in amplifier (EG&G 5209), which distinguishes the desired signal from other noise sources, such as flame emissions and electronic noise, by demodulating it from a square carrier wave induced in the incident beam by a rotating-wheel light chopper (EG&G 196). The ratio of the voltages displayed by the lock-in amplifier for the depolarized and polarized measurements is thus equal to the depolarization ratio R_{VH}. During this measurement, the lock-in amplifier output was directed to the RS-232 port of a Zenith Z-100 computer, which recorded ten data points for each polarization and calculated the mean and standard error of the input voltage using these ten data points. The depolarization ratio computed from these averages, along with its calculated uncertainty, is plotted as a function of height in figure 4.2.12. As expected, the depolarization ratio generally increases with increasing height within the flame as a result of the increasing length of the chainlike agglomerates. This result, when considered along with Jakeman, et al.'s (1971) statistical noise estimate (equation 3.3.7), is also consistent with the observed decrease in the VH correlation function's signal-to-noise ratios with decreasing height implied by comparing the correlation functions of figures 4.2.6 and 4.2.8.

The depolarization ratio measurements presented in figure 4.2.12 are subject to various errors. The main source of error is flame instabilities. While the effects of instabilities could be corrected in the DLS experiments by using the measured baseline, no obvious correction exists for the classical measurement except for averaging the data

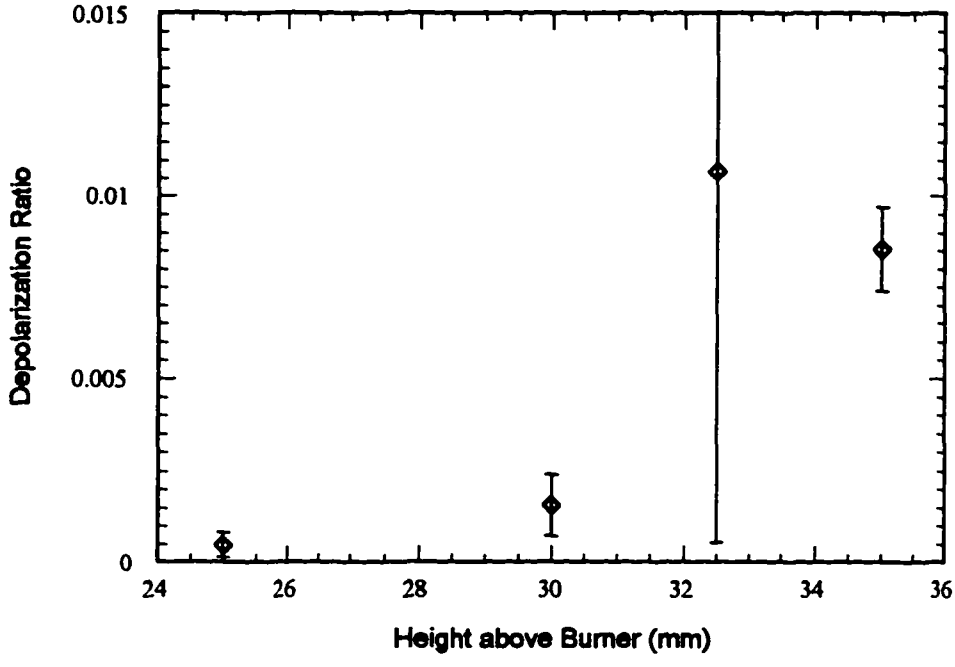

Figure 4.2.12: Experimental variation of classical depolarization ratio with height within the seeded diffusion flame defined by table 4.1.1. (scattering angle = 5°)

from many measurements. In figure 4.2.12, this instability error is most evident at 32.5 mm. An additional source of error is the presence of electronic noise in the power supplied to the current preamplifier. Much of this noise is not effectively filtered by the lock-in amplifier and causes premature signal overloads. A third, and more subtle, potential error source is the possibility that the detection system is sensitive to the polarization of the light being detected. This would cause a systematic error in the depolarization ratio results. Checking for polarization sensitivity requires calibrating the detection system with respect to strongly anisotropic scatterers of known properties, a procedure not performed in this study.

The acquisition of both polarized and depolarized dynamic light scattering data at one scattering angle and polarized data at a second scattering angle, as performed in this study, provides more than enough information for a quantitative analysis based

upon the developments of section 2.4 of Chapter 2. The following discussion presents several decay rate analyses of these measured correlation functions, along with the implications of the results.

4.2.4 Analysis of Optical Results

Analysis of the photon correlation functions discussed in the previous section involves quantifying the decay characteristics of these functions through determination of the statistics of the parameters $\Gamma_{f,k}$ defined by equations 2.4.9 of Chapter 2. The parameter $\Gamma_{f,k}$ is called the *linewidth* of the correlation function because it represents the width at half-maximum of the frequency spectrum obtained from the correlation function's Fourier transform. The most complete extraction of linewidth information from a correlation function is obtained through the determination of the linewidth's probability density function $F_{f,k}(\Gamma_{f,k})$, which is equivalent to the inverse Laplace transforms of the functions $\zeta_{f,k}(\tau)$. As mentioned within the previous section, experiments have demonstrated that these $\zeta_{f,k}(\tau)$ are equivalent to the normalized correlation functions $C_{if,k}(\tau)$, which are experimental approximations of the normalized first order electric field correlation functions $g^{(1)}(\tau)_{if}$. The data analysis methods considered below involve either numerically Laplace inverting the normalized correlation functions or determining the moments of the $\Gamma_{f,k}$-density through the use of the cumulants technique [Koppel, 1972].

4.2.4.1 Techniques for Analyzing the Decay Characteristics of DLS Correlation Functions

The determination of $F_{f,k}(\Gamma_{f,k})$ through the Laplace inversion of experimental data corresponds to numerically solving equations of the form of equation 2.4.4 for the unknown function f(x). The computation of a forward Laplace transform is a stable process because the integration smoothes out fluctuations in the integrand and the exponential factor exp(-sx) reduces the Laplace transform's dependence on f(x) as x increases [Arfken, 1985]. Because of this low sensitivity of the forward Laplace

transform on the details of f(x), the inverse problem of determining f(x) from its Laplace transform F(s) is extremely sensitive to the details of F(s). The random statistical uncertainties that accompany any measured quantity therefore present daunting problems when attempting to numerically determine its inverse Laplace transform. A theoretical illustration of this difficulty is presented by Provencher (1982a) in the form of the Riemann-Lebesgue lemma:

$$\lim_{x \to \infty} \int_a^b K(s) \sin(xs)\, dx = 0, \tag{4.2.1}$$

which can be represented as a Laplace transform by letting the integration limits a and b equal zero and infinity, respectively, and the kernel K(s) equal exp(-sx). This implies that sinusoidal functions of arbitrarily large amplitude can always be found, given a high enough frequency x, that cause a contribution to the Laplace transform of a function f(x) that is less than the function's statistical uncertainty. This results in a large number of vastly different possible solutions for f(x) which all satisfy equation 2.4.4 to within experimental uncertainty [Provencher, 1982a]. Fortunately, due to the simple behavior of most physically appropriate probability density functions and additional limitations that are imposed upon the nature of the solution, previous investigators have been able to successfully evaluate the inverse Laplace transforms of optical correlation functions.

Many numerical estimates of the inverse Laplace transform f(x) of a measured function F(s) involve approximating f(x) as a series of Dirac delta functions ([Pope and Chu, 1984], [Taylor, et al., 1985], [Russo, et al., 1986])

$$f(x) \cong \sum_{i=1}^{N} a_i \delta(x - x_i), \tag{4.2.2}$$

where the a_i are unknown constants and the x_i are decay rates, whose values are either previously specified or considered as floating parameters to be determined through a

least squares analysis. Substitution of equation 4.2.2 into equation 2.4.4 gives the following approximation of the Laplace transform:

$$F(s) \cong \sum_{i=1}^{N} a_i \exp(-sx_i). \tag{4.2.3}$$

This approximation thus provides a set of linear equations, from which the amplitude constants a_i are determined using a least squares technique. In the terminology of dynamic light scattering, this would physically represent a multimodal mixture of particles with N discrete sizes. The spacing of the decay rates x_i are often constrained to be exponentially distributed between successive values so that more emphasis is given to the initial values of f(x), which produce the largest effect on the Laplace transform F(s). Russo, et al. (1986) has reported being able to cleanly resolve decay rates x_i differing by a factor of two or more using a variation of this technique.

A more elaborate numerical Laplace inversion technique that is becoming quite popular in the inversion of dynamic light scattering data (see for example [DeLong and Russo, 1990], [Ruf, et al., 1992], and [Ruf, et al., 1993]) is the regularized least-squares technique developed by Provencher (1982a, 1982b), which is packaged as the software CONTIN. This technique attempts to select the "correct" solution out of the many possible solutions that satisfy equation 2.4.4 to within experimental error by applying user-supplied prior knowledge of absolute constraints (such as the constraint $f(x) \geq 0$, which applies in the present case) and/or the solution's statistical mean and covariance within the inversion process. CONTIN then proceeds to select the "simplest" solution form, in accordance with the principle of *parsimony* [Provencher, 1982a], in an attempt to eliminate artificial detail that results from the uncertainty of the measured data in favor of the fundamental trends that are a necessary part of the solution. Based upon the results of DeLong and Russo (1990) and Ruf (1992), the CONTIN inversion routine currently appears to be one of the most accurate Laplace inversion techniques available for the determination of the functions $F_{f,k}(\Gamma_{f,k})$ from optical correlation functions.

Another technique commonly used in the interpretation of dynamic light scattering data from polydisperse systems is the cumulants technique [Koppel, 1972], which, as discussed in section 2.4 of Chapter 2, determines the weighted moments of f(x) as the coefficients of the expansion of ln[F(s)] about s = 0. These coefficients are determined from the measured data by a least squares analysis. Only the first two moments, however, can be accurately obtained using this technique [Koppel, 1972]. Some investigators, such as Bargeon (1974), Scrivner, et al. (1986), Charalampopoulos and Chang (1988), and Venizelos (1989) have utilized cumulants-derived moments to characterize an assumed morphological distribution function, such as the zeroth-order lognormal distribution function (ZOLD), a process which is equivalent to estimating the inverse Laplace transform f(x).

For the current investigation, two different schemes were considered for inverting the DLS data presented in section 4.2.3: CONTIN and cumulants. As discussed previously, CONTIN utilizes statistical prior information to determine the "best" solution of the Laplace inversion. The fact that the density function $F_{f,k}(\Gamma_{f,k})$ is positive definite provides one important piece of information in that it eliminates the unbounded sinusoidal fluctuations discussed in relation to the Riemann-Lebesgue lemma (equation 4.2.1). Experimentally-determined weights are also supplied to CONTIN in order to concentrate the region of analysis to the most accurate data points. These weights are set equal to the reciprocals of the variances of the normalized correlation data, which are estimated as the squares of the standard errors computed by COMBINE3.BAS for the experimental data points at each delay time τ_j. These variance estimates are also used to determine weights for the cumulants fits of the normalized data.

For the cumulants analysis, use of the cumulants program CUMFIT.EXE that is packaged with the BI-9000AT digital correlator was abandoned because of the presence of built-in restrictions that prevented the accurate analysis of much of the data obtained

in this study. For example, if the second cumulant coefficient is found by CUMFIT.EXE to be a negative number CUMFIT.EXE outputs a default polydispersity index ($\equiv K_2/K_1^2$) of 0.05. Because of these limitations, a FORTRAN cumulants program CUMULANT.FOR was independently developed that not only relaxes the restrictions accompanying CUMFIT.EXE, but also allows the use of the same variance estimates supplied to CONTIN to weigh the cumulants fit. As described in section 2.4, the cumulants method uses a polynomial least squares fit of $\ln[\zeta_{f,k}(\tau)]$ to determine the $|\phi|^2$-weighted moments of $\Gamma_{f,k}$. These cumulants K_l are thus determined by minimizing the quantity

$$\delta^2 \equiv \sum_{l=1}^{N_p} w_l \left(y_l(\tau_j) - \sum_{i=0}^{N_{ord}} \frac{K_i}{i!} (-\tau_j)^i \right)^2, \qquad (4.2.4)$$

where

$$y_l(\tau_j) \equiv \ln[\zeta_{f,k}(\tau_j)]$$

and

$$w_l \equiv \frac{1}{\mathrm{Var}[y_l(\tau_j)]} = \frac{\zeta_{f,k}(\tau_j)^2}{\mathrm{Var}[\zeta_{f,k}(\tau_j)]}$$

is the weighting function calculated using the $\mathrm{Var}[\zeta_{f,k}(\tau_j)]$ estimates computed by COMBINE3.BAS, N_p is the number of correlation function data points selected for the analysis, and N_{ord} is the order of the cumulants fit.

Prior to discussing the results of the application these data inversion techniques to the experimental data presented in section 4.2.3, the results of an analysis of simulated data using these techniques is considered so that the relative strengths of each technique may be assessed and the results obtained from the experimental data may be better understood.

4.2.4.2 A Comparison between the CONTIN and Cumulants Inversion Techniques Using Simulated Data

The results of a comparison between CONTIN and the cumulants inversion technique are presented in the following discussion. This simulation of noisy DLS data

utilizes the polar method [Ross, 1988] for generating random numbers with a Gaussian distribution of a specified mean and variance. The number and spacing of the discrete delay times τ_j are identical to those of the VV data measured at a height H of 35 mm above the burner surface and a scattering angle θ of 5°. To simulate each data point, a Gaussian random number is generated whose mean is equal to a specified theoretical correlation function evaluated at τ_j and whose variance is equal to the variance, as estimated by COMBINE3.BAS, of the normalized VV flame data obtained at H = 35 mm and θ = 5°. To illustrate some of the capabilities and limitations of the inversion techniques, two simulated data sets were generated: a single-exponential-decay correlation function, corresponding to a monomodal linewidth distribution, and a double-exponential-decay correlation function, corresponding to a bimodal linewidth distribution.

The results of the analyses of each simulated correlation function are compared using a series of plots, along with tables presenting the linewidth moments generated by both inversion processes. The plotted results consist of 1) the CONTIN-generated linewidth density function $F(\Gamma)$ (inverse Laplace transform), 2) the fitted functions from both techniques superimposed on a plot of the simulated data, and 3) the weighted residuals of each fit.

The weighted residuals, in particular, provide a useful visual indication of the quality of each fit. The weighted residuals are equal to $(\zeta(\tau_j) - \zeta_{fitted}(\tau_j))/Var[\zeta(\tau_j)]$, where $\zeta(\tau_j)$ is the simulated (or experimental) data point at delay time τ_j, $Var[\zeta(\tau_j)]$ is its variance, and $\zeta_{fitted}(\tau_j)$ is the CONTIN- or cumulants-generated fit of the correlation function. An accurate fit of noisy data is indicated when the weighted residuals spread about the zero value in a randomly scattered, featureless fashion [Provencher, 1984]. Any obvious trends in the weighted residuals are indicative of deficiencies in the model used to fit the data. The range of the spread of the weighted residuals also indicates the closeness of fit: larger ranges indicate less accurate fits.

4.2.4.2.1 Simulated Monomodal Linewidth Density

The following results compare the linewidth statistics inferred by the CONTIN and cumulants inversion techniques for the simulated normalized correlation function

$$\zeta(\tau) = \exp(-0.7 - 7000\tau). \qquad (4.2.5)$$

The true form of $F(\Gamma)$ for this correlation function is proportional to a Dirac delta function centered at $\Gamma = 7000$ rad/s. This physically corresponds to the correlation function of light scattered from a suspension of monodisperse spheres. Results are reported for a third-order cumulants fit.

The linewidth density plotted in figure 3.2.13 demonstrates the characteristics of the CONTIN-generated inverse Laplace transform of the data simulated according to equation 4.2.5. Knowing that the true inverse Laplace transform is proportional to a Dirac delta function centered at $\Gamma = 7000$ rad/s, this figure demonstrates that CONTIN artificially broadens the width of the linewidth density by smoothing the numerical inverse Laplace transform. This broadening is also evident in the calculated variance of the CONTIN linewidth density. The first moment of the density, however, is nearly equal to the input linewidth of 7000, but it is not within CONTIN's uncertainty limits. Likewise, the uncertainty limits of the variance of the CONTIN-generated linewidth density do not encompass the true variance of the simulated data.

The moments calculated using the method of cumulants, as listed in table 4.2.1, are slightly more accurate that those obtained from the CONTIN solution in that the calculated mean and variance of the linewidth are both closer to the input values used to simulate the data. In the cumulants case these input values are encompassed within the estimated error ranges of the cumulants-generated linewidth mean and variance.

The comparison of the fitted functions generated by CONTIN and cumulants for the simulated data shown in figure 4.2.14 reveals that these fits are virtually indistinguishable from the simulated data. The weighted residuals of figures 4.2.15 and 4.2.16 confirm the high quality of these fits through their high degree of scatter.

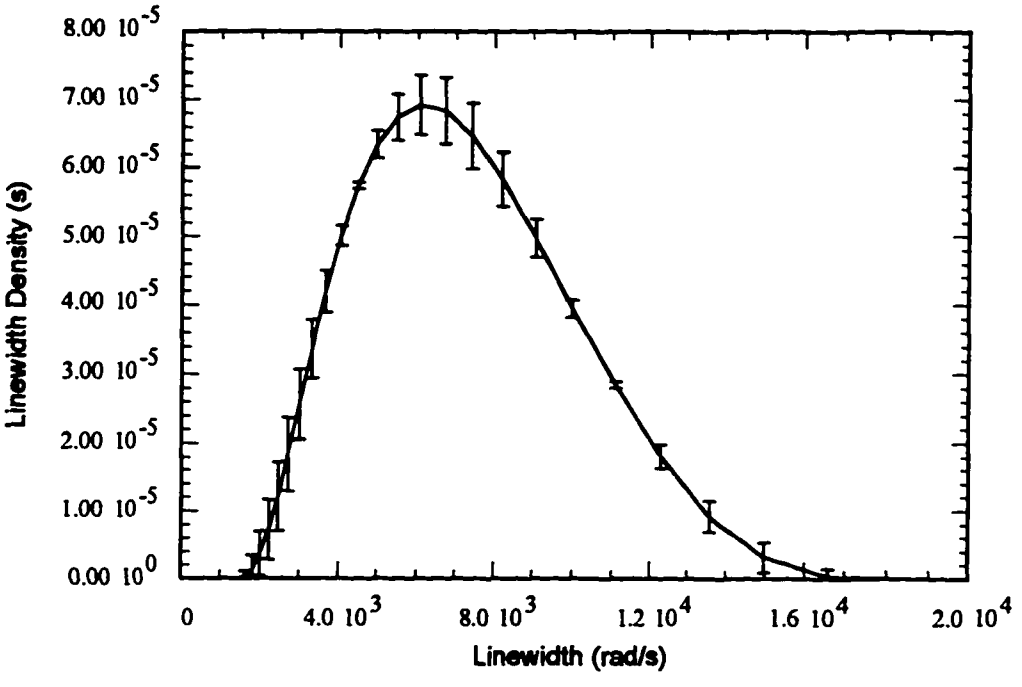

Figure 4.2.13 CONTIN-generated linewidth density corresponding to the simulated monomodal correlation function of equation 4.2.5.

Table 4.2.1: Comparison of CONTIN- and cumulants-generated moments corresponding to the simulated monomodal correlation function of equation 4.2.5.

	Actual	CONTIN	Cumulants
$\langle\Gamma\rangle_\phi$ x 10^{-3} (rad/s)	7	7.4 ± 0.1	7.2 ± 0.4
$Var_\phi(\Gamma)$ x 10^{-6} (rad/s^2)	0	7 ± 3	1 ± 19

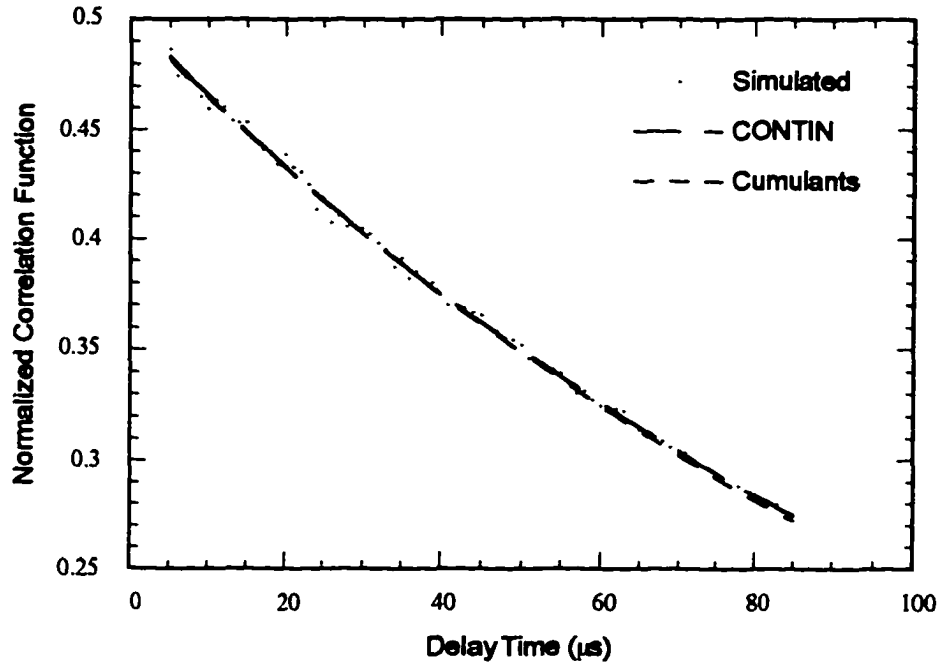

Figure 4.2.14:Comparison of CONTIN and cumulants fits to the simulated monomodal correlation function of equation 4.2.5.

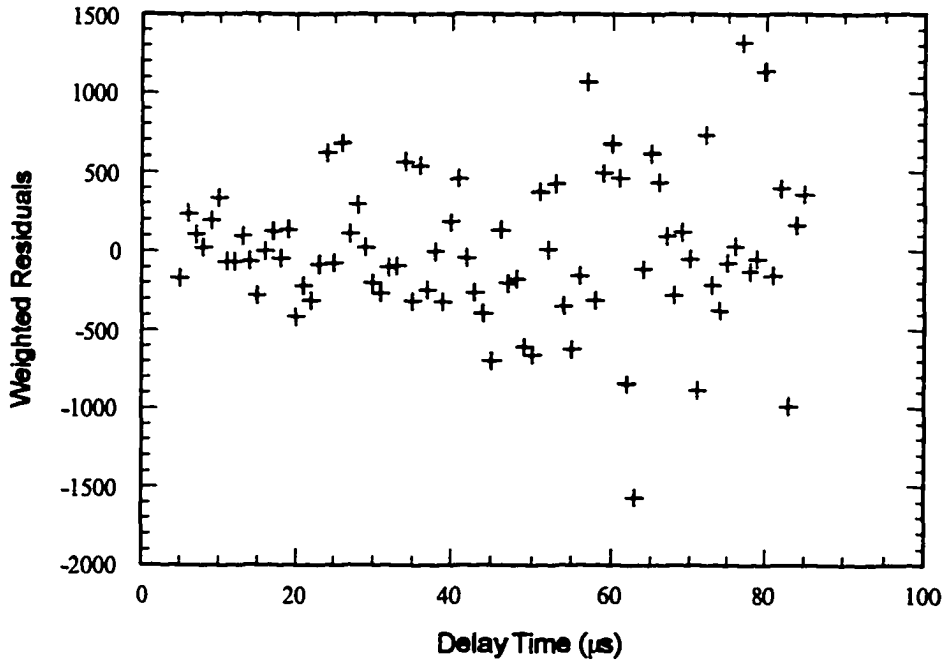

Figure 4.2.15: Weighted residuals of CONTIN fit of the simulated monomodal correlation function of equation 4.2.5.

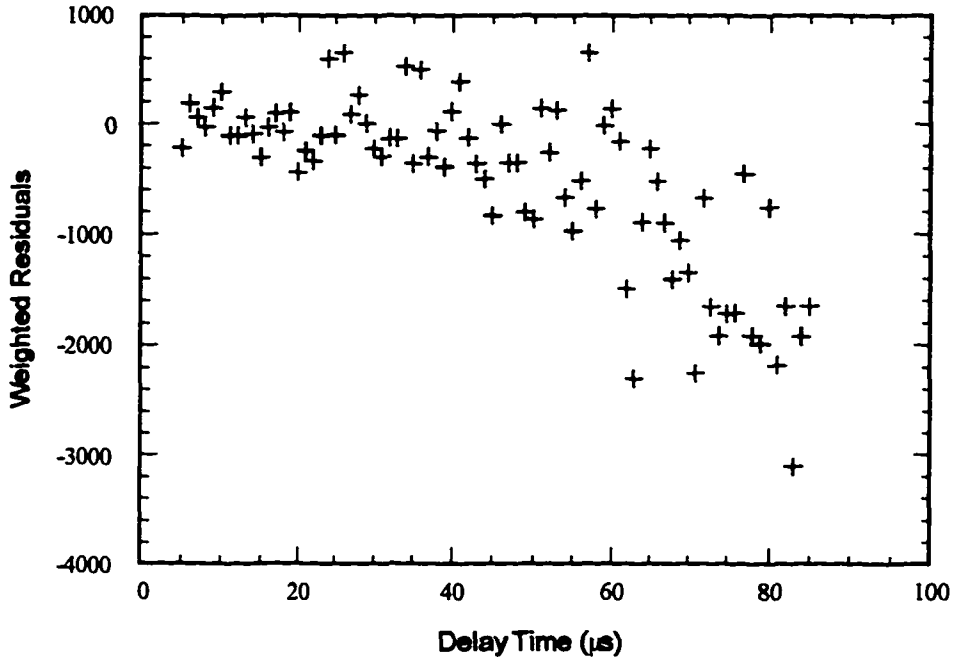

Figure 4.2.16: Weighted residuals of third-order cumulants fit of the simulated monomodal correlation function of equation 4.2.5.

According to the weighted residuals, the function generated by CONTIN produced a more accurate fit of the simulated data in that the weighted residuals show no systematic variations. The general decrease with increasing delay time of the values of the weighted residuals of the cumulants fit demonstrate a slight systematic error in the corresponding fit.

These results imply that CONTIN and cumulants both accurately determine the average linewidth from correlation functions generated by monodisperse particles. In this case, however, the "chosen" solution from CONTIN does not accurately determine the width of the linewidth density function, even though the actual fit to the data is superior to the cumulants fit. A similar investigation by Ruf (1993) using experimental data has demonstrated, however, that when used for analyzing data representing a broader linewidth density [$Var(\Gamma) = 0.2\langle\Gamma\rangle^2$] CONTIN can extract the mean and width with errors as low as 1% and 3%, respectively.

4.2.4.2.2 Simulated Bi-modal Linewidth Density

To provide an example of the relative capabilities of CONTIN and cumulants in analyzing a correlation function with a bimodal linewidth distribution, which physically represents DLS data obtained from a binary mixture of spherical particles, simulated data generated using the function

$$\zeta(\tau) = \exp(-0.7)\,[\exp(-7000\tau) + \exp(-70{,}000\tau)] \qquad (4.2.6)$$

was analyzed using both techniques. The linewidth density function $F(\Gamma)$ corresponding to this normalized correlation function is proportional to the equally-weighted sum of two Dirac delta functions: one centered at 7000 rad/s and the other centered at 70,000 rad/s.

The results of these analyses are presented in figures 4.2.17 to 4.2.20 and in table 4.2.2. Figure 4.2.17 demonstrates one of the primary attributes of CONTIN, which is the ability to resolve the peaks of multimodal distributions. According to DeLong and Russo (1990), CONTIN is able to resolve linewidths differing by a factor of 2 or more. Even though CONTIN was able to distinguish the presence of the two peaks of the simulated data's linewidth density function, the peak in the CONTIN-generated density function that is centered at 7000 rad/s exhibits an amplitude approximately five times greater than the amplitude of the 70,000 rad/s peak, which is contrary to the equal-mode weighting given by the function used to simulate the data. In a manner similar to the monomodal case, the width of each peak was broadened by the smoothing operation applied within CONTIN.

The resulting moments calculated by CONTIN for each peak, as well as for the entire density function, are close to the values obtained from equation 4.2.6, as shown in table 4.2.2. Comparable individual-mode cumulants-generated moments are unavailable since the cumulants method is unable to compute the moments of the individual peaks. The mean $\langle\Gamma_{all}\rangle_\phi$ of the entire linewidth distribution resulting from the fourth-order cumulants analysis is slightly more accurate than the CONTIN-

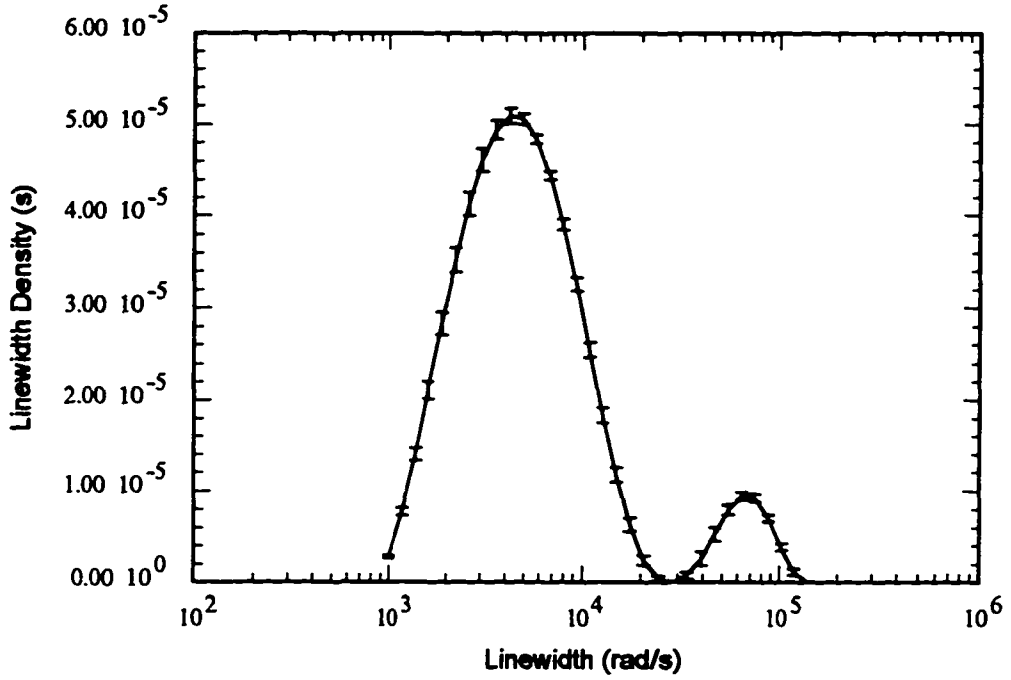

Figure 4.2.17: CONTIN-generated linewidth density corresponding to the simulated bi-modal correlation function of equation 4.2.6.

Table 4.2.2: Comparison of CONTIN- and cumulants-generated moments corresponding to the simulated bi-modal correlation function of equation 4.2.6.

	Actual	CONTIN	Cumulants
$\langle\Gamma_1\rangle_\phi$ x 10^{-3} (rad/s)	7	7.9 ± 0.4	Not Determined
$Var_\phi(\Gamma_1)$ x 10^{-7} (rad/s^2)	0	2.0 ± 0.9	Not Determined
$\langle\Gamma_2\rangle_\phi$ x 10^{-4} (rad/s)	7	7.3 ± 0.2	Not Determined
$Var_\phi(\Gamma_2)$ x 10^{-8} (rad/s^2)	0	4 ± 4	Not Determined
$\langle\Gamma_{all}\rangle_\phi$ x 10^{-4} (rad/s)	3.85	4.1 ± 0.1	3.98 ± 0.08
$Var_\phi(\Gamma_{all})$ x 10^{-8} (rad/s^2)	9.9225	13 ± 2	12.4 ± 0.06

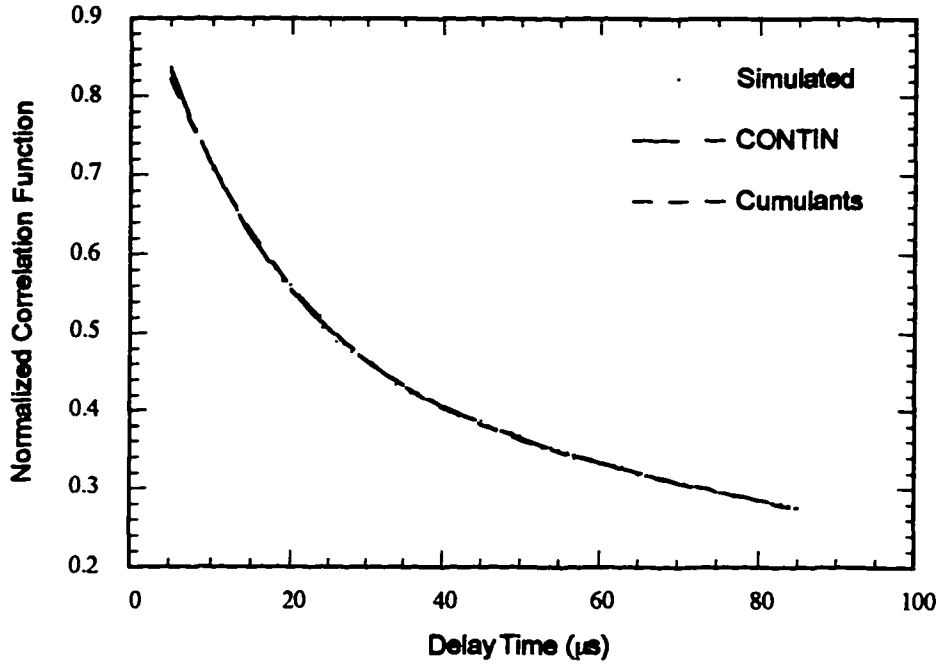

Figure 4.2.18: Comparison of CONTIN and cumulants fits to the simulated bi-modal correlation function of equation 4.2.6.

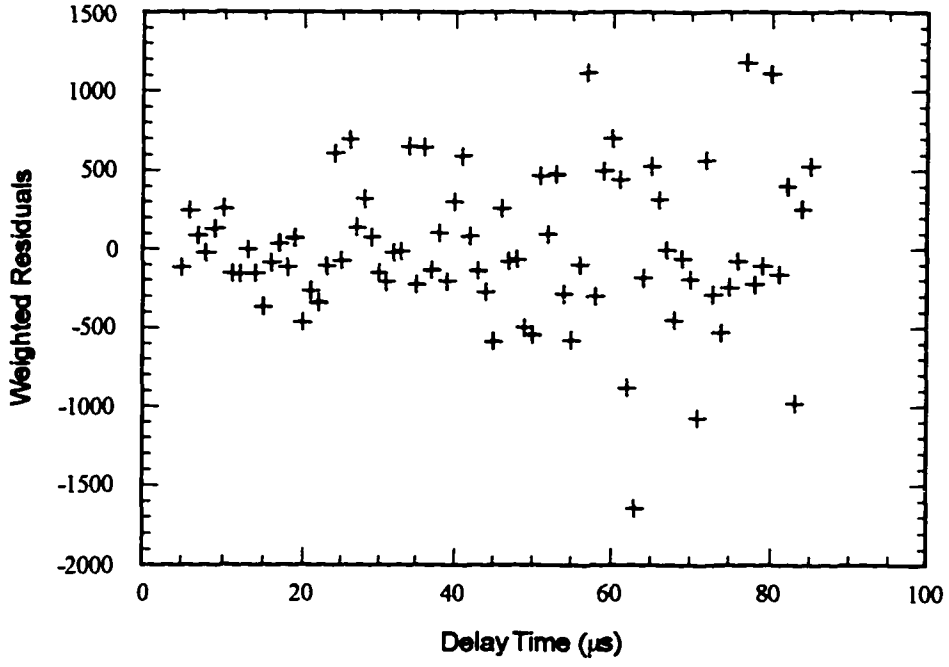

Figure 4.2.19: Weighted residuals of CONTIN fit of the simulated bi-modal correlation function of equation 4.2.6.

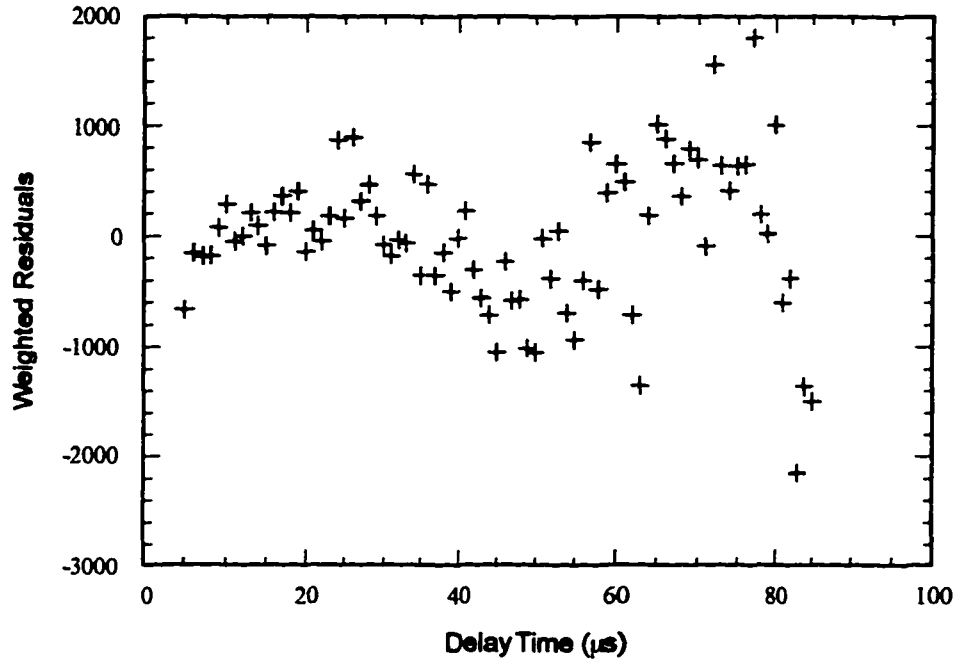

Figure 4.2.20: Weighted residuals of fourth-order cumulants fit of the simulated bi-modal correlation function of equation 4.2.6.

determined mean. Because of the broadening caused by the smoothing of the CONTIN output, the resulting variances are considerably larger than those of the simulated density function. With the exception of the peak centered at 70,000 rad/s, the CONTIN-supplied uncertainty limits do not accurately indicate the extent of this broadening error.

The plots of the fitted data (figure 4.2.18) and the weighted residuals (figures 4.2.19 and 4.2.20) indicate that the simulated data was well fit using both techniques. The weighted residuals of the fourth-order cumulants fit exhibit only very slight trends. The weighted residuals from the CONTIN fit contain no visible trends. Thus, both CONTIN and cumulants provide generally accurate inversions of the bi-modal data. The main limitations of CONTIN are the artificial broadening of narrow distributions and errors in computing the relative heights of each peak. The main limitation of cumulants is its inability to provide any details of the linewidth density other than the first two moments of the entire distribution.

4.2.4.3 Analysis of Experimental DLS Data Using CONTIN and Cumulants Inversion Techniques

With some knowledge of their limitations and advantages in analyzing the decay rates (linewidths) of correlation functions, CONTIN and cumulants are both applied to the polarized (VV) and depolarized (VH) photon correlation functions experimentally obtained from the $Fe(CO)_5$-seeded CO/O_2 diffusion flame generated using the experimental parameters given by table 4.1.1. The results of these analyses are compared in a manner similar to the comparisons for simulated data presented in section 4.2.4.2.

The linewidth densities $F_{V,1}(\Gamma_{V,1})$ and $F_{H,1}(\Gamma_{H,1})$ determined by CONTIN from the polarized (VV) and depolarized (VH) correlation functions obtained 35 mm above the burner surface at a 5° scattering angle are both monomodal functions according to figures 4.2.21 (a) and (b). These density functions exhibit polarizability-weighted means of approximately $\langle\Gamma_{V,1}\rangle_\alpha = 2.5\text{x}10^4$ rad/s for the VV case and $\langle\Gamma_{H,1}\rangle_\beta = 2.5\text{x}10^6$ rad/s for the VH case. Comparisons between these means and those obtained from cumulants, as shown in tables 4.2.3 and 4.2.4, reveal large discrepancies between these values: for each polarization, the average linewidth given by CONTIN is approximately 3.4 times the average linewidth obtained using the cumulants method.

The discrepancies between the calculated variances of the linewidth distributions are even more extreme. In both polarization modes, CONTIN computes variances whose magnitudes are less than their associated uncertainties, making them essentially equal to 0 rad/s^2. In contrast, the second cumulant coefficients K_2 are revealed to be negative quantities for both polarization states, which contradicts their interpretation as variances of the linewidth density functions.

The plots of the fitted functions, as shown in figures 4.2.22 (a) and (b), and those of CONTIN's weighted residuals, which are illustrated in figures 4.2.23 (a) and (b) reveal that the CONTIN analysis technique produced poor fits of the experimental data.

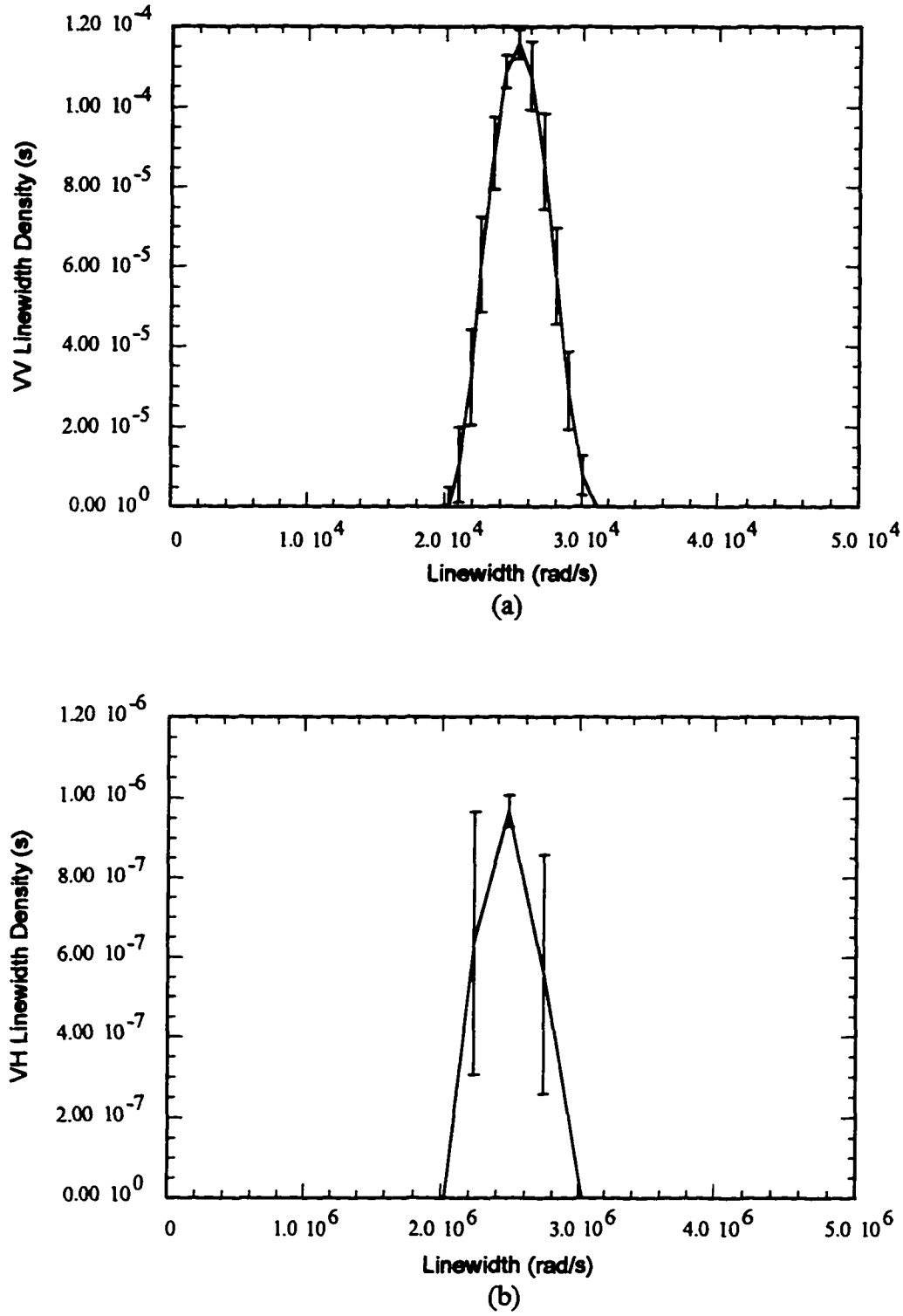

Figure 4.2.21: Linewidth densities computed using CONTIN from (a) polarized and (b) depolarized photon correlation functions measured from the seeded diffusion flame at a 35 mm height and a 5° scattering angle.

Table 4.2.3: Computed linewidth moments of the polarized correlation function measured from the seeded diffusion flame at a 35 mm height and a 5° scattering angle.

	CONTIN	Cumulants
$\langle\Gamma\rangle_\alpha \times 10^{-3}$ (rad/s)	25 ± 1	7 ± 1
$Var_\alpha(\Gamma) \times 10^{-8}$ (rad/s^2)	0.04 ± 0.6	- 5 ± 1

Table 4.2.4: Computed linewidth moments of the depolarized correlation function measured from the seeded diffusion flame at a 35 mm height and a 5° scattering angle.

	CONTIN	Cumulants
$\langle\Gamma\rangle_\beta \times 10^{-5}$ (rad/s)	25 ± 2	7.8 ± 0.9
$Var_\beta(\Gamma) \times 10^{-12}$ (rad/s^2)	0.04 ± 0.9	- 7.0 ± 0.5

The CONTIN-fitted correlation functions deviate significantly from the experimental correlation functions and the corresponding weighted residuals exhibit distinct systematic trends that imply a deficiency of the analytical model (the Laplace integral) used to fit the data.

In contrast, the cumulants fits provided much more accurate matches to the experimental data. In the polarized (VV) fitted function comparison of figure 4.2.22 (a), the cumulants fit is indistinguishable from the experimental data. The depolarized fit of figure 4.2.22 (b) reveals similar characteristics except for visible deviations between the cumulants fit and the experimental data at delay times between 0.7 μs and 0.8 μs and at 0.275 μs. The weighted residuals of the cumulants fit of the

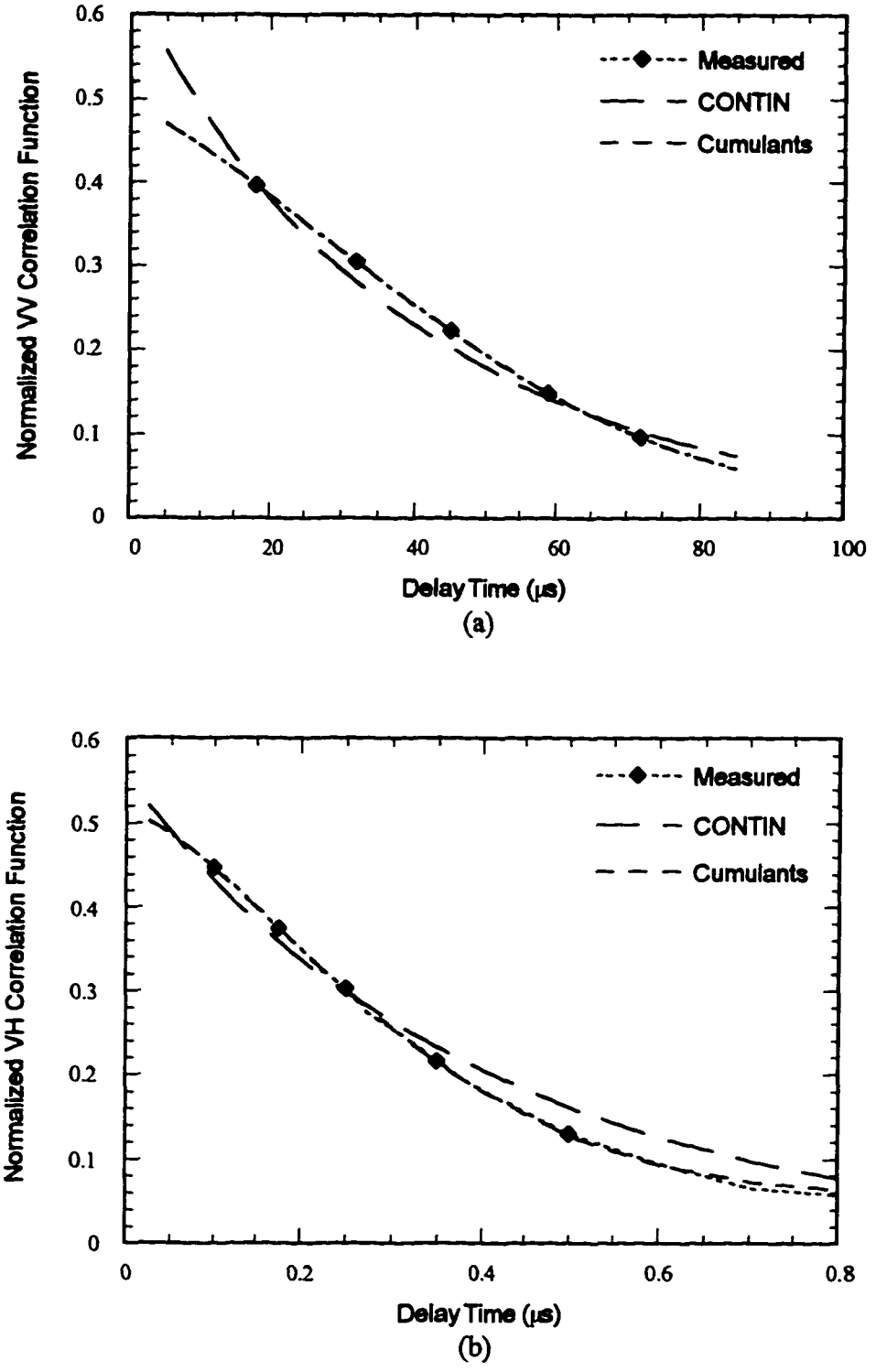

Figure 4.2.22: Comparison of CONTIN and cumulants fits of the (a) polarized and (b) depolarized normalized correlation functions measured from the seeded diffusion flame at a 35 mm height and a 5° scattering angle.

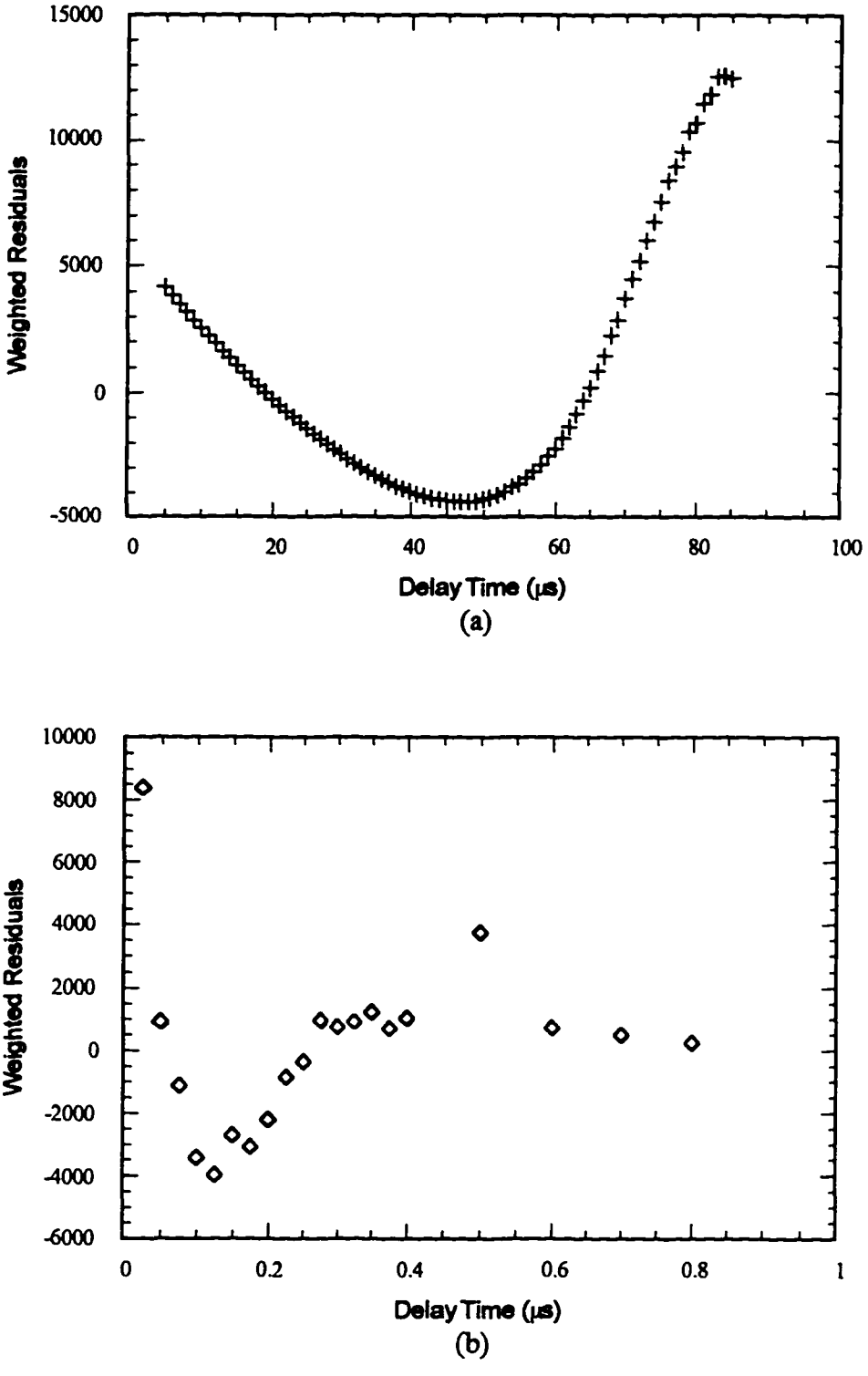

Figure 4.2.23: Weighted residuals of CONTIN fit of the (a) polarized and (b) depolarized normalized correlation functions measured from the seeded diffusion flame at a 35 mm height and a 5° scattering angle.

polarized (VV) correlation function, as depicted in figure 4.2.24 (a), exhibits some systematic trends, but the magnitude of these trends relative to the noise level is considerably less than those of the CONTIN fit. The cumulants-generated weighted residuals for the depolarized case, as shown in figure 4.2.24 (b), reveal no obvious systematic trends. Comparing the ranges of the CONTIN and cumulants weighted residuals reveals that the weighted residuals of the CONTIN fit span a range approximately an order of magnitude greater than the range spanned by the residuals of the cumulants fit, further indicating the superiority of the cumulants method in fitting the experimental data.

Since the performance differences between the CONTIN and cumulants fits were so much more drastic than those obtained from the simulated data considered in section 4.2.4.2, which used variance estimates obtained from the experimental data in order to match the experimental noise level, a third simulation incorporating a negative second cumulant is presented. Based upon the cumulants results for the VV correlation function obtained from the flame at a 30 mm height and a 5° scattering angle, the simulated data was generated using the function

$$\zeta(\tau) = \exp(-0.7 - 7000\tau - 2\times10^{8}\tau^{2}). \qquad (4.2.7)$$

The results of a CONTIN and a third-order cumulants analysis of the resulting simulated data are presented in figures 4.2.25 through 4.2.28 and in table 4.2.5. The results are virtually identical to those obtained from the measured VV correlation function presented above. The principle differences between these sets of results are that the weighted residuals of the third order cumulants fit exhibit a slight trend in that they tend to decrease with increasing delay time and that the simulated correlation function, and thus all plots of the weighted residuals, lacks the smoothness of the measured correlation function.

The comparative roughness of the simulated correlation function most likely originates from the fact the simulated noise was generated under the assumption of zero

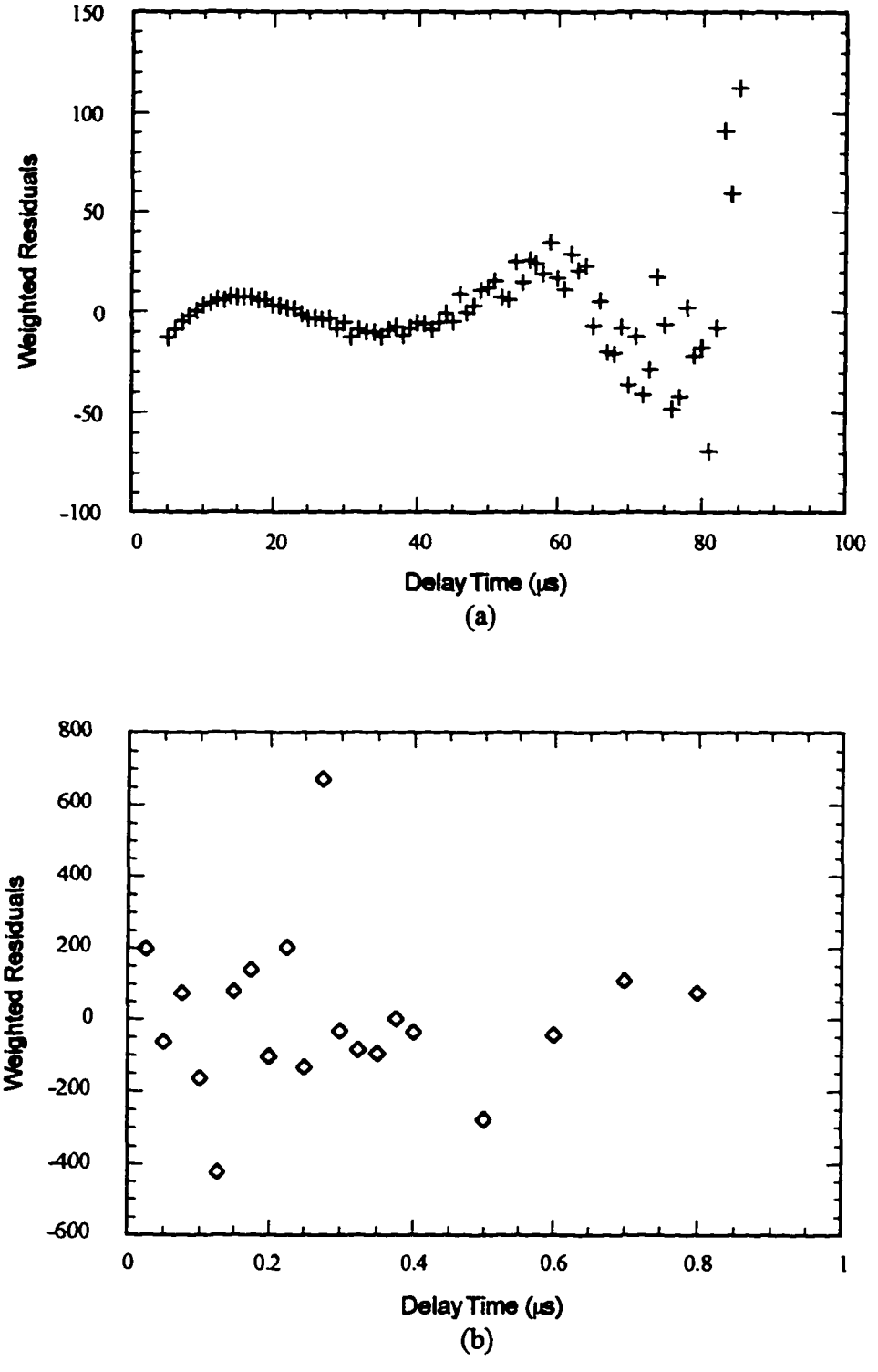

Figure 4.2.24: Weighted residuals of 4th order cumulants fit of the (a) polarized and (b) depolarized normalized correlation functions measured from the seeded diffusion flame at a 35 mm height and a 5° scattering angle.

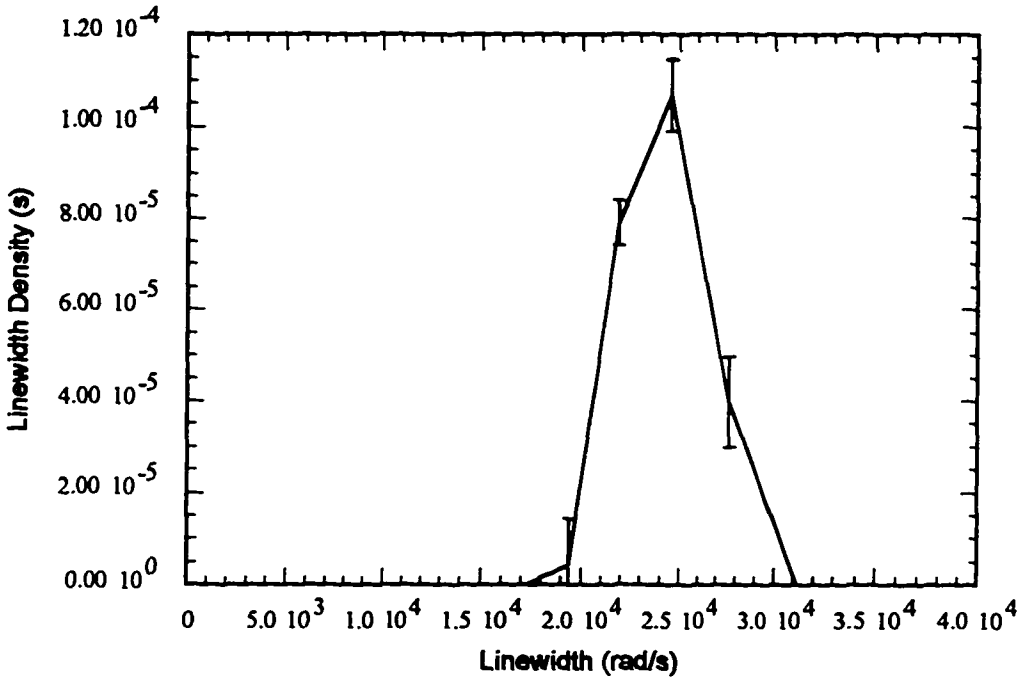

Figure 4.2.25 CONTIN-generated linewidth density corresponding to the simulated correlation function of equation 4.2.7.

Table 4.2.5: Comparison of CONTIN- and cumulants-generated moments corresponding to the simulated correlation function of equation 4.2.7.

	CONTIN	Cumulants
$\langle\Gamma\rangle_\phi \times 10^{-3}$ (rad/s)	24 ± 0.1	7.0 ± 0.6
$Var_\phi(\Gamma) \times 10^{-8}$ (rad/s^2)	0.03 ± 0.6	- 4.0 ± 0.2

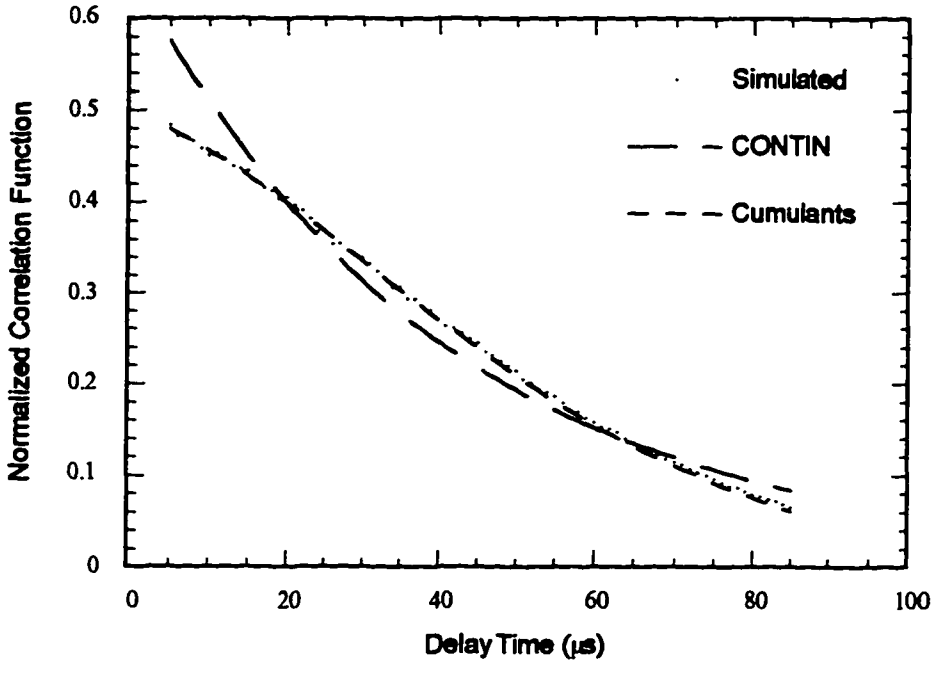

Figure 4.2.26: Comparison of CONTIN and cumulants fits of the simulated correlation function of equation 4.2.7.

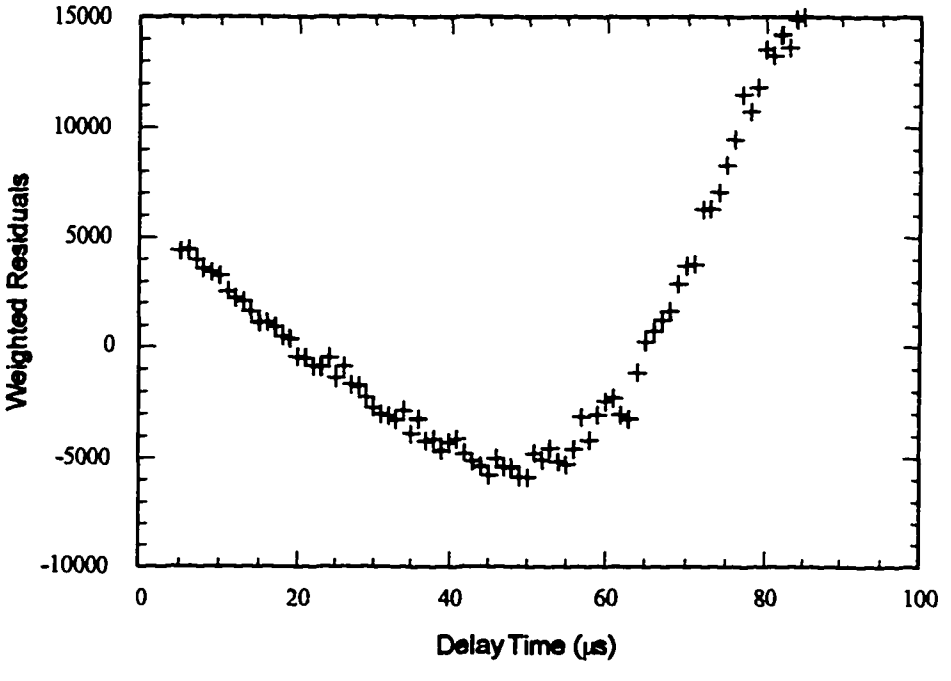

Figure 4.2.27: Weighted residuals of CONTIN fit of the simulated correlation function of equation 4.2.7.

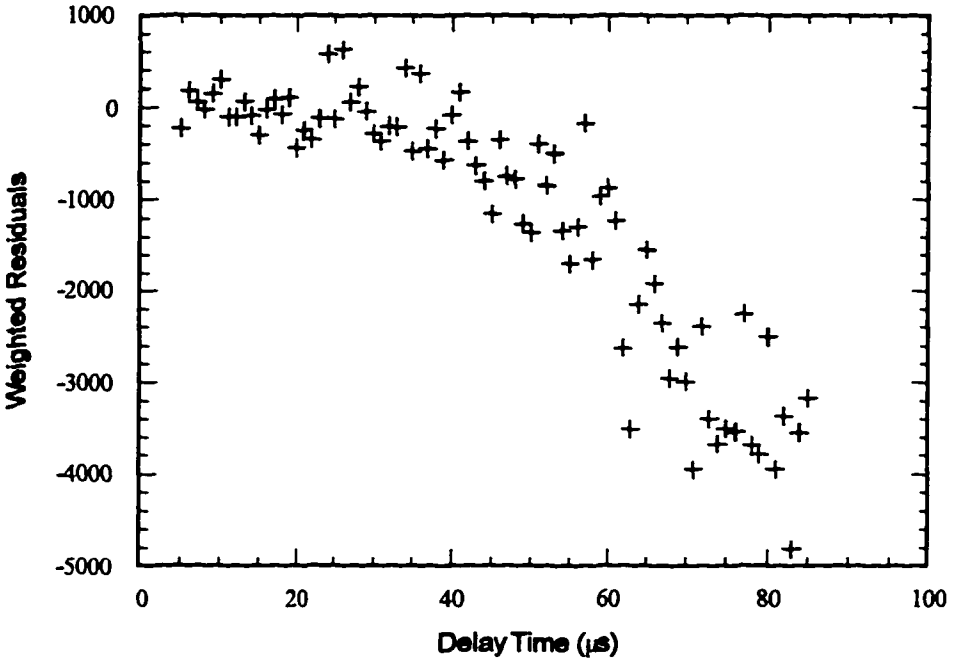

Figure 4.2.28: Weighted residuals of third-order cumulants fit of the simulated correlation function of equation 4.2.7.

covariances between separate data points. Since each point of the experimental correlation function shares the same variance as the corresponding point of the simulated correlation function, the observed smoothness of the measured correlation function implies that this assumption of zero covariances is invalid. This is most likely a result of random errors in the measured baseline. Prior to the evaluation of the variances in the program COMBINE3.BAS, each individual correlation function from the combined set is normalized with respect to the measured baseline obtained from its own data file. Thus, any error in this baseline introduces an identical error in the normalized correlation function values for all points within the same data set. This effect can produce finite covariances between separate data points, even when the raw correlation function data points exhibit zero covariances.

In addition to implying that strong covariances exist between separate points of the normalized measured correlation functions, the results of the simulation presented

above reinforces the assertion that CONTIN cannot provide an acceptable fit of correlation function data exhibiting a negative second cumulant. The presence of the negative second cumulant in the experimentally-obtained correlation functions are verified by plotting the normalized correlation function as a function of delay time on a semi-log graph. A plot of this form appears in figure 4.2.29. Based on equation 2.4.12, a normalized correlation function $\zeta_{f,k}(\tau)$ measured from a suspension of monodisperse particles should appear as a straight line when $\ln[\zeta_{f,k}(\tau)]$ is plotted as a function of τ. Equations 2.4.14 and 2.4.15 also imply that the occurance of polydispersity within the collection of scattering particles produces a finite $\mathrm{Var}_{\phi}(\Gamma_{f,k})$, which causes the $\ln[\zeta_{f,k}(\tau)]$ versus τ curve to exhibit an upward curvature. The semi-log plot of the normalized VV correlation function measured from the seeded flame at H = 35 mm and $\theta = 5^{\circ}$ clearly indicates the presence of a negative second cumulant through its downward curvature, affirming that the negativity of the second cumulants reported in tables 4.2.3 and 4.2.4 are not results of numerical errors within the cumulants inversion technique.

In addition to the values reported in tables 4.2.3 and 4.2.4 for the correlation functions measured at H = 35 mm and $\theta = 5^{\circ}$, the measurements obtained at all other heights considered between 20 mm and 35 mm systematically produced negative second cumulants K_2. The magnitudes of these cumulants are plotted as functions of height for VV detection in figure 4.2.30 and for VH detection in figure 4.2.31. According to the results shown in figure 4.2.30, the VV second-order cumulant coefficient exhibits little variation with flame height but apparently varies considerably with scattering angle θ. Due to a combination of the reduced signal-to-noise ratios of the VH correlation functions and the ill-conditioning of the matrices requiring inversion as part of the cumulants analysis process, no consistent trend is noticeable in the VH second cumulants when plotted as a function of height. A comparison between the second cumulants obtained from the depolarized correlation functions measured at

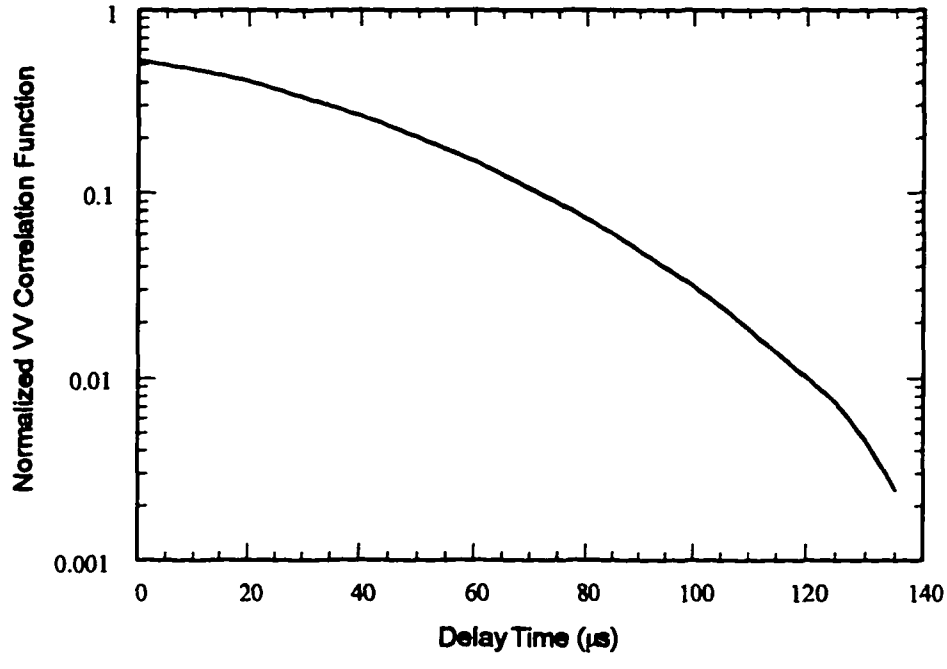

Figure 4.2.29: Semi-log plot of the normalized polarized correlation function measured from the seeded diffusion flame at a 35 mm height and a 5° scattering angle.

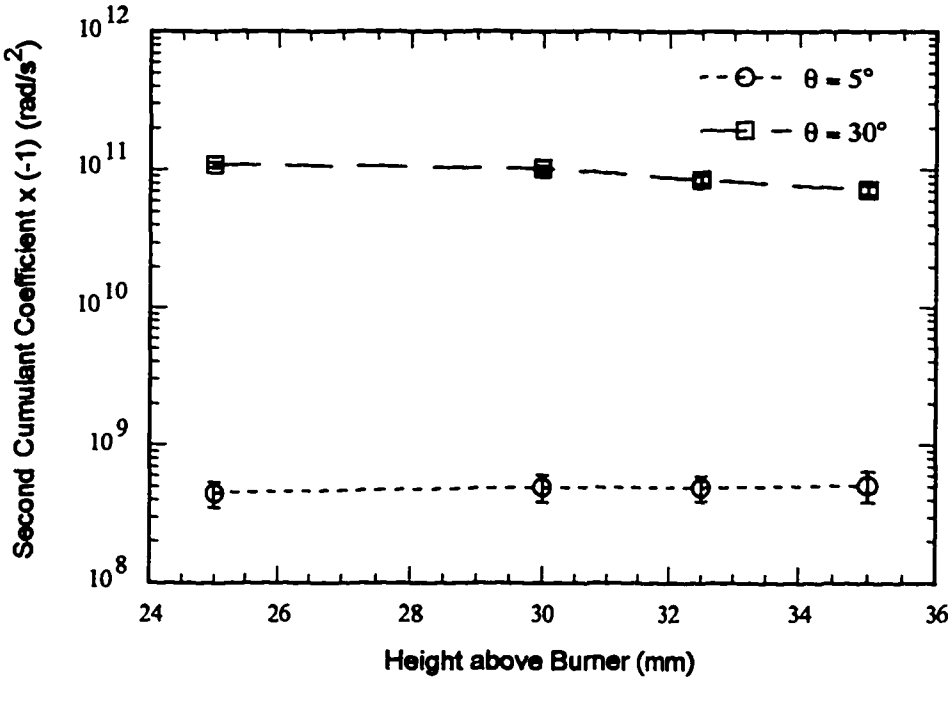

Figure 4.2.30: Variation with height of the second cumulants' absolute values, as determined from polarized photon correlation functions measured from the seeded flame.

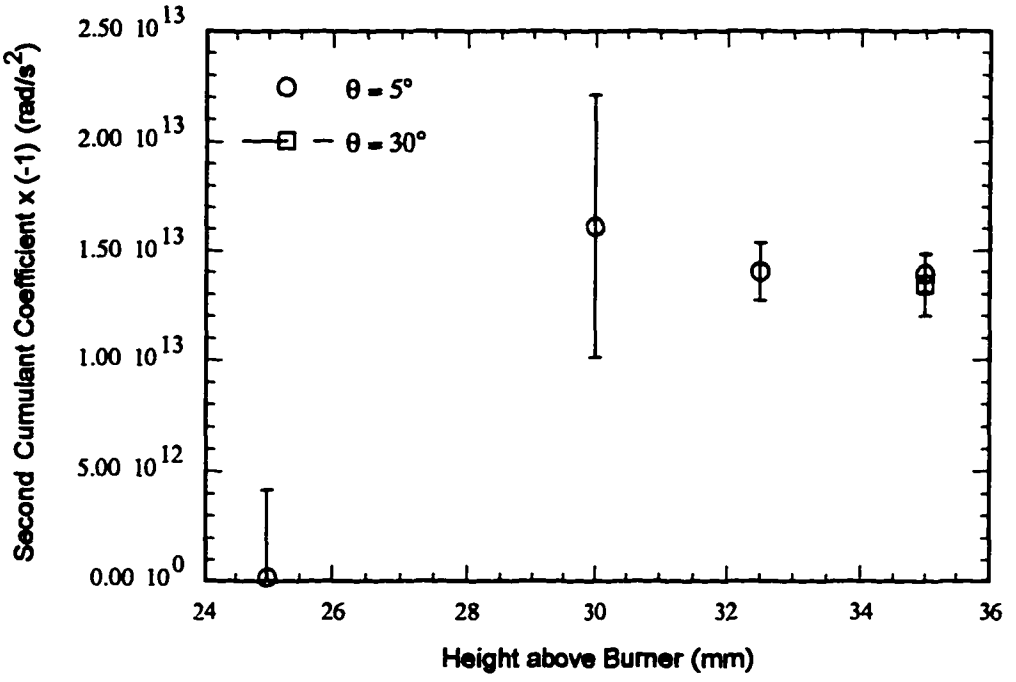

Figure 4.2.31: Variation with height of the second cumulants' absolute values, as determined from depolarized photon correlation functions measured from the seeded flame.

H = 35 mm implies that, contrary to the polarized case, the VH second cumulant exhibits little or no variation with scattering angle θ.

The definite and repeatably measurable negative second cumulants exhibited by the polarized and depolarized photon correlation functions measured from the iron-pentacarbonyl-seeded CO/O_2 diffusion flame indicate a deficiency in the model used to interpret the dynamic light scattering data for this investigated case. This implies that one or more of the assumptions utilized in obtaining equations 2.4.14 and 2.4.15 is invalid. Because the variance information is completely obscured due to the negativity of the second cumulant, a full distribution analysis of the measured correlation functions' decay rates (linewidths) cannot be performed until the cause of this effect is isolated and the data appropriately corrected.

One potential cause of this effect is the possibility that the motions of the agglomerates are significantly influenced by inertial effects. Berne and Pecora (1976) theoretically demonstrate that the VV correlation functions obtained from a simplified system of scattering particles whose motions are completely dominated by inertial effects are modeled by a Gaussian function instead of the exponential decay normally associated particles undergoing Brownian motion. Such motion would produce a zero first cumulant and a negative second cumulant upon analysis. Based upon the effects of the two limiting cases of motion completely governed by Brownian diffusion and motion completely governed by inertial effects, a reasonable assumption for intermediate cases would be that the correlation function would exhibit a positive first cumulant and second cumulant whose value is less than that predicted for the pure diffusion case.

The most obvious potential cause of the observed negative second cumulants, however, is the existence of nonuniformities within the laser light incident upon the agglomerate suspension. The effects of these nonuniformities on dynamic light scattering data obtained from flowing particles was theoretically developed by Penner et. al (1976a) for incident beams exhibiting a Gaussian intensity profile. The resulting effect manifests itself as the quadratic term occurring in equations 2.2.113, which was subsequently dropped prior to the development of the cumulants equations (equations 2.4.14 and 2.4.15) in Chapter 2. When the magnitude of this term is comparable to the other arguments of the exponentials, it can reduce the magnitude of the second cumulant because this quadratic term in τ contains a negative coefficient. The following section presents the results of an experiment designed to determine the extent of influence of the incident beam nonuniformities on the measured correlation functions.

4.2.4.4 Experimental Investigation of the Effects of the Non-Uniform Incident Intensity Profile on the Measured Correlation Functions

According to equations 2.2.113 of Chapter 2, the theoretical correlation functions contain a Gaussian factor that was neglected when developing the Laplace integral and cumulants relationships of section 2.4. This factor results from the fact that lasers operating in the TEM 00 mode exhibit a Gaussian intensity profile. As mentioned in section 2.4, this term is negligible when $(V_\perp\tau_f)^2/(2\omega_o^2) \ll q^2D\tau_f$, where τ_f is the final measured delay time, which was initially assumed valid for the studied flame. The second cumulants obtained from the experimental correlation function data, however, casts a doubt upon this assumption's accuracy. The discussion that follows describes an attempt to optically determine whether or not the non-uniform incident beam profile is responsible for the negativity of the correlation functions' second cumulant coefficients.

If the Gaussian factor in equations 2.2.113 is not neglected prior to the derivation of equations 3.4.15 relating the cumulants coefficients to the linewidth moments, then the operations performed by equations 2.4.6 on the theoretical correlation functions of 2.2.113 result in the following expression for the normalized correlation function $\zeta_{f,k}(\tau)$:

$$\zeta_{f,k}(\tau) = \int_0^\infty F_{f,k}(\Gamma_{f,k}) \exp(-\Gamma_{f,k}\tau - \Lambda\tau^2)\, d\Gamma_{f,k}, \tag{4.2.8}$$

where

$$\Lambda = \frac{V_\perp^2}{2\,\omega_o^2} \tag{4.2.9}$$

and $F_{f,k}(\Gamma_{f,k})$ and $\Gamma_{f,k}$ share the same definitions as in section 2.4. Utilizing equations 2.4.13, 2.4.14, and 2.4.15 with the expansion of $\zeta_{f,k}(\tau)$ as a MacLaurin series in τ yields the following expressions for the first three cumulants:

$$K_0' = K_0 = \ln[\zeta_{f,k}(0)] \tag{4.2.10a}$$

$$K_1' = K_1 = \langle \Gamma_{f,k} \rangle_\phi \tag{4.2.10b}$$

and

$$K_2' = \mathrm{Var}_\phi(\Gamma_{f,k}) - 2\Lambda, \tag{4.2.10c}$$

Relating equation 4.2.9 to the diameter $d_1 = 2\omega_1$ of aperture D1 using equation 3.3.3 of Chapter 3 and substituting the result into equation 4.2.10c yields

$$K_2' = \mathrm{Var}_\phi(\Gamma_{f,k}) - \Xi\, d_1^2 \tag{4.2.11}$$

where

$$\Xi = \frac{1}{2}\left(\frac{\pi V_\perp}{\lambda f_1}\right)^2. \tag{4.2.12}$$

Equations 4.2.11 and 4.2.12 imply that the second cumulant K_2' is a linear function of the square of the diameter of aperture D1. This property is exploited in order to determine $\mathrm{Var}_\alpha(\Gamma_{V,1})$ and Ξ from VV DLS measurements obtained at H = 35 mm and $\theta_1 = 5°$ using various aperture diameters d_1 ranging from 0.6 mm to 3.57 mm. The second cumulants K_2' obtained from the resulting correlation functions are plotted in figure 4.2.32 as functions of d_1^2. As predicted by equation 4.2.11, the second cumulants vary in an approximately linear fashion with d_1^2. Also, in accordance with equation 4.2.11, the slope of this variation is negative. A weighted least squares fit of this data yields $\mathrm{Var}_\alpha(\Gamma_{V,1}) = -1.0 \times 10^8 (\pm 0.1 \times 10^8)$ rad/s^2 and $\Xi = 5.4 \times 10^7 (\pm 0.1 \times 10^7)$ rad/(mm·s)^2, where the uncertainties were determined from the scatter of the second cumulants without considering their individual uncertainties. Even though the second cumulants experimentally vary with d_1^2 in the expected fashion, the second cumulant obtained by extrapolating this data to $d_1^2 = 0$ mm, which should equal $\mathrm{Var}_\alpha(\Gamma_{V,1})$, is a negative number. Thus, the conclusions obtained from this experiment are that the Gaussian intensity profile, which is affected by aperture diameter d_1, partially accounts for the negative second cumulant obtained from the DLS data. Since the $d_1^2 = 0$ mm value of the second cumulant is still negative, however, the non-uniform beam profile effect is apparently not the sole cause of the second cumulant results.

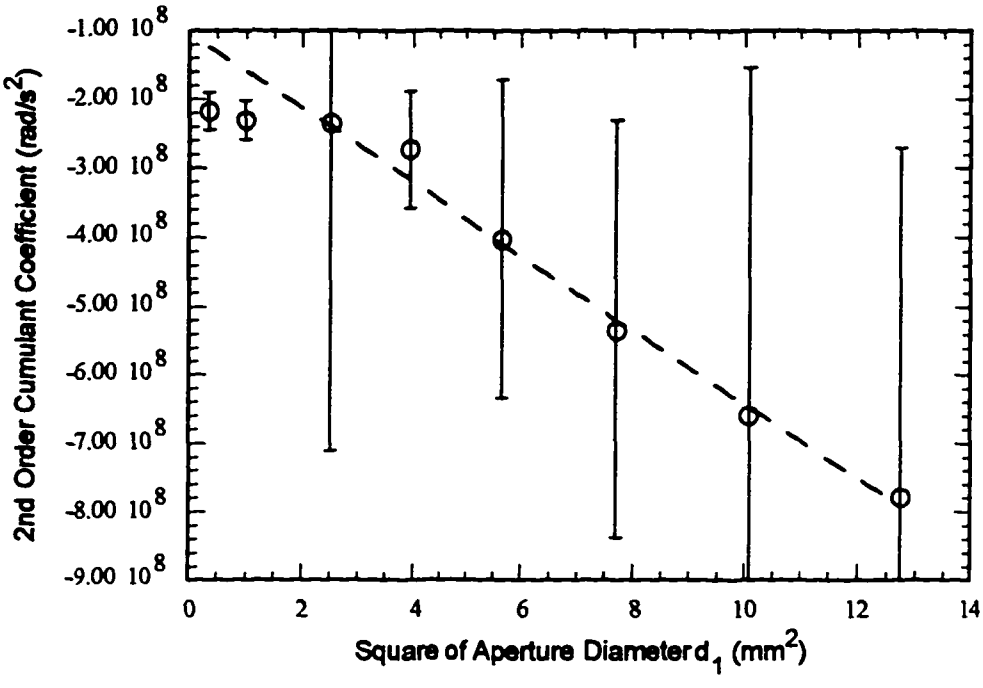

Figure 4.2.32: Experimental dependence of the second order cumulant on the square of the diameter of aperture D1.

4.2.5 Comparison of Optically Obtained Brownian Diffusion Coefficients with Theoretical Estimates

According to equation 4.2.10, the inclusion of the Gaussian factor generated by the motion of the particles through nonuniformities in the incident beam does not affect the interpretation of the first cumulant K_1. Assuming that this cumulant is not influenced by the effect producing the negative second cumulant and thus truly represents the polarizability-weighted mean linewidth $\langle \Gamma_{f,k} \rangle_\phi$, then the first cumulant coefficients extracted from the VV and VH correlation functions can be used to obtain estimates of the Brownian translational and rotational diffusion coefficients using equations 2.4.9 of Chapter 2. The resolution of both diffusion coefficients requires the combination of two independently-measured correlation functions. Two cases are considered:

a) The first cumulants from the polarized (VV) and depolarized (VH) correlation functions obtained at a single scattering angle θ_k are combined to provide the diffusion coefficient estimates according to the following solutions of equations 2.4.9:

$$D = \frac{\Gamma_{V,k}}{q_k^2} \qquad \text{and} \qquad D_R = \frac{\Gamma_{H,k} - \Gamma_{V,k}}{6}. \qquad (4.2.13a,b)$$

b) The first cumulants from the depolarized (VH) correlation functions obtained at two separate scattering angles θ_1 and θ_2 are combined for an estimation of the Brownian diffusion coefficients according to these alternative solutions to equations 2.4.9:

$$D = \frac{\Gamma_{H,1} - \Gamma_{H,2}}{q_1^2 - q_2^2} \quad \text{and} \quad D_R = \frac{q_1^2\Gamma_{H,1} - q_2^2\Gamma_{H,2}}{6(q_1^2 - q_2^2)}. \quad (4.2.14a,b)$$

In both cases the estimate is obtained by replacing each linewidth $\Gamma_{f,k}$ by its $|\phi|^2$-weighted mean $\langle\Gamma_{f,k}\rangle_\phi$, which is given by the corresponding first-order cumulant coefficient. With this substitution, equation 4.2.13a provides the $|\alpha|^2$-weighted mean translational diffusion coefficient $\langle D\rangle_\alpha$ and equations 4.2.14 provide the $|\beta|^2$-weighted mean translational and rotational diffusion coefficients $\langle D\rangle_\beta$ and $\langle D_R\rangle_\beta$. Applying the substitution to equation 4.2.13b to estimate the rotational diffusion coefficient D_R mixes the weighting functions within the average. Using the first-order cumulants with equation 4.2.13b thus provides meaningful results only if the $|\alpha|^2$ and $|\beta|^2$ weights are functionally similar. Based on the prolate ellipsoid polarizability estimates presented in section 2.3.1 of Chapter 2, each polarizability component exhibits a nearly linear functional variation with the volume of the scattering particle, thus having similar functional properties. Deviations are most likely to arise either from the L_j functions of equation 2.3.2 or from deviations between the actual scattered light properties and the simplified dipole solution presented in section 2.3.1.

The Brownian translational diffusion coefficients calculated for each measured height along the seeded flame's central axis through substitution of the first-order

cumulant coefficients from the VV correlation functions into equation 4.2.13a are plotted against the mean aspect ratios of the corresponding thermophoretically-sampled agglomerates in figure 4.2.33. In addition to vertical error bars representing the uncertainty of the diffusion coefficients, horizontal errors representing the uncertainties of the mean aspect ratios are also shown. For both the $\theta = 5°$ and the $\theta = 30°$ cases the translational diffusion coefficient D generally decreases with increasing aspect ratio. The diffusion coefficients extracted from the 5°-scattering-angle data disagree with those found from the 30°-scattering-angle data by a factor of about 2.5, possibly as a result of optical interagglomerate interference at the 30° scattering angle [Berne and Pecora, 1976].

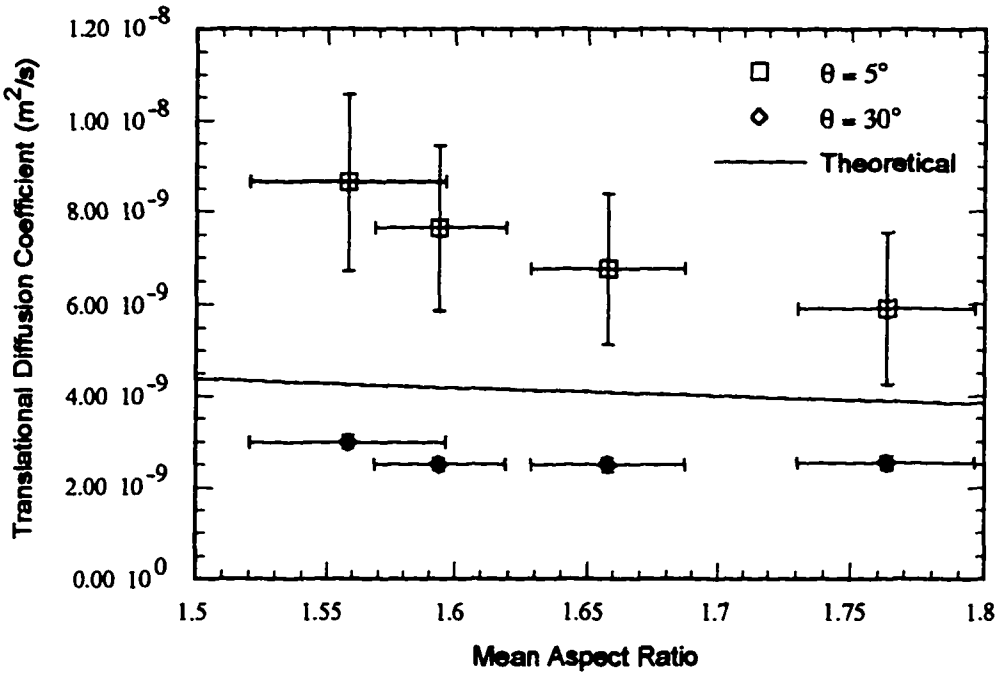

Figure 4.2.33:Functional dependencies of optically-obtained and theoretically estimated translational Brownian diffusion coefficients on aspect ratio.

Theoretical estimates of the Brownian translational diffusion coefficients were also computed for each mean aspect ratio using equations 2.3.12 to 2.3.14 of Chapter 2. A volume-equivalent sphere radius was used in evaluating the Cunningham correction factor, which accounts for non-continuum flow effects. Based on the best-fit ellipses

determined by NIH Image for the thermophoretically-sampled agglomerates, the agglomerates were approximated as prolate ellipsoids with 84 nm minor axis lengths and aspect ratios varying from 1.5 to 1.8. The combustion gas dynamic and kinematic viscosities μ and ν that were needed for these calculations were obtained using published property data data [Incropera and DeWitt, 1985] in conjunction with the average radiation-corrected flame temperature (1134 K) measurement. Because the exact composition of the combustion gases within the scattering volume is unknown, the viscosity of air, which functions as the reaction's oxidizer, is assumed representative of the true flame viscosity. Based upon the published viscosity tables of Incropera and DeWitt (1985), this viscosity lies between the viscosities of CO, CO_2, N_2, and O_2, all of which should be present in the CO/air flame. The results of these diffusion coefficient calculations are also plotted in figure 4.2.33 for comparison with the optically obtained values. The theoretical estimate lies between the two experimental curves and follows the same general trend: the diffusion coefficient decreases with increasing aspect ratio.

Rotational diffusion coefficients obtained from the optical data at various heights using analysis methods (a) and (b) listed above are plotted versus the corresponding mean aspect ratios in figure 4.2.34. Like the translational diffusion coefficients shown in figure 4.2.33, the rotational diffusion coefficients extracted from the 5° polarized and depolarized correlation functions generally decrease with increasing aspect ratio.

Since no adequate theoretical relationship between the agglomerate morphology and rotational diffusion coefficient could be found, two separate theoretical approximations of D_R were evaluated for comparison with the optically determined values. One approximation was obtained using the continuum flow relationship between D_R and the morphological parameters of a prolate ellipsoid given by equation 3.2.15 of Chapter 2. The other estimate was generated by multiplying the continuum flow result by the Cunningham correction factor used for the translational case. Both of

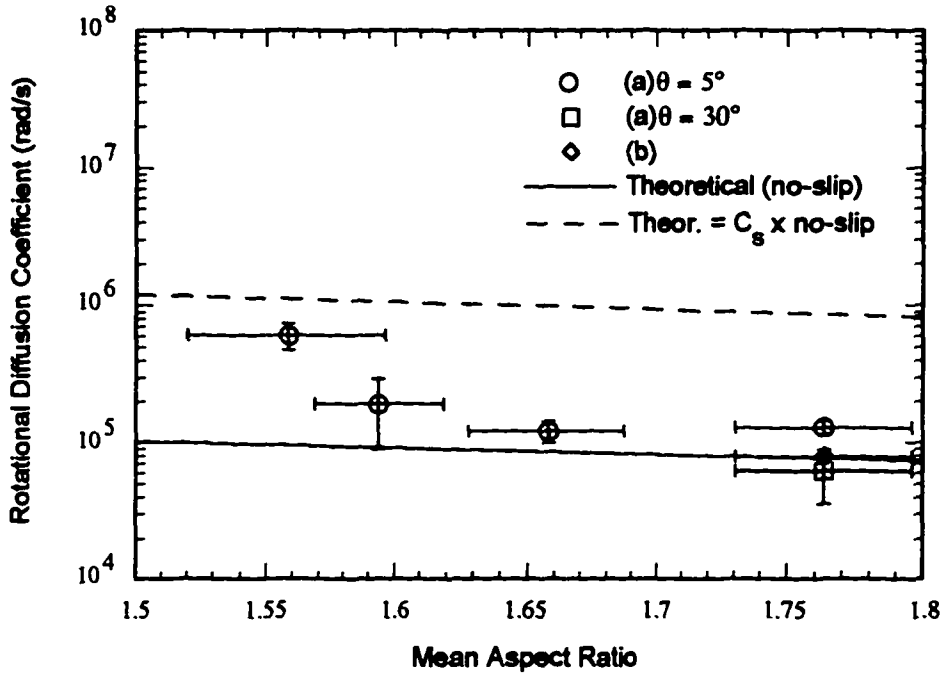

Figure 4.2.34:Functional dependencies of optically-obtained and theoretically estimated rotational Brownian diffusion coefficients on aspect ratio.

these theoretical estimates appear in figure 4.2.34. Most of the optically obtained diffusion coefficients have values between these two theoretical estimates. Additionally, both of these estimates exhibit a decreasing trend with increasing mean aspect ratio similar to, but not as extreme as, the optically-obtained rotational diffusion coefficients.

In conclusion, both the translational and rotational polarizability-weighted mean Brownian diffusion coefficients exhibit an order-of-magnitude agreement with the theoretical estimates obtained using equations 2.3.11 to 2.3.15 with the ex situ morphological results and the radiation-corrected flame temperature measurements. Additionally, all diffusion coefficient results generally decrease with increasing aspect ratio. The combination of the polydispersity of the agglomerates obtained from the flame with the negative second cumulant effect in the optical results prevented a more accurate experimental determination of the diffusion coefficients by requiring the use of

polarizability-weighted averages. Removal of either of these two conditions should result in more reliable linewidth determinations, either by permitting the direct evaluation of equations 4.2.13 and 4.2.14 (the monodisperse case), or by facilitating a linewidth distribution analysis, the results of which could be quantitatively combined with the morphology density functions of section 4.1.2.2 to establish a correspondence between the morphological parameters and the diffusion coefficients.

Chapter 5

Conclusions and Recommendations

5.1 Summary and Conclusions

As a result of the effects of agglomerate morphology on the bulk properties of materials formed from fine particulates, on the radiative heat transfer from sooting flames, and on the filtration and deposition dynamics of air borne particulates, a need exists for the accurate measurement of the morphological properties characterizing sub-micron sized agglomerated particulates. In situ measurement techniques are generally preferrable to the intrusive ex situ methods because they are usually more easily automated and are less likely to affect the properties being measured. The work of this study was directed towards improving the current technology for the in situ optical measurement of the morphological and dynamic properties of agglomerates occuring within flames. This investigation focused primarily on dynamic light scattering (DLS) techniques because of their insensitivity to the typically unknown refractive indices of the particles being studied and because they provide information about the particle dynamics. The incorporation of depolarized DLS measurements, along with its accompaning implied recognition of the non-spherical nature of the agglomerates, distinguishes the current investigation from previous DLS investigations of flames.

In addition to the ability to accurately measure scattered-light correlation functions, the determination of agglomerate morphological parameters from DLS experiments also requires knowledge of a valid theoretical relationship between the optical correlation functions and the particle dynamics, which are typically characterized by the Brownian diffusion coefficients. Additionally, a numerical algorithm, such as CONTIN or the cumulants method, is required for extracting these diffusion coefficients from the DLS data. Finally, the morphological properties can be

determined from the diffusion coefficients, given accurate relationships between thethese two quantities. Such relationships depend on the thermophysical properties of the flame gases, thus requiring flame temperature measurements. For the non-continuum environment characteristic of high temperature flames, accurate relationships between the morphological and dynamic parameters of nonspherical particles are unavailable, neccessitating the determination of such relationships before agglomerate morphologies can be measured directly using DLS experiments.

Within the present study, the theory of dynamic light scattering was reviewed and integrated into a unified perspective for use in designing and interpreting DLS experiments. Measurements were then performed on the chainlike iron oxide agglomerates formed within an iron-pentacarbonyl-seeded carbon monoxide - oxygen diffusion flame.

The flame constituents were characterized with flame temperature and ex situ agglomerate morphology measurements. Flame temperatures were measured using a thermocouple and corrected for energy loss due to radiative heat transfer between the thermocouple and its surroundings. Probability density functions representing the morphological properties of the flame-borne agglomerates were determined using digital image analyses of transmission electron micrographs of agglomerates thermophoretically sampled from the flame at various locations along its central axis. The results of these measurements were used to estimate the agglomerates' Brownian translational and rotational diffusion coefficients using known relationships.

The optical measurements performed for this study include polarized and depolarized dynamic light scattering measurements and classical depolarization measurements along the flame's central axis. The results were analyzed using both the inverse Laplace transformation algorithm CONTIN and the moments determination technique of cumulants. Based upon the optical results, the Brownian translational and rotational diffusion coefficients were estimated, related to the thermophoretically-

obtained agglomerate aspect ratios, and compared to their corresponding theoretical estimates.

The results of this investigation are summarized as follows:

1) Thermophoretically extracted samples reveal the presence of chainlike agglomerates consisting of apparently crystalline iron oxide primary particles, in agreement with previous investigations. These agglomerates exhibit polydispersity in both primary particle diameter and agglomerate length.
2) The systematic noise generated in measured photon correlation functions by afterpulsing and dead time in the detection system are virtually eliminated by cross-correlating the outputs of two separate detectors instead of autocorrelating the output of a single detector. This observation agrees with the reports of previous investigators.
3) Accurate depolarized photon correlation functions have been sucessfully measured from the flame using the cross-correlation detection scheme discussed above by combining the results of 6 to 12 five-minute-long experiments performed using laser powers from 2.50 W to 2.75 W. Deposition of iron oxide particles on the burner and honeycomb stabilizer prevent the use of a single long-duration experiment.
4) Numerical inverse Laplace transforms of the measured correlation functions using CONTIN produce an unacceptable fit of the original data. Variations in the weighted residuals imply that, under the measured conditions, the Laplace integral does not accurately represent the measured correlation function.
5) Contrary to the CONTIN results, a cumulants analysis provided an acceptable fit of the original data.

6) The cumulants analyses consistently revealed the presence of negative second cumulant coefficients, which contradicts the conventional interpretation of the second-order coefficients as positive definite quantities representing the polarizability-weighted variances of the linewidths. This result implies that one or more of the assumptions used in the interpretation of the DLS data are invalid. Simulated data studies imply that the existence of this negative second cumulant prevents CONTIN from generating accurate fits of the experimental data.

7) By varying the focused-beam spot size at the scattering location, incident beam nonuniformities were identified as a contributor to the negative second cumulant effect. The results imply, however, that these nonuniformities are not the exclusive cause of this effect.

8) Polarizability-weighted mean Brownian translational and rotational diffusion coefficients generated from the first-order cumulant coefficients of the optical correlation functions compare favorably with theoretical estimates obtained using flame temperature measurements and ex situ morphology results. These diffusion coefficients all decrease with increasing aspect ratio and agree numerically within an order of magnitude.

5.2 Recommendations for Future Research

Within the present investigation, polarized and depolarized correlation functions were successfully measured from a $Fe(CO)_5$-seeded CO/O_2 diffusion flame, the results of which were compared with computations performed using agglomerate morphology data obained from TEM micrographs of thermophoretically-sampled agglomerates. The accuracy of the analysis, however, was limited by the complexity of the physical system being measured. The presence of polydispersity of the agglomerate morphology in combination with the phenomena responsible for the negativity of the second cumulant coefficients prevented individual comparisons between the diffusion coefficients and

agglomerate aspect ratios. For this study, only mean quantities could be compared. Therefore, the main recommendations for future research concern simplifying the conditions of the experiment so that individualized comparisons can be made between the Brownian diffusion coefficients and the agglomerate morphological parameters and so that the causes of the observed negative second cumulant can be conclusively identified. These recommendations, along with a few others, are as follows:

1) Experimental relationships between the Brownian diffusion coefficients and the morphologies of nonspherical particles could be more accurately determined if the number of variables in the experiment were reduced. In the study by Hinds and Reist (1972), a DLS investigation was performed on an aerosol of polystyrene spheres that was generated by first sending an aqueous suspension of the spheres through a nebulizer to generate a fine spray. This spray was then combined with dry air to evaporate the liquid water. If an independent source of monodisperse elongated particles with known size is found and these particles are introduced into a non-sooting flat flame using a similar technique, their diffusion coefficients diffusion coefficients could be accurately determined using DLS measurements without the analytical complexities accompanying polydisperse particles, such as the ones obtained in this experiment. With prior knowledge of the particles' morphologies, a more accurate experimental morphology/diffusion-coefficient relationship could be obtained.
2) For comparison with experimental morphology/diffusion-coefficient relationships and for use in interpreting DLS data from flames, a theoretical relationship between the morphological parameters and rotational diffusion coefficients of cylindrical or ellipsoidal particles should be developed for the free-molecule flow regime. This would involve determining the rotational friction factor and substituting the result

into the Stokes-Einstein equation for diffusion coefficients. Since the presence of the particle does not affect the velocity distribution of the surrounding gas molecules under free-molecule conditions, the determination of the rotational friction factor should be analytically possible.

3) Inertial effects on the motions of the scattering particles and the resulting effects on the measured correlation functions should be investigated for flame environments. As mentioned in section 4.2.4.2, inertial effects are likely causes for the negative second cumulants observed in this experiment.
4) Measurements of the vertical flame velocity (possible using laser doppler velocimetry) and the incident laser intensity profile should be performed to verify the results of section 4.2.4.4, which reports the results of optical experients designed to ascertain the effect of the incident beam non-uniformities on the measured photon correlation functions.
5) Magnetic interactions between independent agglomerates may influence the optical correlation functions and should be investigated. In this study, the agglomerate motions were assumed independent of each other.
6) Independent classical light scattering experiments may provide an independent source of agglomerate morphology information for comparison with the DLS results and those from the thermophoretically-obtained samples.

References

Arfken, G., *Mathematical Methods for Physicists.* (3rd ed.) Academic Press, Orlando, 1985.

Asgharian, B., Yu, C. P., and Gradon, L., "Diffusion of Fibers in a Tubular Flow." *Aerosol Sci. Technol.* 9: 213 - 219 (1988).

Bargeron, C. B., "Measurement of a Continuous Distribution of Spherical Particles by Intensity Correlation Spectroscopy: Analysis by Cumulants." *J. Chem. Phys.* 61: 2134 - 2138 (1974).

Benedek, G. B., "Optical Mixing Spectroscopy, with Applications to Problems in Physics, Chemistry, Biology and Engineering." *Polarization, Matter, and Radiation.* pp. 49 - 84 (1969).

Berne, B. J., and Pecora, R., *Dynamic Light Scattering with Applications to Chemistry, Biology, and Physics.* Wiley, New York, 1976.

Bohren, C. F., and Huffman, D. R., *Absorption and Scattering of Light by Small Particles.* Wiley, New York, 1983.

Borse, G. J., *FORTRAN 77 and Numerical Methods for Engineers.* PWS Engineering, Boston, 1985.

Brock, J. R., "On the Theory of Thermal Forces Acting on Aerosol Particles." *J. Colloid Sci.* 17: 768 - 780 (1962).

Brookhaven Instruments Corporation, *Instruction Manual for Model BI-9000AT Digital Correlator.* 1993.

Burstyn, H. C., Chang, R. F., and Sengers, J. V., "Nonexponential Decay of Critical Concentration Fluctuations in a Binary Liquid." *Phys. Rev. Lett.* 44: 410 - 413 (1980).

Cai, J., and Sorensen, C. M., "Diffusion of Fractal Aggregates in the Free Molecular Regime." *Phys. Rev. E.* 50: 3397 - 3400 (1994).

Cantor, C. A., and Schimmel, P. R., *Biophysical Chemistry.* W. H. Freeman, San Francisco, 1980.

Charalampopoulos, T. T., "An Automated Light Scattering System and a Method for the *In Situ* Measurement of the Index of Refraction of Soot Particles." *Rev. Sci. Instrum.* 58: 1638 - 1646 (1987).

Charalampopoulos, T. T., "Morphology and Dynamics of Agglomerated Particulates in Combustion Systems Using Light Scattering Techniques." *Prog. Energy Combust. Sci.* 18: 13 - 45 (1992).

Charalampopoulos, T. T., and Chang, H., "*In Situ* Optical Properties of Soot Particles in the Wavelength Range from 340 nm to 600 nm." *Combust. Sci. and Tech.* 59: 401 - 421 (1988).

Charalampopoulos, T. T., and Chang, H., "Agglomerate Parameters and Fractal Dimension of Soot Using Light Scattering - Effects on Surface Growth." *Combust. Flame.* 87: 89 - 99 (1991).

Cheng, M-T, Xie, G-W, Fu, T-H, and Shaw, D. T., "Filtration of Ultrafine Chain Aggregate Aerosols by Nuclepore Filters." *J. Aerosol Sci. Technol.* 15: 30 - 35 (1991).

Chowdhury, D. P., Sorensen, C. M., Taylor, T. W., Merklin, J. F., and Lester, T. W., "Application of Photon Correlation Spectroscopy to Flowing Brownian Motion Systems." *Appl. Opt.* 23: 4149 - 4154 (1984).

Cramer, H., *Mathematical Methods of Statistics.* Princeton University Press, Princeton, 1946 (pp. 283 - 285).

Crosby, C. R., III, Ford, N. C., Jr., Karasz, F. E., and Langley, K. H., "Depolarized Dynamic Light Scattering of a Rigid Macromolecule Poly(*P*-Phenylene Benzbisthiazole)." *J. Chem. Phys.* 75: 4298 - 4306 (1981).

Cummins, H. Z., and Swinney, H. L., "Light Beating Spectroscopy." *Progress in Optics.* 8: 133 - 200 (1970).

Dahneke, B. E., "Slip Correction Factors for Nonspherical Bodies - I. Introduction and Continuum Flow." *J. Aerosol Sci.* 4: 139 - 145 (1973a).

Dahneke, B. E., "Slip Correction Factors for Nonspherical Bodies - II. Free Molecule Flow." *J. Aerosol Sci.* 4: 147 - 161 (1973b).

Dahneke, B. E., "Slip Correction Factors for Nonspherical Bodies - III. The Form of the General Law." *J. Aerosol Sci.* 4: 163 - 170 (1973c).

DeLong, L. M., and Russo, P. S., "Particle Size Distribution by Zero-Angle Depolarized Light Scattering." in *Polymer Characterization: Physical Property, Spectroscopic, and Chromatographic Methods.* (C. D. Carver and T. Provder, eds.) American Chemical Society, Washington DC, 1990.

Dobbins, R. A., and Megaridis, C. M., "Morphology of Flame-Generated Soot as Determined by Thermophoretic Sampling." *Langmuir.* 3: 254 - 259 (1987).

Driscoll, J. F., Mann, D. M., and McGregor, W. K., "Submicron Particle Size Measurements in an Acetylene-Oxygen Flame." *Combust. Sci. Technol.* 20: 41 - 47 (1979).

Drolen, B. L., and Tien, C. L., "Absorption and Scattering of Agglomerated Soot Particulate." *J. Quant. Spectrosc. Radiat. Transfer.* 37: 433 - 448 (1987).

Favro, L. D., "Theory of the Rotational Brownian Motion of a Free Rigid Body." *Phys. Rev.* 119: 53 - 62 (1960).

Favro, L. D., "Rotational Brownian Motion," in *Fluctuation Phenomena in Solids.* (R. E. Burgess, ed.), Academic, New York, 1965, pp. 79 - 102.

Flower, W. L., "Optical Measurements of Soot Formation in Premixed Flames." *Combust. Sci. Technol.* 33: 17 - 33 (1983).

Ford, N. C., Jr., "Biochemical Applications of Laser Rayleigh Scattering." *Chemica Scripta* 2: 193 - 206 (1972).

Ford, N. C., Jr., "Light Scattering Apparatus." in *Dynamic Light Scattering - Applications of Photon Correlation Spectroscopy.* (R. Pecora, ed.), Plenum Press, New York, 1985.

Forrester, A. T., Gudmundsen, R. A., and Johnson, P. O., "Photoelectric Mixing of Incoherent Light." *Phys. Rev.* 99: 1691 - 1700 (1955).

Forrester, A. T., "Photoelectric Mixing as a Spectroscopic Tool." *J. Opt. Soc. Am.* 51: 253 - 259 (1961).

Fowles, G. R., *Introduction to Modern Optics.* (2nd ed.) Dover, New York, 1975.

Fox, R. W., and McDonald, A. T., *Introduction to Fluid Mechanics.* (3rd ed.) Wiley, New York, 1985.

Fucile, E., Borghese, F. Denti, P., and Saija, R., "Theoretical Description of Dynamic Light Scattering From an Assembly of Large Axially Symmetric Particles." *J. Opt. Soc. Am. A.* 10: 2611 - 2617 (1993).

Glauber, R. J., "Coherent and Incoherent States of the Radiation Field." *Phys. Rev.* 131: 2766 - 2788 (1963).

Guenther, R. D., *Modern Optics.* Wiley, New York, 1990.

Hahn, D. W., and Charalampopoulos, T. T., "The Role of Iron Additives in Sooting Premixed Flames." *Twenty Fourth Symp. (Intl.) on Combustion.* The Combustion Institute, Pittsburgh, 1992, pp. 1007 - 1014.

Hinds, W. and Reist, P. C., "Aerosol Measurement by Laser Doppler Spectroscopy - 1. Theory and Experimental Results for Aerosols Homogeneous." *Aerosol Science.* 3: 501 - 514 (1972).

Incropera, F. P., and DeWitt, D. P., *Introduction to Heat Transfer.* Wiley, New York, 1985.

Jackson, J. D., *Classical Electrodynamics.* (2nd ed.) Wiley, New York, 1975.

Jakeman, E., "Theory of Optical Spectroscopy by Digital Autocorrelation of Photon-Counting Fluctuations." *J. Phys. A: Gen. Phys.* 3: 201 - 215 (1970).

Jakeman, E., Oliver, E. J., and Pike, E. R., "The Effects of Spatial Coherence on Intensity Fluctuation Distributions of Gaussian Light." *J. Phys. A.* 3: L45 - L48 (1970).

Jakeman, E., Pike, E. R., and Swain, S., "Statistical Accuracy in the Digital Autocorrelation of Photon Counting Fluctuations." *J. Phys. A: Gen. Phys.* 517 - 534 (1971).

Jakeman, E., Pusey, P. N., and Vaughan, J. M., "Intensity Fluctuation Light-Scattering Spectroscopy Using a Conventional Light Source." *Optics Communications.* 17: 305 - 308 (1976).

Jones, A. R., "Electromagnetic Wave Scattering by Assemblies of Particles in the Rayleigh Approximation" *Proc. R. Soc. Lond. A.* 366: 111 - 127 (1979).

Jones, A. R., "Correction to 'Electromagnetic Wave Scattering by Assemblies of Particles in the Rayleigh Approximation'" *Proc. R. Soc. Lond. A.* 375: 453 - 454 (1981).

Kasper, G., Shon, S-N., and Shaw, D.T., "Controlled Formation of Chain Aggregates from Very Small Metal Oxide Particles." *Am. Ind. Hyg. Assoc. J.* 41: 288 - 296 (1980).

Kerker, M., *The Scattering of Light and Other Electromagnetic Radiation.* Academic Press, New York, 1969.

King, T. A., and McAdam, J. D. G., "Translational and Rotational Diffusion of Tobacco Mosaic Virus from Polarized and Depolarized Light Scattering." *Biopolymers.* 12: 1917 - 1926 (1973).

King, G. B., Sorensen, C. M., Lester, T. W., and Merklin, J. F., "Determination of Soot Particle Size Distributions by Photon Correlation Spectroscopy." *AIAA/ASME 3rd Joint Thermophysics, Fluids, Plasma and Heat Transfer Conference.* (1982).

King, G. B., Sorensen, C. M., Lester, T. W., and Merklin, J. F., "Direct Measurements of Aerosol Diffusion Constants in the Intermediate Knudsen Regime." *Phys. Rev. Lett.* 50: 1125 - 1128 (1983).

Koppel, D. E., "Analysis of Macromolecular Polydispersity in Intensity Correlation Spectroscopy: The Method of Cumulants." *J. Chem. Phys.* 57: 4814 - 4820 (1972).

Mandel, L., "Fluctuations of Photon Beams: The Distribution of the Photo-Electrons." *Proc. Phys. Soc. (London).* 74: 233 - 243 (1959).

Mandel, L., "Heterodyne Detection of a Weak Light Beam." *J. Opt. Soc. Am.* 56: 1200 - 1206 (1966).

Mandel, L., Sudarshan, E. C. G., and Wolf, E., "Theory of Photoelectric Detection of Light Fluctuations." *Proc. Phys. Soc. (London).* 84: 435 - 444 (1964).

Mandel, L., and Wolf, E., "Coherence Properties of Optical Fields." *Rev. Mod. Phys.* 37: 231 - 287 (1965).

Medalia, A. I., and Heckman, F. A., "Morphology of Aggregates - II. Size and Shape Factors of Carbon Black Aggregates from Electron Microscopy." *Carbon.* 7: 567 - 582 (1969).

Michielsen, S., and Pecora, R., "Solution Dimensions of the Gramicidin Dimer by Dynamic Light Scattering." *Biochemistry.* 20: 6994 - 6997 (1981).

Neel, L. "Some New Results of Antiferromagnetism and Ferromagnetism." *Reviews of Modern Physics.* 25: 58-63 (1953).

Omega Engineering, Inc., *The Temperature Handbook.* 1989.

Pecora, R., "Doppler Shifts in Light Scattering from Pure Liquids and Polymer Solutions." *J. Chem. Phys.* 40: 1604 - 1614 (1964).

Pecora, R., "Spectral Distribution of Light Scattered by Monodisperse Rigid Rods." *J. Chem. Phys.* 48: 4126 - 4128 (1968).

Pecora, R. (ed.), *Dynamic Light Scattering - Applications of Photon Correlation Spectroscopy.* Plenum Press, New York, 1985.

Penner, S. S., Bernard, J. M., and Jerskey, T., "Power Spectra Observed in Laser Scattering from Moving, Polydisperse Particle Systems in Flames - I. Theory." *Acta Astron.* 3: 69 - 91 (1976).

Penner, S. S., Bernard, J. M., and Jerskey, T., "Light Scattering from Moving, Polydisperse Particles in Flames - II. Preliminary Experiments." *Acta Astron.* 3: 93 - 105 (1976).

Penner, S. S., and Chang, P. H. P., "Particle Sizing in Flames." in *Combustion in Reactive Systems* (J. R. Bowen, A. K. Openheim, and R. I. Soloukhin, eds.), *Progress in Astronautics and Aeronautics* 76 AIAA, New York, 1981, pp. 1 - 30.

Perrin, P. F., "Mouvement Brownien d'un Ellipsoide (I). Dispersion Dielectrique pour des Molecules Ellipsoidales." *J. Phys. Rad.* 5: 497 - 511 (1934).

Perrin, P. F., "Mouvement Brownien d'un Ellipsoide (II). Rotation Libre et Depolarisation des Fluorescences Translation et Diffusion de Molecules Ellipsoidales." *J. Phys. Rad.* 7: 1 - 11 (1936).

Phillies, G. D. J., "Utility of Multidetector Methods in Quasi-Elastic Light-Scattering Spectroscopy." in *Measurement of Suspended Particles by Quasi-Elastic Light Scattering.* (B. E. Dahneke, ed.), Wiley, New York, 1985, pp. 291 - 326.

Pope, J. W., and Chu, B., "A Laser Light Scattering Study on Molecular Weight Distribution of Linear Polyethylene." *Macromolecules.* 17: 2633 - 2640 (1984).

Pratsinis, S. E., and Mastrangelo, S. V. R., "Material Synthesis in Aerosol Reactors." *Chemical Engineering Progress.* May, 1989, pp. 62 - 66.

Provencher, S. W., "A Constrained Regularization Method for Inverting Data Represented by Linear Algebraic or Integral Equations." *Comput. Phys. Commun.* 27: 213 - 227 (1982a).

Provencher, S. W., "CONTIN: A General Purpose Constrained Regularization Program for Inverting Noisy Linear Algebraic and Integral Equations." *Comput. Phys. Commun.* 27: 229 - 242 (1982b).

Provencher, S. W., "CONTIN (Version 2) User's Manual." EMBL Technical Report DA07, European Molecular Biology Laboratory (1984).

Rodeick, B., Comments in module *ellipse.p* of *NIH Image* source code available on the Internet at http://rsb.info.nih.gov/nih-image/ (date unknown).

Rosner, D. E., Mackowski, D. W., and Garcia-Ybarra, P., "Size- and Structure-Insensitivity of the Thermophoretic Transport of Aggregated 'Soot' Particles in Gases." Combust. Sci. and Tech. 80: 87 - 101 (1991).

Ross, S., *A First Course in Probability.* (3rd ed.) Macmillan, New York, 1988.

Ruf, H., "Data Accuracy and Resolution in Particle Sizing by Dynamic Light Scattering." *Adv. Colloid Interface Sci.* 46: 333 - 342 (1993).

Ruf, H., Grell, E., Stelzer, E. K. G., "Size Distributions of Submicron Particles by Dynamic Light Scattering Measurements: Analyses Considering Normalization Errors." *Eur. Biophys. J.* 21: 21 - 28 (1992).

Russo, P. S., Saunders, M. J., and DeLong, L. M., "Zero-Angle Depolarized Light Scattering of a Colloidal Polymer." *Analyt. Chim. Acta.* 189: 69 - 87 (1986).

Russo, P. S., personal communications, Summer, 1996.

Saleh, B. E. A., and Cardoso, M. F., "The Effect of Channel Correlation on the Accuracy of Photon Counting Digital Autocorrelators." *J. Phys. A: Math., Nucl. Gen.* 6: 1897 - 1909 (1973).

Samuelsen, G. S., Hack, R. L., Himes, R. M., and Azzazy, M., "Effects of Fuel Specification and Additives on Soot Formation." UCI Combustion Laboratory, University of California, Irvine, 1983. ESL TR-83-17, GA #AD-A13720815.

Santoro, R. J., Semerjian, H. G., and Dobbins, R. A., "Soot Particle Measurements in Diffusion Flames." *Combust. Flame.* 51: 203 - 218 (1983).

Schatzel, K., Kalstrom, R., Stampa, B., and Ahrens, J., "Correction of Detection-System Dead-Time Effects on Photon-Correlation Functions." *J. Opt. Soc. Am. B.* 6: 937 - 947 (1989).

Schurr, J. M., and Schmitz, K. S., "Rotational Relaxation of Macromolecules Determined by Dynamic Light Scattering. I. Tobacco Mosaic Virus." *Biopolymers.* 12: 1021 - 1045 (1973a).

Schurr, J. M., and Schmitz, K. S., "Rotational Relaxation of Macromolecules Determined by Dynamic Light Scattering. II. Temperature Dependence for DNA." *Biopolymers.* 12: 1543 - 1564 (1973b).

Scrivner, S. M., Taylor, T. W., Sorensen, C. M., and Merklin, J. F., "Soot Particle Size Distribution Measurements in a Premixed Flame Using Photon Correlation Spectroscopy." *Appl. Opt.* 25: 291 - 297 (1986).

Seshadri, K. and Rosner, D. E., "Optical Methods and Results of Dew Point and Deposition Rate Measurements in Salt/Ash-Containing Combustion Gases." *AIChE Journal.* 30: 187 (1984).

Sorensen, C. M., Cai, J., and Lu, N., "Light-Scattering Measurements of Monomer Size, Monomers per Aggregate, and Fractal Dimension for Soot Aggregates in Flames." *Appl. Opt.* 31: 6547 - 6557 (1992).

Taylor, T. W., Scrivner, C. M., Sorensen, C. M., and Merklin, J. F., "Determination of the Relative Number Distribution of Particle Sizes Using Photon Correlation Spectroscopy." *Appl. Opt.* 24: 3713 - 3717 (1985).

THORN EMI Electron Tubes Ltd., *Photomultipliers.* 1986.

Ueyama, K., Ono, T., Matsukata, M., and Osima, R., "Application of Dynamic Light Scattering Based on a Monodisperse Model as an In-Situ Method of Measuring Ultrafine Particles Growing and Aggregating in a Flame." *Journal of Chemical Engineering of Japan.* 26: 686 - 691 (1993).

Ulrich, G. D., "Flame Synthesis of Fine Particles." *Chem. Eng. News.* August 6, 1984, pp. 22 - 29.

Ulrich, G. D., and Subramanian, N. S., "Particle Growth in Flames - III. Coalescence as a Rate-Controlling Process." *Combustion Science and Technology* 17: 119 - 126 (1977).

van de Hulst, H. C., *Light Scattering by Small Particles.* Dover, New York, 1981.

Venizelos, D. T., *Particle Size Distribution Measurements in Flame Systems Using Dynamic Light Scattering Techniques.* Masters Thesis, Louisiana State University, 1989.

Waldmann, L., "On the Motion of Spherical Particles in Nonhomogeneous Gases." *Z. Naturforsch.* 14a: 589 (1959).

Wada, A., Suda, N., Tsuda, T., and Soda, K., "Rotatory-Diffusion Broadening of Rayleigh Lines Scattered from Optically Anisotropic Macromolecules in Solution." *J. Chem. Phys.* 50: 31 - 35 (1969).

Wada, A., Soda, K., Tanaka, T., and Suda, N., "Depolarized Light Mixing for Light Beating Spectroscopy." *Rev. Sci. Instrum.* 41: 845 - 853 (1970).

Weast, R. C. (ed.), *CRC Handbook of Chemistry and Physics.* (53rd ed.) The Chemical Rubber Co., Cleveland, 1972.

Wu, M. K., Windeler, R. S., Steiner, C. K. R., Bors, T., and Friedlander, S. K., "Controlled Synthesis of Nanosized Particles by Aerosol Processes." *Aerosol Sci. Tech.* 19: 527 - 548 (1993).

Xie, G. W., Patel, S., Wong, F. C. H., and Shaw, D. T., "In Situ Dynamic Measurement of Polydisperse Chain Aggregate Aerosols Using Photocorrelation Spectroscopy Technique." *J. Aerosol. Sci. Technol.* 22: 219 - 235 (1995).

Zero, K. M., and Pecora, R., "Rotational and Translational Diffusion in Semidilute Solutions of Rigid-Rod Macromolecules." *Macromolecules.* 15: 87 - 93 (1982).

Zero, K., "Dynamic Depolarized Light-Scattering Studies of Rodlike Particles," in *Measurement of Suspended Particles by Quasi-Elastic Light Scattering.* (B. E. Dahneke, ed.), Wiley, New York, 1983, pp. 377 - 400.

Zhang, Z., *Controlled Combustion Synthesis of Iron Oxide Nanoparticles.* Masters Thesis, Louisiana State University, 1995.

Appendix A

Preliminary Burner Tests

As mentioned in Chapter 3, three different types of burners were tested as part of this study in an attempt to generate chainlike iron oxide agglomerates in a suitable flame. These burners consisted of a flat flame diffusion burner, a premixed flat flame burner, and a concentric tube diffusion burner. In testing these burners, the ultimate goal was to generate a one-dimensional, stable flame containing chainlike agglomerates of iron oxide. Ultimately, radial uniformity (one-dimensionality) was sacrificed by using a concentric tube diffusion burner so that clogging problems could be minimized. The following discussion presents the burners considered for this study and the results of the preliminary tests of their capabilities.

A.1 Flat Flame Diffusion Burner

The multi-element flat flame diffusion burner (Research Technologies RD15) is designed to produce a diffusion flame that is nearly one-dimensional. This burner, which is illustrated in figure A.1.1, consists of a 1.5" diameter hastelloy honeycomb with stainless steel hypodermic steel tubes interspersed uniformly throughout the mesh. During operation the fuel is fed into the flame through the hypodermic tubes as the oxidizer emerges from the surrounding honeycomb cells. Thus, the fuel and oxidizer are kept separate until they both leave the burner. Upon leaving the burner, the fuel and oxidizer mix due to mutual diffusion, forming a combustible mixture that is then ignited. This diffusion process is also responsible for smoothing the small-scale spatial inhomogeneities in the composition of the reactant flow at the burner surface in order to produce a one-dimensional flame. The central mesh of the burner, through which the fuel and oxidizer passes, is surrounded by a separate annular honeycomb to

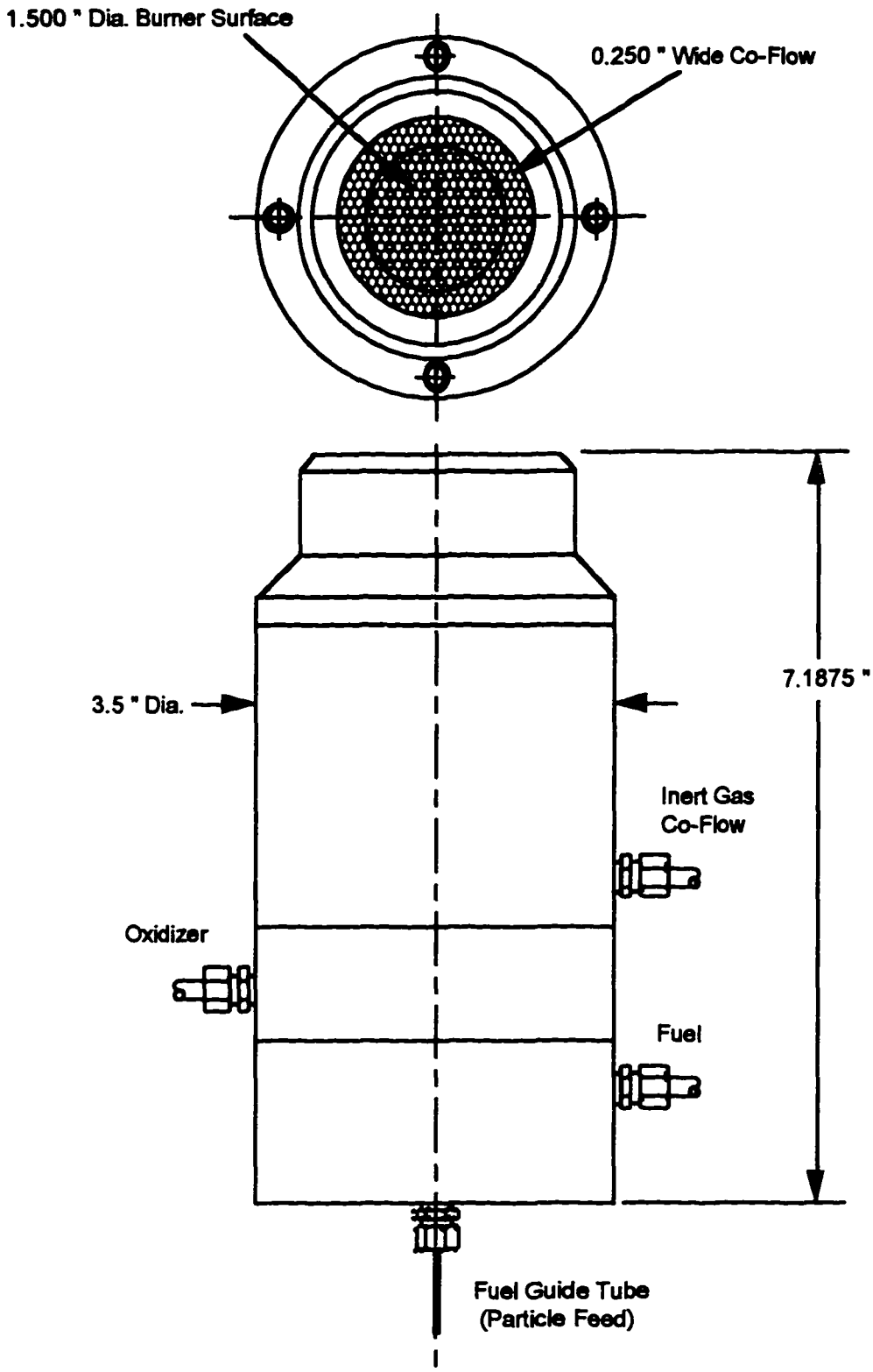

Figure A.1.1: Multi-element flat flame diffusion burner (Research Technologies RD15)

accommodate an inert gas co-flow. This co-flow shrouds the flame with an inert gas to isolate it from the ambient air and to provide a stabilizing annular flow around the flame.

The main advantage of initially keeping the fuel and oxidizer separate is that the iron pentacarbonyl vapor within the CO flow is not exposed to oxygen until it leaves the burner. Thus, burner clogging should be avoided by eliminating the vital component necessary to oxidize the $Fe(CO)_5$ into iron oxide particles, namely oxygen, until the $Fe(CO)_5$ has exited the burner tubes.

Tests performed using this burner, however, were inconclusive because the fuel tubes did eventually clog despite the fact that the burner was run in the diffusion mode. Qualitative observations made during the testing of this burner indicated that the flame temperature was typically higher at its periphery than its center. The addition of iron pentacarbonyl caused yellow streaks in the typically blue $CO/O_2/N_2$ flame, possibly indicating insufficient diffusion to smooth the small scale spatial nonuniformities in the reactant composition. The degree of clogging present in the burner during the observation of these qualitative results is unknown. Following the final tests performed on this burner, the fuel tubes were observed to be severely clogged. The most extensive clogging occurred near the center of the burner's honeycomb mesh.

The cause of the clogging in the flat flame diffusion burner is unknown; however, various hypotheses can be offered. During the time of these tests, the reactant supply system had a much cruder design than the one presented in this document: the fuel line was not properly heated to minimize the deposition of $Fe(CO)_5$ on the line's walls and no purging systems were incorporated into the reactant supply system. During the burner tests meter purging was accomplished by respectively removing the CO and O_2 lines from their canisters and connecting them to nitrogen canisters to send nitrogen through the meters. Burner purging was accomplished by directing high pressure air through the burner instead of the nitrogen that is currently used. This was

accomplished only after disconnecting the fuel and oxidizer lines from the burner's inlet ports and replacing them with a line from the source of high pressure air. The exposure of the burner fuel tubes to oxygen both prior to and during purging may have contributed to the formation of oxides within the tubes. The most likely cause of the clogging was probably deposition and oxidation of $Fe(CO)_5$ within the burner's fuel tubes. Deposition could have occurred during the operation of the burner either by condensation on the walls of the hypodermic fuel tubes (which would require cool spots within the burner) or by some form of molecular adsorption mechanism. More likely, the deposition probably occurred during the burner's down time by the diffusion and recondensation of $Fe(CO)_5$ vapors into the burner from the contaminated CO line. Though the burner is designed to avoid the oxidation of $Fe(CO)_5$ in the fuel tubes by keeping oxygen out of the fuel tubes during burner operation, oxygen is definitely present in the fuel tubes during the burner's down time as a result of purging the burner with high pressure air and as a result of the diffusion of room air into the fuel tubes. Prolonged exposure to oxygen, particularly at high temperatures, would cause the $Fe(CO)_5$ to oxidize, thus forming solid contaminants within the burner tubes.

An alternative conceivable mechanism for the burner clogging is that the clogging resulted from the condensation of metallic iron within the burner tubes. Upon reaching approximately 300°C iron pentacarbonyl decomposes. If the resulting iron ions condense from the vapor phase, clogging of the fuel tubes would result. Later observations of deposits within the fuel tube of a concentric tube diffusion burner that *was* frequently purged with nitrogen tend to support the theory that this condensation was not directly related to oxygen contamination, though no chemical analysis of these deposits was performed. These later observations indicate that had the flat flame diffusion burner been purged with inert nitrogen, clogging would most likely have still occurred.

Ultimately, the flat flame diffusion burner could not be properly cleaned once the clogging was detected, thus making it unsuitable for further experiments. Instead of replacing this rather expensive burner with an identical one, the reactant supply system was modified to incorporate heated fuel lines and nitrogen-based meter and burner purging systems and testing was resumed using a premixed flat flame burner.

A.2 Premixed Flat Flame Burner

The premixed flat flame burner is designed to produce a one-dimensional flame by passing a mixture of fuel and oxygen through a series of screens, perforated stainless steel disks, and a ceramic honeycomb plug to produce a reactant flow out of the burner that is nearly uniform across the burner's surface. This burner is illustrated in figure A.2.1. The combustion gases, which are mixed prior to entering the burner, flow through a stainless steel cylinder that contains the above-mentioned series of screens and perforated stainless steel disks, whose function is to distribute the combustion gases evenly throughout the cylinder. Mounted in the exit end of this cylinder is a ceramic honeycomb plug (Corning Celcor, 400 cells/sq. in.). The combustion gases pass through this honeycomb plug, undergoing a Poiseuille flow within each cell. Upon leaving the burner plug, the jets of reactant gas leaving each cell diffuse together to form a smooth velocity profile across the burner surface. Since the mean velocity through each cell is approximately the same for all cells, the diffusion-smoothed velocity profile at the burner outlet is uniform.

Like the flat flame diffusion burner described earlier, the premixed burner also accommodates an annular shroud of nitrogen (or another inert gas) surrounding the flame to prevent entrainment of ambient air into the flame and to help stabilize the flame. The shroud gas passes through an annular cavity between the outer burner housing and the steel cylinder containing the combustion gases. This gas exits the cavity through a porous, sintered bronze ring, which surrounds the ceramic plug and distributes the flow of nitrogen around the flame.

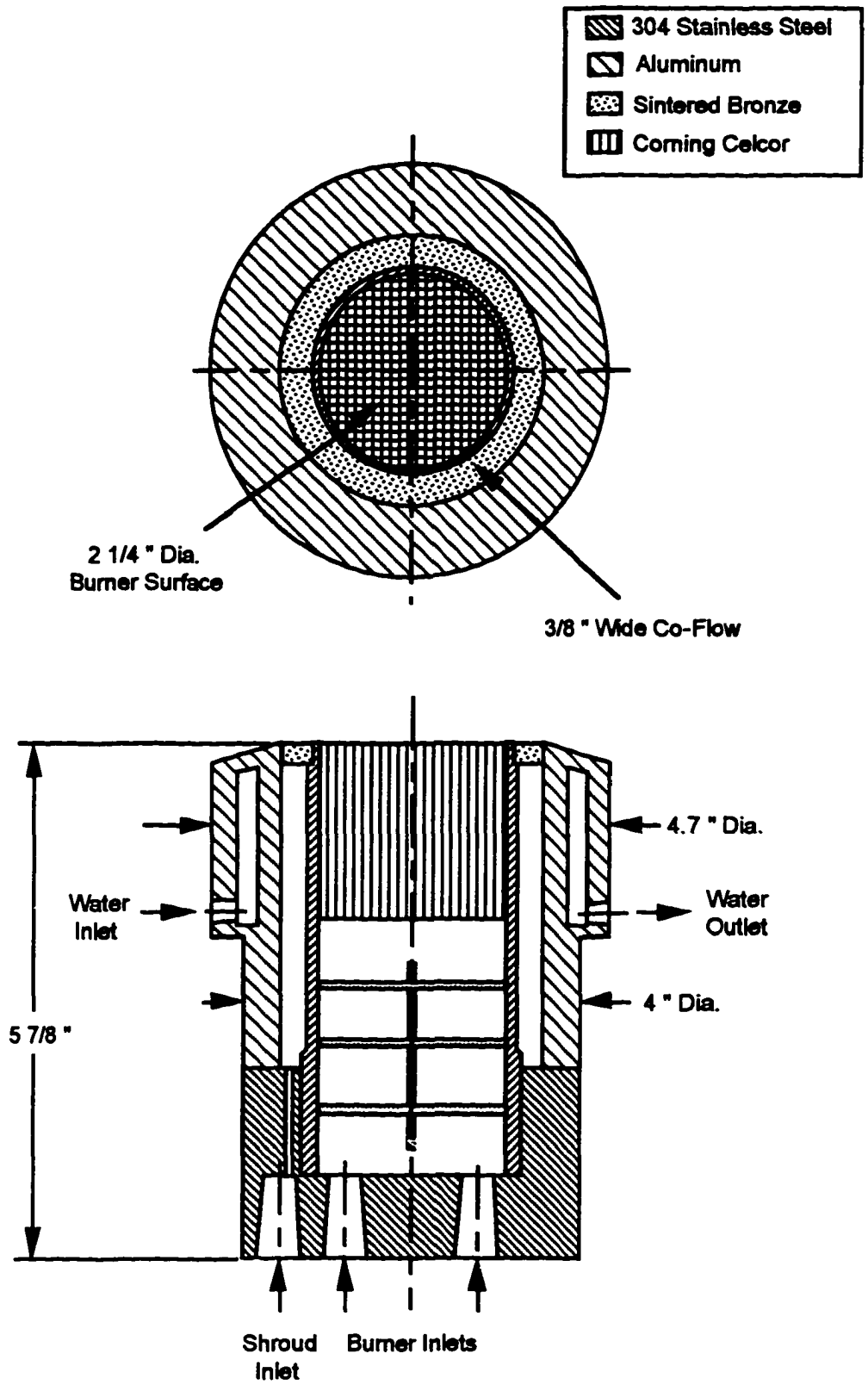

Figure A.2.1 Premixed flat flame burner

Initial tests of this burner using a $CO/O_2/N_2$ flame revealed a blue cylindrical flame that acquired a yellowish tint when seeded with $Fe(CO)_5$. The unseeded flame was relatively stable for fuel equivalence ratios larger than approximately 2; however, when the equivalence ratio was reduced in an attempt to obtain stoichiometric conditions, the flame would extinguish itself. The flame produced under the necessary fuel rich conditions exhibited characteristics of a room-air diffusion flame: a hot luminescent periphery surrounding a cooler core. Additionally, the flame would extinguish in the presence of any significant shroud.

The presence of particulates within the seeded flame was qualitatively indicated by the visual observation of scattering from an argon ion laser directed through the flame. After running the flame for several minutes with seeding, however, the flame returned to its blue color and the visible scattering of the laser light ceased. Disassembly of the burner indicated that this phenomenon was caused by the formation of iron oxide particles within the burner. The high temperature (> 300°C) within the burner had heated the $CO/O_2/N_2/Fe(CO)_5$ mixture enough to oxidize the iron pentacarbonyl prematurely. The resulting iron oxide particles then deposited on the inner burner cylinder and the inner flow-distributing screens, which effectively filtered the particles out of the mixture of combustion gases. The result was a flame that appeared to be completely unseeded.

In an attempt to cool the combustion gases within the burner cylinder to prevent the premature oxidation of the $Fe(CO)_5$, an annular cavity was cut into the outer burner housing to accommodate cooling water. Subsequent tests yielded results virtually identical to the results obtained without cooling water, indicating that the premature particle formation and burner clogging was not eliminated.

To further study the behavior of the $CO/O_2/N_2$ flame in this burner, a series of thermocouples were attached to different locations inside the burner for monitoring the corresponding temperatures during burner operation. Three thermocouples were

attached to the outside of the inner burner cylinder, one was mounted inside the inner cylinder approximately 1 cm beneath the bottom of the ceramic honeycomb plug, and one was inserted into one of the cells of the honeycomb plug. Measurements of the temperatures at these locations obtained while running the unseeded flame under various reactant flow combinations implied that combustion occurs somewhere inside the burner under these conditions. This combustion provided the high temperature environment that prematurely oxidized the iron pentacarbonyl. Under fuel-rich conditions the products of this internal combustion should contain unburnt CO, which could theoretically react with the ambient air upon exiting the burner to form a diffusion flame over the burner plug. This would explain why the flame visible on the outside of the burner quenches when either the oxygen flowrate is increased or a significant shroud flow is used. Increasing the amount of oxygen in the reactant gas mixture decreases the amount of unburnt CO present in the products of the initial combustion occurring inside the burner while producing a larger proportion of the effectively inert combustion product CO_2, thus causing the visible outer flame to eventually blow off. Increasing the flow rate of the shroud gas isolates the unburnt CO from the ambient air, extinguishing the outer flame by separating the fuel (unburnt CO) from the oxidizer (room air).

This final experiment using this burner caused the ceramic honeycomb plug to crack. Additionally, severe clogging was noted within the honeycomb cells. The exact reason for this failure is unknown; however, a reasonable postulate would be that the honeycomb cracked due to thermal fatigue caused by repeatedly running experiments during which the flame front would actually enter the honeycomb cells. The poor performance of this burner, along with its eventual structural failure, necessitated the eventual use of a concentric tube diffusion burner for subsequent tests.

A.3 Concentric Tube Diffusion Burner

A concentric tube diffusion burner produces a nearly conical diffusion flame by separately directing the fuel and oxidizer through concentric stainless steel tubes into

the flame. After the failure of the premixed flat flame burner described in the last section, a series of tests were conducted on the concentric tube burner of figure A.3.1, which is a preliminary version of the burner described in section 3.1.2 of Chapter 3. The primary difference between the burner of figure A.3.1 and that of figure 3.1.3 is the presence of an additional 1/4" inner diameter tube in the former burner. For the tests on this burner, which were extensively reported by Zhang (1995), this central 1/4" i.d. tube was utilized as the fuel tube. The extra annular outlet surrounding the central fuel tube was originally intended to support a stream of nitrogen to separate the fuel from its oxidizer at locations close to the burner surface in order to minimize overheating of the burner tubes and to reduce particle deposition on the fuel tube outlet. This option was not utilized during the current study.

The inherent radial nonuniformity of flame properties from flames generated by this class of burner is a disadvantage that accompanies the use of this burner because of the difficulties that would result in interpreting zero-angle dynamic light scattering and optical extinction measurements. This particular burner, however, does offer several advantages not exhibited by the other burners tested. Due to the large scale of the passages within the burner, small deposits of solids upon the inner walls should not significantly affect the flow field of the reactant gases. Also, this burner is easy to disassemble and clean if deposits do form on the inner walls. These attributes provide the conditions necessary for reproducibility of the experimental conditions, which is vital for the successful completion of an experimental study.

During the testing of this burner, Zhang (1995) has obtained acceptable results by allowing the seeded CO to react with the ambient room air with no flow through any of the outer tubes in the burner. Also, no nitrogen dilution of the CO stream was used. These tests determined that a stable seeded CO-air diffusion flame is obtainable for CO flow rates ranging from 0.20 to 0.45 lpm. Flow rates lower than 0.20 lpm cannot sustain a flame and flow rates higher than 0.45 lpm induce flickering in the flame. The

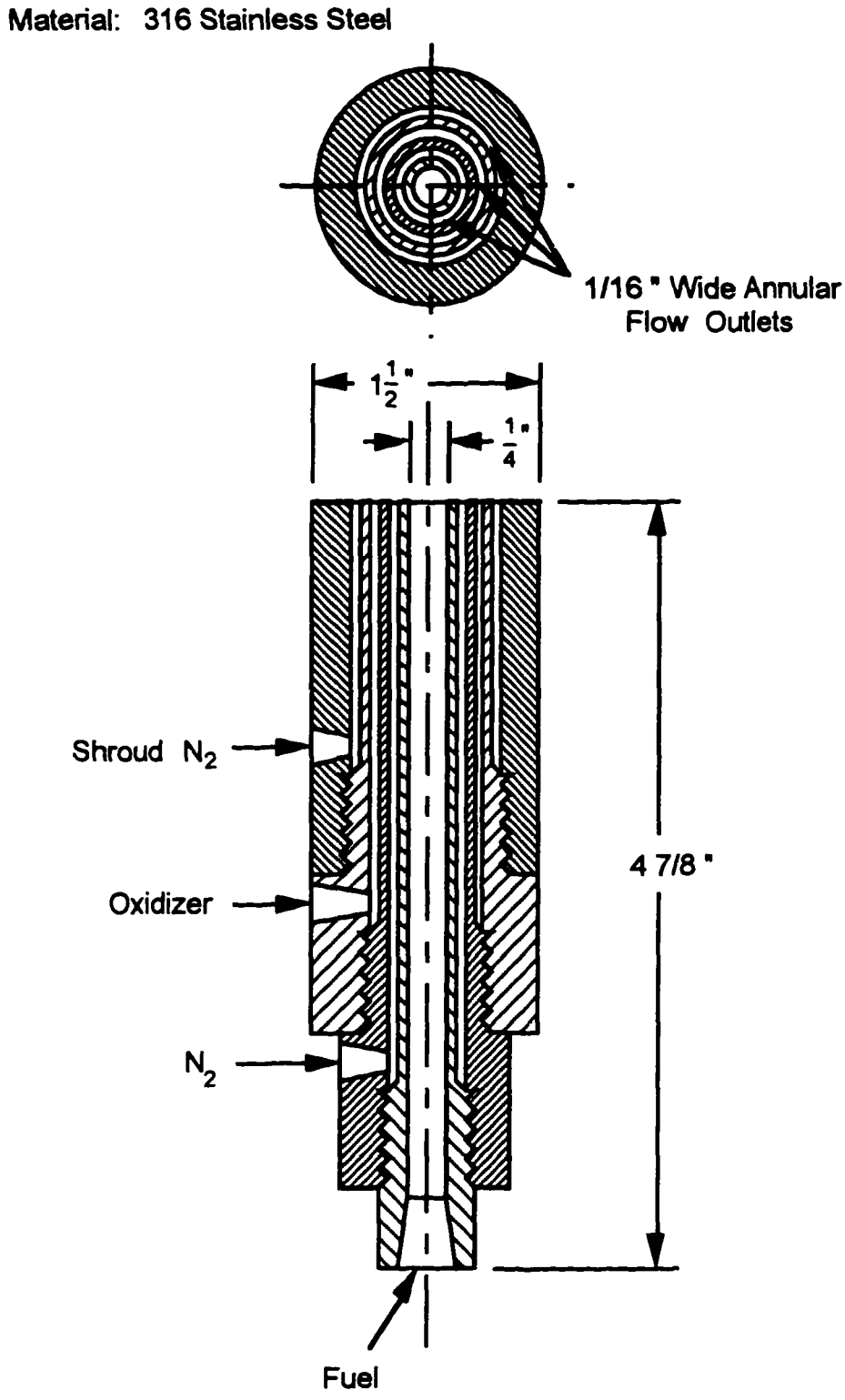

Figure A.3.1: Concentric tube diffusion burner

upper limit of this range increases to 0.55 lpm when the flame is unseeded [Zhang, 1995]. The visible structure of this flame under unseeded and seeded conditions is illustrated in figure A.3.2. Seeding the flame with $Fe(CO)_5$ causes bright yellow emissions, which is thermal radiation from the iron oxide particles formed within the flame. Emissions from the unseeded flame are much less intense than the seeded flame. The unseeded flame is a predominantly blue flame with a distinct conical white flame front. Yellow regions occurring in the upper portions of the unseeded flame imply the possible presence of some solids within the flame. The presence of these solids in the unseeded flame may possibly be attributed to contamination within the reactant supply system or to formerly deposited solids falling from the honeycomb stabilizer into the flame. Thermophoretic sampling of both the seeded and unseeded flames has shown that the size of the particulates occurring in the unseeded flame is negligible compared to the particle sizes resulting from the seeding process.

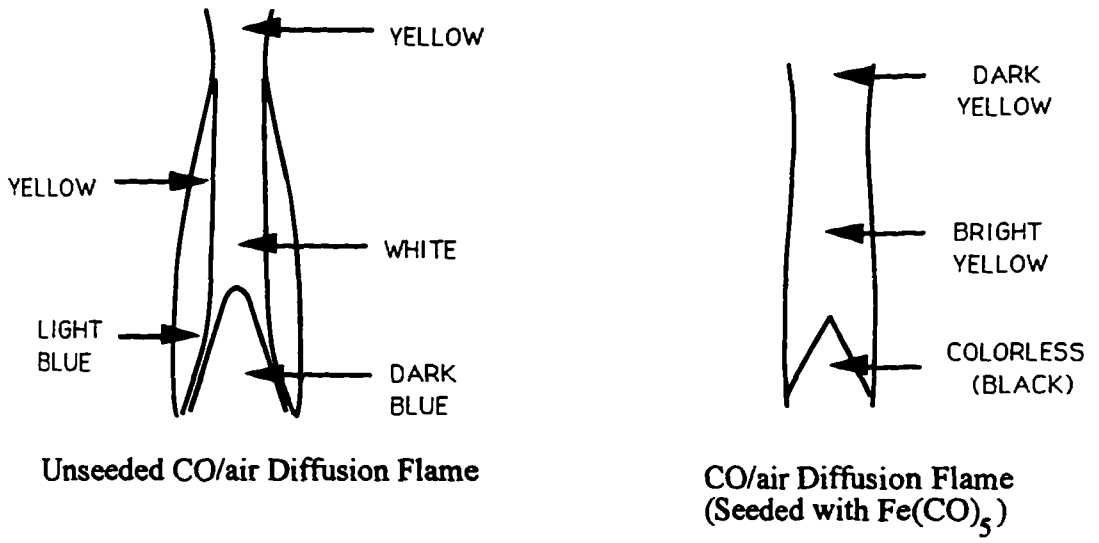

Unseeded CO/air Diffusion Flame

CO/air Diffusion Flame (Seeded with $Fe(CO)_5$)

Figure A.3.2: Visible flame structures of unseeded and $Fe(CO)_5$ - seeded CO/air diffusion flames.

Ex-situ tests performed on the seeded flame with carrier CO flow rates ranging from 15 to 35 cc/min and an evaporator cylinder temperature ranging from 23°C to 55°C indicated the presence of the desired chainlike agglomerates of iron oxide particulates within the flame. X-ray diffraction measurements and chemical equilibrium calculations both agree that these particulates consist of predominantly Fe_2O_3 [Zhang, 1995]. These agglomerates are qualitatively similar to those depicted in figure 4.1.2 of Chapter 4 from the modified burner of figure 3.1.6. Like the results reported in Kasper, et al. (1980) the primary particles exhibit a polyhedral shape, implying a distinct crystalline structure. During these preliminary tests, the flame was observed to be very sensitive to ambient air disturbances, periodically leaning away from vertical direction. In an effort to reduce this instability, the burner was modified by removing the central fuel tube so that diameter of the fuel stream could be increased, thus producing the burner described in Chapter 3.

Appendix B

Derivation of Equation 3.3.8

Equation 3.3.8 of Chapter 3 is an expression of the product of the average number of photon counts $\langle n(0) \rangle$ within sample time Δt and the spatial coherence factor f(A), as expressed in terms of instrumentation parameters. This product occurs in the denominator of the photodetection-dominated noise estimate of Jakeman, et al. (1971), which is given by equation 3.3.7. The adjustment of the experimental parameters discussed in section 3.3.4 is partially based upon the maximization of this product to minimize the resulting noise in the measured correlation function. A derivation of the relationship between $\langle n(0) \rangle f(A)$ and experimental parameters, such as the incident laser power P_o and wavelength λ, the number density ρ of agglomerates within the scattering volume, the sample time Δt, the scattering angle θ, the spot size of the focused incident beam ω_o, and the quantum efficiency η of the photomultiplier tube, involves separately estimating each of the factors $\langle n(0) \rangle$ and f(A) and then multiplying the two together.

The mean number of counts $\langle n(0) \rangle$ during sample time Δt is determined through the use of the photodetection statistics described in section 2.2.1, the scattered electric field representation of section 2.1.1, and the dipole approximations of equations 2.2.94. Using the probability $p(n,\Delta t)$ of detecting n photons during sample time Δt, as given by equation 2.2.3, the average number of counts $\langle n(0) \rangle$ during this time is expressed as

$$\langle n(0) \rangle = \sum_{n=0}^{\infty} n\, p(n,\Delta t) = \int_0^{\infty} \sum_{n=0}^{\infty} \frac{n\,(\alpha U)^n}{n!} \exp(-\alpha U)\, f(U)\, dU$$

$$= \int_0^{\infty} (\alpha U) \left\{ \sum_{n=1}^{\infty} \frac{(\alpha U)^{n-1}}{(n-1)!} \right\} \exp(-\alpha U)\, f(U)\, dU, \qquad \text{(B.1)}$$

where

$$\alpha \equiv \frac{\eta}{h\nu}, \tag{B.2}$$

$$\langle U \rangle = \frac{c}{8\pi} \int_{t-\Delta t/2}^{t+\Delta t/2} dt' \int_{A} d^2R \, \langle E^*(\mathbf{R}, 0) \cdot E(\mathbf{R}, 0) \rangle$$

$$\approx \frac{c}{8\pi} \Delta t \, A \, \langle E^*(\mathbf{R}, 0) \cdot E(\mathbf{R}, t') \rangle, \tag{B.3}$$

h is Planck's constant, and ν is the optical frequencyThe last equality in equation B.3 results from the assumption that the mean detected light intensity is uniform over the detector area A and is approximately constant during the sample time Δt. Noting that the term in the braces {} of equation B.1 is the MacLaurin series expansion of $\exp(-\alpha U)$, this equation is reducable to

$$\langle n(0) \rangle = \int_{0}^{\infty} \alpha \, U \, f(U) \, dU = \alpha \langle U \rangle. \tag{B.4}$$

In order to evaluate the mean incident optical energy $\langle U \rangle$, the total detected electric field $E_f(\mathbf{R},t)$ is determined by summing the electric fields $E_{fj}(\mathbf{R},t)$ scattered by each particle within the scattering volume and substituting the result into equation B.3. Using this sum in equations B.2, B.3, and B.4, the following expression is obtained:

$$\langle n(0) \rangle = \frac{\eta \, c \, \Delta t \, A}{8\pi \, h \, \nu} \left\langle \sum_{j=1}^{N_T} \sum_{k=1}^{N_T} E_j^*(\mathbf{R}, 0) \cdot E_k(\mathbf{R}, 0) \right\rangle \tag{B.5}$$

Interchanging the averaging process and the summations and decomposing the summations into $j = k$ sums and $j \neq k$ sums produces

$$\langle n(0) \rangle = \frac{\eta \, c \, \Delta t \, A}{8\pi \, h \, \nu} \left\{ \sum_{j=1}^{N_T} \langle E_j^*(\mathbf{R}, 0) \cdot E_j(\mathbf{R}, 0) \rangle + \sum_{k \neq j=1}^{N_T} \sum_{j=1}^{N_T} \langle E_j^*(\mathbf{R}, 0) \rangle \cdot \langle E_k(\mathbf{R}, 0) \rangle \right\}, \tag{B.6}$$

where the electric fields scattered by separate particles $j \neq k$ are considered statistically independent. In accordance with the arguments presented in section 2.2.4.2.4, the $j \neq k$ terms are all equal to zero.

The nonzero averages in equation B.6 are recast using the general form of the scattered electric field given by equation 2.1.9 to produce the following:

$$\langle E_j^*(\mathbf{R}, 0) \cdot E_j(\mathbf{R}, 0) \rangle = \frac{|E_o|^2}{k^2 R^2} \langle |S_l|^2 \rangle, \tag{B.7}$$

where $|E_o|^2$ is the square of the magnitude of the incident electric field and S_l is the appropriate element of the amplitude scattering matrix. Expressing the elements of the amplitude scattering matrix in terms of the polarizability tensor α using $S_l = -ik^3 \mathbf{n_i} \cdot \alpha \cdot \mathbf{n_f}$, where $\mathbf{n_i}$ and $\mathbf{n_f}$ are the respective unit vectors characterizing the incident and scattered light polarizations, the non-zero terms of equation B.6 are summed using equation B.7 to produce

$$\langle n(0) \rangle = \frac{\eta \, \Delta t \, A \, k^4 \langle N \rangle I_o}{h \nu R^2} \langle |\mathbf{n_i} \cdot \alpha \cdot \mathbf{n_f}|^2 \rangle, \tag{B.8}$$

where I_o is the intensity of the incident light, as given by

$$I_o = \frac{c}{8\pi} |E_o|^2,$$

and $\langle N \rangle$ is the average number of agglomerates in the scattering volume. This average number of agglomerates is equal to the product of the agglomerate number density ρ and the volume V_{sv} of the scattering volume. Based on the finite-angle scattering volume geometry of figure 3.3.2, the volume of the scattering volume is approximated as

$$V_{sv} = \frac{\pi \omega_o^2 d_3}{\sin\theta}, \tag{B.9}$$

where d_3 is the diameter of aperture(s) D3 (a,b) in figures 3.3.1 and 3.3.3 and θ is the scattering angle. Utilizing the above developments, equation B.8 is recast as

$$\langle n(0)\rangle = \frac{\eta\, \Delta t\, A\, P_o\, \rho\, d_3\, k^4}{h\, \nu\, R^2 \sin\theta} \langle |\mathbf{n}_i \cdot \alpha \cdot \mathbf{n}_f|^2 \rangle, \tag{B.10}$$

where the incident light intensity I_o has been expressed in terms of the corresponding laser power P_o using

$$I_o = \frac{P_o}{\pi\, \omega_o^2}.$$

The derivation of equation 3.3.8 also requires an evaluation of the spatial coherence factor f(A), which is approximately equal to the reciprocal of the number of detected coherence areas N_c when this number is greater than unity. Thus, $f(A) \approx A_c/A$, where A_c is the size of a typical coherence area and A is the area of the detector surface. Using equation 3.3.10 for A_c and the fact that the distance from the scattering volume to the detector aperture D2 is equal to twice the focal length f_2 of the detector lens, the size of a coherence area is expressed as

$$A_c \approx \frac{\lambda^2}{\Omega} = \frac{\lambda^2 (2f_2)^2}{A_{sv}}. \tag{B.11}$$

Noting that the scattering volume area A_{sv} equals $2\omega_o\, d_3$ (see figure 3.3.2) and that the detector area A equals $\pi d_2^2/4$, the spatial coherence factor f(A) is expressed as

$$f(A) \approx \frac{8\, \lambda^2\, f_2^2}{\pi\, d_2^2\, \omega_o\, d_3}. \tag{B.12}$$

Equation 3.3.8 is thus obtained by multiplying equations B.10 and B.12:

$$\langle n(0)\rangle f(A) = \frac{8\, \pi^4\, \rho\, \eta\, P_o\, \Delta t \langle |\mathbf{n}_i \cdot \alpha \cdot \mathbf{n}_f|^2 \rangle}{h\, c\, \lambda\, \omega_o \sin\theta}, \tag{B.13}$$

where use has been made of the optical frequency ν and wavenumber k relationships: $\nu = c/\lambda$ and $k = 2\pi/\lambda$.

Appendix C

Experimental Data Sheets

The following pages present representative data sets from the optical measurements performed in this study. These data sets consist of the data sheets used when obtaining the data, followed by raw correlation function results from each representative DLS data set and the equivalent correlation function of the data sets after combination using COMBINE3.BAS. The data sets provided include the polarized (VV) and depolarized (VH) data obtained at a scattering angle of 5° and a height of 35 mm above the burner surface. The correlator channel contents given in the plots are the sums of the products of photon counts registered during each pair of sample intervals separated by delay time τ.

Date: 2/6/97

Experimental Data Sheet

Brief Description: VV DLS; height = 35 mm

Measurements Performed: Dynamic Light Scattering √

Classical Light Scattering _

Flame Conditions

Initial CO Cylinder Pressure _____ (psi)

CO Flowrate: 0.35 (lpm) Carrier CO Flowrate: 8 (mlpm)

O_2 Flowrate: 0.25 (lpm)

Stabilizer height (above burner surface): 43 (mm)

Evaporator Temperature T_{evap} = 308 (K)

Volume of $Fe(CO)_5$ in Evaporator: 200 ml

Flame Temperature:

Thermocouple Voltage V_{TC} = _____ (mV)

Flame Temperature (uncorrected) = _____ (K)

Flame Temperature (corrected) = _____ (K)

Spectrometer Settings

Laser Power P_L = 0.400 (W) Laser Aperture = 6

Laser Wavelength λ = 488 nm Scattering Angle θ = 5 (degrees)

Measurement Height (above burner surface): 35 (mm)

Aperture diaphragms: d_1 = 2.78 mm d_2 = 0.6 mm $d_{3\text{-}A} = d_{3\text{-}B}$ = 0.6 mm

Lens focal lengths: f_{l_1} = 400 mm f_2 = 150 mm

Dynamic Light Scattering

Detection Mode: VV

Correlation Function: Cross- correlation

High Voltage Power Supply:

V_A = 1865 (V) V_B = 1865 (V)

Correlation File Directory: C:\BI\DATFIL\F06V

Correlation File Name(s): F06VA#.DAT (Correlation) F06VA#.RAT (Count Rate)

Experiment Duration (of each data set): 30 (secs)

Was a delay file used? √ Yes _ No

If yes, delay file name: C:\BI\DLYFIL\DLY161.DLY

Classical Light Scattering

Light Chopper Frequency: _____ (Hz)

PMT Supply Voltage: _____ (V)

Detected Voltages:

VV: _____

VH: _____

Depolarization Ratio R_{VH}: _____

Raw Correlation Data

File: F06VA5.DAT

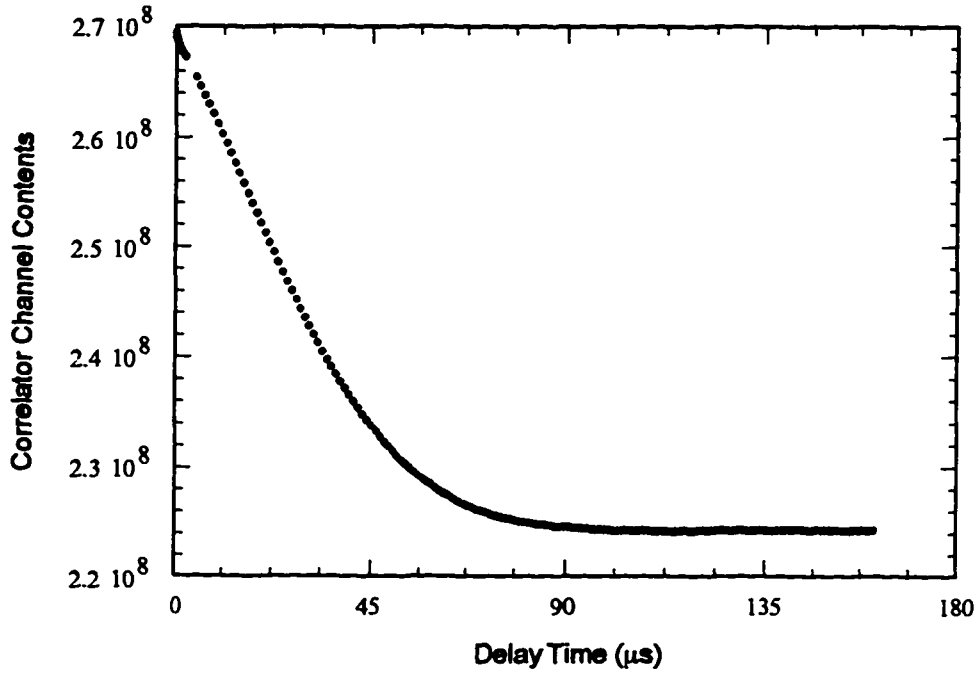

Detection mode:	VV
Duration:	30 s
Number of Samples:	6.750208×10^6
Total Counts - A Input:	5.596663×10^7
Total Counts - B Input:	2.499412×10^7
Calculated Baseline:	2.072287×10^8
Measured Baseline:	2.242399×10^8

(Last 10 channels used for measured baseline evaluation.)

Combined Correlation Data

File: F06VA.DAT

(Output from COMBINE3.BAS)

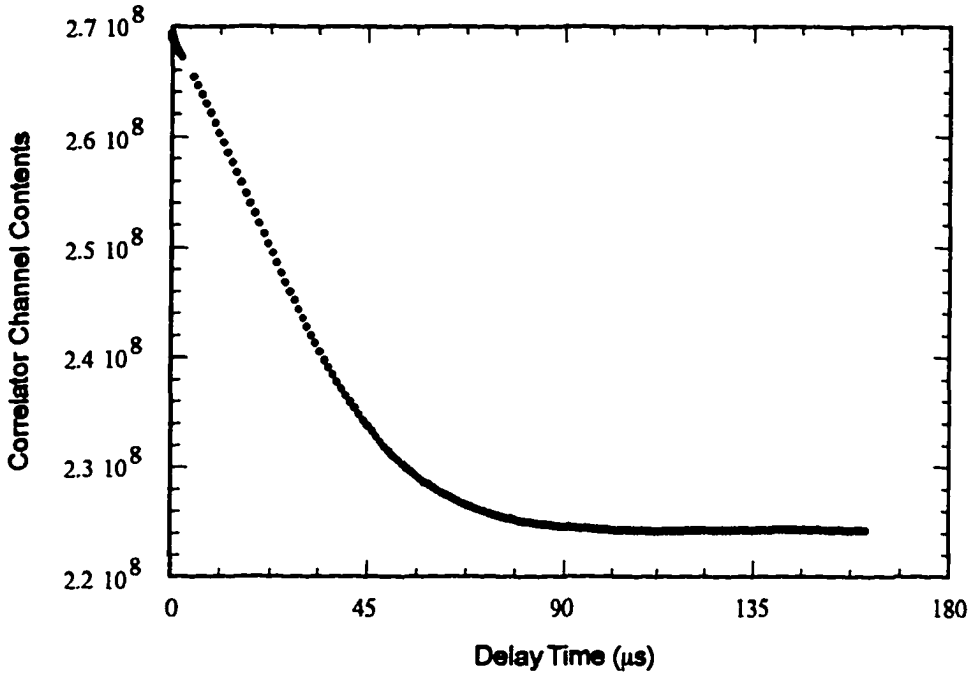

Detection mode:	VV
Total Duration:	28 min
Number of Samples:	3.792241×10^8
Total Counts - A Input:	2.422299×10^9
Total Counts - B Input:	1.027396×10^9
Calculated Baseline:	6.562505×10^9
Measured Baseline:	7.842229×10^9
1st Channel Used in Analysis:	Ch# 27 (τ = 5 μs)
Last Channel Used in Analysis:	Ch# 107 (τ = 85 μs)

Rejected Data Sets: F06VA1.DAT, F06VA2.DAT, F06VA37.DAT, F06VA41.DAT

(Last 10 channels used for measured baseline evaluation.)

Date: 1/31/97

Experimental Data Sheet

Brief Description: VH DLS; height = 35 mm

Measurements Performed: Dynamic Light Scattering √

Classical Light Scattering √

Flame Conditions

Initial CO Cylinder Pressure 730 (psi)

CO Flowrate: 0.35 (lpm) Carrier CO Flowrate: 8 (mlpm)

O_2 Flowrate: 0.25 (lpm)

Stabilizer height (above burner surface): 43 (mm)

Evaporator Temperature T_{evap} = 308 (K)

Volume of $Fe(CO)_5$ in Evaporator: 200 ml

Flame Temperature:

Thermocouple Voltage V_{TC} = 6.98 (mV)

Flame Temperature (uncorrected) = 1023 (K)

Flame Temperature (corrected) = 1122 (K)

Spectrometer Settings

Laser Power P_L = 2.50 (W) Laser Aperture = 6

Laser Wavelength λ = 488 nm Scattering Angle θ = 5 (degrees)

Measurement Height (above burner surface): 35 (mm)

Aperture diaphragms: d_1 = 2.78 mm d_2 = 0.6 mm $d_{3\text{-}A} = d_{3\text{-}B}$ = 0.6 mm

Lens focal lengths: f_{l_1} = 400 mm f_2 = 150 mm

Dynamic Light Scattering

Detection Mode: VH

Correlation Function: Cross- correlation

High Voltage Power Supply:

V_A = 1865 (V) V_B = 1865 (V)

Correlation File Directory: C:\BI\DATFIL\J31H

Correlation File Name(s): J31H#.DAT (Correlation) J31H#.RAT (Count Rate)

Experiment Duration (of each data set): 30 (secs)

Was a delay file used? √ Yes _ No

If yes, delay file name: C:\BI\DLYFIL\DLY5.DLY

Classical Light Scattering

Light Chopper Frequency: 508 (Hz)

PMT Supply Voltage: 1500 (V)

Laser Power: 0.250 (W)

Number of Samples in Average: 10

Detected Voltages:

VV: 484 ± 63 mV

VH: 4.13 ± 0.15 mV

Depolarization Ratio R_{VH}: 0.85 ± 0.12

Raw Correlation Data

File: J31H5.DAT

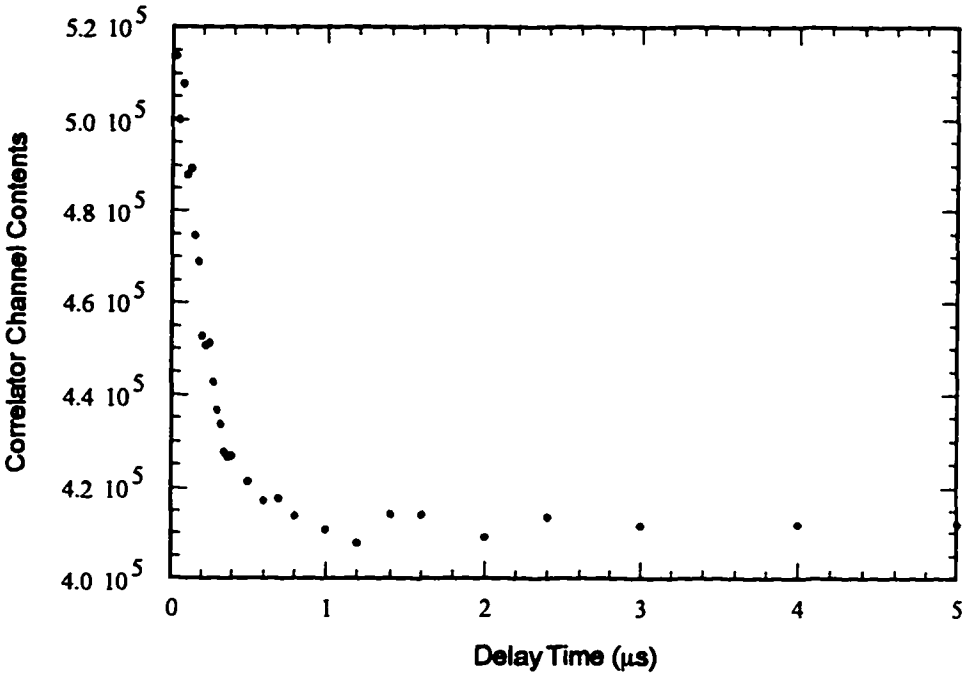

Detection mode:	VH
Duration:	30 s
Number of Samples:	2.919629×10^7
Total Counts - A Input:	5.323254×10^6
Total Counts - B Input:	2.042955×10^6
Calculated Baseline:	3.724846×10^5
Measured Baseline:	4.123159×10^5

(Last 4 channels used for measured baseline evaluation.)

Combined Correlation Data

File: J31H.DAT

(Output from COMBINE3.BAS)

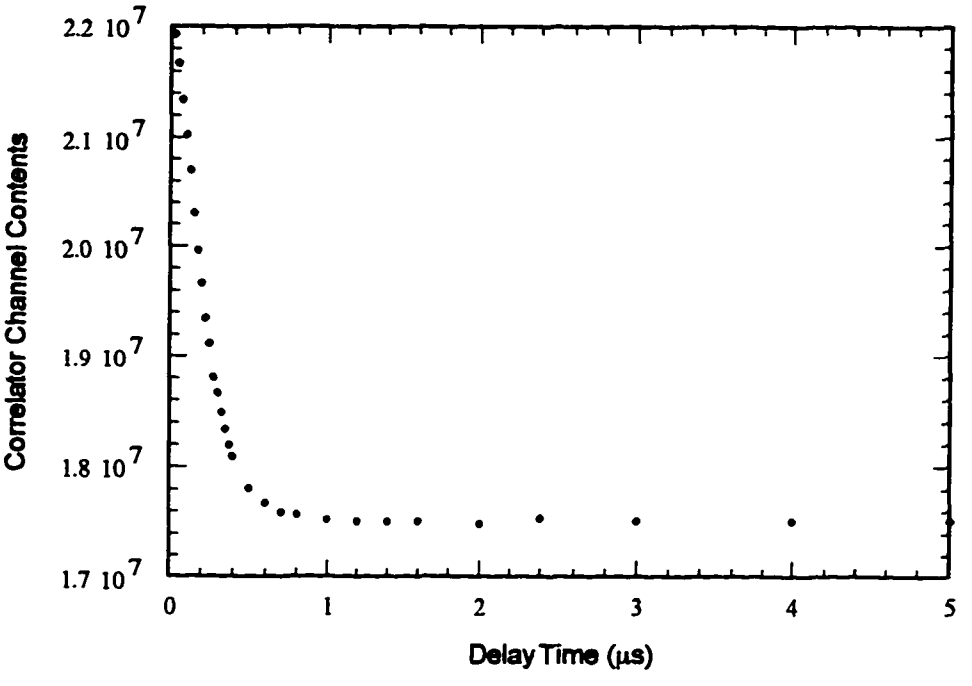

Detection mode:	VH
Total Duration:	59.5 min
Number of Samples:	1.721827×10^9
Total Counts - A Input:	2.577452×10^8
Total Counts - B Input:	9.959682×10^7
Calculated Baseline:	1.490893×10^7
Measured Baseline:	1.751208×10^7
1st Channel Used in Analysis:	Ch# 1 ($\tau = 0.025$ μs)
Last Channel Used in Analysis:	Ch# 20 ($\tau = 0.8$ μs)
Rejected Data Sets:	J31H22.DAT

(Last 4 channels used for measured baseline evaluation.)

Appendix D

Delay File Descriptions

The following tables present the channel spacing and sample time structures determined by the delay files utilized in the experimental portion of this study. The delay files are customizable computer files that permit correlation function acquisition using non-conventional channel-spacing/sample-time combinations. All delay files used in this study utilize the fixed high speed section of the correlator in addition to its variable middle speed section. The fixed *high speed* channels are configured as follows:

Channel Spacings:	Sample Time Δt:
0.025 μs to 0.400 μs in 0.025 μs steps	0.025 μs
0.500 μs to 1 μs in 0.100 μs steps	0.100 μs
1.200 μs to 2.400 μs in 0.200 μs steps	0.100 μs

All delay files used in this study add the corresponding middle speed channel configurations presented below to the high speed channel configuration listed above.

Filename: 39US.DLY

Usage: VV DLS measurements at $\theta = 30°$

Middle Speed Channel Layout:

Channel Spacings:	Sample Time Δt:
3 μs to 39 μs in 1 μs steps	1 μs

Extended Baseline Channels: 160 μs, 161 μs, 162 μs

Filename: DLY5.DLY

Usage: VH DLS measurements at $\theta = 5^\circ$ and $\theta = 30^\circ$

Middle Speed Channel Layout:

Channel Spacings:	Sample Time Δt:
3 μs to 5 μs in 1 μs steps	1 μs

Extended Baseline Channels: none

Filename: DLY161.DLY

Usage: VV DLS measurements at $\theta = 5^\circ$

Middle Speed Channel Layout:

Channel Spacings:	Sample Time Δt:
5 μs to 161 μs in 1 μs steps	1 μs

Extended Baseline Channels: none

Appendix E

Description of Programs

The following is a description of the FORTRAN and QBASIC computer programs developed specifically for this study.

Name:	CREATE.BAS
Language:	QBASIC
Program Location:	BIC 486DX PC in directory C:/BI/CTLFIL
Description:	Creates sequential control files used to automate the correlator measurements
Input Files:	None
Output Files:	Control files: *filename*+A.CTL, *filename*+B.CTL, ...
Libraries Used:	None
Link Command:	None
Execution Statement:	QBASIC/RUN CREATE
Special Notes:	Edit the first three lines of the source code to set the combined experiment duration, the experiment durations, and the individual data set durations. Control files are initiated within the correlator's operating software by pressing *Alt* and F1, typing the name of the control file, and then pressing *Enter*.

Name:	COMBINE3.BAS
Language:	QBASIC
Program Location:	Gateway 2000 P5-75 pentium PC in directory C:/CONTIN
Description:	Interactive program to combine multiple correlation function data sets

Input Files:	Sequentially numbered correlation data files *filename#*.DAT and count rate data files *filename#*.RAT (output from the BI-9000AT correlator)
Output Files:	Combined correlation data file *filename*.DAT and weight files computed using the measured (*filename*.WTM) and calculated (*filename*.WTC) baselines
Libraries Used:	None
Link Command:	None
Execution Statement:	QBASIC/RUN COMBINE3
Special Notes:	The *Caps Lock* key must be active for proper program execution. Type H to display an online help screen.

Name:	DCONV6.BAS
Language:	QBASIC
Program Location:	Gateway 2000 P5-75 pentium PC in directory C:/CONTIN
Description:	Converts combined or individual BI-9000AT correlation data files to CONTIN input file format Creates .CDT and .CWT files for use with CUMULANT.FOR
Input Files:	Combined or individual correlation data file *filename*.DAT and (optional) weight files computed using the measured (*filename*.WTM) or calculated (*filename*.WTC) baseline
Output Files:	CONTIN input data file: *filename*.CON CUMULANT.FOR input data file: *filename*.CDT CUMULANT.FOR weight data file: *filename*.CWT
Libraries Used:	None
Link Command:	None
Execution Statement:	QBASIC/RUN DCONV6
Special Notes:	The *Caps Lock* key must be active for proper program execution. Uses Brookhaven-supplied cumulants program CUMFT.EXE

Name:	RDATA9.BAS
Language:	QBASIC
Program Location:	Gateway 2000 P5-75 pentium PC in directory C:/CONTIN
Description:	Interactive graphical display for CONTIN output
Input File:	CONTIN output file: *filename*.TIN
Output Files:	CONTIN and Cumulants (CUMFT.EXE) moment comparisons in *filename*.MOM (optional) Inverse Laplace transform data with uncertainties in *filename*.OUT (optional)
Libraries Used:	None
Link Command:	None
Execution Statement:	QBASIC/RUN RDATA9
Special Notes:	The *Caps Lock* key must be active for proper program execution. Uses Brookhaven-supplied cumulants program CUMFT.EXE

Name:	CUMULANT.FOR
Language:	FORTRAN
Program Location:	LSU VAX directory: [MEWAGU.MEDISK.PROGRAMS.CUMULANTS]
Description:	Performs weighted polynomial least squares fit of the natural logarithm of the normalized correlation function. The output coefficients are equal to $(-1)^n K_n/n!$, where K_n is the nth order cumulant coefficient.
Input Files:	Correlation function data file: *filename*.CDT Weight data file: *filename*.CWT Both input files are outputs of DCONV6.BAS and must be placed in the directory [MEWAGU.MEDISK.PROGRAMS.CUMULANTS.DATA].

Output Files:	*filename*.OUT - List of least squares coefficients and fit statistics
	filename.PS - Plots of fitted functions and weighted residuals
Libraries Used:	IMSL, PGPLOT
Link Command:	LINK CUMULANT, IMSLIB/LIB, IMSLIB_STATIC/OPT, PGPLOT_DIR:GRPSHR/LIB
Execution Statement:	RUN CUMULANT

Name:	RADCORR.FOR
Language:	FORTRAN
Program Location:	LSU VAX directory: [MEWAGU.MEDISK.PROGRAMS.RADCORR]
Description:	Evaluates uncorrected and radiation-corrected flame temperatures from the voltage output from an iron oxide coated type S thermocouple inserted in an iron-pentacarbonyl-seeded carbon-monoxide/oxygen flame.
Input Files:	None - uses interactive input
Output Files:	None - uses screen output
Libraries Used:	IMSL
Link Command:	LINK RADCORR, STEMP, TCFN, VFLEST, SEEDRATE, AIRPROP, IMSLIB/LIB, IMSLIB_STATIC/OPT
Execution Statement:	RUN RADCORR
Special Notes:	RADCORR.FOR uses subroutines located in the files STEMP.SUB, TCFN.SUB, VFLEST.SUB, SEEDRATE.SUB, AND AIRPROP.SUB.

Vita

Glenn Michael Waguespack was born at the Baton Rouge General Hospital in Baton Rouge, Louisiana, on August 16, 1966 to Mrs. Gerard N. Waguespack and Mr. Robert G. Waguespack. The youngest of three siblings, he spent most of his life in Plaquemine, Louisiana, where he attended St. John the Evangelist school from 1972 to 1984. In 1984 he resumed his schooling at Louisiana State University, where he graduated *summa cum laude* in Mechanical Engineering in 1989. He enrolled in the graduate program later in 1989 at Louisiana State University, where he was granted a three year LSU Board of Regents Fellowship. His studies at LSU have afforded him the opportunity to obtain hands-on and theoretical experience with optical and combustion systems and to deliver professional conference presentations in San Antonio, Texas, and Point Clear, Alabama.

DOCTORAL EXAMINATION AND DISSERTATION REPORT

Candidate: Glenn Waguespack

Major Field: Mechanical Engineering

Title of Dissertation: Studies of the Morphology and Dynamics of Flame-Generated Agglomerates Using Dynamic Light Scattering

Approved:

Major Professor and Chairman

Dean of the Graduate School

EXAMINING COMMITTEE:

Date of Examination:

3-31-97